EXPLAINING EXTREME EVENTS OF 2016

From A Climate Perspective

EXPLAINING EXTREME EVENTS OF 2016 FROM A CLIMATE PERSPECTIVE

Editors

Stephanie C. Herring, Nikolaos Christidis, Andrew Hoell, James P. Kossin,
Carl J. Schreck III, and Peter A. Stott

AMERICAN METEOROLOGICAL SOCIETY

CORRESPONDING EDITOR:

Stephanie C. Herring, PhD
NOAA National Centers for Environmental Information
325 Broadway, E/CC23, Rm 1B-131
Boulder, CO 80305-3328
E-mail: stephanie.herring@noaa.gov

HOW TO CITE THIS DOCUMENT
_____

Citing the complete report:

Herring, S. C., N. Christidis, A. Hoell, J. P. Kossin, C. J. Schreck III, and P. A. Stott, Eds., 2018: Explaining Extreme Events of 2016 from a Climate Perspective. *Bull. Amer. Meteor. Soc.*, **99** (1), S1–S157.

Citing a section (example):

Quan, X.W., M. Hoerling, L. Smith, J. Perlwitz, T. Zhang, A. Hoell, K. Wolter, and J. Eischeid, 2018: Extreme California Rains During Winter 2015/16: A Change in El Niño Teleconnection? [in "Explaining Extreme Events of 2016 from a Climate Perspective"]. *Bull. Amer. Meteor. Soc.*, **99** (1), S54–S59, doi:10.1175/BAMS-D-17-0118.1.

EDITORIAL AND PRODUCTION TEAM

Riddle, Deborah B., Lead Graphics Production, NOAA/NESDIS National Centers for Environmental Information, Asheville, NC

Love-Brotak, S. Elizabeth, Graphics Support, NOAA/NESDIS National Centers for Environmental Information, Asheville, NC

Veasey, Sara W., Visual Communications Team Lead, NOAA/NESDIS National Centers for Environmental Information, Asheville, NC

Fulford, Jennifer, Editorial Support, Telesolv Consulting LLC, NOAA/NESDIS National Centers for Environmental Information, Asheville, NC

Griffin, Jessicca, Graphics Support, Cooperative Institute for Climate and Satellites-NC, North Carolina State University, Asheville, NC

Misch, Deborah J., Graphics Support, Telesolv Consulting LLC, NOAA/NESDIS National Centers for Environmental Information, Asheville, NC

Osborne, Susan, Editorial Support, Telesolv Consulting LLC, NOAA/NESDIS National Centers for Environmental Information, Asheville, NC

Sprain, Mara, Editorial Support, LAC Group, NOAA/NESDIS National Centers for Environmental Information, Asheville, NC

Young, Teresa, Graphics Support, Telesolv Consulting LLC, NOAA/NESDIS National Centers for Environmental Information, Asheville, NC

TABLE OF CONTENTS

ABSTRACT—Stephanie C. Herring, Nikolaos Christidi, Andrew Hoell, James P. Kossin, Carl J. Schreck III, and Peter A. Stott

This sixth edition of explaining extreme events of the previous year (2016) from a climate perspective is the first of these reports to find that some extreme events were not possible in a preindustrial climate. The events were the 2016 record global heat, the heat across Asia, as well as a marine heat wave off the coast of Alaska. While these results are novel, they were not unexpected. Climate attribution scientists have been predicting that eventually the influence of human-caused climate change would become sufficiently strong as to push events beyond the bounds of natural variability alone. It was also predicted that we would first observe this phenomenon for heat events where the climate change influence is most pronounced. Additional retrospective analysis will reveal if, in fact, these are the first events of their kind or were simply some of the first to be discovered.

Last year, the editors emphasized the need for additional papers in the area of "impacts attribution" that investigate whether climate change's influence on the extreme event can subsequently be directly tied to a change in risk of the socio-economic or environmental impacts. Several papers in this year's report address this challenge, including Great Barrier Reef bleaching, living marine resources in the Pacific, and ecosystem productivity on the Iberian Peninsula. This is an increase over the number of impact attribution papers than in the past, and are hopefully a sign that research in this area will continue to expand in the future.

Other extreme weather event types in this year's edition include ocean heat waves, forest fires, snow storms, and frost, as well as heavy precipitation, drought, and extreme heat and cold events over land. There were a number of marine heat waves examined in this year's report, and all but one found a role for climate change in increasing the severity of the events. While human-caused climate change caused China's cold winter to be less likely, it did not influence U.S. storm Jonas which hit the mid-Atlantic in winter 2016.

As in past years, the papers submitted to this report are selected prior to knowing the final results of whether human-caused climate change influenced the event. The editors have and will continue to support the publication of papers that find no role for human-caused climate change because of their scientific value in both assessing attribution methodologies and in enhancing our understanding of how climate change is, and is not, impacting extremes. In this report, twenty-one of the twenty-seven papers in this edition identified climate change as a significant driver of an event, while six did not. Of the 131 papers now examined in this report over the last six years, approximately 65% have identified a role for climate change, while about 35% have not found an appreciable effect.

Looking ahead, we hope to continue to see improvements in how we assess the influence of human-induced climate change on extremes and the continued inclusion of stakeholder needs to inform the growth of the field and how the results can be applied in decision making. While it represents a considerable challenge to provide robust results that are clearly communicated for stakeholders to use as part of their decision-making processes, these annual reports are increasingly showing their potential to help meet such growing needs.

1. INTRODUCTION TO EXPLAINING EXTREME EVENTS OF 2016 FROM A CLIMATE PERSPECTIVE

Stephanie C. Herring, Nikolaos Christidis, Andrew Hoell,
James P. Kossin, Carl J. Schreck III, and Peter A. Stott

Over the past six years, more than 130 peer-reviewed papers evaluating the potential connection between extreme weather and anthropogenic climate change have been presented in this annual special edition of the *Bulletin of the American Meteorological Society*. Of the roughly 89 papers that did identify a climate change signal in the authors' analysis of an extreme event, each found climate change had shifted the odds of an event happening. Prior to this year, however, none had determined that human-caused climate change was an essential factor in the occurrence of the event. In this year's report, for the first time, we present three new research papers that conclude the extreme magnitude of a particular weather event was not possible without the influence of human-caused climate change.

- In a paper analyzing the 2016 global heat record by NOAA scientist Tom Knutson et al., the authors concluded that record global warmth "was only possible due to substantial centennial-scale human-caused warming."
- Similarly, a study of the record heat over Asia led by Yukiko Imada of the Japanese Meteorological Agency found that the extreme warmth across Asia in 2016 "would not have been possible without climate change."
- In addition to these two papers looking at atmospheric temperatures, a team led by John Walsh of the University of Alaska determined that a large, persistent area of anomalously warm ocean water off the coast of Alaska (often referenced as "the Blob") found "no instances of 2016-like anomalies in the preindustrial climate" for sea surface temperatures in the Bering Sea.

These results are novel, and we would argue, sig-

nificant for two reasons. First, it is important to note that climate scientists have been predicting that, based on the ongoing global warming of Earth's climate, the influence of human-caused climate change would at some point become sufficiently strong and emergent to push an extreme event beyond the bounds of natural variability alone. It was also anticipated that we would likely first see this result for heat events where the human-caused influences are most strongly observed. It is striking how quickly we are now starting to see such results, though their dependence on model-based estimates of natural variability in the absence of human-induced change will require ongoing validation of the time-of-emergence for extreme event magnitudes at local scales. Second, because of the small sample size of events shown in this report, it is possible that other temperature-related extreme events occurring in prior years may also have been impossible to achieve without human-induced climate change. Retrospective studies would be needed to explore this possibility. The 2016 results do not necessarily indicate that some climate threshold or tipping point has been reached.

It is helpful to consider the methodology used in these studies to understand the conclusions. Each used the commonly accepted event attribution technique of calculating the fraction of attributable risk (FAR) for the event, a statistical approach borrowed from epidemiology and public health, establishing the probability of the event happening with greenhouse gas emissions at current levels due to human activity. For heat events, this probability relies in large part on the observational record. This result is compared with model runs of a "control" world that only include natural forcing mechanisms and ignore the changes to atmospheric composition driven by human greenhouse gas emissions.

All three papers concluded that the FAR was 1, meaning that the event was not possible in the "control" planet, and only possible in a world with human-emitted greenhouse gases. It should also be recognized that although FAR = 1 in relation to a human-induced impact in these cases, other climate drivers that also affect the probability of such ex-

Fig. 1.1. Location and types of events analyzed in this publication.

tremes may have been major additional contributors to the likelihood of the event occurring. Each of these papers applied large model ensembles (CMIP5 for both the global heat and Alaska marine heat wave analyses and the atmospheric general circulation model MIROC5 for the Asia heat study) to determine the FAR for these events.

As in past years, this sixth edition of *Explaining Extreme Events from a Climate Perspective* includes studies of extreme events from around the world that did not find a role for climate change in influencing the magnitude or frequency of an event. It is important to note that papers are selected for consideration in this report by reviewing author proposals that do not indicate whether a role for climate change will or will not be found. Thus, there is no selection bias on the part of the editorial team toward one particular conclusion, and this publication prides itself as a venue that accepts papers without consideration for whether a role for climate change is found. This year there may be a slight bias toward events that do not find a signal relative to previous years because the editors have begun to limit the number of heat papers in the report which is the event type where a signal is most commonly found. Given that the majority of heat papers now use a widely established and accepted

methodology, the scientific value of continuing to include a large number of heat studies began to seem limited.

Extreme weather event types included in this year's edition include ocean heat waves, forest fires, snow storms, and frost, as well as heavy precipitation, drought, and extreme heat and cold events over land. A number of papers also look at the impacts of extremes (Fig. 1.1). The Summary of Results Table (Table 1.1) gives readers a general overview of the results.

Twenty-one of the 27 papers in this current edition identified climate change as a significant driver of an event, while six did not. Of the 131 papers now examined in this report over the last six years, approximately 65% have identified a role for climate change, while about 35% have not found an appreciable effect.

Nevertheless, over the past six years, researchers have identified the robust influence of climate change on temperature-related extremes, making such high-temperature events quantifiably more intense and more frequent. The events studied by these 131 papers were not chosen randomly and may not be representative of all extreme events. They are concentrated mostly on the continents of North America, Europe, Asia, and Australia, so there remains an open question of how human-caused climate change may be

influencing extreme weather in parts of the world that are not as well studied.

Last year, the editors called on scientists submitting research proposals to investigate potential links between an extreme event and its subsequent impact, and we were excited to see five research teams take on this challenge in this year's report. Lewis and Mallela concluded that the risk of the extreme Great Barrier Reef bleaching event was increased through anomalously high sea surface temperature and the accumulation of thermal stress caused by human-caused climate change. Jacox et al. and Brainard et al. both examined how high ocean temperatures caused in part by human-caused climate change impacted living marine resources like coral bleaching, reduced fish stocks, and a decrease in seabird counts in the California current and the equatorial Pacific, respectively. On land, Sippel et al. found that human-caused climate change is causing warmer winters on the Iberian Peninsula and, when coupled with a wet spring, drove higher ecosystem productivity in the region in 2016. However, these papers represent early approaches, and more work is needed to develop impact attribution methodologies.

As is always the case, we would caution that the results of any single study should not be interpreted as the final word on the matter for that event, nor be generalized to a broader class of extremes. For example, authors of these papers selected specific modeling approaches and made other choices about factors that are important in how the models replicate extreme events, such as terrestrial heat or sea surface temperatures. If other study designs were applied to these events, it is possible a different result would be reached. The importance of the methodological approach in attribution research is further discussed in the summary of this report (Stott et al.).

A big question raised by this collection of research is whether these findings undermine the axiom that "no event is caused by climate change alone and that natural variability always plays some role." The short answer is no. While several of the studied events were found not to be possible without climate change, natural variability still laid the foundation for the events to occur, and the authors acknowledge this in their papers. Extreme events are always the result of a cumulative set of factors. The building blocks that form the foundation of any event continue to include natural variability, with factors such as El Niño potentially adding to the strength of the event. These temperature-related extremes would likely still have been warm events even without human-caused climate change, but according to these analyses, the events could not have surpassed the extreme warm thresholds that they did without climate change. This was especially the case for the record-setting globally averaged temperature. At the global scale, the natural variations of Earth's temperature are increasingly seen to pale in comparison to the growing intensity of human-induced warming. Overall, human-caused climate change allowed them to pass a threshold that they could not otherwise have exceeded.

These papers also emphasize why clearer understanding of how human-caused climate change impacts extreme events is an important area of research. Retrospective analysis of previous extreme events may yield new insights into the history of human-caused climate change impacts, and we can expect to see insights into the extent and timing of the changes in the future.

Table 1.1. SUMMARY of RESULTS

	ANTHROPOGENIC INFLUENCE ON EVENT		
	INCREASE	**DECREASE**	**NOT FOUND OR UNCERTAIN**
Heat	Ch. 3: Global Ch. 7: Arctic Ch. 15: France Ch. 19: Asia		
Cold		Ch. 23: China Ch. 24: China	
Heat & Dryness	Ch. 25: Thailand		
Marine Heat	Ch. 4: Central Equatorial Pacific Ch. 5: Central Equatorial Pacific Ch. 6: Pacific Northwest Ch. 8: North Pacific Ocean/Alaska Ch. 9: North Pacific Ocean/Alaska Ch. 9: Australia		Ch. 4: Eastern Equatorial Pacific
Heavy Precipitation	Ch. 20: South China Ch. 21: China (Wuhan) Ch. 22: China (Yangtze River)		Ch. 10: California (failed rains) Ch. 26: Australia Ch. 27: Australia
Frost	Ch. 29: Australia		
Winter Storm			Ch. 11: Mid-Atlantic U.S. Storm "Jonas"
Drought	Ch. 17: Southern Africa Ch. 18: Southern Africa		Ch. 13: Brazil
Atmospheric Circulation			Ch. 15: Europe
Stagnant Air			Ch. 14: Western Europe
Wildfires	Ch. 12: Canada & Australia (Vapor Pressure Deficits)		
Coral Bleaching	Ch. 5: Central Equatorial Pacific Ch. 28: Great Barrier Reef		
Ecosystem Function		Ch. 5: Central Equatorial Pacific (Chl-a and primary production, sea bird abundance, reef fish abundance) Ch. 18: Southern Africa (Crop Yields)	
El Niño	Ch. 18: Southern Africa		Ch. 4: Equatorial Pacific (Amplitude)
TOTAL	**18**	**3**	**9**

	METHOD USED			Total Events
Heat	Ch. 3: CMIP5 multimodel coupled model assessment with piCont, historicalNat, and historical forcings Ch. 7: CMIP5 multimodel coupled model assessment with piCont, historicalNat, and historical forcings Ch. 15: Flow analogues conditional on circulation types Ch. 19: MIROC-AGCM atmosphere only model conditioned on SST patterns			
Cold	Ch. 23: HadGEM3-A (GA6) atmosphere only model conditioned on SST and SIC for 2016 and data fitted to GEV distribution Ch. 24: CMIP5 multimodel coupled model assessment			
Heat & Dryness	Ch. 25: HadGEM3-A N216 Atmosphere only model conditioned on SST patterns			
Marine Heat	Ch. 4: SST observations; SGS and GEV distributions; modeling with LIM and CGCMs (NCAR CESM-LE and GFDL FLOR-FA) Ch. 5: Observational extrapolation (OISST, HadISST, ERSST v4) Ch. 6: Observational extrapolation; CMIP5 multimodel coupled model assessment Ch. 8: Observational extrapolation; CMIP5 multimodel coupled model assessment Ch. 9: Observational extrapolation; CMIP5 multimodel coupled model assessment			
Heavy Precipitation	Ch. 10: CAM5 AMIP atmosphere only model conditioned on SST patterns and CESM1 CMIP single coupled model assessment Ch. 20: Observational extrapolation; CMIP5 and CESM multimodel coupled model assessment; auto-regressive models Ch. 21: Observational extrapolation; HadGEM3-A atmosphere only model conditioned on SST patterns; CMIP5 multimodel coupled model assessment with ROF Ch. 22: Observational extrapolation, CMIP5 multimodel coupled model assessment Ch. 26: BoM seasonal forecast attribution system and seasonal forecasts Ch. 27: CMIP5 multimodel coupled model assessment			
Frost	Ch. 29: *weather@home* multimodel atmosphere only models conditioned on SST patterns; BoM seasonal forecast attribution system			
Winter Storm	Ch. 11: ECHAM5 atmosphere only model conditioned on SST patterns			
Drought	Ch. 13: Observational extrapolation; weather@home multimodel atmosphere only models conditioned on SST patterns; HadGEM3-A and CMIP5 multimodel coupled model assessent; hydrological modeling Ch. 17: Observational extrapolation; CMIP5 multimodel coupled model assessment; VIC land surface hdyrological model, optimal fingerprint method Ch. 18: Observational extrapolation; *weather@home* multimodel atmosphere only models conditioned on SSTs, CMIP5 multimodel coupled model assessment			
Atmospheric Circulation	Ch. 15: Flow analogues distances analysis conditioned on circulation types			
Stagnant Air	Ch. 14: Observational extrapolation; Multimodel atmosphere only models conditioned on SST patterns including: HadGEM3-A model; EURO-CORDEX ensemble; EC-EARTH+RACMO ensemble			
Wildfires	Ch. 12: HadAM3 atmospere only model conditioned on SSTs and SIC for 2015/16			
Coral Bleaching	Ch. 5: Observations from NOAA Pacific Reef Assessment and Monitoring Program surveys Ch. 28: CMIP5 multimodel coupled model assessment; Observations of climatic and environmental conditions (NASA GES DISC, HadCRUT4, NOAA OISSTV2)			
Ecosystem Function	Ch. 5: Observations of reef fish from NOAA Pacific Reef Assessment and Monitoring Program surveys; visual observations of seabirds from USFWS surveys. Ch. 18: Empirical yield/rainfall model			
El Niño	Ch. 4: SST observations; SGS and GEV distributions; modeling with LIM and CGCMs (NCAR CESM-LE and GFDL FLOR-FA) Ch. 18: Observational extrapolation; *weather@home* multimodel atmosphere only models conditioned on SSTs, CMIP5 multimodel coupled model assessment			
				30

ACRONYMS

AMIP: Atmospheric Model Intercomparison Project

BOM: Bureau of Meteorology, Australia

CAM: Community Atmosphere Model, www.cesm.ucar.edu/

CESM: Community Earth System Model

CMIP: Coupled Model Intercomparison Project

GEV: Generalized extreme value

GFDL FLOR: Geophysical Fluid Dynamics Laboratory Forecast-Oriented Low Ocean Resolution

HadGEM3-A: Hadley Centre Global Environmental Model version 3-A

LIM: Linear inverse model

MIROC5-AGCM: Model for Interdisciplinary Research on Climate - Atmospheric General Circulation Model

ROF: Regularized optimal fingerprinting

SGS: Stochastically-generated skewed

SIC: Sea ice concentration

SST: Sea Surface Temperature

USFWS: U.S. Fish and Wildlife Service

VIC: Variable infiltration capacity

weather@home: www.climateprediction.net/weatherathome/

REFERENCES

Brainard, R., and Coauthors, 2018: Ecological impacts of the 2015/16 El Niño in the central equatorial Pacific [in "Explaining Extreme Events of 2016 from a Climate Perspective"]. *Bull. Amer. Meteor. Soc.*, **99** (1), S21–S26, doi:10.1175/10.1175/BAMS-D-17-0128.1.

Imada, Y., H. Siogama, C. Takahashi, M. Watanabe, M. Mori, Y. Kamae, and S. Maeda, 2018: Climate change increased the likelihood of the 2016 heat extremes in Asia [in "Explaining Extreme Events of 2016 from a Climate Perspective"]. *Bull. Amer. Meteor. Soc.*, **99** (1), S97–S101, doi:10.1175/BAMS-D-17-0109.1.

Jacox, M. G., M. A. Alexander, N. J. Mantua, J. D. Scott, G. Hervieux, R. S. Webb, and F. E. Werner, 2018: Forcing of multiyear extreme ocean temperatures that impacted California Current living marine resources in 2016 [in "Explaining Extreme Events of 2016 from a Climate Perspective"]. *Bull. Amer. Meteor. Soc.*, **99** (1), S27–S33, doi:10.1175/BAMS-D-17-0119.1

Knutson, T. R., J. Kam, F. Zeng, and A. T. Wittenberg, 2018: CMIP5 model-based assessment of anthropogenic influence on record global warmth during 2016 [in "Explaining Extreme Events of 2016 from a Climate Perspective"]. *Bull. Amer. Meteor. Soc.*, **99** (1), S11–S15, doi:10.1175/BAMS-D-17-0104.1

Lewis, S. C., and J. Mallela, 2018: A multifactor risk analysis of the record 2016 Great Barrier Reef bleaching [in "Explaining Extreme Events of 2016 from a Climate Perspective"]. *Bull. Amer. Meteor. Soc.*, **99** (1), S144–S149, doi:10.1175/BAMS-D-17-0074.1.

Sippel, S., and Coauthors, 2018: Warm winter, wet spring, and an extreme response in ecosystem functioning on the Iberian Peninsula [in "Explaining Extreme Events of 2016 from a Climate Perspective"]. *Bull. Amer. Meteor. Soc.*, **99** (1), S80–S85, doi:10.1175/BAMS-D-17-0135.1.

Stott, P. A., N. Christidis, S. C. herring, A. Hoell, M. P. Hoerling, J. P. Kossing, C. J. Schreck III, 2018: Future challenges in event attribution methodologies [in "Explaining Extreme Events of 2016 from a Climate Perspective"]. *Bull. Amer. Meteor. Soc.*, **99** (1), S155–S159, doi:10.1175/BAMS-D-17-0265.1.

Walsh, J. E., and Coauthors, 2018: The high latitude marine heat wave of 2016 and its impacts on Alaska [in "Explaining Extreme Events of 2016 from a Climate Perspective"]. *Bull. Amer. Meteor. Soc.*, **99** (1), S39–S43, doi:10.1175/BAMS-D-17-0105.1.

2. EXPLAINING EXTREME OCEAN CONDITIONS IMPACTING LIVING MARINE RESOURCES

Robert S. Webb and Francisco E. Werner

The Food and Agriculture Organization of the United Nations (FAO) (2016) estimates for 2014 that the global trade in fish and fishery products was near $148 billion (U.S. dollars) and employed close to 38 million people. Healthy ecosystems are also important for sustaining coastal marine tourism activities estimated globally to be over $160 billion (U.S. dollars) per year (FAO 2016). Additionally, estimates from the World Bank (2017) indicate that additional benefits could be gained (e.g., $83 billion dollars in 2012) with higher sustainable harvest attainable due to larger fish biomass; lower fishing costs due to lower fishing effort; and higher unit prices of landings due to improved species composition of the global stock. Given the important socioeconomic value of coastal and marine resources [Fisheries Economics of the United States (NMFS 2015)], when confronted with fluctuations in fisheries or significant changes in marine ecosystems, stakeholders (e.g., the public, commercial and sport fishing industries, fishery managers, scientists, coastal community conservationists, environmental groups, and the media) are increasingly asking the scientific research community if the observed, and perceived to be unprecedented, extremes and trends in ocean conditions that impact living marine resources are due to natural variability (i.e., potential recurrences of past events) or a manifestation of long-term changes in climate (i.e., "new normals" or "regime shifts" not experienced before; King et al. 2005).

A clear understanding of the background conditions and underlying processes resulting in extremes and trends in ocean conditions impacting living marine resources are of value to guide decision making. Without this knowledge, policy, planning, and decision makers face greater uncertainties in making informed decisions to minimize disruptive impacts, to guide management choices to better prepare for future changes, and to inform sustainability strategies to ensure the continued benefits of healthy and productive marine ecosystems. Regional Fisheries

Management Councils in the United States, and similar regulatory bodies in other parts of the world, allow participatory governance by knowledgeable people with a stake in their individual regions to develop marine fisheries management plans (such as fishing seasons, quotas, and closed areas) based on sound scientific advice. When confronted with extreme ocean conditions impacting marine ecosystems and fisheries, in order to make informed decisions on how to best manage the impacted living marine resources, fisheries management organizations can use answers to four fundamental questions: *What happened? Why did it happen? Is it predictable? and What is the likelihood of it happening again?* To answer these questions, the *BAMS* 2016 report "Explaining Extreme Events from a Climate Perspective" includes three studies that strive to connect attribution of an extreme ocean condition with the socioeconomic impacts on living marine resources: "A multifactor analysis of the record 2016 Great Barrier Reef bleaching" (Lewis and Mallela 2018); "Ecological impacts of the 2015/16 El Niño in the central equatorial Pacific" (Brainard et al. 2018); and "Multiyear extreme ocean temperatures with impacts on living marine resources off the U.S. West Coast during 2016" (Jacox et al. 2018).

These and previous studies (see Table 2.1 for selected examples) describe physical and biogeochemical characteristics impacting living marine resources, and strive to identify climate mechanisms and forcings that led to their occurrence. Large-scale patterns of coupled ocean–atmospheric circulation are assessed in terms of their influence on the statistics of extreme events regionally. The goal of these studies is to explain the effects of individual extreme ocean condition events (e.g., marine heat waves, Hobday et al. 2016; Ummenhofer and Meehl 2017), or cumulative effects of trends and trajectories in ocean conditions that can result in abrupt shifts, and potentially to tipping points, in marine ecosystems that can last for prolonged periods (e.g., deYoung et al. 2008; Möllmann et al. 2015), and ultimately provide process-understanding of the resulting impacts (e.g., Rocha et al. 2015). Such effects include the physical or biogeochemical characteristics of the environment (temperature, salinity, nutrient levels), ecosystem

TABLE 2.1. Examples of climate attribution studies of an extreme ocean conditions impacting on living marine resources (also see Brainard et al. 2018, Jacox et al. 2018, and Lewis and Mallela 2018, chapters 5, 6, and 28, in this report).

Title	Author	Geographic Location	Timing of Event
What caused the Sacramento River fall Chinook stock collapse?	Lindley et al. 2009	U.S West Coast/ California Current	2008
Climate change impact on the northeast Atlantic cusk	Hare et al. 2012	Gulf of Maine, Georges Bank, and the Scotian Shelf	mid-1990s
West Coast Dungeness crab fishery	Marshall et al. 2017	U.S. West Coast	2016
New England Cod Collapse	Meng et al. 2016	Gulf of Maine	2014
Beluga whale migration altered by delayed sea ice formation	Hauser et al. 2016	Eastern Chukchi Sea and Eastern Beaufort Sea	2004–2012
California Current large marine ecosystem	Cavole et al. 2016	Northeast Pacific	2014–2016

living marine resources can be used to assess vulnerabilities and to guide adaptation and mitigation decision making by fisheries management councils to improved resilience in a varying and changing climate (e.g., Hare et al. 2016).

Management decisions on how to respond to extreme environmental conditions will clearly benefit from a mechanistic understanding. Such understanding can provide quantitative estimates of the relative contributions of natural variability, anthropogenic climate change, and other factors through fraction of attributable risk (FAR; Stott et al. 2004) and other statistical analyses. The added insights will assist fisheries management bodies in considering strategies to deal with extreme events, anticipate the risks (and their confidence intervals) to human and natural systems, and thereby support management and protection of marine resources at national regional, state, and local levels.

In the short term, these studies provide resource managers with better understanding of the current and future risk of extreme ocean conditions impacting living marine resources that enable better-informed policies, planning, and decisions made based upon the best available scientific understanding. In the longer term, the rigorous understanding of the predictability and future risk of extreme ocean conditions can advance both the science and decision criteria needed to improve the certainty of threat assessments for ocean conditions impacting commercial and recreational fisheries and other marine resources. While the impacts on, and responses by, living marine resources are typically the result of the cumulative effect of multiple stressors, risk-based analyses of extreme ocean conditions are of value to inform integrated ecosystem-based fisher-

structure (changes in community make-up, shifts between benthic and pelagic production), fisheries (shifts in distribution and/or abundance of important commercial and recreational species), and the socioeconomic impacts on the human communities that depend on them.

For example, consider recent extreme regional ocean conditions events resulting in changes in ecosystems and regional fishery stocks (e.g., Cavole et al. 2016) following a previous and perceived to be unprecedented collapse in some of the same fishery stocks ten years earlier (e.g., Lindley et al. 2009). Critical risk management questions are whether there has been a shift in the probability of ocean conditions leading to such an extreme impact, and whether living marine resource managers can, or should, adapt to an apparent increased risk[1]. Assessments of how natural and human causes influence the probability of extremes and trends in ocean conditions impacting

---

[1] www.st.nmfs.noaa.gov/ecosystems/climate/activities/assessing -vulnerability-of-fish-stocks and www.st.nmfs.noaa.gov/ecosystems /climate/national-climate-strategy

ies management decisions (e.g., Fulton et al. 2013; NOAA's 2016 Ecosystem Based Fisheries Management Roadmap, www.st.nmfs.noaa.gov/Assets/ecosystems/ebfm/EBFM_Road_Map_final.pdf) to maximize the global, national, regional, and local socioeconomic value of living marine resources.

REFERENCES

Brainard, R. E., and Coauthors, 2018: Ecological impacts of the 2015/16 El Niño in the central equatorial Pacific [in "Explaining Extreme Events of 2016 from a Climate Perspective"]. *Bull. Amer. Meteor. Soc.*, **99** (1), S21–S26, doi:10.1175/BAMS-D-17-0128.1.

Cavole, L. M., and Coauthors, 2016: Biological impacts of the 2013–2015 warm-water anomaly in the northeast Pacific. *Oceanography*, **29** (2), 273–285, doi:10.5670/oceanog.2016.32.

deYoung, B., M. Barange, G. Beaugrand, R. Harris, R. I. Perry, M. Scheffer, and F. Werner, 2008: Regime shifts in marine ecosystems: Detection, prediction and management. *Trends Ecol. Evol.*, **23**, 402–409, doi:10.1016/j.tree.2008.03.008.

FAO, 2016: *The State of World Fisheries and Aquaculture 2016*: *Contributing to Food Security and Nutrition for All.* Food and Agricultural Organization of the United Nations, 200 pp. [Available online at www.fao.org/publications/sofia/2016/en/.]

Fulton, E. A., A. D. Smith, D. C. Smith, and P. Johnson, 2014: An integrated approach is needed for ecosystem based fisheries management: Insights from ecosystem-level management strategy evaluation. *PLoS One*, **9**, e84242, doi:10.1371/journal.pone.0084242.

Hare, J. A., and Coauthors, 2012: Cusk (*Brosme brosme*) and climate change: Assessing the threat to a candidate marine fish species under the US Endangered Species Act. *ICES J. Mar. Sci.*, **69**, 1753–1768, doi:10.1093/icesjms/fss160.

——, and Coauthors, 2016: A vulnerability assessment of fish and invertebrates to climate change on the Northeast U.S. continental shelf. *PLoS One*, **11**, e0146756, doi:10.1371/journal.pone.0146756.

Hauser, D. D. W., K. L. Laidre, K. M. Stafford, H. L. Stern, R. S. Suydam, and P. R. Richard, 2016: Decadal shifts in autumn migration timing by Pacific Arctic beluga whales are related to delayed annual sea ice formation. *Global Change Biol.*, **23**, 2206–2217, doi:10.1111/gcb.13564.

Hobday, A. J., and Coauthors, 2016: A hierarchical approach to defining marine heatwaves. *Prog. Oceanogr.*, **141**, 227–238, doi:10.1016/j.pocean.2015.12.014.

Jacox, M. G., M. A. Alexander, N. J. Mantua, J. D. Scott, G. Hervieux, R. S. Webb and F. E. Werner, 2018: Forcing of multiyear extreme ocean temperatures that impacted California Current living marine resources in 2016 [in "Explaining Extreme Events of 2016 from a Climate Perspective"]. *Bull. Amer. Meteor. Soc.*, **99** (1), S27–S33, doi:10.1175/BAMS-D-17-0119.1.

King, J. R., Ed., 2005: Report of the study group on fisheries and ecosystem responses to recent regime shifts. PICES Scientific Rep. 28, 162 pp. [Available online at www.pices.int/publications/scientific_reports/Report28/Rep_28_FERRRS.pdf.]

Lewis, S., and J. Mallela, 2018: A multifactor analysis of the record 2016 Great Barrier Reef bleaching [in "Explaining Extreme Events of 2016 from a Climate Perspective"]. *Bull. Amer. Meteor. Soc.*, **99** (1), S144–S149, doi:10.1175/BAMS-D-17-0074.1.

Lindley, S. T., and Coauthors, 2009: What caused the Sacramento River fall chinook stock collapse? NOAA Tech. Memo. NMFS-SWFSC-447, 121 pp. [Available online at https://swfsc.noaa.gov/publications/TM/SWFSC/NOAA-TM-NMFS-SWFSC-447.pdf.]

Marshall, K. N., and Coauthors, 2017: Risks of ocean acidification in the California Current food web and fisheries: Ecosystem model projections. *Global Change Biol.*, **23**, 1525–1539, doi:10.1111/gcb.13594.

Meng, K. C., K. L. Oremus, and S. D. Gaines, 2016: New England cod collapse and the climate. *PLoS One*, **11**, e0158487, doi:10.1371/journal.pone.0158487.

Möllmann, C., C. Folke, M. Edwards, and A. Conversi, 2015: Marine regime shifts around the globe: Theory, drivers and impacts. *Philos. Trans. Roy. Soc. London B*, **370**, 20130260, doi:10.1098/rstb.2013.0260.

NMFS, 2016: Fisheries economics of the United States 2014. NOAA Tech. Memo. NMFS-F/SPO-163, 235 pp. [Available online at https://spo.nmfs.noaa.gov/sites/default/files/TM163.pdf.]

Rocha, J., J. Yletyinen, R. Biggs, T. Blenckner, and G. Peterson, 2015: Marine regime shifts: Drivers and impacts on ecosystems services. *Philos. Trans. Roy. Soc. B*, **370**, 20130273, doi:10.1098/rstb.2013.0273.

Stott, P. A., D. A. Stone, and M. R. Allen, 2004: Human contribution to the European heatwave of 2003. *Nature*, **432**, 610–614, doi:10.1038/nature03089.

Ummenhofer, C. C., and G. A. Meehl, 2017: Extreme weather and climate events with ecological relevance: A review. *Philos. Trans. Roy. Soc. B*, **372**, 20160135, doi:10.1098/rstb.2016.0135.

World Bank, 2017: *The Sunken Billions Revisited: Progress and Challenges in Global Marine Fisheries*. World Bank, 99 pp., doi:10.1596/978-1-4648-0919-4.

3. CMIP5 MODEL-BASED ASSESSMENT OF ANTHROPOGENIC INFLUENCE ON RECORD GLOBAL WARMTH DURING 2016

Thomas R. Knutson, Jonghun Kam, Fanrong Zeng, and Andrew T. Wittenberg

According to CMIP5 simulations, the 2016 record global warmth was only possible due to substantial centennial-scale anthropogenic warming. Natural variability made a smaller contribution to the January–December 2016 annual-mean global temperature anomaly.

Global annual-mean surface temperature set a record high in 2016 in at least three observational datasets—GISTEMP (Hansen et al. 2010), HadCRUT4.5 (Morice et al. 2012), and NOAA (Karl et al. 2015)—exceeding the previous record set in 2015 (Fig. 3.1a). In contrast, the last global mean annual *cold* record occurred around 1910. Record global warmth implies some record warmth on regional scales as well (Kam et al. 2016), which can cause important impacts such as thermal stress, coral bleaching, and melting of sea and land ice (IPCC 2013). Decreased land ice, combined with ocean heat uptake, contributes to sea level rise, which can exacerbate coastal flooding extremes (e.g., Lin et al. 2016).

Figure 3.1 compares observed global-mean temperature anomalies with simulations from the Coupled Model Intercomparison Project 5 (CMIP5; Taylor et al. 2012; Table ES3.1). Record warmth in 2016 largely follows a pronounced century-scale warming trend, and was far outside the range of internal (unforced) climate variability sampled across over 24 000 years of CMIP5 Control simulations (Fig. 3.1c). It was also well outside the range of CMIP5 Natural Forcing-Only simulations incorporating solar and volcanic forcing changes (Fig. 3.1b). In contrast, the observed warming lies within the range of CMIP5 All-Forcing simulations that include both anthropogenic and natural forcing (Fig. 3.1a). These results suggest that observed global-mean temperatures emerged from

the natural variability background (natural forcing response plus internal variability) around 1980, and have become increasingly detectable since.

The inconsistency of observed long-term global warming with simulated natural variability (detection), and its consistency with simulations incorporating anthropogenic forcing (attribution), are in agreement with previous studies and assessments (e.g., IPCC 2001, 2007, 2013; Knutson et al. 2013; Kam et al. 2016). Detection and attribution of human influence on global mean temperature is well-established in the climate sciences, including through more sophisticated approaches than shown here (e.g., regressions or pattern scaling; Bindoff et al. 2013 and references therein). The adequacy of CMIP5 model simulations of internal variability for detection and attribution has also been assessed previously (e.g., IPCC 2013; Knutson et al. 2013, 2016).

Figure 3.1d examines shorter term global-mean temperature variability since 1970, highlighting the timing of four major El Niño events and two major volcanic eruptions. The 2015/16 global temperature event appears as a temporary bump with a magnitude (for January–December 2016) of a little over 0.1°C, superimposed on a long-term warming trend of about 1°C—the latter being largely attributable to anthropogenic forcing according to CMIP5 models (Figs. 3.1a,b). While the El Niño events of 1972/73, 1997/98, and 2015/2016 have apparent warming signatures in global temperature, the 1982/83 event's imprint was apparently muted by the almost-coincident eruption of El Chichón.

Monthly maps of observed surface temperature internal climate variability for 2016 are discussed in the online supplement material. From these and previous studies (e.g., Trenberth et al. 2002) we infer that the short-term calendar-year global mean warmth in 2015 and 2016 is likely to have been at least partly
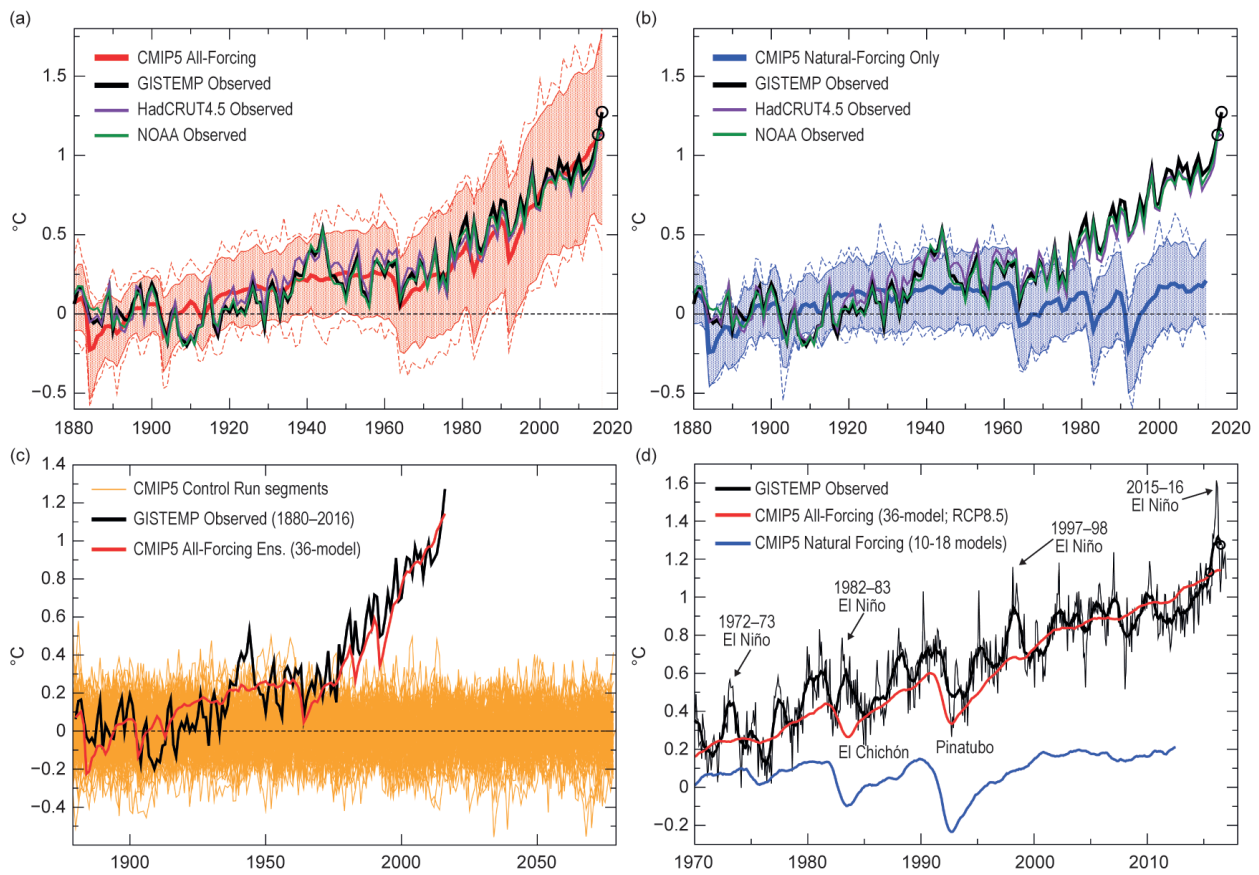
FIG. 3.1. Observed global-mean temperature anomalies vs. CMIP5 simulations (°C; 1881–1920 reference period). (a) CMIP5 All-Forcing (anthropogenic plus natural forcing) grand ensemble mean of individual ensemble means from 36 models (thick red curve); ±2 std. dev. (red shading) and minimum–maximum spread (dashed red) of annual means across individual simulations; and observed GISTEMP (black), HadCRUT4.5 (purple) and NOAA (green) anomalies. (b) As in (a) but for natural forcings (18 models; blue curves and shading). (c) Observed (GIS-TEMP; black) and All-Forcing grand ensemble mean (red) anomalies compared to 200-year segments from 36 CMIP5 control runs (orange). (d) 12-month running mean anomalies for GISTEMP observations (thick black; monthly anomalies are thin black) and CMIP5 All-Forcing (red) and Natural Forcing (blue) grand ensemble means. GISTEMP observed annual means (Jan–Dec) for 2015 and 2016 are highlighted by circles in panels (a), (b), and (d). See also online supplement materials.

El Niño-driven. Note that a calendar-year average generally leads to some cancellation between El Niño and the subsequent La Niña, since ENSO's equatorial Pacific SST anomalies tend to peak near the end of the calendar year, and its effect on global-mean temperature peaks a few months later.

For event attribution, we estimate the occurrence rate of annual-mean global temperature anomalies reaching 2015 or 2016 observed levels for simulated climates with and without anthropogenic forcing. Figure 3.2 explores the upper limits of simulated natural variability contributions to 2015 and 2016 global temperature. It depicts the maximum internal variability anomalies (from long control runs) and the Natural and Anthropogenic Forcing ensemble 2016 responses. Results are shown for each of seven CMIP5

models having at least two ensemble members each for the Natural-Forcing, All-Forcing, and RCP8.5 scenarios (the latter are needed for extending All-Forcing to 2016). Within this framework, the anthropogenic contribution dominates over the Natural Forcing and potential internal variability contributions. Figure 3.2 shows the ensemble-mean and most- and least-conservative estimates (see caption), across the models, of the natural + internal variability contribution to 2016's anomaly. None of the CMIP5 models produce natural + internal variability large enough to reproduce the observed 2015 and 2016 extremes—even using very long control simulations (in one case 5200 years). We therefore conclude that, according to the CMIP5 simulations, 2015- or 2016-level warmth (relative to the ~1900 baseline) never occurs without
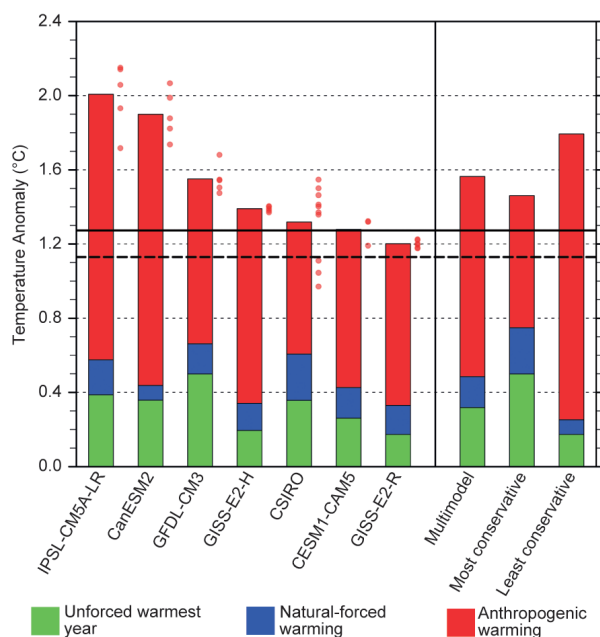
FIG. 3.2. Observed 2015 (dashed black line) and 2016 (solid) global mean temperature anomalies (°C, relative to 1881–1920) vs. simulated 2016 anomalies from the seven CMIP5 models having multiple All-Forcing/ RCP8.5 and Natural Forcing ensemble members. Each model's largest positive internal variability anomaly (green) is combined with that model's ensemble mean Natural- (blue) or Anthropogenic-forcing (red, computed as All-Forcing minus Natural-Forcing) response. The "Multimodel" estimate uses the grand ensemble mean of ensemble means of the Natural and Anthropogenic responses along with the average of the maximum positive internal variability anomalies of the individual models. The "Most conservative" combines the largest internal and Natural Forcing contributions, from any model, with the smallest anthropogenic contribution. The "Least conservative" combines the smallest maximum internal and smallest natural forcing, from any of model, with the largest anthropogenic contribution.

anthropogenic forcing, and is only possible with anthropogenic forcing.

Estimated contributions from different forcing sets to the 2016 observed global mean anomaly (1.27°C)—with internal variability computed as a residual—are presented in Table ES3.1 for each model. Using all 36 CMIP5 models, the mean estimated internal variability residual for 2016 was 0.12°C (10% of the total 2016 anomaly relative to 1881–1920). For the 12 models having at least two All-Forcing and RCP8.5 scenario members, the internal variability estimate was 0.09°C (7%). For the seven of twelve models that also passed a consistency test for 2011 and 2016 (online supplement material), the internal variability mean (and range)

were 0.14°C (−0.14° to +0.31°C), that is, 11% (−11% to +24%). There were also seven models having at least two ensemble members each for All-Forcing, RCP8.5, and Natural Forcing scenarios; their ensemble-mean contributions were 1.04°C (82%) from Anthropogenic Forcing, and 0.16°C (13%) from Natural-Forcing. Using only the four of these seven models that also passed the consistency test, the mean and range of contributions across the models were 0.88°C (69%), with range 0.71° to 1.05 °C (56% to 83%) for Anthropogenic Forcing, and 0.18°C (14%) with range 0.15° to 0.25°C (12% to 20%) for Natural Forcing.

The margins of error for some of our assessments are also illustrated in Fig. 3.2. Using each of seven models' ensemble Natural Forcing response estimates, the internal variability in these models would need to be 2.2 to 6.4 (1.9 to 5.6) times larger than simulated for the Natural Forcing plus internal variability alone to reach the 2016 (2015) observed value, even given the model's most extreme internal event. For example, for GFDL-CM3, the Natural-Forcing estimate for 2016 is +0.16°C and the model's strongest internal variability event (0.50°C) would need to be multiplied by 2.22 to reach the observed anomaly level (1.27°C). Alternatively, using each model's most extreme internal variability event, the Natural Forcing mean response from the models would need to be 3.6 to 11 (3.1 to 9.7) times larger than simulated to match the observed temperature anomalies for 2016 (2015).

The fraction of attributable risk (FAR) is defined as FAR = $1 - (p_0/p_1)$, where p_0 is the modeled probability of the event in a climate without anthropogenic influence, and p_1 is the probability in a climate with anthropogenic influence (Stott et al. 2004). For the CMIP5 models, we have already shown that $p_0 \sim 0$; that is, an event like 2015 or 2016 appears to be essentially impossible under the available estimates of natural forcings, without including anthropogenic forcings. However, events as warm as 2016 are clearly possible in at least some of the All-Forcing experiments with anthropogenic forcing (Fig. 3.1a). We therefore estimated ensemble and individual model p_1's, for the seven models having more than one All-Forcing/RCP8.5 ensemble member and that also passed the consistency test (online supplement material); ensemble p_1 was estimated from the grand ensemble mean and the aggregate distribution of annual anomalies from the individual control runs. The estimated p_1 for exceeding the 2015 (2016) observed threshold is 0.86 (0.42), implying a return period of only 1.2 (2.4) years. However, these return time estimates are highly uncertain, as they depend on

(uncertain) estimates of the All-Forcing response for 2015 and 2016; even in this case where we exclude inconsistent CMIP5 models, the return time for the 2016 threshold ranges from 1 to 39 years. We have not attempted to estimate return times for cases where the event is outside the modeled distribution, or for the observations directly (with 2016 being the single most extreme event in the observed distribution). We conclude that for the seven individual CMIP5 models having adequate numbers of ensemble members and having All-Forcing runs that are consistent with recent observations, the risk of exceeding the 2015 (2016) threshold is entirely attributable to anthropogenic forcing (FAR = 1).

Our analysis has important caveats. The internal variability of the climate system and the response to historical forcings have been estimated here using a combination of observations and models following Knutson et al. (2013, 2016). Uncertainties also remain in historical climate forcings by various agents, including anthropogenic aerosols. However, simulated internal variability would need to be more than twice as large as the most extreme case found in the CMIP5 models, for even the most extreme simulated natural warming event to match the 2016 observed record.

Summary. According to the CMIP5 simulations, 2016's record global January–December warmth would not have been possible under climate conditions of the early 1900s—anthropogenic forcing was a necessary condition (Hannart et al. 2016) for the event. Anthropogenic forcing contributed most of this warmth (relative to 1881–1920 conditions), while natural forcings and intrinsic variability (including El Niño) made relatively small contributions to the January–December 2016 global mean.

REFERENCES

Bindoff, N. L., and Coauthors, 2013: Detection and attribution of climate change: From global to regional. *Climate Change 2013: The Physical Science Basis*, T. F. Stocker et al., Eds. Cambridge University Press, 867–952, doi:10.1017/CBO9781107415324.022.

Hannart, A., J. Pearl, F. E. L. Otto, P. Naveau, and M. Ghil, 2016: Causal counterfactual theory for the attribution of weather and climate-related events. *Bull. Amer. Meteor. Soc.,* **97**, 99–110, doi:10.1175/bams-d-14-00034.1.

Hansen, J., R. Ruedy, M. Sato, and K. Lo, 2010: Global surface temperature change. *Rev. Geophys.*, **48**, RG4004, doi:10.1029/2010RG000345.

IPCC, 2001: *Climate Change 2001.* J. T. Houghton et al., Eds. Cambridge University Press, 881 pp.

——, 2007: *Climate Change 2007: The Physical Science Basis.* S. Solomon et al., Eds. Cambridge University Press, 996 pp.

——, 2013: *Climate Change 2013: The Physical Science Basis. Contribution of Working Group I to the Fifth Assessment Report of the Intergovernmental Panel on Climate Change.* T. F. Stocker et al., Eds., Cambridge University Press, 1535 pp.

Kam, J., T. R. Knutson, F. Zeng, and A. T. Wittenberg, 2016: Multimodel assessment of anthropogenic influence on record global and regional warmth during 2015 [in "Explaining Extreme Events of 2015 from a Climate Perspective"]. *Bull. Amer. Meteor. Soc.*, **97** (12), S4–S8, doi:10.1175/BAMS-D-16-0138.1.

Karl, T. R., and Coauthors, 2015: Possible artifacts of data biases in the recent global surface warming hiatus. *Science,* **348**, 1469–1472, doi:10.1126/science.aaa5632.

Knutson, T. R., F. Zeng, and A. T. Wittenberg, 2013: Multimodel assessment of regional surface temperature trends: CMIP3 and CMIP5 twentieth-century simulations. *J. Climate*, **26**, 8709–8743, doi:10.1175/JCLI-D-12-00567.1.

——, T. R., R. Zhang, and L. W. Horowitz, 2016: Prospects for a prolonged slowdown in global warming in the early 21st century. *Nat. Comm.*, **7**, 13676, doi:10.1038/ncomms13676.

Lin, N., R. E. Kopp, B. P. Horton, and J. P. Donnelly, 2016: Hurricane Sandy's flood frequency increasing from year 1800 to 2100. *Proc. Nat. Acad. Sci. USA*, **113**, 12,071–12,075, doi:10.1073/pnas.1604386113.

Morice, C. P., J. J. Kennedy, N. A. Rayner, and P. D. Jones, 2012: Quantifying uncertainties in global and regional temperature change using an ensemble of observational estimates: The HadCRUT4 data set. *J. Geophys. Res.*, **117**, D08101, doi:10.1029/2011JD017187.

Stott, P. A., D. A. Stone, and M. R. Allen, 2004: Human contribution to the European heatwave of 2003. *Nature*, **432**, 610–614, doi:10.1038/nature03089.

Taylor, K. E., R. J. Stouffer, and G. A. Meehl, 2012: An overview of CMIP5 and the experimental design. *Bull. Amer. Meteor. Soc.,* **93**, 485–498, doi:10.1175/BAMS-D-00094.1.

Trenberth, K. E., J. M. Caron, D. P. Stepaniak, and S. Worley, 2002: Evolution of El Niño–Southern Oscillation and global atmospheric surface temperatures. *J. Atmos. Res.*, **107**, 4065, doi:10.1029/2000JD000298.

4. THE EXTREME 2015/16 EL NIÑO, IN THE CONTEXT OF HISTORICAL CLIMATE VARIABILITY AND CHANGE

Matthew Newman, Andrew T. Wittenberg, Linyin Cheng,
Gilbert P. Compo, and Catherine A. Smith

Record warm central equatorial Pacific Ocean temperatures during the 2015/16 El Niño appear to partly reflect an anthropogenically forced trend. Whether they reflect changes in El Niño variability remains uncertain.

Introduction. Recent studies have investigated whether both the amplitude and key characteristics of El Niño–Southern Oscillation (ENSO) events have been changing, potentially due to some natural and/or anthropogenic change in the tropical Pacific Ocean state during recent decades (e.g., Yeh et al. 2009; Lee and McPhaden 2010; Newman et al. 2011; McGregor et al. 2013). If so, when might this change be identifiable in individual ENSO events? Was the extreme warmth in the equatorial Pacific seen in the recent 2015/16 El Niño, particularly near the dateline (L'Heureux et al. 2017), a harbinger of this change? To address these questions, we assess this event using statistics of Niño3 (5°N–5°S, 150°–90°W) and Niño4 (5°N–5°S, 160°E–150°W) sea surface temperature (SST) indices, derived from observational datasets and coupled general circulation model simulations. We use two indices to capture differences between events, important to both forecasts and diagnosis of ENSO and its impacts (Compo and Sardeshmukh 2010; Capotondi et al. 2015).

How extreme was the 2015/16 El Niño? We compare the December 2015 (DEC2015) equatorial SST anomaly (SSTA) to the SSTA distribution during 1891–2000, to more stringently test against potentially recent nonstationarity. (Other winter months yielded similar results.) Figure 4.1 shows histograms of monthly ERSST.v5 Niño3 and Niño4 indices, compared with two different probability distribution functions (PDFs) determined not by fitting the histogram, but by fitting two different Markov processes to each index time series: an AR1 process (or red noise; e.g., Frankignoul and Hasselmann 1977) with a memory time scale on the order of several months, yielding a Gaussian (normal) distribution; and a "stochastically generated skewed" process (SGS; Sardeshmukh et al. 2015), similar to the AR1 process but with noise that is asymmetric and depends linearly on the SSTA, yielding a non-Gaussian (skewed and heavy-tailed) distribution. Confidence intervals for these PDFs are determined from large ensembles of 110-year realizations generated by each process. (See online supplement for details.)

The SGS distribution captures the significant positive skewness of the Niño3 PDF (Fig. 4.1a). The observed tail probability (the probability of Niño3 reaching its observed DEC2015 magnitude) is underestimated by the Gaussian AR1 PDF, but not by the skewed SGS PDF. This result is insensitive to the dataset or to removing the 1891–2015 linear trend. Overall, the SGS distributions suggest that the probability of a monthly Niño3 value reaching or exceeding the DEC2015 magnitude is about 0.5%, consistent with previous occurrences of strong El Niño events in the observational record.

Results are quite different for Niño4, where weak negative skewness (Fig. 4.1b) means that the Gaussian distribution overestimates the DEC2015 tail probability. The DEC2015 Niño4 value was unprecedented in all five datasets, apparently impacted by a secular warming trend. Relative to its linear trend, however, the ERSST.v5 dataset had higher Niño4 values earlier in the record.

How likely was the 2015/16 El Niño? We next evaluate the likelihood and severity of the 2015/16 event relative to the gradually warming background by applying the generalized extreme value (GEV) distribution (e.g., Coles 2001; Ferreira and de Haan
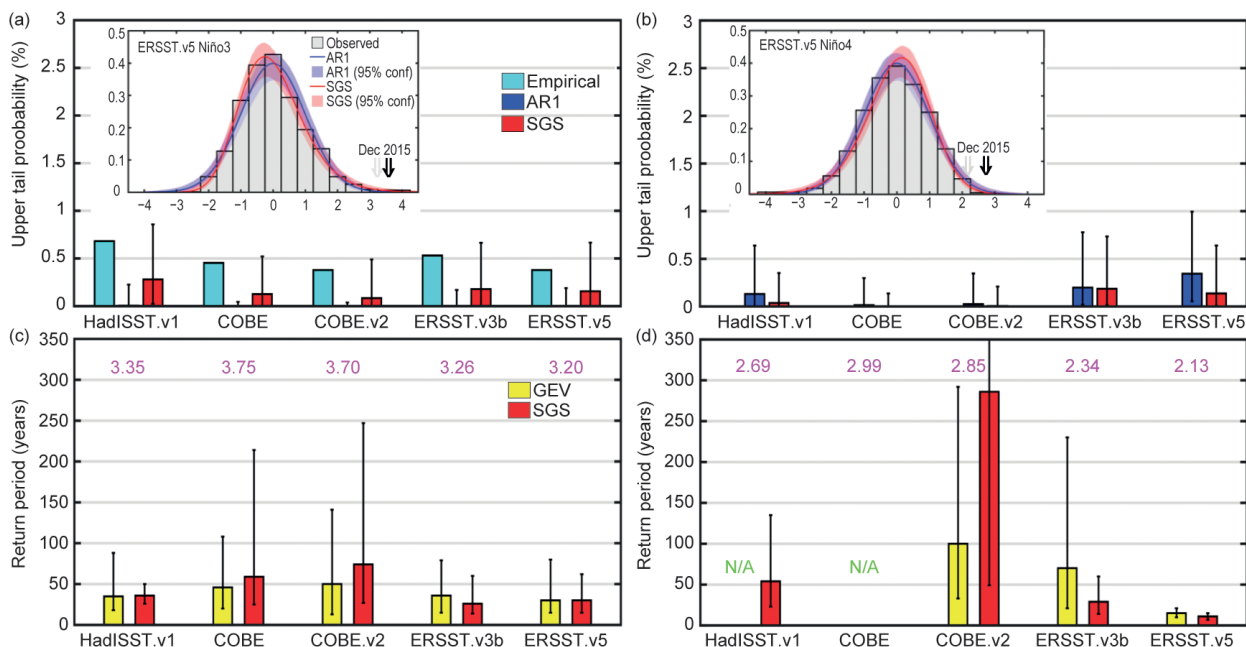
FIG. 4.1. Estimations of DEC2015 (a) Niño3 and (b) Niño4 upper tail probabilities (%). For each SST reconstruction, bars show the scalar tail probability empirically derived from the dataset and also its median value from AR1 and SGS distributions; ranges are shown by the whiskers. Insets compare SGS and AR1 PDFs with data histograms, using ERSST.v5 values standardized with respect to 1891–2000 (other datasets yielded similar results). Corresponding 95% confidence intervals are shaded; DEC2015 amplitudes are indicated by arrows, where the linear trend is (gray) or is not (black) first removed. Return period estimation (years) of linearly detrended 2015/16 (c) Niño3 and (d) Niño4 indices using the annual maximum of monthly SSTs. For each SST reconstruction, the bars show the 110-year sampling distribution of the return period matching the observed 2015/16 standardized values (magenta numbers), with ranges shown by the whiskers. N/A indicates return periods not derivable using the GEV technique (see text).

2015) to the historical annual maximum of linearly detrended monthly Niño3 and Niño4 indices during 1891–2000. [See online supplement for our Bayesian analysis (Cheng et al. 2014).] The return period, or (re) occurrence probability of an El Niño event with the observed 2015/16 intensity (a "2015/16-level" event), is derived for both indices from each dataset. The same assessment is repeated with the SGS ensembles discussed above.

Our analysis suggests that a 2015/16-level event could be expected for Niño3 roughly once every 40 years. This median return period is reasonably robust to the observational or synthetic SGS dataset used. However, the uncertainty estimates for the return period, and thus the likelihood of the 2015/16 event, are less robust. Both ERSST datasets showed the least uncertainty and shortest return periods, with a 2015/16-level Niño3 SSTA occurring every 5 to 50 years, while COBE2 showed the greatest uncertainty with a range of 10 to 120 years. The SGS distributions, which have more extreme tail events, reduced the return period uncertainty for the ERSST and Had-

ISST.v1 datasets and suggested a greater likelihood of 2015/16-level SSTA extremes.

For Niño4, there is much less agreement among the datasets (Fig. 4.1d), with the return period of a 2015/16-level event lowest for the ERSST datasets. For those datasets where the 2015/16 Niño4 SSTA was unprecedented, the return period cannot be derived using the GEV approach. From ERSST.v5, however, such an event could occur one year in ten.

Was the 2015/16 El Niño impacted by multidecadal trends in equatorial Pacific SST or ENSO variability? Figure 4.2 illustrates the evolution of 30-year mean SST and 30-year ENSO amplitude over the past 160 years, for two observational reconstructions and two model simulations. For simplicity we discuss only the HadISST.v1.1 and ERSST.v5 reconstructions, which generally bound the behavior of the other products we examined (HadISST.v2, ERSST.v3b, ERSST.v4, COBE, COBE.v2, Kaplan.v2, SODA-si.v3).

For both Niño3 and Niño4, the 1987–2016 epoch was observed to be either the warmest or the second
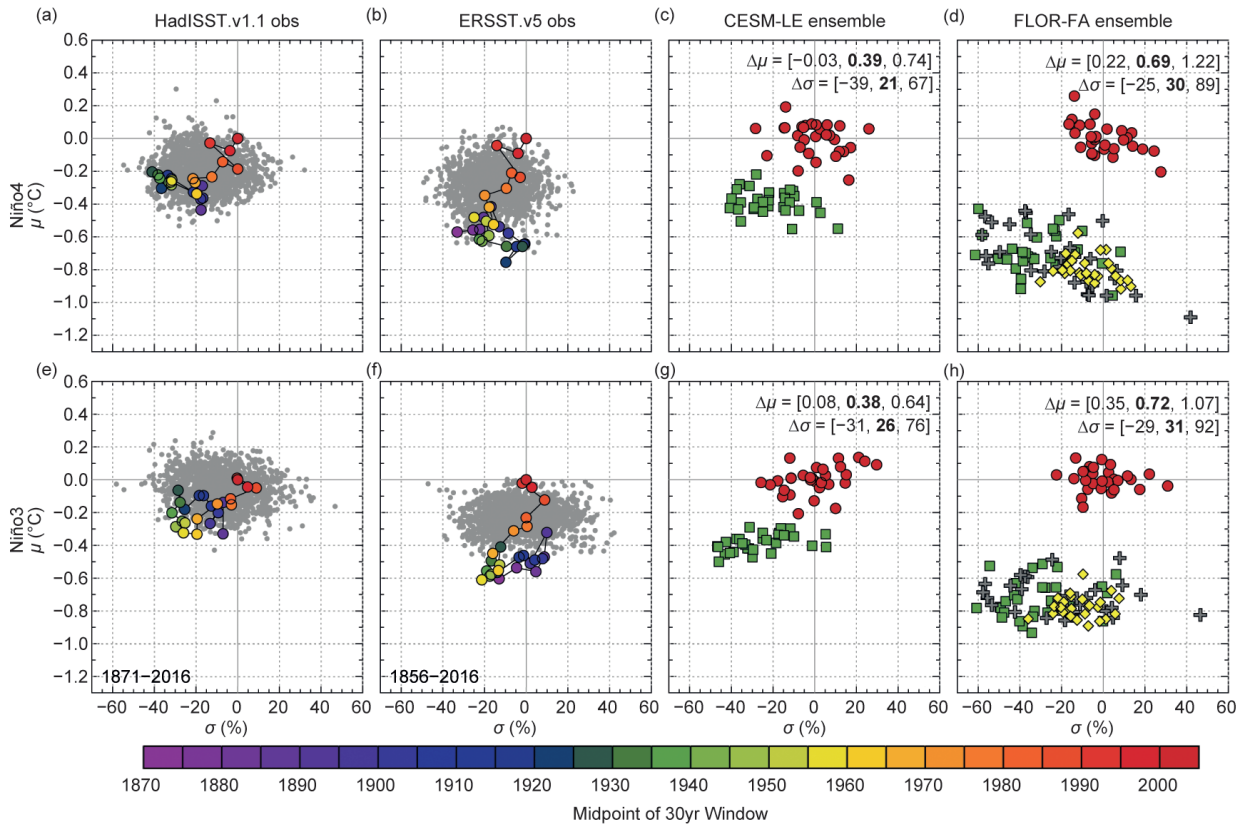
Fig. 4.2. Statistics for annually smoothed SSTs averaged over (a)–(d) Niño4 and (e)–(h) Niño3. Y-axis is the 30-year mean (μ, °C departure from 1987–2016); x-axis is the 30-year std dev (σ, % departure from 1987–2016). (a),(b),(e),(f) sample the observationally reconstructed 30-year statistics every 5 years (colored dots). Gray dots show analogous statistics from 8000-year LIM simulations trained using detrended 1959–2000 data from HadISST.v1.1 or ERSST.v5. (c),(g) show the CESM-LE 30-member ensemble simulation with "ALL" (anthropogenic + natural) historical forcings, for 1987–2016 (red dots) and 1920–49 (green squares) relative to the 1987–2016 ensemble mean; inset indicates ALL ensemble [minimum, average, maximum] change in μ and σ from 1920–49 to 1987–2016. (d),(h) show analogous statistics for the FLOR-FA 30-member ALL ensemble, along with a 30-member "NAT" ensemble with natural forcings only for 1920–49 (gray crosses) and 1987–2016 (yellow diamonds), also relative to the ALL ensemble mean.

warmest 30-year epoch on record, depending on the observational dataset. The warming trend is clearest after 1970 and in Niño4. It is more pronounced in ERSST.v5 than HadISST.v1.1. The centennial warming of both indices is marginally within the bounds of what could be expected from intrinsic multidecadal variations for HadISST.v1.1, but is outside the bounds for ERSST.v5, relative to a statistically stationary multivariate AR1 process [a linear inverse model (LIM), constructed from detrended observed tropical SSTAs during 1959–2000; see online supplement and Newman et al. 2011]. This is consistent with earlier analysis (Solomon and Newman 2012) finding equatorial Pacific 1900–2010 warming trends to be significant near and west of the dateline, despite uncertainty in amplitude.

Robust equatorial Pacific warming from 1920–49 to 1987–2016 is evident in ensemble simulations

from the NCAR CESM-LE and GFDL FLOR-FA global coupled GCMs driven by historical natural and anthropogenic ("ALL") forcings (Figs. 4.2c,d,g,h). CESM-LE's warming is compatible with all the reconstructions, though most of its members warm more than HadISST.v1.1 and less than ERSST.v5. FLOR-FA's warming is strong enough to be detected with any pair of 30-year means drawn randomly from each epoch. It is marginally compatible with ERSST.v5 but not with HadISST.v1.1. The FLOR-FA ensemble simulation with only natural (solar and volcanic, "NAT") forcings shows ensemble-mean cooling from 1920–49 to 1987–2016, so the FLOR-FA ALL warming must be entirely anthropogenic.

Compared to the historical changes in 30-year mean SST, there is less observational consensus about changes in ENSO SSTA variance. In Niño4, HadISST.v1.1 shows a fairly monotonic 40% amplifi-

cation of ENSO from the 1920s to the present, while ERSST.v5 shows only a 10% amplification and more interdecadal modulation of ENSO amplitude; neither exceeds the expected bounds of intrinsic multidecadal variations. In Niño3, ENSO amplitudes strengthen by 10% in HadISST.v1.1 since 1900, but weaken by 10% in ERSST.v5.

The CESM-LE and FLOR-FA ALL simulations both show ensemble-mean ENSO amplification from 1920–49 to 1987–2016. However, the strong intrinsic interdecadal modulation of ENSO means that some individual realizations experience greater or smaller amplification; a few even weaken. The simulations are broadly consistent with the reconstructed historical changes in ENSO amplitude, but this is primarily due to the reconstruction uncertainty and to intrinsic modulation of ENSO that produces large sampling variability of amplitudes over 30-year epochs (Wittenberg 2009; Newman et al. 2011). Interestingly, the FLOR-FA ALL and NAT simulations both show ENSO amplification (and reduced ENSO modulation) during 1987–2016, mainly because the quietest epochs vanish, suggesting natural forcings are key to the FLOR-FA results.

Conclusions. The 2015/16 El Niño was a strong but not unprecedented warm event in the eastern equatorial Pacific (Niño3), comparable to events occurring every few decades or so. However, central equatorial Pacific (Niño4) 2015/16 warmth was unprecedented in all SST reconstruction datasets except ERSST.v4. This exceptional warmth was unlikely, although not impossible, to have occurred entirely naturally, and appears to reflect an anthropogenically forced trend.

Whether this extreme warmth was associated with a change in ENSO variability, however, is less clear, given the substantial disagreement between datasets including uncertainty in their anthropogenic trend estimates (Deser et al. 2010; Solomon and Newman 2012). Interestingly, SST reconstructions with relatively higher Niño3 and Niño4 variances around the start of the 20th century (e.g., ERSST.v5) are also based on newer ICOADS releases, which include additional observations during that time (Freeman et al. 2016). Moreover, equatorial Pacific sea level pressure variance (i.e., Darwin and Tahiti) shows no pronounced centennial increase (e.g., Torrence and Compo 1998). Finally, our model results illuminate, but do not reconcile, continuing disparities among climate models concerning anthropogenic impacts on ENSO variability (Collins et al. 2010; Watanabe et al. 2012; Capotondi et al. 2015) due to lingering dynami-

cal biases in the models (Bellenger et al. 2014; Graham et al. 2017). These issues suggest that we cannot yet confidently detect whether a secular change in ENSO variability (apart from the background warming) has occurred over the past century. Our study thus highlights the need to further reduce uncertainty in observational reconstructions, and further improve dynamical models, to better gauge future ENSO risks.

REFERENCES

Bellenger, H., E. Guilyardi, J. Leloup, M. Lengaigne, and J. Vialard, 2014: ENSO representation in climate models: From CMIP3 to CMIP5. *Climate Dyn.,* **42**, 1999–2018, doi:10.1007/s00382-013-1783-z.

Capotondi, A., and Coauthors, 2015: Understanding ENSO diversity. *Bull. Amer. Meteor. Soc.*, **96**, 921–938, doi:10.1175/BAMS-D-13-00117.1.

Cheng, L., A. AghaKouchak, E. Gilleland, and R. W. Katz, 2014: Non-stationary extreme value analysis in a changing climate. *Climatic Change*, **127**, 353–369, doi:10.1007/s10584-014-1254-5.

Coles, S., 2001: *An Introduction to Statistical Modeling of Extreme Values.* Springer, 209 pp.

Collins, M., and Coauthors, 2010: The impact of global warming on the tropical Pacific Ocean and El Niño. *Nat. Geosci.*, **3**, 391–397, doi:10.1038/ngeo868.

Compo, G. P., and P. D. Sardeshmukh, 2010: Removing ENSO-related variations from the climate record. *J. Climate*, **23**, 1957–1978, doi:10.1175/2009JCLI2735.1.

Deser, C., A. S. Phillips, and M. A. Alexander, 2010: Twentieth century tropical sea surface temperature trends revisited. *Geophys. Res. Lett.*, **37**, L10701, doi:10.1029/2010GL043321.

Ferreira, A., and L. de Haan, 2015: On the block maxima method in extreme value theory: PWM estimators. *Annals of Statistics*, **43**, 276–298, doi:10.1214/14-AOS1280.

Frankignoul, C., and K. Hasselmann, 1977: Stochastic climate models. Part II: Application to sea-surface temperature anomalies and thermocline variability. *Tellus A*, **29**, 289–305.

Freeman, E., and Coauthors, 2016: ICOADS Release 3.0: A major update to the historical marine climate record. *Int. J. Climatol.*, **37**, 2211–2232, doi:10.1002/joc.4775.

Graham, F. S., A. T. Wittenberg, J. N. Brown, S. J. Marsland, and N. J. Holbrook, 2017: Understanding the double peaked El Niño in coupled GCMs. *Climate Dyn.*, **48**, 2045–2063, doi:10.1007/s00382-016-3189-1.

L'Heureux, M. L., and Coauthors, 2017: Observing and predicting the 2015/16 El Niño. *Bull. Amer. Meteor. Soc.*, **98**, 1363–1382, doi:10.1175/BAMS-D-16-0009.1.

Lee, T., and M. J. McPhaden, 2010: Increasing intensity of El Niño in the central-equatorial Pacific. *Geophys. Res. Lett.,* **37**, L14603, doi:10.1029/2010GL044007.

McGregor, S., A. Timmermann, M. H. England, O. Elison Timm, and A. T. Wittenberg, 2013: Inferred changes in El Niño–Southern Oscillation variance over the past six centuries. *Climate Past*, **9**, 2269–2284, doi:10.5194/cp-9-2269-2013.

Newman, M., S.-I. Shin, and M. A. Alexander, 2011: Natural variation in ENSO flavors. *Geophys. Res. Lett.,* **38**, L14705, doi:10.1029/2011GL047658.

Sardeshmukh, P. D., G. P. Compo, and C. Penland, 2015: Need for caution in interpreting extreme weather statistics. *J. Climate*, **28**, 9166–9187, doi:10.1175/JCLI-D-15-0020.1.

Solomon, A., and M. Newman, 2012: Reconciling disparate twentieth-century Indo-Pacific ocean temperature trends in the instrumental record. *Nat. Climate Change*, **2**, 691–699, doi:10.1038/nclimate1591.

Torrence, C., and G. P. Compo, 1998: A practical guide to wavelet analysis. *Bull. Amer. Meteor. Soc.* **79**, 61–78, doi:10.1175/15200477(1998)079<0061:APGTWA>2.0.CO;2.

Watanabe, M., J.-S. Kug, F.-F. Jin, M. Collins, M. Ohba, and A. T. Wittenberg, 2012: Uncertainty in the ENSO amplitude change from the past to the future. *Geophys. Res. Lett.*, **39**, L20703, oi:10.1029/2012GL053305.

Wittenberg, A. T., 2009: Are historical records sufficient to constrain ENSO simulations? *Geophys. Res. Lett.*, **36**, L12702, doi:10.1029/2009GL038710.

Yeh, S.-W. J.S. Kug, B. Dewitte, M.-H. Kwon, B. P. Kirtman, and F.F. Jin, 2009: El Niño in a changing climate. *Nature*, **461**, 511–514, doi:10.1038/nature08316

5. ECOLOGICAL IMPACTS OF THE 2015/16 EL NIÑO IN THE CENTRAL EQUATORIAL PACIFIC

Russell E. Brainard, Thomas Oliver, Michael J. McPhaden, Anne Cohen, Roberto Venegas, Adel Heenan, Bernardo Vargas-Ángel, Randi Rotjan, Sangeeta Mangubhai, Elizabeth Flint, and Susan A. Hunter

Coral reef and seabird communities in the central equatorial Pacific were disrupted by record-setting sea surface temperatures, linked to an anthropogenically forced trend, during the 2015/16 El Niño.

Introduction. In the equatorial Pacific Ocean, the El Niño–Southern Oscillation substantially affects atmospheric and oceanic conditions on interannual time scales. The central and eastern equatorial Pacific fluctuates between anomalously warm and nutrient-poor El Niño and anomalously cool and nutrient-rich La Niña conditions (Chavez et al. 1999; McPhaden et al. 2006; Gierach et al. 2012). El Niño events are characterized by an eastward expansion of the Indo-Pacific warm pool (IPWP) and deepening of the thermocline and nutricline in response to weakening trade winds (Strutton and Chavez 2000; Turk et al. 2001). El Niño events are typically associated with significant decreases in primary productivity in the eastern and central tropical Pacific and corresponding increases in productivity in the western tropical Pacific (Boyce et al. 2010).

The IPWP has warmed and expanded in recent decades (Weller et al. 2016). The eastern Pacific cold tongue, on the other hand, has exhibited signs of a cooling trend over the past century (Deser et al. 2010). Newman and Wittenberg (2018) found that anomalously warm sea surface temperatures (SST) in the Niño-4 region (5°N–5°S, 150°E–150°W) of the central equatorial Pacific (CEP) during the 2015/16

El Niño were likely unprecedented and unlikely to have occurred naturally, thereby reflecting an anthropogenically forced trend. Lee and McPhaden (2010) earlier reported increasing amplitudes of El Niño events in Niño-4 that is also evident in our study region (Figs. 5.1b,c).

Remote islands in the CEP (Fig. 5.1a), including Jarvis Island (0°22′S, 160°01′W), Howland Island (0°48′N, 176°37′W), Baker Island (0°12′N, 176°29′W), and Kanton Island (2°50′S, 171°40′W), support healthy, resilient coral reef ecosystems characterized by exceptionally high biomass of planktivorous and piscivorous reef fishes due to the combined effects of equatorial and topographic upwelling (Gove et al. 2006; Williams et al. 2015). Coral reef communities at these islands are exposed to extended periods of thermal stress during El Niño events. Mass coral bleaching and mortality were reported in the Phoenix Islands during the moderate 2002/03 El Niño (Obura and Mangubhai 2011), and coral bleaching with limited mortality was reported at Howland and Baker Islands during the moderate 2009/10 El Niño (Vargas-Ángel et al. 2011). There were no observations of coral bleaching or mortality at these uninhabited islands during the major El Niño events of 1982/83 or 1997/98. Corals in the eastern equatorial Pacific (>7600 km to the east) did experience mass bleaching and mortality during those major El Niño events (Glynn 1984; Glynn et al. 2001).

We describe variations in SST and biological productivity to characterize the 2015/16 El Niño (McPhaden 2015) in relation to previous El Niño events in the CEP (Fig. 5.1a) and in the context of climate trends. We then describe some of the ecological responses, which were catastrophic at Jarvis and modest at Howland, Baker, and Kanton Islands.

Data and methods. The duration and magnitude of El Niño events for the period 1981–2017 for our region of interest (ROI; 5°N–5°S, 150°W–180°) were identified
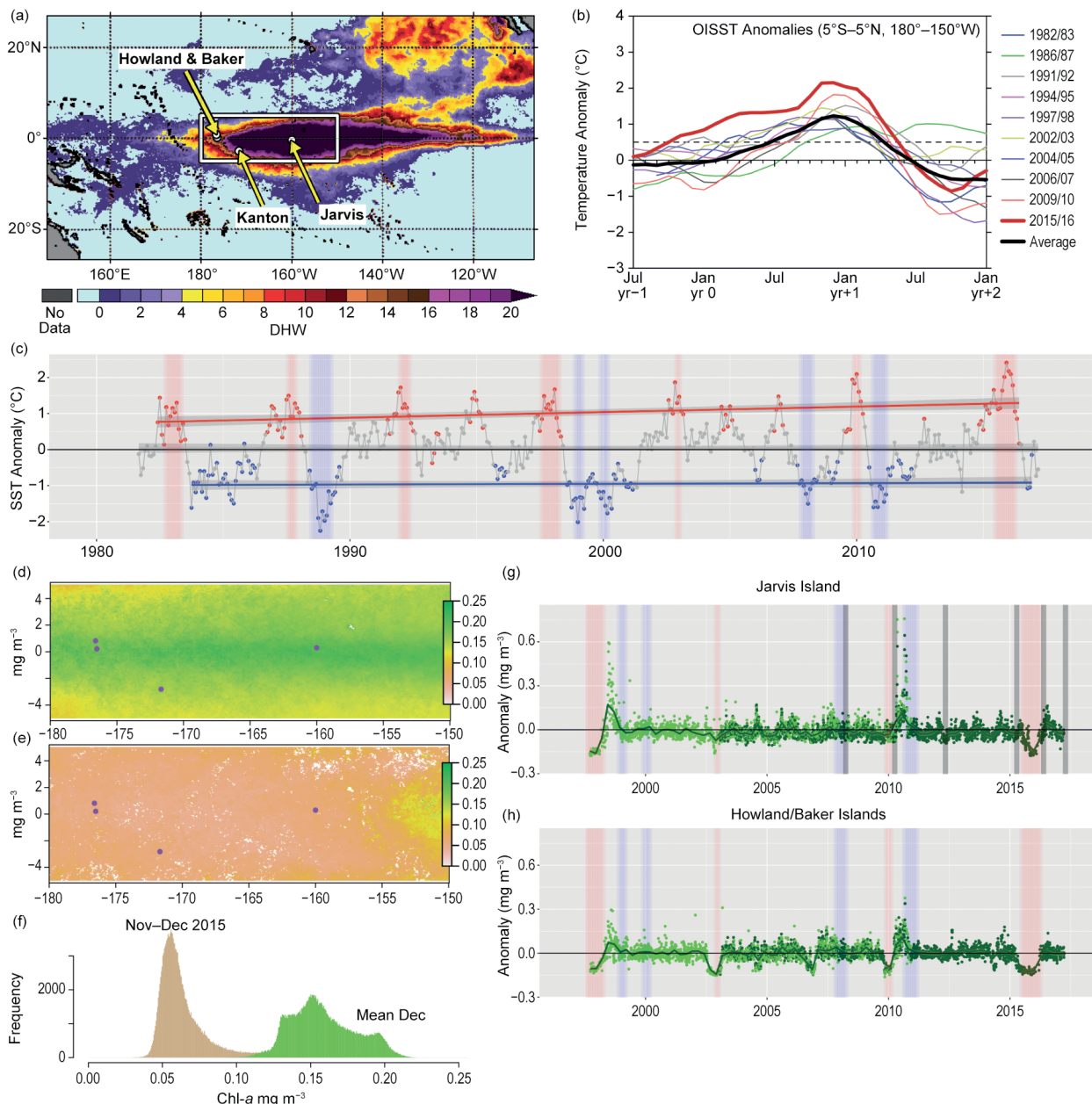
Fig. 5.1. (a) NOAA Coral Reef Watch 5-km degree heating weeks for the Pacific Ocean for 1 Jan 2016 (https://coralreefwatch.noaa.gov/satellite/bleaching5km/images_archive/b05kmnn_dhw_20160101_pacific_930x580.gif) overlaid with ROI boundaries and locations of Jarvis, Howland, Baker, and Kanton Islands. (b) ROI SST anomalies (°C) for El Niño events since 1981 based on OISST data. Thick black line is average of all events since 1981 excluding the 2015/16 event. Thick red line is Jul 2014–Jan 2017, encompassing the 2015/16 El Niño. (c) Time series of monthly OISST anomaly (°C) for ROI; El Niño and La Niña periods are shown as vertical red and blue bands, respectively. Trends for El Niño, neutral, and La Niña conditions are shown as red, gray, and blue lines. (d) Map of mean Chl-*a* (mg m⁻³) for all Dec from 2002–16 for ROI using MODIS data showing strong equatorial upwelling; (e) mean Chl-*a* (mg m⁻³) for Nov–Dec 2015 for ROI using MODIS data showing 'desertification' conditions; (f) frequency of occurrences of Chl-*a* (mg m⁻³) concentrations over the ROI for Dec mean over 2003–17 (green) and Nov–Dec 2015 (tan); (g) time series of Chl-*a* (mg m⁻³) anomalies at Jarvis Island (2° × 2°; 0.63°N–1.37°S, 159°–161°W) from SeaWiFS (1997–2010) and MODIS (2003–17) datasets https://coastwatch.pfeg.noaa.gov/erddap, (h) time series of Chl-*a* anomalies (mg m⁻³) at Howland/Baker Islands (2° × 2°; 1.5°N–0.5°S, 175.5°–177.5°W) from SeaWiFS and MODIS datasets.

using the NOAA 1/4° daily optimum interpolation SST (OISST; online supplement material). El Niño or La Niña events were defined following the convention for the ONI index, that is, when the 3-month running mean SST anomaly in Niño-3.4 exceeded ±0.5°C. We computed trends during El Niño, La Niña, and neutral conditions during the El Niño events. We examined long-term trends of SST anomaly and cumulative heat stress in the ROI and at Jarvis Island using OISST, the NOAA extended reconstructed SST (ERSSTv4; Huang et al. 2014), and Hadley Centre sea ice and SST dataset (HadISST; online supplement material). To identify the location and variations in primary biological productivity, estimates of chlorophyll concentration (Chl-*a*) were obtained from SeaWiFS (9-km) from 1997–2010 and MODIS (4-km) from 2002–17 (NASA 2014; online supplement material).

From 2000–17, coral reef benthic and fish communities were surveyed during 11 research cruises by NOAA's Pacific Reef Assessment and Monitoring Program. The cruise monitoring data were used to examine the ecological responses to recent El Niño events. Surveys included visual estimates of coral cover (%) collected during towed-diver surveys at mid-depths (~15 m) from 2001–17 (Kenyon et al. 2006) and visual estimates from stratified random benthic surveys since 2010. Fish assemblages were surveyed since 2008 using a stationary point count method under a random depth-stratified sampling design (Ayotte et al. 2015). Changes in seabird populations were based on visual surveys conducted immediately before and after the 1982/83 and 2015/16 El Niño events and using fixed cameras that captured images every 30 minutes from April 2015 to May 2016.

Results and discussion: Oceanographic patterns. Exceptionally warm SST anomalies for the ROI (Figs. 5.1b,c) and Jarvis Island (Figs. ES5.1b,c) show that the 2015/16 El Niño was the strongest in magnitude and longest on record in the satellite era. Though SST was also anomalously warm in the CEP for extended durations during other major El Niño events in 1982/83, 1997/98, 2009/10, the warming at Jarvis Island during the 2015/16 El Niño was exceptional. Observed daily SST anomalies exceeded the 1982/83, 1997/98, and 2009/10 events by +0.51°, +0.52°, and +0.71°C, respectively (difference among events of 95% quantiles of daily SST; Figs. ES5.1b,c). At Howland and Baker Islands, ~1830 km west of Jarvis Island, the 2015/16 El Niño showed SST maxima on par with the 2009/10 event, but exceeded levels observed in 1982/83 and 1997/98 by +0.61° and +0.68°C, respectively (Fig.

ES5.1d). SST anomalies were substantially smaller at Howland and Baker Island than at Jarvis Island for all events, by 0.42° to 1.28°C, respectively.

Time series of daily OISST anomalies during El Niño events show statistically significant warming trends of +0.596° (0.166°C decade⁻¹) and +0.352° (0.098°C decade⁻¹) over 36 years in the ROI and at Jarvis Island, respectively (Figs. 5.1c and ES5.1b). This trend is robust to the exclusion of 2015/16 El Niño across the ROI, but not at Jarvis Island alone (Table ES5.1). Combining magnitude and duration of SST anomalies using the ERRSTv4 and HadISST reconstructions since 1950, cumulative heat stress during El Niño periods demonstrates warming trends of +0.43° (0.064°C decade⁻¹) and +0.50° (0.074°C decade⁻¹) over the past 67 years in the ROI and at Jarvis Island, respectively (Figs. ES5.4a,b; Table ES5.2), though again, the significance of this warming trend depends on the inclusion of the 2015/16 El Niño. With the observed warming trend in the IPWP (Weller et al. 2016), it appears that the significant warming across the CEP, including Jarvis Island, during El Niño events may be due to eastward advection of these increasingly warmer waters.

During strong El Niño events, a cessation of upwelling can lead to extended periods of anomalously low Chl-*a*, as occurred at Jarvis Island during only the strongest El Nino events in 1997/98 and 2015/16 (Fig. 5.1g). At Howland and Baker Islands, low Chl-*a* events were more frequent, occurring during these major El Niño events and the moderate El Niño events of 2002/03 and 2009/10 (Fig. 5.1h). The strong El Niño events of 1982/83 and 1997/98 were followed by strong La Niña events, but this did not occur following the 2015/16 El Niño. La Niña events that followed the 1997/98 and 2009/10 El Niño events were characterized by robust Chl-*a* phytoplankton blooms that lasted ~6 months at Jarvis, Howland, and Baker Islands. Without a strong La Niña following the 2015/16 El Niño, no such Chl-*a* bloom was observed in 2016–17. In summary, primary productivity fluctuated between 'desertification' conditions during strong El Niño events and robust phytoplankton blooms during strong La Niña events (Figs. 5.1e–h).

Ecological responses. The 2015/16 El Niño was a major driver of the longest, most widespread, and most damaging global coral bleaching event on record (NOAA 2017). In the CEP, impacts to corals were catastrophic at Jarvis, but only moderate or modest at Howland, Baker, and Kanton Islands. Specifically, NOAA reported severe coral mortality at Jarvis Island
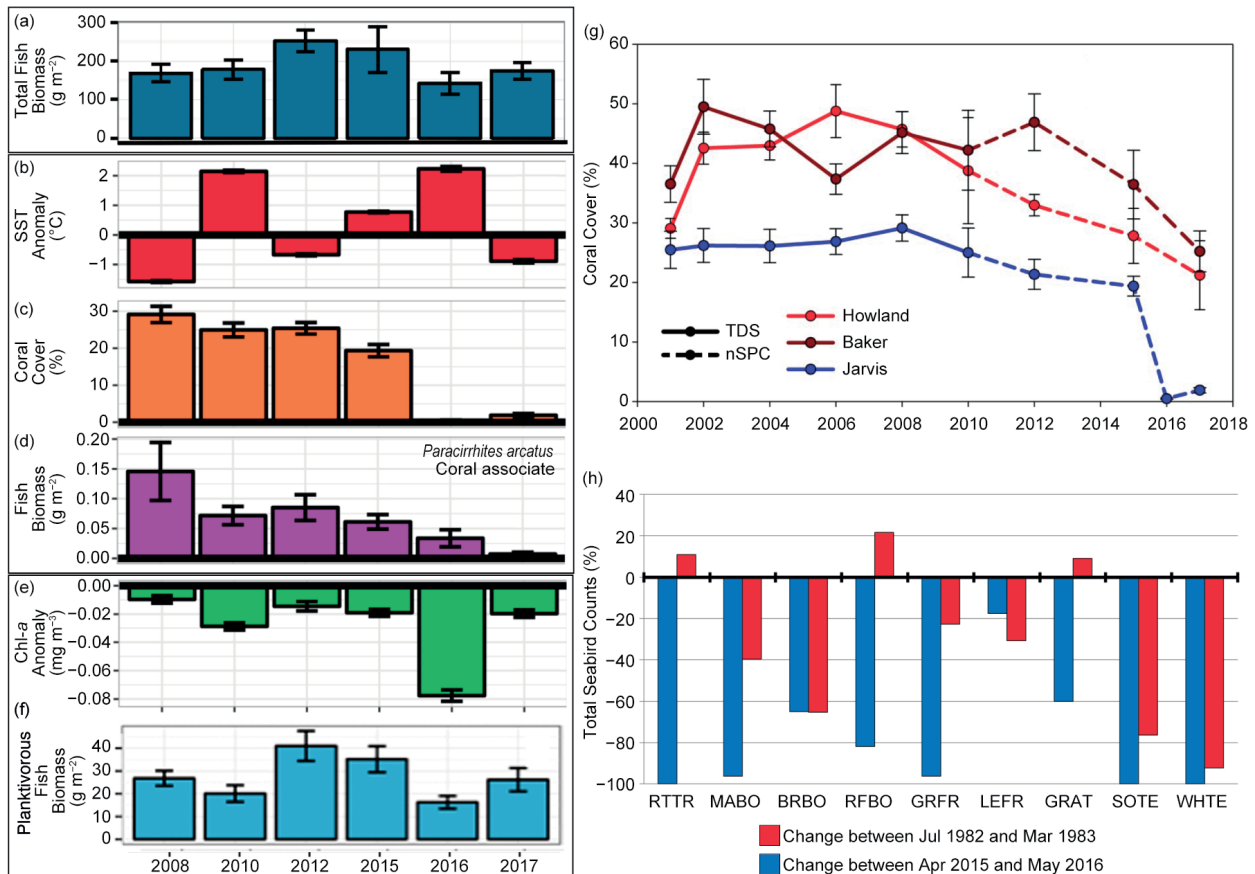
Fɪɢ. 5.2. (a)–(f) Jarvis Island. (a) Mean fish biomass (g m⁻²) and standard error (SE) computed from stratified random reef fish surveys of abundance and size; (b) 6-mo running mean SST anomalies (°C) and SE for 6-mo prior to NOAA fish and coral surveys using OISST; (c) mean coral cover (%) and SE from NOAA towed-diver surveys (2008 only) and stratified random stationary point count (SPC) surveys (2010–17): (d) mean biomass (g m⁻²) of coral associate *Paracirrhites arcatus*. (e) 6-mo running mean Chl-*a* anomalies (mg m⁻³) for 6-mo prior to NOAA fish and coral surveys using MODIS. (f) Island-wide mean plantivorous fish biomass (g m⁻²) and SE computed from stratified random SPC reef fish surveys of abundance and size. (g) Mean coral cover (%) and SE (2001–08 from NOAA towed-diver surveys at mean 15-m depth (solid lines) ; 2010–17 from NOAA stratified random SPC surveys). (h) Change of Jarvis Island seabird counts (%) before and after 1982–83 (blue) and 2015–16 (red) El Niño events. [Data were normalized using census data from 19 island surveys from 1973 to 2016 (x-min. count)/(max.-min.).]; RTTR = *Phaethon rubricauda*; MABO, BRBO, & RFBO = *Sula dactylatra, S. leucogaster, & S. sula*; GRFR & LEFR = *Fregata minor & F. ariel*; GRAT & SOTE = *Onychoprion lunatus* and *O. fuscatus*; WHTE = *Gygis alba*.

with island-wide coral cover declining from 17.8% in April 2015 (pre-bleaching) to 0.3% in May 2016 (post-bleaching), representing a devastating decline of >95% (Fig. 5.2g; Table ES5.3; Boyle et al. 2017; Vargas-Ángel et al. 2017, manuscript submitted to *Coral Reefs*). Corals at Jarvis Island experienced thermal stress of 35.8 degree heating weeks and exceeded the bleaching threshold (28.7°C) for 43 consecutive weeks between 2015 and 2016 (Boyle et al. 2017). Extensive mass bleaching observed visually during the peak of the El Niño in November 2015 (Cohen 2016, personal communication) caused mass mortality across all coral taxa, reef habitats, and depths

by May 2016 (Figs. 5.2c,g; Table ES5.3). Only a few hardy and resilient corals survived, including some massive Porites colonies that had survived previous El Niño events over many decades and a few colonies of Acropora, Pocillopora, and Hydnophora (Boyle et al. 2017; Vargas-Ángel et al. 2017, manuscript submitted to *Coral Reefs*).

In contrast, Howland, Baker, and Kanton Islands experienced substantially less thermal stress. At Howland and Baker Islands, we observed 23%–31% reductions in coral cover from 2015 to 2017, though there were no observations to confirm bleaching during the 2015/16 El Niño (Fig. 5.2g; Table ES5.3).

The reduction in coral cover between 2015 and 2017 is smaller than the reduction in coral cover from 2012 to 2015, which was an ENSO neutral period. At Kanton Island, 5%–25% of the corals were observed to be bleached during the peak of the 2015/16 El Niño, but little discernable coral mortality was observed in 2016, dramatically lower than the mortality observed following the 2002/03 El Niño (Mangubhai and Rotjan 2017, personal commmunication; Obura and Mangubhai 2011).

A preliminary assessment of reef fish survey data at Jarvis Island revealed decreased total fish biomass in 2016 relative to other years (Fig. 5.2a; Table ES5.4), consistent with previous findings from the Phoenix Islands following the 2002/03 bleaching (Mangubhai et al. 2014). In addition, biomass of planktivores was lower during both the moderate and strong El Niño events of 2009/10 and 2015/16 (Fig. 5.2f). With the island-wide reduction in coral cover observed since 2008, a concomitant reduction in the biomass of *Parracirrhites arcatus,* a fish species dependent on live coral for habitat, was observed (Figs. 5.2c,d). These combined data suggest that the 2015/16 El Niño caused reduced food availability (Fig. 5.2e) that depleted planktivore populations (Fig. 5.2f) and reduced coral cover (Fig. 5.2c) which in turn reduced live-coral dependent fish species (Fig. 5.2d).

Seabird counts at Jarvis Island showed a decrease in total individuals and a scarcity of older nestlings, indicating a lack of reproduction, after the 2015/16 El Niño (Fig. 5.2h). Wildlife cameras recorded a decrease in birds flying to and from the sea and loss of colonies from flooding events. Nineteen seabird counts from 1973–2016 showed a negative relationship between the abundance of most species and the Niño-3.4 index.

Conclusions. The long-term warming trend in the IPWP has coincided with a corresponding warming trend across the CEP during major El Niño events, culminating in record high SST and Chl-*a* anomalies across the CEP in association with the extreme 2015/16 El Niño that disrupted coral reef and seabird communities, especially at Jarvis Island, where catastrophic coral bleaching and mortality were observed.

REFERENCES

Ayotte, P., K. McCoy, A. Heenan, I. Williams, and J. Zamzow, 2015: Coral Reef Ecosystem Program standard operating procedures: Collection for rapid ecological assessment fish surveys. Pacific Islands Fisheries Science Center Administrative Report H-15-07, 33 pp., doi:10.7289/V5SN06ZT.

Boyce, D. G., M. R. Lewis, and B. Worm, 2010: Global phytoplankton decline over the past century. *Nature*, **466**, 591–596, doi:10.1038/nature09268.

Boyle, S., and Coauthors, 2017: *Coral reef ecosystems of the Pacific Remote Islands Marine National Monument: A 2000–2016 overview*. PIFSC Special Pub. SP-17-003, 62 pp., doi.org/10.7289/V5/SP-PIFSC-17-003.

Chavez, F. P., P. G. Strutton, G. E. Friederich, R. A. Feely, G. C. Feldman, D. G. Foley, and M. J. McPhaden, 1999: Biological and chemical response of the equatorial Pacific Ocean to the 1997–1998 El Niño. *Science*, **286**, 2126–2131, doi:10.1126/science.286.5447.2126.

Deser, C., A. S. Philips, and M. A. Alexander, 2010: Twentieth century tropical sea surface temperature trends revisited. *Geophys. Res. Lett.*, **37**, L10701, doi:10.1029/2010GL043321.

Gierach, M. M., T. Lee, D. Turk, and M. J. McPhaden, 2012: Biological response to the 1997-98 and 2009-2010 El Niño events in the equatorial Pacific Ocean. *Geophys. Res. Lett.*, **39**, L10602, doi:10.1029/2012GL051103.

Glynn, P. W., 1984: Widespread coral mortality and the 1982–83 El Niño warming event. *Environ. Conserv.*, **11**, 133–146, doi:10.1017/S0376892900013825.

——, J. L. Maté, A. C. Baker, and M. O. Calderón, 2001: Coral bleaching and mortality in Panama and Ecuador during the 1997–1998 El Niño–Southern Oscillation event: Spatial/temporal patterns and comparisons with the 1982–1983 event. *Bull. Mar. Sci.*, **69**, 79–109.

Gove, J. M., M. A. Merrifield, and R. E. Brainard, 2006: Temporal variability of current-driven upwelling at Jarvis Island. *J. Geophys. Res.*, **111**, C12011, doi:10.1029/2005JC003161.

Huang, B., and Coauthors, 2014: Extended reconstructed sea surface temperature version 4 (ERSST.v4): Part I. Upgrades and intercomparisons. *J. Climate*, **28**, 911–930, doi:10.1175/JCLI-D-14-00006.1.

Kenyon J., R. Brainard, R. Hoeke, F. Parrish, and C. Wilkinson, 2006: Towed-diver surveys, a method for mesoscale spatial assessment of benthic reef habitat: A case study at Midway Atoll in the Hawaiian Archipelago. *Coastal Manage.*, **34**, 339–349, doi:10.1080/08920750600686711.

Lee, T., and M. J. McPhaden, 2010: Increasing intensity of El Niño in the central equatorial Pacific. *Geophys. Res. Lett.*, **37**, L14603, doi:10.1029/ 2010GL044007.

Mangubhai, S., A. M. Strauch, D. O. Obura, G. Stone, and R. D. Rotjan, 2014: Short-term changes of fish assemblages observed in the near-pristine reefs of the Phoenix Islands. *Rev. Fish Biol. Fish.*, **24**, 505–518, doi:10.1007/s11160-013-9327-5.

McPhaden, M. J., 2015: Playing hide and seek with El Niño. *Nat. Climate Change*, **5**, 791–795, doi:10.1038 /nclimate2775.

——, S. E. Zebiak, and M. H. Glantz, 2006: ENSO as an integrating concept in Earth science. *Science*, **314**, 1740–1745, doi:10.1126/science.1132588.

NOAA, 2017: Global coral bleaching event likely ending. News & Features [online], National Oceanic and Atmospheric Administration. [Available online at www.noaa.gov/media-release/global-coral -bleaching-event-likely-ending.]

Newman, M. and A. Wittenberg, 2018: The extreme 2015/16 El Niño in the context of historical climate variability and change [in "Explaining Extreme Events of 2016 from a Climate Perspective"]. *Bull. Amer. Meteor. Soc.*, **99** (1), S16–S20, doi;10.1175 /BAMS-D-17-0116.1

Obura, D., and S. Mangubhai, 2011: Coral mortality associated with thermal fluctuations in the Phoenix Islands, 2002–2005. *Coral Reefs*, **30**, 607–619, doi:10.1007/s00338-011-0741-7.

Strutton, P. G., and F. P. Chavez, 2000: Primary productivity in the equatorial Pacific during the 1997–998 El Niño. *J. Geophys. Res.,* **105**, 26,089–26,101, doi:10.1029/1999JC000056.

Turk, D., M. J. McPhaden, A. J. Busalacchi, and M. R. Lewis, 2001: Remotely-sensed biological production in tropical Pacific during 1992–1999 El Niño and La Niña. *Science*, **293**, 471–474, doi:10.1126 /science.1056449.

Vargas-Ángel, B., E. E. Looney, O. J. Vetter, and E. F. Coccagna, 2011: Severe, widespread El Niño–associated coral bleaching in the US Phoenix islands. *Bull. Mar. Sci.*, **87**, 623–638.

Weller, E., S.-K. Min, W. Cai, F. W. Zwiers, Y.-H. Kim, and D. Lee, 2016: Human-caused Indo-Pacific warm pool expansion. *Sci. Adv.*, **2**, e1501719, doi:10.1126 /sciadv.1501719.

Williams, I. D., J. K. Baum, A. Heenan, K. M. Hanson, M. O. Nadon, and R. E. Brainard, 2015: Human, oceanographic and habitat drivers of central and western Pacific coral reef fish assemblages. *PLoS One*, **10**, e0120516, doi:10.1371/journal.pone.0120516.

6. FORCING OF MULTIYEAR EXTREME OCEAN TEMPERATURES THAT IMPACTED CALIFORNIA CURRENT LIVING MARINE RESOURCES IN 2016

Michael G. Jacox, Michael A. Alexander, Nathan J. Mantua, James D. Scott, Gaelle Hervieux, Robert S. Webb, and Francisco E. Werner

Significant impacts on California Current living marine resources in 2016 resulted from sustained extremely high ocean temperatures forced by a confluence of natural drivers and likely exacerbated by anthropogenic warming.

Introduction. Recent record high sea surface temperature anomalies (SSTa) in the California Current Large Marine Ecosystem (CCLME; Fig. 6.1a) produced dramatic impacts on marine life (Cavole et al. 2016; Peterson et al. 2016; Welch 2016). While effects on many species and fisheries may have been short-lived, salmon fisheries, for example, were heavily impacted in 2016 due to multiyear persistence of unfavorable conditions. Negative impacts on CCLME salmon fisheries are likely to persist until at least 2019, as poor stream and 2014–16 ocean conditions directly influence the 2016–19 Chinook salmon abundance. U.S. West Coast Chinook salmon catches in 2016 were approximately 52% of the average catch since 2006, quotas for Chinook salmon fisheries were not met, and spawning escapements to the Klamath and Sacramento River basins were very low (PFMC 2017a). For 2017, the Klamath River Chinook salmon abundance forecast is the lowest on record, and salmon fishing has been sharply restricted from southern Oregon to southern California (PFMC 2017b).

Our analysis focuses on the climatic drivers of the 2014–16 CCLME warm period and its extremity in the context of the past century. This study is motivated by an important question from a fisheries management perspective: to what extent were the 2014–16 extremes due to natural variability versus anthropogenic climate change?

Temperature impacts on salmon. Salmon are a subarctic species that thrive in marine habitats featuring lipid-rich food-webs with cool-water plankton and fish communities. Warm periods in the CCLME are characterized by sharp reductions in cool, nutrient-rich, highly productive upwelled and subarctic water (Chavez et al. 2002; Checkley and Barth 2009), a shift from lipid-rich to lipid-poor zooplankton (Peterson and Schwing 2003), and an influx of predators to the nearshore areas critical for salmon early marine survival (e.g., Pearcy 1992; Wells et al. 2017). These shifts in the prey base and predator distributions favor reduced growth and survival rates for CCLME salmon (e.g., Daly et al. 2017), and anomalously warm CCLME SSTs are associated with low post-release survival rates for hatchery-origin coho and Chinook salmon from southeast Alaska to California (Sharma et al. 2012; Kilduff et al. 2015). While links between salmon abundance (or catch) and SST are not easily evaluated with time series correlations (see online supplement material), a strong link between record-warm 2014–16 CCLME SSTs and negative impacts on the West Coast salmon fishery in 2016 is evidenced by a shift to subtropical species and widespread negative impacts (increased mortality rates, reduced reproductive success and/or abundance) on top predators like sea birds, salmon, and marine mammals that typically thrive under neutral or cool SST conditions (Cavole et al. 2016; Peterson et al. 2016; Welch 2016).

Data and methods. For 1920–2016 CCLME SST observations, we used the 1° Hadley Centre Sea Ice and Sea

FIG. 6.1. (a) Observed (HadISST) 2014–16 mean northeast Pacific SSTa (°C) relative to the 1920–2016 mean. Black line outlines the CCLME. (b),(c) CCLME annual mean SSTa (°C) from HadISST (black line), model ensemble mean (red line), and range of individual ensemble members in percentiles (gray shading): 25%–75% (dark), 10%–90% (medium) and 0–100% (light). (d),(e) Smoothed histograms of CCLME annual mean SSTa (°C) for 1920–2016 observations (black) and from all model ensemble members during 1920–50 (green), 1920–2016 (blue) and 2000–30 (red). Histograms were calculated using a SSTa bin width of 0.2°C. Model values are from (b),(d) CESM-LENS and (c),(e) CMIP5 Observed annual mean CCLME SSTa in °C (and standardized units) were 1.15°C (2.2σ), 1.71°C (3.3σ), and 0.95°C (1.8σ) in 2014, 2015, and 2016, respectively.

Surface Temperature (HadISST; Rayner et al. 2003) dataset. For spatial SSTa correlation analyses we used the 1982–present, higher resolution (0.25°) NOAA Optimum Interpolation Sea Surface Temperature, version 2 (Banzon et al. 2016; Reynolds et al. 2007).

Anthropogenic forcing contributions to extreme warming were assessed using SSTa distributions from "historical" (1920–50) and "present" (2000–30) periods in the Coupled Model Intercomparison Project Phase 5 (CMIP5; Taylor et al. 2012) ensemble and the Community Earth System Model Large Ensemble Project (CESM-LENS; Kay et al. 2015). We used 26 and 30 members from the CMIP5 and CESM-LENS ensembles, respectively. For each ensemble, historical external forcing was applied until 2005, after which representative concentration pathway 8.5 (RCP8.5) external forcing was applied (Lamarque et al. 2010, 2011) to provide continuous simulations of the twentieth and twenty-first centuries. The change in risk of an extreme event due to anthropogenic forcing is estimated using the fraction of attributable risk, $FAR = 1 - (P_0/P_1)$, where P_0 is the probability of an event in the historical period and P_1 is the probability of the same event in the present period (Stott et al. 2004).

Forcing of CCLME SSTa is explored using first-order auto-regressive [AR(1)] models of the form

$$SSTa_t = a*SSTa_{t-1} + b_i*F_i + \varepsilon_t$$

where a is the lag–1 autoregression coefficient such that $a*SSTa_{t-1}$ represents damped persistence, F_i are b_i are forcing functions and their regression coefficients, respectively, and ε is a residual error term (noise).

CCLME SST anomalies in the context of variability and change. The 1920–2016 distribution of observed annual mean CCLME SSTa is positively skewed, with more extreme warm anomalies than cold, and the 2014–16 values in the tail of the distribution (Fig. 6.1d). The CESM-LENS and CMIP5 distributions are nearly Gaussian and generally match the observed histogram (Figs. 6.1d,e), with the observed record 2015 SSTa near the upper bound of both ensembles (Figs. 6.1b,c). From the historical period (1920–50) to the present period (2000–30), increases in the ensemble mean (standard deviation) of SSTa are 0.47°C (0.10°C) in CESM-LENS and 0.65°C (0.06°C) in CMIP5. There is a long-term tendency for warmer SSTa to occur later in the observed record, although it is unclear if the increase is linear (Johnstone and Mantua 2014). Indeed, simulated CCLME SSTa exhibit little trend from 1920 to ~2000, after which they increase rapidly (Figs. 6.1b,c), similar to nonlinear changes that emerge for

coastal upwelling in the CCLME (Brady et al. 2017).

In 2015, the observed annual mean CCLME SSTa was 1.7°C, or 3.3 standard deviations (σ) above the mean, the highest value in the 1920–2016 record (Fig. 6.1b). The persistence of this heat wave was also remarkable; 2014–16 was the warmest 3-year period on record, with mean SSTa of 1.3°C, 3.1σ above the mean of all 3-year periods from 1920–2016 (Fig. ES6.1). The annual and three-year mean SSTa observed in 2015 and 2014–16 are never reached in the historical period for either CMIP5 or CESM-LENS (~1700 total simulated years under 1920–50 external forcing). In the "present" period, mean 2015 SSTa and 2014–16 SSTa occur approximately 2%–4% and 7%–9% of the time, respectively (Table ES6.1). Therefore, for these events, FAR = 1. However, one must take care when interpreting FAR as over shorter periods it can be influenced by natural variability; we discuss this variability in the next section.

Forcing of SST anomalies in the CCLME. Bond et al. (2015) showed that record SSTa in the Gulf of Alaska (GOA) in 2014 were caused by a persistent ridge of high sea level pressure anomalies that reduced surface wind speeds and weakened normal cooling processes over the 2013/14 winter. In 2015, northeast Pacific SST extremes expanded to include an area encompassing Alaska to Baja California (Gentemann et al. 2017). Di Lorenzo and Mantua (2016; hereafter DM2016) showed this persistent marine heatwave was a consequence of two atmospheric forcing/ocean response patterns, the 2014 GOA pattern and the 2015 northeast Pacific Arc pattern, linked with ENSO via teleconnections.

We examined the forcing of CCLME SST anomalies using AR(1) models in which observed SSTa derive from damped persistence of pre-existing anomalies plus some forcing. As the CCLME is a coastal upwelling system, the alongshore wind is a dominant forcing via mechanisms that include coastal and offshore upwelling, horizontal advection, and surface heat fluxes (Johnstone and Mantua 2014). The SSTa tendency has maximum correlations with meridional wind stress off the coasts of California and Baja California, from ~130° to 140°W (Fig. 6.2a). An AR(1) model forced by this index of local atmospheric forcing reproduces much of the observed SSTa variance (Fig. 6.2b). However, it fails to reproduce the extreme 2014–16 warming.

A lag-correlation analysis of residuals from the AR(1) model suggests an important influence of GOA SSTa at lead times of ~6 months (Fig. 6.2c), and
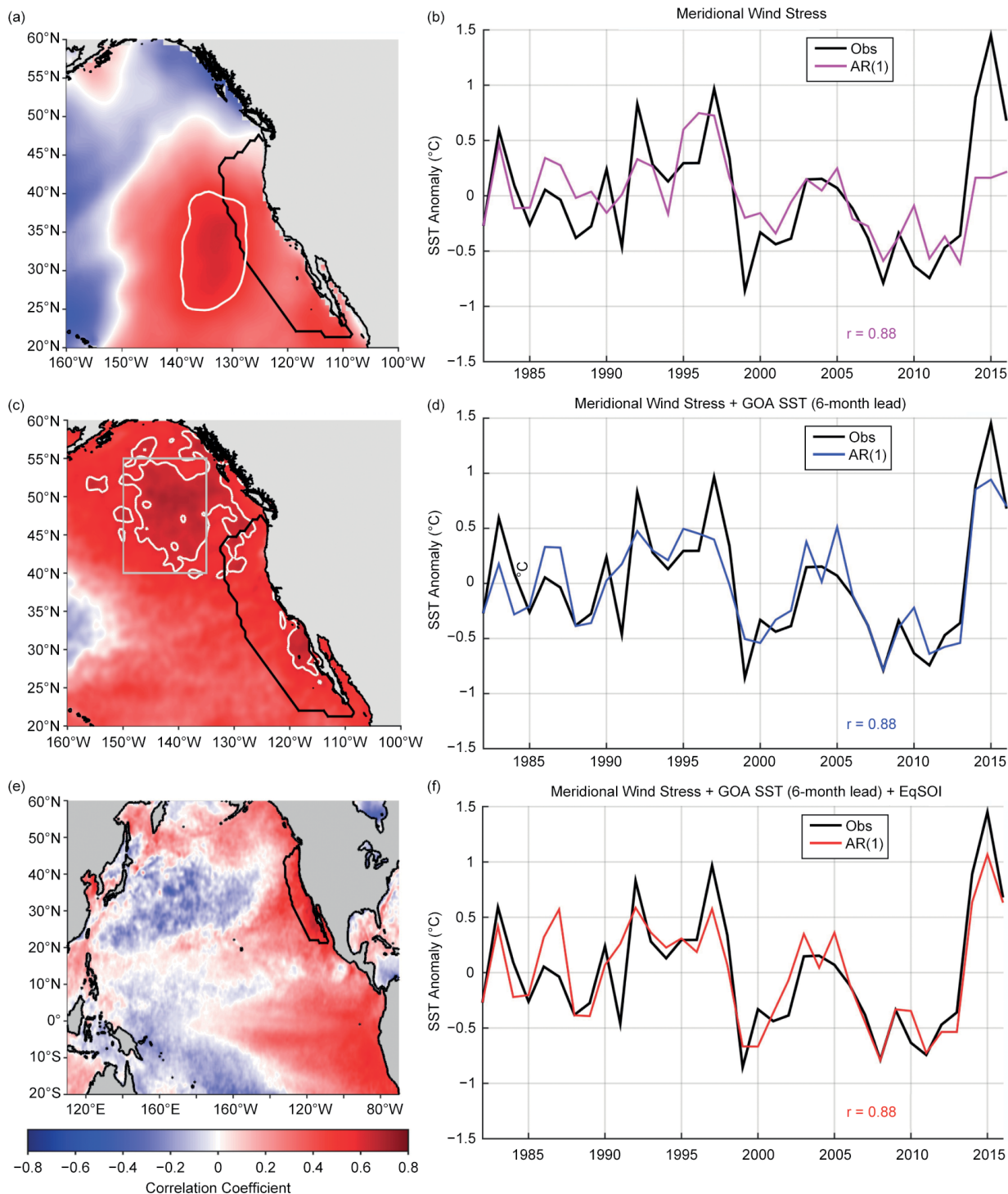
Fig. 6.2. Forcing of SST anomalies (°C) in the CCLME. (a) Correlation of meridional wind stress and SSTa tendency. Black contour outlines the CCLME, white contour bounds the region of highest correlation (r > 0.6), which was used to force the AR(1) model shown in (b). (c) Residual of the AR(1) model in (b) correlated with SSTa 6 months prior suggests GOA (gray box) SSTa as a precursor to CCLME SSTa (white contour bounds r > 0.5). (d) AR(1) model with 6-month lead SSTa in the GOA added as a second forcing term. (e) Residual of the AR(1) model in (d) correlated with basin-wide SSTa suggests a role for ENSO variability. (f) AR(1) model with the EqSOI added as a third forcing term.

inclusion of 6-month lead GOA SSTa dramatically improves the AR(1) model, particularly in 2014. While a mechanistic evaluation of the GOA influence on the CCLME is beyond the scope of this paper, this finding is consistent with a tendency found in the historical record for warm GOA SSTa to evolve into an Arc pattern warming the following year (DM2016).

Correlating residuals from our second AR(1) model with basin-wide SSTa produces a spatial pattern that implicates ENSO variability (Fig. 6.2e). While one pathway for ENSO forcing is through the alongshore wind (Alexander et al. 2002; Jacox et al. 2015), which is already in our model, ENSO may impart additional variance through coastal trapped waves or anomalous poleward advection. Inclusion of the NOAA/CPC Equatorial Southern Oscillation Index (EqSOI) only modestly improves the overall performance of the AR(1) model, but improvements are visible for calendar years impacted by strong El Niños (Fig. 6.2f). The influence of the 2015/16 El Niño is visible in our AR(1) model, though its timing was earlier (a larger ENSO influence in 2015 than 2016; Frishknecht et al. 2017) and its impact on the CCLME weaker (Jacox et al. 2016) than common ENSO indices (e.g., Niño3.4) suggest.

Discussion. While a FAR calculation of the 2014–16 CCLME SSTa suggests an important role for anthropogenic warming, over shorter timescales the FAR is also influenced by natural internal variability, especially in the CCLME (Weller et al. 2015). The analysis outlined in Fig. 6.2 suggests roles for multiple drivers of SSTa in the CCLME, specifically atmospheric variability off the North American west coast, a lagged response to GOA SSTa, and ENSO teleconnections impacting the CCS. While these forcing mechanisms share some variance (r = 0.4–0.6), the 2014–16 period had notably strong and sustained forcing from all three (Fig. ES6.2). The superposition of multiple drivers (weakened poleward winds, an extremely warm GOA, and El Niño) contributed heavily to the CCLME anomalies, and additional mechanisms are also likely at play [e.g., reemergence, where anomalies are sequestered beneath the mixed layer in spring/summer and reemerge when the mixed layer deepens in winter (Fig. ES6.3)]. Nonetheless, climate model ensembles suggest that anthropogenic warming increased the likelihood of the 2014–16 SST extremes through both a shift to a warmer mean state and an increase in temperature variability (Fig. 6.1; DM2016).

Marine resource management decisions will benefit greatly from mechanistic understanding, risk assessments, and attribution studies of extreme events (Oliver et al. 2017; Webb and Werner 2018). To that end, we find that the recent extreme ocean temperatures off the U.S. West Coast, which significantly impacted many marine species and fisheries, were caused by the confluence of multiple complementary natural drivers and were likely exacerbated by long-term anthropogenic warming.

REFERENCES

Alexander, M. A., I. Blade, M. Newman, J. R. Lanzante, N.-C. Lau, and J. D. Scott, 2002: The atmospheric bridge: The influence of ENSO teleconnections on air–sea interaction over the global oceans. *J. Climate*, **15**, 2205–2231.

Banzon, V., T. M. Smith, T. M. Chin, C. Liu, and W. Hankins, 2016: A long-term record of blended satellite and in situ sea-surface temperature for climate monitoring, modeling and environmental studies. *Earth Syst. Sci. Data*, **8**, 165–176, doi:10.5194/essd-8-165-2016

Bond, N. A., M. F. Cronin, H. Freeland, and N. Mantua, 2015: Causes and impacts of the 2014 warm anomaly in the NE Pacific. *Geophys. Res. Lett.*, **42**, 3414–3420, doi:10.1002/2015GL063306.

Brady, R. X., M. A. Alexander, N. S. Lovenduski, and R. R. Rykaczewski, 2017: Emergent anthropogenic trends in California Current upwelling. *Geophys. Res. Lett.*, **44**, 5044–5052, doi:10.1002/2017GL072945.

Cavole, L. M., and Coauthors, 2016: Biological impacts of the 2013–2015 warm-water anomaly in the Northeast Pacific. *Oceanography*, **29** (2), 273–285, doi:10.5670/oceanog.2016.32.

Chavez, F. P., and Coauthors, 2002: Biological and chemical consequences of the 1997–1998 El Niño in central California waters. *Prog. Oceanogr.*, **54**, 205–232, doi:10.1016/S0079-6611(02)00050-2.

Checkley, Jr., D. M., and J. A. Barth: 2009: Patterns and processes in the California Current System. *Prog. Oceanogr.*, **83**, 49–64, doi:10.1016/j.pocean.2009.07.028.

Daly, E. A., R. D. Brodeur, and T. D. Auth, 2017: Anomalous ocean conditions in 2015: Impacts on spring Chinook salmon and their prey field. *Marine Ecol. Prog. Ser.*, **566**, 169–182, doi:10.3354/meps12021.

Di Lorenzo, E., and N. J. Mantua, 2016: Multi-year persistence of the 2014/15 North Pacific marine heatwave. *Nat. Climate Change*, **6**, 1042–1047, doi:10.1038/nclimate3082.

Frischknecht, M., M. Münnich, and N. Gruber, 2017: Local atmospheric forcing driving an unexpected California Current System response during the 2015–2016 El Niño. *Geophys. Res. Lett.*, **44**, 304–311, doi:10.1002/2016GL071316.

Gentemann, C. L., M. R. Fewings, and M. García-Reyes, 2017: Satellite sea surface temperatures along the West Coast of the United States during the 2014–2016 northeast Pacific marine heat wave. *Geophys. Res. Lett.*, **44**, 312–319, doi:10.1002/2016GL071039.

Jacox, M. G., J. Fiechter, A. M. Moore, and C. A. Edwards, 2015: ENSO and the California Current coastal upwelling response. *J. Geophys. Res. Oceans*, **120**, 1691–1702, doi:10.1002/2014JC010650.

——, E. L. Hazen, K. D. Zaba, D. L. Rudnick, C. A. Edwards, A. M. Moore, and S. J. Bograd, 2016: Impacts of the 2015–2016 El Niño on the California Current System: Early assessment and comparison to past events. *Geophys. Res. Lett.*, **43**, 7072–7080, doi:10.1002/2016GL069716.

Johnstone, J. A., and N. J. Mantua, 2014: Atmospheric controls on northeast Pacific temperature trends and variations, 1900-2012. *Proc. Natl. Acad. Sci. USA*, **111**, 14360–14365, doi:10.1073/pnas.1318371111.

Kay, J. E., and Coauthors, 2015: The Community Earth System Model (CESM) Large Ensemble project: A community resource for studying climate change in the presence of internal climate variability. *Bull. Amer. Meteor. Soc.*, **96**, 1333–1349, doi:10.1175/BAMS-D-13-00255.1.

Kilduff, D. P., E. Di Lorenzo, L. W. Botsford, and S. L. H. Teo, 2015: Changing central Pacific El Niños reduce stability of North American salmon survival rates. *Proc. Natl. Acad. Sci. USA*, **112**, 10962–10966, doi:10.1073/pnas.1503190112.

Lamarque, J.-F., and Coauthors, 2010: Historical (1850–2000) gridded anthropogenic and biomass burning emissions of reactive gases and aerosols: Methodology and application. *Atmos. Chem. Phys.*, **10**, 7017–7039, doi:10.5194/acp-10-7017-2010.

——, G. P. Kyle, M. Meinshausen, K. Riahi, S. J. Smith, D. P. van Vuuren, A. J. Conley, and F. Vitt, 2011: Global and regional evolution of short-lived radiatively-active gases and aerosols in the representative concentration pathways. *Climatic Change*, **109**, 191–212, doi:10.1007/s10584-011-0155-0.

Oliver, E. C. J., J. A. Benthuysen, N. L. Bindoff, A. J. Hobday, N. J. Holbrook, C. N. Mundy, and S. E. Perkins-Kirkpatrick, 2017: The unprecedented 2015/16 Tasman Sea marine heatwave. *Nat. Comms.*, **8**, 16101, doi:10.1038/ncomms16101.

Pearcy, W.G. 1992: *Ocean Ecology of North Pacific Salmonids*. Washington Sea Grant Program, 179 pp.

Peterson, W. T., and F. B. Schwing, 2003: A new climate regime in northeast Pacific ecosystems. *Geophys. Res. Lett.*, **30**, 1896, doi:10.1029/2003GL017528

——, N. Bond, and M. Robert, 2016: The Blob (Part three): Going, going, gone? *PICES Press*, **24**, 46–48. [Available online at www.pices.int/publications/pices_press/volume24/PPJan2016.pdf.]

PFMC, 2017a: Review of 2016 ocean salmon fisheries: Stock assessment and fishery evaluation document for the Pacific coast salmon fishery management plan. Pacific Fishery Management Council, 342 pp. [Available online at www.pcouncil.org/wp-content/uploads/2017/03/Review_of_2016_Ocean_Salmon_Fisheries_03032017.pdf.]

——, 2017b: Preseason report I: Stock abundance analysis and environmental assessment part 1 for 2017 ocean salmon fishery regulations. Pacific Fishery Management Council, 131 pp. [Available online at www.pcouncil.org/salmon/stock-assessment-and-fishery-evaluation-safe-documents/preseason-reports/2017-preseason-report-i/.]

Rayner, N.A., D. E. Parker, E. B. Horton, C. K. Folland, L. V. Alexander, D. P. Rowell, E. C. Kent, and A. Kaplan, 2003: Global analyses of sea surface temperature, sea ice, and night marine air temperature since the late nineteenth century. *J. Geophys. Res.*, **108**, 4407, doi:10.1029/2002JD002670.

Reynolds, R. W., T. M. Smith, C. Liu, D. B. Chelton, K. S. Casey, and M. G. Schlax, 2007: Daily high-resolution-blended analyses for sea surface temperature. *J. Climate*, **20**, 5473–5496, doi:10.1175/2007JCLI1824.1.

Sharma, S., L. A. Vélez-Espino, A. C. Wertheimer, N. Mantua, and R. C. Francis, 2012: Relating spatial and temporal scales of climate and ocean variability to survival of Pacific Northwest Chinook salmon (*Oncorhynchus tshawytscha*). *Fisheries Oceanogr.*, **22**, 14–31, doi:10.1111/fog.12001.

Stott, P. A., D. A. Stone, and M. R. Allen, 2004: Human contribution to the European heatwave of 2003. *Nature*, **432**, 610–614, doi:10.1038/nature03089.

Taylor, K. E., R. J. Stouffer, and G. A. Meehl, 2012: An overview of CMIP5 and the experiment design. *Bull. Amer. Meteor. Soc.*, **93**, 485–498, doi:10.1175/BAMS -D-1100094.1.

Webb, R. S., and F. E. Werner, 2018: Explaining extreme ocean conditions impacting living marine resources [in "Explaining Extreme Events of 2016 from a Climate Perspective"]. *Bull. Amer. Meteor. Soc.*, **99** (1), S7–S10, doi:10.1175/BAMS-D-17-0265.1.

Welch, C., 2016: The blob that cooked the Pacific. *Nat. Geogr.*, **230** (3), 54+ (~11 pages).

Weller, E., S.-K. Min, D. Lee, W. Cai, S.-W. Yeh, and J.-S. Kug, 2015: Human contribution to the 2014 record high sea surface temperatures over the western tropical and northeast Pacific Ocean [in "Explaining Extreme Events of 2014 from a Climate Perspective"]. *Bull. Amer. Meteor. Soc.*, **96** (12), S100–S104, doi:10.1175/BAMS-D-15-00055.1.

Wells, B. K., and Coauthors, 2017: Environmental conditions and prey-switching by a seabird predator impacts juvenile salmon survival. *J. Mar. Syst.*, **174**, 54–63, doi:10.1016/j.jmarsys.2017.05.008.

7. CMIP5 MODEL-BASED ASSESSMENT OF ANTHROPOGENIC INFLUENCE ON HIGHLY ANOMALOUS ARCTIC WARMTH DURING NOVEMBER–DECEMBER 2016

Jonghun Kam, Thomas R. Knutson, Fanrong Zeng, and Andrew T. Wittenberg

According to CMIP5 simulations, the highly anomalous Arctic warmth during November–December 2016, as estimated in five observed datasets, most likely would not have been possible without anthropogenic forcing.

Introduction. Arctic surface temperatures during November–December 2016 were anomalously warm (Fig. 7.1a). An Arctic area-averaged temperature index (Fig. 7.1b and Fig. ES7.2) set a new high record in the GISS Surface Temperature Analysis data (Hansen et al. 2010), and was either a record high or anomalously high—compared to early 20th century levels—according to four other observational products (online supplement material; Fig. ES7.2; Table ES7.2). Arctic sea ice extent was at record low levels (for the season) during November and December 2016 according to the National Snow and Ice Data Center (NSIDC) website (http://nsidc.org/arcticseaicenews/charctic-interactive-sea-ice-graph/). Arctic sea ice loss has been important for recent Arctic surface temperature amplification (Screen and Simmonds 2010; Kirchmeier-Young et al. 2016).

Here we compare observed Arctic temperature anomalies for 2016 from multiple datasets to CMIP5 model simulations (Taylor et al. 2012) to investigate whether such extreme seasonal warmth would have been likely to occur without anthropogenic forcing. Table ES7.1 lists the 18 CMIP5 models, their run lengths, and ensemble sizes for unforced Control simulations (CMIP5-CONT), Natural Forcing-Only historical simulations (CMIP5-NAT), and All Forcing (natural + anthropogenic) historical simulations (CMIP5-ALL).

Data and methods. We assess observed high-latitude warm anomalies for November–December 2016 by defining an observed Arctic temperature index (zonal average over 64°–84°N; Fig. 7.1b; Fig. ES7.2). The index is assumed non-missing for a given year if at least 33% of area has coverage, where coverage at a grid cell requires at least one of the two months to be available. Model data were masked with the GISTEMP observed data availability mask. The GISTEMP dataset uses 1200-km spatial smoothing, resulting in more spatial coverage in the data-sparse Arctic regions, at the expense of relying on the spatial smoothing to fill data gaps. The small region north of 84°N (5.4% of total Arctic area) is not included due to the large fraction of unavailable estimates over the region, especially prior to 1950, even in the smoothed GISTEMP analysis (see Fig. ES7.1). We also analyzed the HadCRUT4 (Morice et al. 2012), NOAA (Vose et al. 2012), Berkeley Earth Land+Ocean (Rohde et al. 2014), and Cowtan & Way version 2.0 (Cowtan and Way 2014) datasets to assess uncertainties in the Arctic temperature index derived from the GISTEMP data (online supplement material).

From the CMIP5 models, we use surface air temperature over land points, and either sea surface temperature or ice surface temperature over ocean points, depending on the simulated sea-ice coverage. The GISTEMP data uses air temperature over land and near-surface water temperature over oceans, with their extrapolation of temperatures being especially prominent over large sea ice regions.

We estimate the fraction of attributable risk (FAR; Stott et al. 2004) for the observed anomalies (FAR = $1 - P_{nat}/P_{all}$), following the procedures used in our previous regional temperature extremes assessments (e.g., Kam et al. 2016). The FAR analysis begins by assessing the probability of exceeding the second-ranked extreme November–December
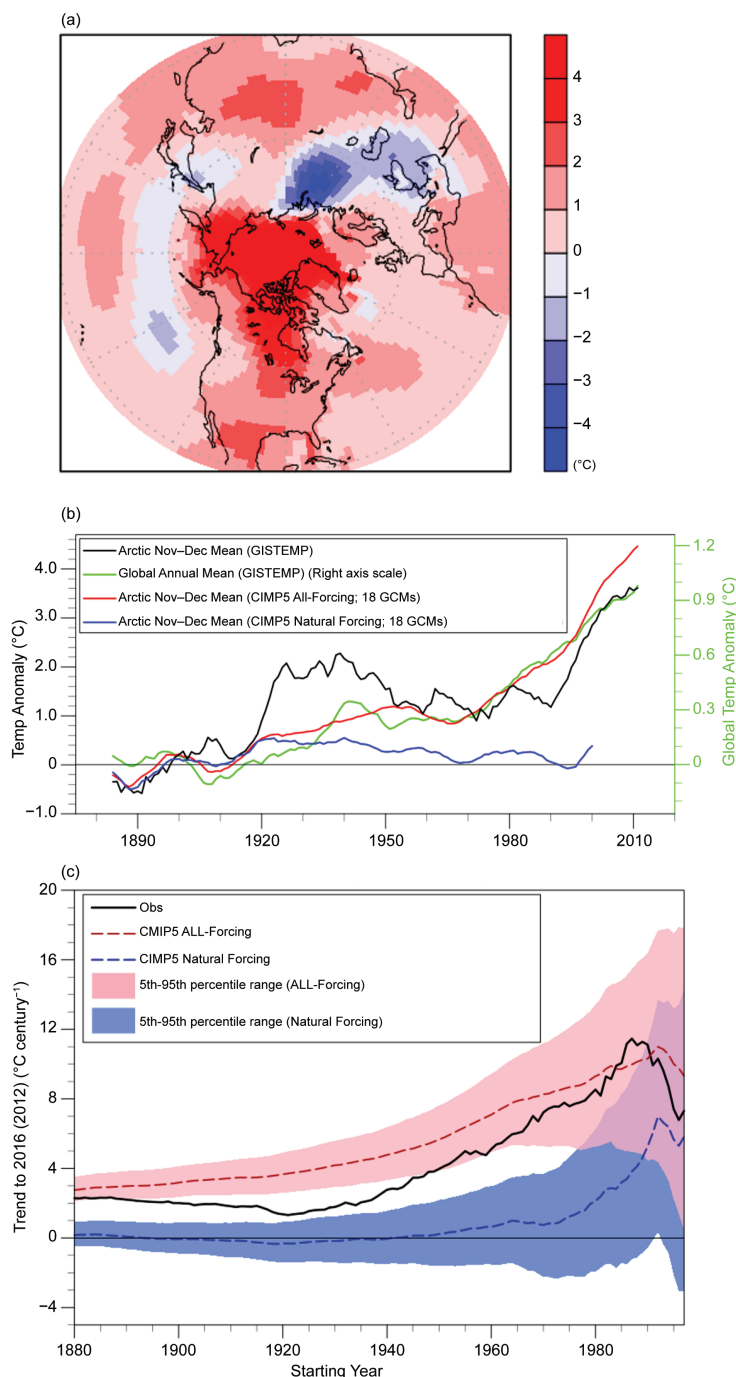
FIG. 7.1. Arctic Nov–Dec 2016 surface temperature anomalies (°C, relative to 1881–1920): (a) GISTEMP observed anomalies; (b) Arctic index (64°–84°N) 10-yr running mean Nov–Dec values. Black curves: observed GISTEMP; red (blue): average of ensemble-means of CMIP5 All-Forcing (Natural-Forcing) anomalies from 18 models, respectively. Green curve: global annual-mean temperature anomalies using the y-axis labels along right edge. (c) Sliding trends (°C century⁻¹) as a function of start years varying from 1880 to 1997. All trends are for data segments ending in 2016 for GISTEMP observations (black curve) or CMIP5 All-Forcing (red curve, with 5th–95th percentile shown by pink shading). Trends end in 2012 for the Natural Forcing-Only data (blue curve and shading). See further details of methods in Fig. ES7.3.

warmth in the Arctic, for both present-day and preindustrial conditions, using 1881–1920 as our reference period. Here, we use the second-ranked year value as our main threshold value since, for GISTEMP, 2016 was the single year that exceeded the second-ranked extreme, and so in determining the probability of a year like 2016, we explore the probability of anomaly exceeding the previous record. We used the first-ranked extreme value as an alternative threshold, as a sensitivity test. The first- and second-ranked extreme values and years for the five observational datasets are presented in Table ES7.2.

For the present-day climate, we estimate the probability of exceeding the second-ranked threshold values, as of the year 2016, in the CMIP5 All-Forcing simulations. A multimodel probability distribution for the All-Forcing (Natural-Forcing) runs is constructed by adding the grand ensemble mean (multimodel mean of the ensemble means from the individual CMIP5 models) to the aggregate distribution of annual anomalies from the CMIP5 control runs. For each individual model, the All-Forcing (Natural-Forcing) distribution consists of the All-Forced (Natural-Forced) ensemble mean for 2016, combined with the distribution of annual anomalies from that model's control run.

For the preindustrial case, we estimate the probability of exceeding the threshold value in the CMIP5 Natural Forcing-Only simulations, extrapolated to 2016. The extrapolated value was based on the ensemble-mean time-mean value from 2001 to the last year of each simulation of the 18 CMIP5 models (2005 or 2012, depending on the model). The probability distributions are computed for each of the eight individual climate models with at least three NAT runs and three All-Forcing runs. All-Forcing runs were extended from 2006 through 2016 using the RCP8.5 scenario. For the multimodel mean, we used the grand ensemble mean from all 18 climate models that provided Natural Forcing-Only runs (including those with a single CMIP5-NAT forcing run).

Lastly, we estimate the observed internal variability by subtracting the grand ensemble mean of the CMIP5–ALL runs from the observations, to attempt to remove the forced variability component. We then filtered the observed residuals using a low-pass filter with a half-power point at nine years, and computed their standard deviation. We also computed the standard deviations of each the eight CMIP5 models' low-passed filtered control run series.

Results. The 10-year moving average of the Arctic November–December temperature index (Fig. 7.1b) shows very strong warming during the early 20th century prior to about 1930. A second major warming period began around 1990, culminating in the 2016 value (Fig. ES7.2) which was the warmest ever recorded in the GISTEMP and Berkeley datasets. In Fig. 7.1b, global-mean annual-mean temperature anomalies are compared with the November–December Arctic temperature index, indicating that in the GISTEMP dataset, Arctic warming over the last century has been almost three times that of observed global mean temperature. Compared to global temperature, the Arctic November–December index also has much more pronounced multidecadal variability. Despite this large multidecadal variability, the observed Arctic warming trend is highly unusual compared to the trends caused by natural variability, according to the average distribution of trends from CMIP5-NAT runs (Fig. 7.1c). This is the case for various trend periods ending in 2012—at least for all trend start years prior to about 1990. The century-scale warming trend and strong multidecadal variability are common features of Arctic temperature indices from a number of observed datasets in addition to GISTEMP (e.g., Fig. ES7.2), including an analysis using only meteorological stations over the region north of 60°N (Bekryaev et al. 2010).

While the century-scale Arctic warming observed since the late 1800s resembles that in the CMIP5 All-Forcing ensemble mean (Fig. 7.1b), the latter does not show the strong warm phase during 1920–40, suggesting that this observed warming may contain a large contribution from internal climate variability [e.g., the Atlantic multidecadal oscillation (Johannessen et al. 2015)] in addition to a contribution of anthropogenic forcing (Najafi et al. 2015; Fyfe et al. 2013). The sliding trend analysis (Fig. 7.1c) indicates that observed trends to 2016 beginning from the first half of the 20th century are typically inconsistent (significantly too low), compared to the CMIP5 All-Forcing ensemble. This inconsistency between the observations and the CMIP5 All-Forcing ensemble could be due to a number of factors including: 1) mis-specified or missing climate forcing agents in the models; 2) errors in the model responses to the climate forcings; 3) underestimation of Arctic internal climate variability in the models; or 4) data issues, including problems with comparing modeled and observed Arctic data as discussed above.

We estimate the FAR for the multimodel ensemble for the first- and second-ranked year threshold values. The FAR ranges from 0.96 to 0.99 across the five observational datasets (Fig. 7.2a). A FAR of 1.0 for a particular set of forcings would indicate that that particular forcing set (e.g., anthropogenic forcing) alone is responsible for the entire risk of exceeding the given threshold. We also explore uncertainties in the FAR estimates, by computing the FAR for the second-ranked year threshold value for each individual CMIP5 model. The spread in these FAR estimates indicates the influence of observational uncertainties as well as uncertainties across the models. The lowest FAR estimate (0.82) is from a combination of the second-ranked year value from NOAA observations and the CSIRO-Mk3-6-0 model (Fig. 7.2a), and reflects that model having the weakest 2016 All-Forcing response among the eight models, along with the second-highest 2016 Natural Forcing-Only response. Most of the individual model FAR estimates in Fig. 7.2a are above 0.9, however.

We evaluate the modeled vs. estimated observed internal decadal variability of Arctic November–December temperatures in Fig. 7.2b. The GFDL-CM3 model's (M4) standard deviation (0.78°C) exceeds the observed estimated range of 0.62°C (Berkeley Earth) to 0.77°C (HadCRUT4). The remaining model control runs have weaker simulated decadal variability than observed, ranging from 0.45° to 0.58°C. Due to the relatively short observational record, and uncertainties in the forced response mean, the estimate of real-world decadal internal variability remains uncertain (e.g., Knutson et al. 2016), and will require further evaluation in the future, for example with paleoclimate data (e.g., Delworth and Mann 2000). The strong intrinsic variability of GFDL-CM3 contributes to its having the second-lowest FAR estimate (for the second-ranked threshold value) among the eight climate models (Fig. 7.2a). Further study is needed to assess the causes of possible under/over-estimates of internal decadal Arctic variability, and to address other caveats and uncertainties identified above.
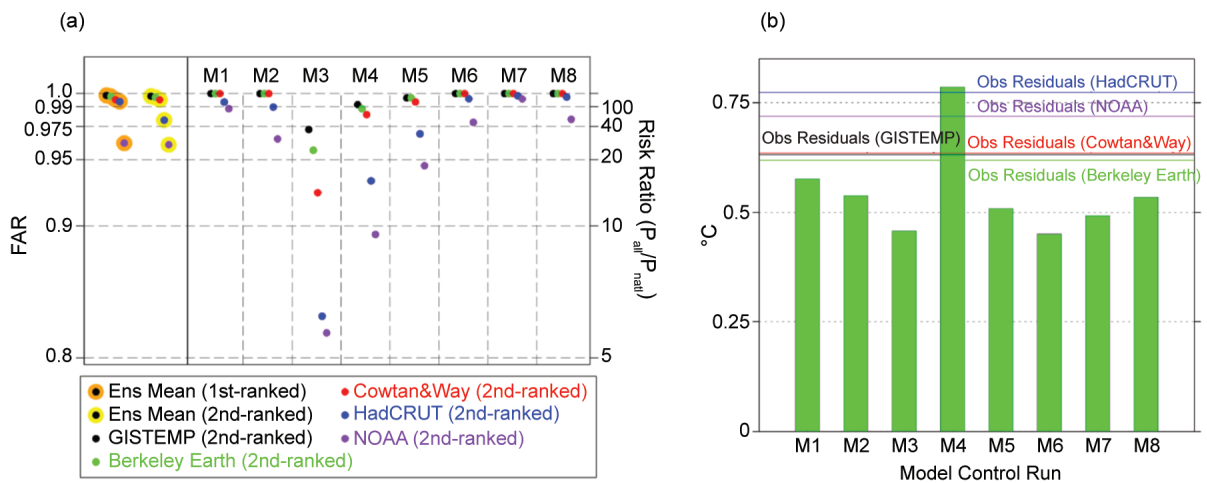
Fɪɢ. 7.2. (a) Estimated FAR of exceeding the first- and second-ranked observed Arctic Nov–Dec temperature anomaly thresholds (large orange and yellow circles, respectively), based on the CMIP5 multimodel ensemble. Small dots indicate the observational dataset used. Columns M1–M8 show estimates from individual CMIP5 models (second-ranked observed anomaly threshold) for each observational dataset. (M1–M8 correspond to the model IDs in Table ES7.1.) Risk ratios are indicated by the y-axis labels along right edge. (b) Simulated internal decadal standard deviation of M1–M8 control runs (green bars), along with observational-based estimates from low-pass-filtered Nov–Dec Arctic temperatures (°C) from five observational datasets (horizontal colored lines), with the model-estimated All-Forcing (natural + anthropogenic) response removed.

Conclusions. In summary, we find highly anomalous surface warmth over the Arctic during November-December 2016 in five observed datasets. According to CMIP5 model simulations, this anomalous Arctic warmth most likely would not have been possible without a long-term warming contribution from anthropogenic forcing.

REFERENCES

Bekryaev, R. V., I. V. Polyakov, and V. A. Alexeev, 2010: Role of polar amplification in long-term surface air temperature variations and modern Arctic warming. *J. Climate*, **23**, 3888–3906, doi:10.1175/2010JCLI3297.1.

Cowtan, K., and R. G. Way, 2014: Coverage bias in the HadCRUT4 temperature series and its impact on recent temperature trends. *Quart. J. Roy. Meteor. Soc.*, **140**, 1935–1944, doi:10.1002/qj.2297.

Delworth, T. L., and M. E. Mann, 2000: Observed and simulated multidecadal variability in the Northern Hemisphere. *Climate Dyn.*, **16**, 661–676, doi:10.1007/s003820000075.

Fyfe, J. C., K. von Salzen, N. P. Gillett, V. K. Arora, G. M. Flato, and J. R. McConnell, 2013: One hundred years of Arctic surface temperature variation due to anthropogenic influence. *Sci. Rep.*, **3**, 2645, doi:10.1038/srep02645.

Hansen, J., R. Ruedy, M. Sato, and K. Lo, 2010: Global surface temperature change. *Rev. Geophys.*, **48**, RG4004, doi:10.1029/2010RG000345.

Johannessen, O. M., S. I. Kuzmina, L. P. Bobylev, and M. W. Miles, 2016: Surface air temperature variability and trends in the Arctic: New amplification assessment and regionalisation. *Tellus A*, **68**, 28234, doi:10.3402/tellusa.v68.28234.

Kam, J., T. R. Knutson, F. Zeng, and A. T. Wittenberg, 2016: Multimodel assessment of anthropogenic influence on record global and regional warmth during 2015 [in "Explaining Extreme Events of 2015 from a Climate Perspective"]. *Bull. Amer. Meteor. Soc.*, **97** (12), S4–S8, doi:10.1175/bams-D-16-0138.1.

Kirchmeier-Young, M. C., F. W. Zwiers, and N. P. Gillett, 2016: Attribution of extreme events in Arctic sea ice extent. *J. Climate*, **30**, 553–571, doi:10.1175/JCLI-D-16-0412.1.

Knutson, T. R., R. Zhang, and L. W Horowitz, 2016: Prospects for a prolonged slowdown in global warming in the early 21st century. *Nat. Comm.*, **7**, 13676, doi:10.1038/ncomms13676.

Morice, C. P., J. J. Kennedy, N. A. Rayner, and P. D. Jones, 2012: Quantifying uncertainties in global and regional temperature change using an ensemble of observational estimates: The HadCRUT4 data set. *J. Geophys. Res.*, **117**, D08101, doi:10.1029/2011JD017187.

Najafi, M. R., F. W. Zwiers, and N. P. Gillett, 2015: Attribution of Arctic temperature change to greenhouse-gas and aerosol influences. *Nat. Clim. Change*, **5**, 246–249, doi:10.1038/nclimate2524.

Rohde, R., and Coauthors, 2014: A new estimate of the average Earth surface land temperature spanning 1753 to 2011. *Geoinfo. Geostat. Overv.*, **1** (1), doi:10.4172/2327-4581.1000101.

Screen, J. A., and I. Simmonds, 2010: The central role of diminishing sea ice in recent Arctic temperature amplification. *Nature*, **464**, 1334–1337, doi:10.1038/nature09051.

Stott, P. A., D. A. Stone, and M. R. Allen, 2004: Human contribution to the European heatwave of 2003. *Nature*, **432**, 610–614, doi:10.1038/nature03089.

Taylor, K. E., R. J. Stouffer, and G. A. Meehl, 2012: An overview of CMIP5 and the experimental design. *Bull. Amer. Meteor. Soc.,* **93**, 485–498, doi:10.1175/BAMS-D-00094.1.

Vose, R. S., and Coauthors, 2012: NOAA's merged land–ocean surface temperature analysis. *Bull. Amer. Meteor. Soc.*, **93**, 1677–1685, doi:10.1175/BAMS-D-11-00241.1.

8. THE HIGH LATITUDE MARINE HEAT WAVE OF 2016 AND ITS IMPACTS ON ALASKA

John E. Walsh, Richard L. Thoman, Uma S. Bhatt, Peter A. Bieniek, Brian Brettschneider,
Michael Brubaker, Seth Danielson, Rick Lader, Florence Fetterer, Kris Holderied, Katrin Iken,
Andy Mahoney, Molly McCammon, and James Partain

The 2016 Alaska marine heat wave was unprecedented in terms of sea surface temperatures and ocean heat content, and CMIP5 data suggest human-induced climate change has greatly increased the risk of such anomalies.

Earth System Observations. The Gulf of Alaska (GOA) and Bering Sea have been anomalously warm for several years with the warmth peaking in 2016. As a consequence of the high marine heat content (HC) and SSTs, coastal areas of Alaska had their warmest winter–spring of record in 2016 (Walsh et al. 2017) and earliest river ice breakup for multiple Alaska rivers (www.weather.gov/aprfc/breakupDB). Observed marine warmth, impacts on the marine ecosystem, and an attribution analysis using CMIP5 models are presented here.

The marine heat wave was first noted over deep waters of the northeastern Pacific Ocean in January 2014 (Freeland 2014; Bond et al. 2015); anomalous temperatures at coastal GOA stations arrived variously between January and June. Warm temperature anomalies were confined to the top 100 meters until late 2014, after which they penetrated to depths of 300 meters and reached strengths greater than 2 standard deviations (Roemmich and Gilson 2009).

AFFILIATIONS: Walsh and Brettschneider—Alaska Center for Climate Assessment and Policy, University of Alaska, Fairbanks, Alaska; Thoman—NOAA/National Weather Service Alaska, Fairbanks, Alaska; Bhatt—Geophysical Institute, and Department of Atmospheric Sciences, University of Alaska, Fairbanks, Alaska; Mahoney—Geophysical Institute, University of Alaska, Fairbanks, Alaska; Lader—International Arctic Research Center, University of Alaska, Fairbanks, Alaska; Bieniek—Alaska Climate Science Center, University of Alaska, Fairbanks, Alaska; Brubaker—Alaska Native Tribal Health Consortium, Anchorage, Alaska; Danielson and Iken —College of Fisheries and Ocean Sciences, University of Alaska, Fairbanks, Alaska; Fetterer—NSIDC and NOAA/NESDIS National Centers for Environmental Information, Boulder, Colorado; Holderied—NOAA/National Ocean Service, National Centers for Coastal Ocean Science, Seldovia, Alaska; McCammon—Alaska Ocean Observing System, Anchorage, Alaska; Partain—NOAA/NESDIS National Centers for Environmental Information, Anchorage, Alaska

The consensus of previous studies is that atmospheric circulation anomalies played a key role in initiating and maintaining the North Pacific "blob" of warm water (Bond et al. 2015). Unusually high pressure south of the Gulf of Alaska reduced heat loss to the atmosphere and also reduced cold advection over the region. Forcing of the atmospheric anomalies has been linked to SST anomalies in the western tropical Pacific Ocean (Seager et al. 2015) and to decadal-scale modes of North Pacific Ocean variability (Di Lorenzo and Mantua 2016). Lee et al. (2015) have argued that sea ice anomalies also contributed to the atmospheric circulation anomalies in 2013/14. By contrast, the winter of 2015/16 was characterized by negative sea level pressure anomalies of more than 12 hPa centered in the eastern Bering Sea (Fig. ES8.1d). The associated northward airflow evident throughout the depth of the atmosphere (Fig. ES8.1b) likely drove lingering heat from the blob into the GOA and Bering Sea regions. An unusually deep Aleutian low is a typical feature of the El Niño conditions that characterized early 2016 (Walsh et al. 2017).

The positive HC anomalies (Fig. 8.1a) reached an extreme in 2016 for the GOA and Bering Sea (Figs. 8.1d,e), with most of the region ranking in the top five warmest HCs of record (Fig. ES8.2a). Oceanic temperatures are from GODAS (Saha et al. 2006), NCEP's high-resolution ocean analysis. HC was calculated by integrating ocean temperature (°C) from the surface to 300 meters or the bottom of each model water column. This value was then divided by the depth of its respective water column, the 1981–2010 mean was removed, and the quantity was normalized to allow comparison between the Bering Sea (51°–64.5°N, 180°–160°W) and GOA (50°–60°N, 150°–130°W) regions (Figs. 8.1d,e).

FIG. 8.1. (a) Jan–Dec 2016 ocean heat content anomaly (°C) from the surface to 300 m or bottom of ocean column. Boxes outline GOA and Bering Sea regions. Normalized area-weighted SST anomalies for (b) Bering Sea and (c) GOA. Normalized area-weighted heat content anomalies for (d) Bering Sea and (e) GOA. (f) Select impacts of 2016 marine heat in Alaska waters.

Normalized SST anomalies from 1900 provide context for the anomalies. The 2016 SSTs were the warmest on record for the Bering Sea and the second warmest in the GOA (Figs. 8.1b,c) where 2015 was warmest. SSTs were anomalously warm starting in 2012 (Weller et al. 2015), and most of the GOA and

Bering Sea ranked in the top five SSTs of record (Fig. ES8.2b). SST data are from NOAA's Extended Reconstructed Sea Surface Temperature dataset, version 4 (Huang et al. 2014), and anomalies use the 1981–2010 mean. Negative anomalies greater than 2 sigma are evident in both regions from 2006–13.

The warming was primarily confined to the inner GOA shelf in September 2014, suggesting that heat was advected along-shore within the Alaska Coastal Current. By spring 2015 the shelf was uniformly warm and water remained 1°–2°C warmer than normal through September 2016. This heat was accompanied by surface mixed layer shoaling and a strengthening of the near-surface stratification, impacting nutrient availability and the ecosystem.

Impacts. Ecological and societal impacts of the 2016 marine heat wave are complex but unequivocal. Some marine ecological impacts resulted from the multiyear nature of the marine heat wave, so cannot be attributed solely to the 2016 event.

The consequences of this persistent warming were felt through the entire marine food web. The warm conditions favored some phytoplankton species, and one of the largest harmful algal blooms on record reached the Alaska coast in 2015 (Peterson et al. 2016a). Kachemak Bay had uncommon paralytic shellfish poisoning events and oyster farm closures in 2015 and 2016. Copepods, the crustaceans that form the cornerstone of the open ocean food web, had a higher abundance of smaller species, which provide less nutritious food source to higher trophic levels, including forage fish. The occurrence of more southern copepod species in the GOA likely resulted from the anomalous warmth (Kintisch 2015; Peterson et al. 2016b).

The dramatic mortality events in seabird species such as common murres (*Uria aalge*) in 2015/16 (tens of thousands of dead birds counted) were attributed to starvation and presumed to be a result of warming-induced effects on food supply (H. Renner 2017, U.S. Fish and Wildlife Service, personal communication). Increased occurrences of diseases were also observed, including sea star wasting disease, first recognized in Kachemak Bay in 2015. (K. Iken 2017, personal observations; Fig. 8.1f).

Over 100 observations of impacts on communities across Alaska were posted to the Local Environmental Observer (LEO) network (http://leonetwork.org) between October 2013 and December 2016. These impacts relate to changes in the acquisition, preservation, quality, and quantity of wild foods. Local observers noted changes in seasonality, weather, ocean conditions, plants, and wildlife, which challenge people engaged in subsistence and commercial activities with increased variability and uncertainty. The lack of winter sea ice in western Alaska delayed or prevented ice-based harvesting of fish, crab, seal, and whale. For shellfish harvests, the warm waters translated into persistent high levels of harmful algae across the GOA and North Pacific as far west as the Aleutian Islands, with concerns about food safety extending to the Bering Strait.

Attribution. The role of anthropogenic climate change in the marine heat wave of 2016 was assessed through an evaluation of CMIP5 model output. Attribution was estimated by comparing SSTs and HC in 60-year segments (to resolve relevant decadal variability such as the Pacific decadal oscillation; PDO) from present and preindustrial climate simulations. Five CMIP5 models were selected (see online supplement material; Walsh et al. 2017b, manuscript submitted to *Environ. Modell. Software*): CCSM4, GFDL-CM3, GISS-E2-R, IPSL-CM5A-LR, and MRI-CGCM3. The models' trends of SST over the 1900–2005 historical simulations ranged from 0.27° to 0.52°C century^{-1} (mean = 0.41°C) for the Bering Sea and 0.22° to 0.90°C century^{-1} (mean = 0.46°C) for the GOA. The corresponding observational values from Figs. 8.1b,c are 0.70° and 0.84°C century^{-1} for the Bering Sea and GOA. If the models' century-scale trends represent the anthropogenic forcing signal, then one may argue that the larger values of the observed trends are partially attributable to internal variability.

For the attribution analysis, the present climate period is centered on 2016 and incorporates the historical simulation (1987–2005) and RCP8.5 (2006–46), which is the current trajectory of climate forcing, while the preindustrial climate incorporates a random 60-year period from each model. Monthly HC was calculated using ocean potential temperatures with a procedure similar to that used for GODAS. The SSTs and HCs were then interpolated to the GODAS grid, annual averages were computed, and area-weighted averages were extracted over the Bering Sea and GOA. This yielded 60-year time series for each region, model, and variable (present and preindustrial).

Annual values of SST and HC are warmer in GOA than the Bering Sea. Normalized anomalies using a 1987–2016 base period were used to account for differences in means. For SST and HC the present climate has increasing trends while the preindustrial does not (Figs. 8.2a,b). In all cases the preindustrial climate is
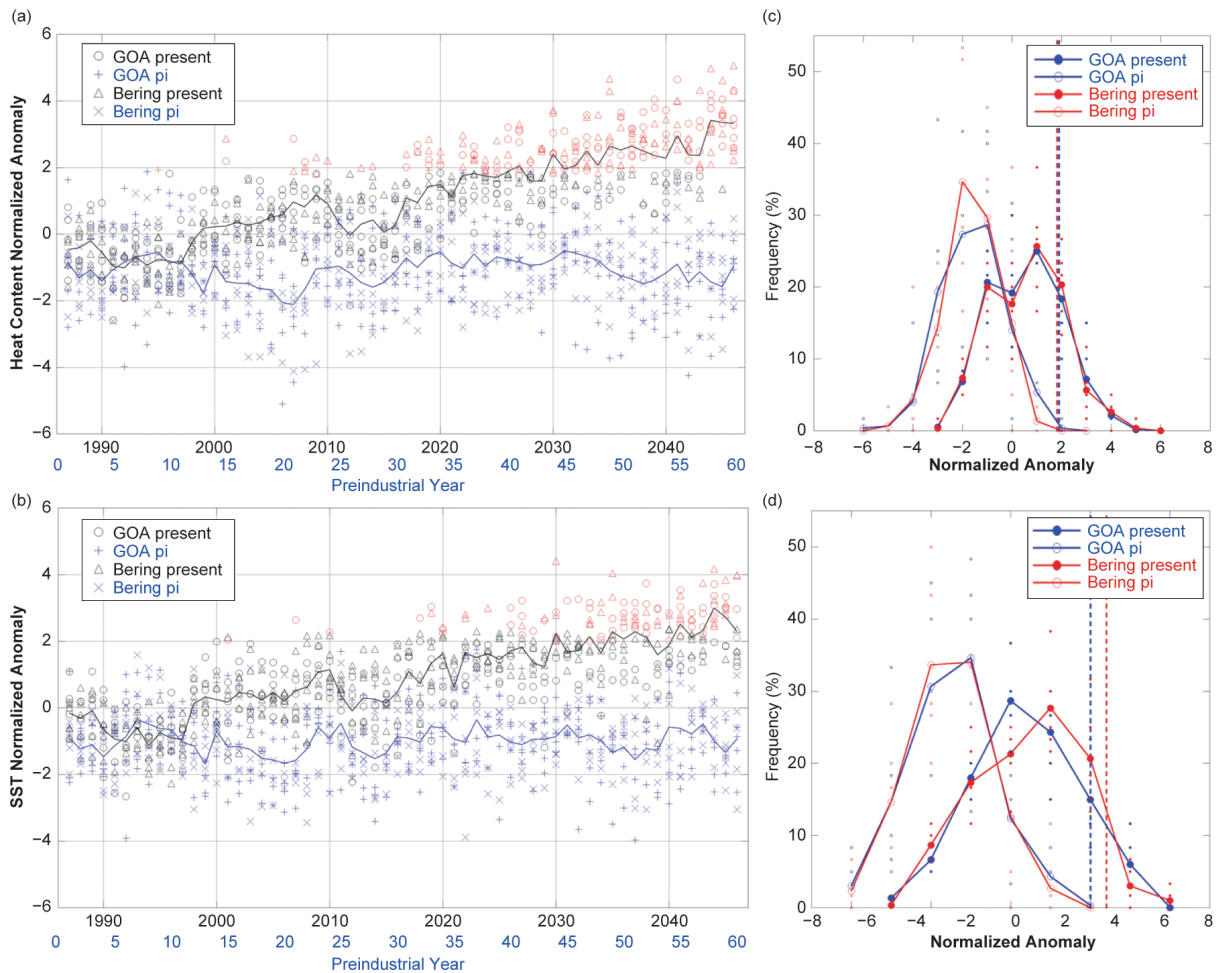
Fig. 8.2. Normalized anomalies of (a) heat content and (b) SSTs for the present (black) and preindustrial (blue) climate of the GOA (circle and plus) and Bering Sea (triangle and x) regions from the five model ensembles. Anomalies exceeding 2016 value are in red (shapes as indicated), and the ensemble/region means are shown by the solid lines. Mean probability distributions (%) of (c) heat content and (d) SSTs from the model ensembles; solid (open) circles indicate present (preindustrial) climate for the GOA (blue) and Bering Sea (red). Spread of individual models is shown by the smaller, corresponding open/closed circles. Dashed vertical lines show the 2016 anomalies: GOA (blue), Bering Sea (red).

generally cooler with no extreme positive anomalies comparable to the present climate (Figs. 8.2c,d).

Each model/variable/region was compared with its corresponding 2016 observed normalized anomaly value (see red coloring in Figs. 8.2a,b and vertical dashed lines in Figs. 8.2c,d). The preindustrial period had few cases meeting or exceeding the 2016 anomaly for any region or variable, while the present climate had many more, especially later in the period. For HC the number of years each model exceeded the 2016 anomaly ranged from 11 to 20 (0–2) cases in the present (preindustrial) climate for GOA and 16–24 (0) for Bering Sea. Fewer cases reached 2016 values in SSTs, with 5–18 (0–1) for GOA and 4–11 (0) for Bering Sea. For both variables the Bering Sea region's

preindustrial climate never reached the 2016 observed magnitude.

In this analysis the fraction of attributable risk (FAR; Stott et al. 2004; NASEM 2016) was computed as $FAR = 1 - Prob_{preindustrial}/Prob_{present}$ with the probability being the exceedance of the observed 2016 normalized anomaly. Bering Sea SSTs had FAR = 1 for all cases, while the GOA's FARs were 0.88–1 for SST and 0.82–1 for HC (but most models had FAR = 1, i.e., no instances of 2016-like anomalies in the preindustrial climate).

Conclusion. The warmth of the Bering Sea in 2016 was unprecedented in the historical record, and the warmth of the GOA nearly so. The FAR values

based on an ensemble of five global climate models indicate that the 2016 warm ocean anomalies cannot be explained without anthropogenic climate warming, although the region's large internal variability was also a contributing factor (Fig. 8.1 and online supplement material). A strong El Niño with a positive PDO (warm) phase, together with preconditioning of the waters during 2014/15 and the anomalous atmospheric circulation of early 2016, made for a "perfect storm" of marine heating around Alaska. Both anthropogenic forcing and internal variability were necessary for the extreme warmth of the subarctic seas. Our conclusions are consistent with and extend previous findings concerning the 2014 warm SST anomalies in the northeast Pacific (Weller et al. 2015). Additionally, the trajectory of the present climate with RCP8.5 indicates that SST and HC extreme anomalies like 2016 will become common in the coming decades. Given the many impacts of the 2016 anomaly, the future climate projected here will result in a profound shift for people, systems, and species when such warm ocean temperatures become common and not extreme in the GOA and Bering regions.

REFERENCES

Bond, N. A., M. F. Cronin, H. Freeland, and N. Mantua 2015: Causes and impacts of the 2014 warm anomaly in the NE Pacific. *Geophys. Res. Lett.,* **42**, 3414–3420, doi:10.1002/2015GL063306.

Di Lorenzo, E., and N. Mantua, 2016: Multi-year persistence of the 2014/15 North Pacific marine heatwave. *Nat. Climate Change*, **6**, 1042–1047, doi:10.1038/nclimate3082.

Freeland, H., 2014: Something odd in the Gulf of Alaska, February 2014. *CMOS Bulletin SCMO*, **42**, 57–59. [Available online at http://cmos.ca/uploaded/web/members/Bulletin/Vol_42/b4202.pdf.]

Huang, B., and Coauthors, 2014: Extended reconstructed sea surface temperature version 4 (ERSST.v4): Part I. Upgrades and intercomparisons. *J. Climate*, **28**, 911–930, doi:10.1175/JCLI-D-14-00006.1

Lee, M.-Y., C.-C. Hong and H.-H. Hsu, 2015: Compounding effects of warm sea surface temperature and reduced sea ice extent on the extreme circulation over the extratropical North Pacific and North America during the 2013-2014 boreal winter. *Geophys. Res. Lett.*, **42**, 1612–1618, doi:10.1002/2014GL062956.

Kintisch, E., 2015: 'The Blob' invades Pacific, flummoxing climate experts. *Science*, **348**, 17–18.

NASEM, 2016: *Attribution of extreme weather events in the context of climate change.* National Academies Press, 186 pp., doi:10.17226/21852.

Peterson, W., N. Bond, and M. Robert, 2016a: The blob (part three): Going, going, gone? *PICES Press*, **24** (1), 46–48. [Available online at https://pices.int/publications/pices_press/volume24/PPJan2016.pdf.]

——, ——, and ——, 2016b: The blob is gone but has morphed into a strongly positive PDO/SST pattern. *PICES Press*, **24** (2), 46–47, 50. [Available online at http://meetings.pices.int/publications/pices-press/volume24/issue2/PPJuly2016.pdf.]

Roemmich, D., and J. Gilson, 2009: The 2004–2008 mean and annual cycle of temperature, salinity, and steric height in the global ocean from the Argo Program. *Progr. Oceanogr.,* **82**, 81–100, doi:10.1016/j.pocean.2009.03.004.

Saha, S., and Coauthors, 2006: The NCEP climate forecast system. *J. Climate,* **19**, 3483–3517, doi:10.1175/JCLI3812.1.

Seager, R., M. Hoerling, S. Schubert, H. Wang, B. Lyon, A. Kumar, J. Nakamura, and N. Henderson, 2015: Causes of the 2011–14 California drought. *J. Climate*, **28**, 6997–7024, doi:10.1175/JCLI-D-14-00860.1.

Stott, P., D. Stone, and M. Allen, 2004: Human contribution to the European heatwave of 2003. *Nature*, **432**, 610–614, doi:10.1038/nature03089.

Walsh, J. E., P. A. Bieniek, B. Brettschneider, E. S. Euskirchen, R. Lader, and R. L. Thoman, 2017: The exceptionally warm winter of 2015-16 in Alaska: Attribution and anticipation. *J. Climate*, **30**, 2069–2088, doi:10.1175/JCLI-D-16-0473.1.

Weller, E., S.-K. Min, D. Lee, W. Cai, S.-W. Yeh, and J.-S. Kug, 2015: Human contribution to the 2014 record high sea surface temperatures over the western tropical and northeast Pacific Ocean [in "Explaining Extreme Events of 2014 from a Climate Perspective"]. *Bull. Amer. Meteor. Soc.,* **96** (12), S100–S104, doi:10.1175/BAMS-D-15-00055.1.

9. ANTHROPOGENIC AND NATURAL INFLUENCES ON RECORD 2016 MARINE HEAT WAVES

Eric C. J. Oliver, Sarah E. Perkins-Kirkpatrick, Neil J. Holbrook, and Nathaniel L. Bindoff

Two of the longest and most intense marine heat waves in 2016 were up to fifty times more likely due to anthropogenic climate change.

Introduction. In 2016 a quarter of the ocean surface experienced either the longest or most intense marine heatwave (Hobday et al. 2016) since satellite records began in 1982. Here we investigate two regions—Northern Australia (NA) and the Bering Sea/Gulf of Alaska (BSGA)—which, in 2016, experienced their most intense marine heat waves (MHWs) in the 35-year record. The NA event triggered mass bleaching of corals in the Great Barrier Reef (Hughes et al. 2017) while the BSGA event likely fed back on the atmosphere leading to modified rainfall and temperature patterns over North America, and it is feared it may lead to widespread species range shifts as was observed during the "Blob" marine heat wave which occurred immediately to the south over 2013–15 (Belles 2016; Cavole et al. 2016). Moreover, from a climate perspective it is interesting to take examples from climate zones with very different oceanographic characteristics (high-latitude and tropics). We demonstrate that these events were several times more likely due to human influences on the climate.

Data and methods. Observations consisted of sea surface temperatures (SSTs) from the daily NOAA OI SST v2 0.25° gridded dataset over 1982–2016 (Reynolds et al. 2007). We also used the in situ-based monthly HadISST 1° gridded dataset over 1900–2016 (Kennedy et al. 2011a,b). SST time series were generated by spatially averaging over (20°–5°S, 110°–155°E) for NA and (50°–65°N, 178°–127°W,) for the BSGA (Figs. 9.1a,b, black boxes). Anomalies were calculated relative to a base period of 1961–90. Daily climatologies were calculated from NOAA OI SST over the period 1982–2005, and in order to reference this to the chosen base period, we offset by the mean warming from 1961–90 to 1982–2005 calculated from HadISST (+0.19°C for both NA and BSGA; see Oliver et al. 2017 for more details).

Marine heat waves were defined as periods when SSTs were above the seasonally varying 90th percentile for at least five consecutive days (Oliver 2015; Hobday et al. 2016). We considered two MHW metrics: duration (time between the start and end dates) and maximum intensity (peak temperature anomaly).

We employed Coupled Model Intercomparison Project Phase 5 (CMIP5; Taylor et al. 2012) global climate model simulations of historical and projected future climates. We used daily SST outputs from the historicalNat (representing historical conditions without anthropogenic influence; models are forced by natural volcanic and solar forcing only) and the historical and RCP8.5 experiments (representing historical conditions with anthropogenic influence; models include anthropogenic greenhouse gas and aerosol forcing in addition to natural forcing) from seven models (Table ES9.1). Model climatologies were calculated using a base period of 1961–90; RCP8.5 anomalies were defined relative to the historical run climatology. The nonseasonal daily SST variance (i.e., after removing the climatology) was bias-corrected for each model based on the ratio between the standard deviations of the daily observations and the daily historical runs (see Oliver et al. 2017 for more details).
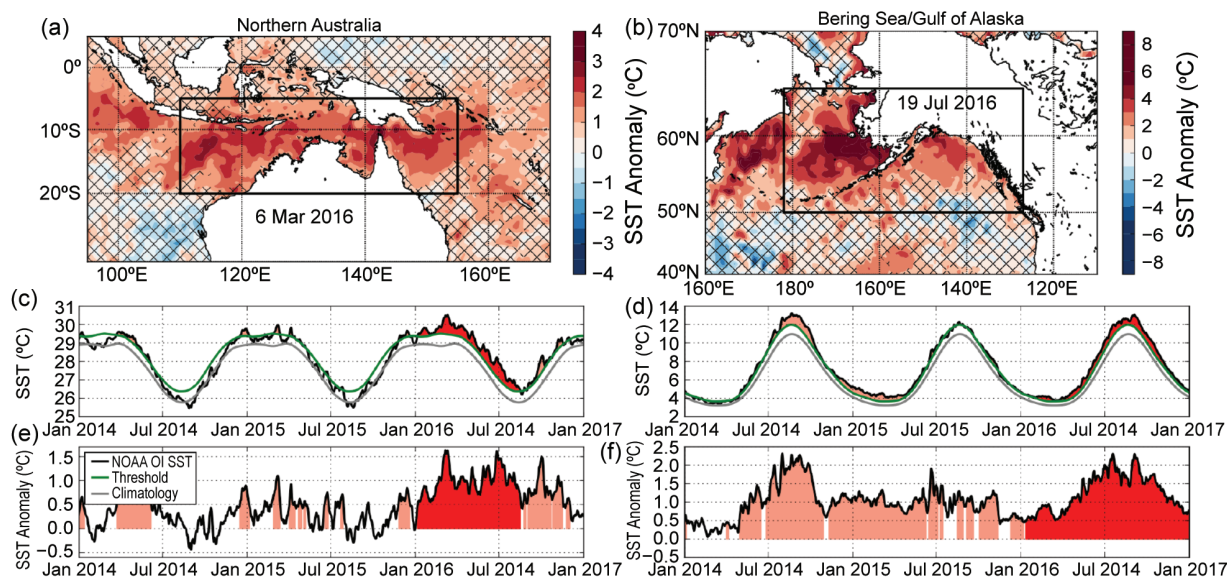
FIG. 9.1. 2016 MHWs in (left) NA and (right) BSGA. (a),(b) SST anomalies (°C) during the peak of each event (date indicated in panel) and unhatched areas indicate regions defined as MHW on that date according to the Hobday et al. (2016) definition. (c),(d) Daily SSTs (°C): NOAA OI SST (black), threshold (green), and 1961–90 climatology (gray) (e),(f) SST anomalies (°C) averaged over NA and BSGA during 2014–16. In (c)–(f) red shading indicates the 2016 MHW; lighter shading indicates other detected marine heat waves over the period.

MHWs were then identified in all model experiments using the Hobday et al. (2016) definition.

The fraction of attributable risk (FAR) methodology (Lewis and Karoly 2013; King et al. 2015) was used to examine how anthropogenic forcing modified likelihoods of the MHW events. Probability distributions (PDFs) of MHW durations and intensities were calculated from historicalNat (1850–2005, representative of the natural world) and RCP8.5 (2006–20, representative of the present day) experiments. We attributed event duration and intensity separately, and the value attributed was of the next least intense and next shortest event in the observed distribution (Lewis and Karoly 2013). The area of the PDF for values larger than that of the events being attributed was calculated to define the FAR statistic. We calculated 10 000 FAR values by bootstrap sampling with replacement ($N = 14$ random ensemble members sampled each iteration, half the total number of historical ensemble members), and quoted the first percentile of the resulting FAR distribution (with each ensemble weighted by the inverse of the number of ensembles for that particular model, thereby weighting equally across models). This quantified the degree to which we could be *virtually certain* (at least 99% probability in IPCC Fifth Assessment Report terminology; http://ipcc.ch/report/ar5/) that anthropogenic forcing modified the event likelihood. Return periods were estimated by taking the number of event occurrences

in a model experiment, dividing the total number of model years in that experiment (across all models and ensembles,) and then inverting. Note that the results presented here (FAR and return periods) are dependent on the models used and may change as the models are refined or if a different subset of models and experiments are used.

We also quantified the role of the dominant internally varying climate modes—noting that these two MHW events co-occurred with the 2015/16 El Niño, the negative phase of the Indian Ocean dipole (IOD) in 2016, and a strongly positive interdecadal Pacific oscillation (IPO) since 2014. Specifically, we examined how the probabilities of all MHWs in the records changed according to the phases of these three modes and quantified statistically how these modes modulated the likelihoods of MHWs generally, rather than the specific events considered above. Climate modes were quantified by the relevant indices calculated from the historicalNat experiment: the Niño-3.4 index, the dipole mode index (DMI), and the tripole mode index (TPI; see online supplement for details). All MHWs in the historicalNat simulations were identified and assigned the climate mode phases during the date of maximum MHW intensity. We compared the distributions of MHW intensities/durations according to their climate mode phases, using a Kolmogorov–Smirnov (KS) test to determine if the distributions were significantly different. We also cal-

culated whether the probability of occurrence of the MHWs were significantly modified according to the phases of the modes, and performed bootstrap resampling as above to estimate statistical significance.

Results. The 2016 marine heat waves in NA and BSGA were contiguous over broad swaths of the ocean (within the boxed regions: 4.76 Mkm² for NA, 2.45 Mkm² for BSGA; Figs. 9.1a,b). After averaging SSTs regionally, the NA event (Figs. 9.1c,e, red shading) was the most intense (maximum intensity of +1.6°C on 6 March 2016) and the second longest (224 days, 6 January–16 August 2016) on record; the BSGA event (Figs. 9.1d,f, red shading) was the most intense (maximum intensity of +2.3°C on 19 July 2016) and longest (≥355 days, 12 January 2016–31 December 2016, and extending into 2017 beyond the analysis period).

The probability distributions of NA and BSGA event intensities and durations from the observations and model runs, and the corresponding FAR values are shown in Fig. 9.2. For both intensity and duration, there were clear shifts towards larger events becoming more probable (Figs. 9.2a,b,e,f) in the 2006–20 world (RCP8.5, red lines) over the natural world (1850–2005, historicalNat, blue lines). The NA event intensity was *virtually certain* to be at least 8.5 times as likely in 2006–20 as compared to a natural world (Fig. 9.2c, dashed line) and NA event duration was *virtually certain* to be at least 53 times as likely in 2006–20 under anthropogenic climate change as compared to a natural world (Fig. 9.2g, dashed line). The BSGA event intensity was *virtually certain* to be at least 7.3 times as likely in 2006–20 as compared to a natural world (Fig. 9.2d, dashed line) and BSGA event duration was *virtually certain* to be at least 7.4 times as likely in 2006–20 under anthropogenic climate change as compared to a natural world (Fig. 9.2h, dashed line). Return periods of these events in the natural world were 1-in-970 years (NA duration), 1-in-170 years (NA intensity), 1-in-130 years (BSGA duration) and 1-in-120 years (BSGA intensity) and in all cases reduced to 1-in-5 years under anthropogenic forcing (RCP8.5, 2006–20).

The pattern of warming associated with anthropogenic forcing is more spatially uniform than the pattern of SST anomalies present during these events (Fig. ES9.1). Therefore, natural internal variability may have also played a role in the occurrence of these events (Table ES9.2). For NA, the distributions of MHW intensities and durations were significantly different between the DMI+ and DMI– phases ($p < 0.01$). The larger events, measured by the 90th percentiles of these distributions, showed MHWs as being longer in duration (74 vs. 40 days) but slightly less intense (0.99°C vs. 1.04°C) during DMI– phases. Frequency also showed a strong response: MHW events were significantly ($p < 0.01$) more/less frequent during DMI– (46.0%) / DMI+ (15.4%). There were no significant differences ($p > 0.01$) between the phases of Niño-3.4 or TPI for either MHW duration or intensity in the NA region; the frequency response was not significant for Niño-3.4 or TPI.

For the BSGA region, the distributions of MHW intensities were significantly different between DMI+ and DMI– phases ($p < 0.01$), with the 90th percentiles showing MHW events as being slightly more intense (1.39°C vs. 1.32°C) during the DMI+ phase. The distributions of durations were significantly different between Niño-3.4+ and Niño-3.4– phases ($p < 0.01$), with 90th percentiles showing MHW events being longer in duration (86 vs. 59 days) during the Niño-3.4+/- phase. The distributions of durations were also significantly different between TPI+ and TPI– phases ($p < 0.01$), with 90th percentiles showing MHW events being longer (85 vs. 65 days) during TPI+. Frequency also showed a significant ($p < 0.01$) response: 41.8% (39.3%) of MHW events occurred during Niño-3.4+ (TPI+) and only 19.3% (23.3%) during Niño-3.4– (TPI–); the frequency response was weaker (but significant) for DMI.

Conclusions. In 2016, both the NA and BSGA regions experienced their most intense MHWs across the 35-year satellite SST record. For BSGA, it was also the longest. We are *virtually certain* anthropogenic climate change played a role in increasing the likelihood of their event durations and intensities. Importantly, we find that there is attributable human influence regardless of the phase of El Niño, IOD, or IPO, although our findings suggest that natural internal variability also contributed to raising likelihoods. Specifically, we expect the negative IOD in 2016 to have played a role in increasing the NA region MHW event likelihood and duration and, interestingly, not the 2015/16 El Niño. We expect that the 2015/16 El Niño and positive IPO contributed to increasing the BSGA MHW event likelihood and duration in 2016. While both anthropogenic climate change and natural internal variability contributed to the occurrence of these extreme MHWs in 2016, the fact that anthropogenic forcing reduced return periods by a factor of up to two hundred indicated that it was extremely unlikely that natural variability alone led to the observed anomalies.
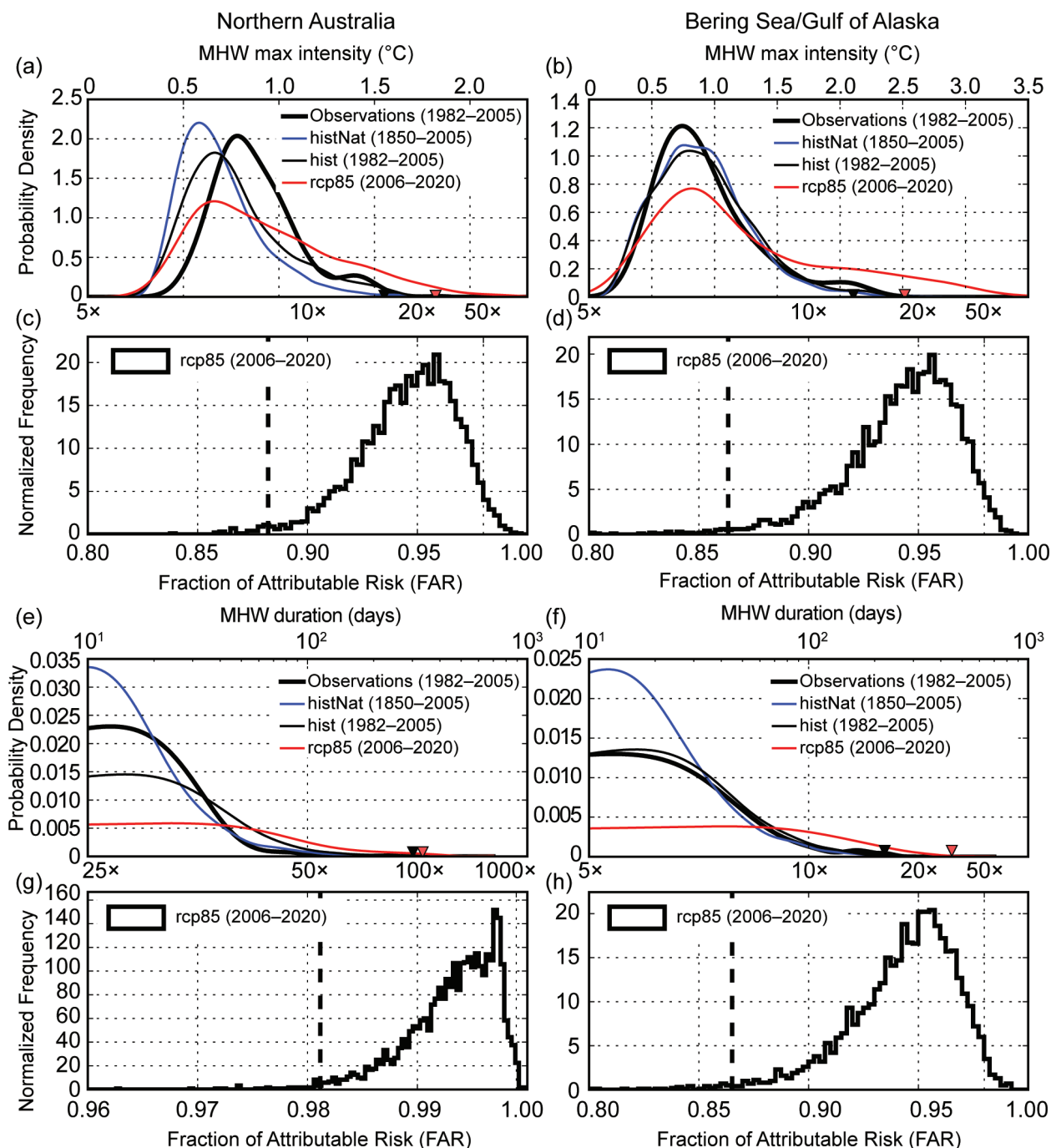
Northern Australia

(a)
MHW max intensity (°C)

Probability Density

- Observations (1982–2005)
- histNat (1850–2005)
- hist (1982–2005)
- rcp85 (2006–2020)

(c)
rcp85 (2006–2020)

Normalized Frequency

Fraction of Attributable Risk (FAR)

Bering Sea/Gulf of Alaska

(b)
MHW max intensity (°C)

- Observations (1982–2005)
- histNat (1850–2005)
- hist (1982–2005)
- rcp85 (2006–2020)

(d)
rcp85 (2006–2020)

Normalized Frequency

Fraction of Attributable Risk (FAR)

(e)
MHW duration (days)

Probability Density

- Observations (1982–2005)
- histNat (1850–2005)
- hist (1982–2005)
- rcp85 (2006–2020)

(g)
rcp85 (2006–2020)

Normalized Frequency

Fraction of Attributable Risk (FAR)

(f)
MHW duration (days)

- Observations (1982–2005)
- histNat (1850–2005)
- hist (1982–2005)
- rcp85 (2006–2020)

(h)
rcp85 (2006–2020)

Normalized Frequency

Fraction of Attributable Risk (FAR)

Fɪɢ. 9.2. Attribution of the 2016 MHWs in (left) NA and (right) BSGA using global climate models. Probability distributions of (a),(b) maximum intensity, and (e),(f) duration of all MHWs detected from the observations (thick black line) and the ensemble of CMIP5 historical simulations over 1982–2005 (thin black line), historical-Nat simulations (blue line), and RCP8.5 simulations over 2006–20 (red line). Black and red triangles indicate the properties of the event being attributed and of the 2016 event, respectively. The distribution of FAR values from the RCP85 runs for (c),(d) maximum intensity, and (g),(h) duration (distribution of all bootstrapped values: solid line; 1st percentile: dashed line).

REFERENCES

Belles, J., 2016: The blob is back: Anomalous warmth returns to the North Pacific Ocean. ("The Weather Channel" story, with related video.) [Available online at https://weather.com/news/climate/news/the-blob -pacific-ocean-temperatures/.]

Cavole, L. M., and Coauthors, 2016: Biological impacts of the 2013–2015 warm-water anomaly in the Northeast Pacific: Winners, losers, and the future. *Oceanography*, **29** (2), 273–285, doi:10.5670 /oceanog.2016.32.

Hobday, A. J., and Coauthors, 2016: A hierarchical approach to defining marine heat waves. *Prog. Oceanogr.,* **141**, 227–238, doi:10.1016/j.pocean.2015.12.014.

Hughes, T. P., and Coauthors, 2017: Global warming and recurrent mass bleaching of corals. *Nature*, **543**, 373–377, doi:10.1038/nature21707.

Kennedy, J. J., N. A. Rayner, R. O. Smith, D. E. Parker, and M. Saunby, 2011a: Reassessing biases and other uncertainties in sea surface temperature observations measured in situ since 1850: 1. Measurement and sampling uncertainties. *J. Geophys. Res.*, **116**, D14103, doi:10.1029/2010JD015218.

——, ——, ——, ——, and ——, 2011b: Reassessing biases and other uncertainties in sea surface temperature observations measured in situ since 1850: 2. Biases and homogenization. *J. Geophys. Res.*, **116**, D14104, doi:10.1029/2010JD015220.

King, A. D., G. J. van Oldenborgh, D. J. Karoly, S. C. Lewis, and H. Cullen, 2015: Attribution of the record high Central England temperature of 2014 to anthropogenic influences. *Environ. Res. Lett.*, **10**, 54002, doi:10.1088/1748-9326/10/5/054002.

Lewis, S. C., and D. J. Karoly, 2013: Anthropogenic contributions to Australia's record summer temperatures of 2013. *Geophys. Res. Lett.*, **40**, 3705–3709, doi:10.1002/grl.50673.

Oliver, E. C. J., 2015: Marine Heat waves detection code (Python module). [Available online at http://github .com/ecjoliver/marineHeat waves.]

Oliver, E. C. J., J. A. Benthuysen, M. L. Bindoff, A. J. Hobday, N. J. Holbrook, C. N. Mundy, and S. E. Perkins-Kirkpatrick, 2017: The unprecedented 2015/16 Tasman Sea marine heatwave. *Nat. Comm.*, **8**, 16101, doi:10.1038/ncomms16101.

Reynolds, R. W., T. M. Smith, C. Liu, D. B. Chelton, K. S. Casey, and M. G. Schlax, 2007: Daily high-resolution-blended analyses for sea surface temperature. *J. Climate*, **20**, 5473–5496, doi:10.1175/2007JCLI1824.1.

Taylor, K. E., R. J. Stouffer, and G. A. Meehl, 2012: An overview of CMIP5 and the experiment design. *Bull. Amer. Meteor. Soc.*, **93**, 485–498, doi:10.1175 /BAMS-D-00094.1.

10. EXTREME CALIFORNIA RAINS DURING WINTER 2015/16: A CHANGE IN EL NIÑO TELECONNECTION?

Xiao-Wei Quan, Martin Hoerling, Lesley Smith, Judith Perlwitz, Tao Zhang, Andrew Hoell, Klaus Wolter, and Jon Eischeid

Failure of heavy rain in Southern California during the 2016 strong El Niño compared to flooding rains during the 1983 strong El Niño does not constitute a climate change effect.

Introduction. This is a story of two extreme events—one that was expected *but failed to occur* and the other that actually *did occur* but was not anticipated. The one that failed was extreme wetness over Southern California (SCAL) during winter 2015/16, which was predicted by seasonal forecasts. The extreme event that did occur was dryness whose considerable magnitude exacerbated one of the worst droughts on record over SCAL.

Ranked among the three strongest historical El Niño events, the 2015/16 event fueled apprehensions for flooding rains over California. Analogs were drawn from abundant winter rain during the strong El Niño events of 1982/83 and 1997/98. NOAA's winter outlook indicated a greater than 60% probability that rain totals over SCAL would be in the upper tercile of the historical distribution (www.cpc.ncep.noaa.gov /products/archives/long_lead/llarc.ind.php).

December 2015–February 2016 precipitation over SCAL was 112 mm, which ranked in the lower tercile of the historical distribution of winter precipitation since 1895 (Fig. 10.1). While not unusual from a historical perspective (Fig. ES10.1a), this dryness was an extreme event when taking account of precipitation likelihoods during strong El Niño conditions (e.g., Hoell et al. 2016). We pose the attribution question whether a transformation of El Niño teleconnections has occurred due to climate change, the effect of which may have made such an extreme dry outcome during 2015/16 more likely than during 1982/83 and 1997/98. Such a transformation could arise from changes in atmospheric circulation that mediates

trajectories of tropically forced waves (e.g., Diaz et al. 2001; Meehl and Teng 2007), or from shifts in the intensity and longitude of equatorial Pacific rainfall during El Niño events (e.g., Kug et al. 2009; Wang et al. 2015; Zhou et al. 2014). In this study, we explore whether SCAL rainfall sensitivity to a strong El Niño occurring in 2016 has changed compared to a comparably strong El Niño in 1983.

Datasets and methods. Observed monthly precipitation for 1901–2016 is from the GPCC gridded 1° resolution analysis (Schneider et al. 2013). Monthly atmospheric circulation for 1948–2016 is from the NCEP/ NCAR Reanalysis (Kalnay et al. 1996). Monthly sea surface temperature (SST) and sea ice concentration (SIC) data are based on Hurrell et al. (2008).

Two ensemble suites of climate simulations are analyzed. The first is a 40-member historical transient simulation of the NCAR Community Earth System Model version 1 (CESM1; Kay et al. 2015). These "All-Forcings" simulations span 1920–2005, and use RCP8.5 for 2006–2100. The second is a 20-member ensemble of atmospheric model simulations (AMIP) generated from the atmospheric component of CESM1, named Community Atmospheric Model version 5 (CAM5; Neale et al. 2012). In these AMIP-style experiments spanning 1871–2016, observed time evolving lower boundary conditions (SSTs and SIC) are prescribed globally, while time varying external radiative forcings identical to those used in CESM1 are also specified. The atmospheric model uses horizontal resolution of 0.94° × 1.25° and 30 vertical levels for all simulations.

While the historical AMIP ensemble size is 20-members, the ensemble size was increased to 50 members for the strong El Niño cases of 1982/83 and 2015/16. A parallel set of 50-member AMIP-style runs were conducted for these two strong El Niño events in which SST forcing over an El Niño-core region (15°N– 15°S, 175°E–South America) only was specified, while
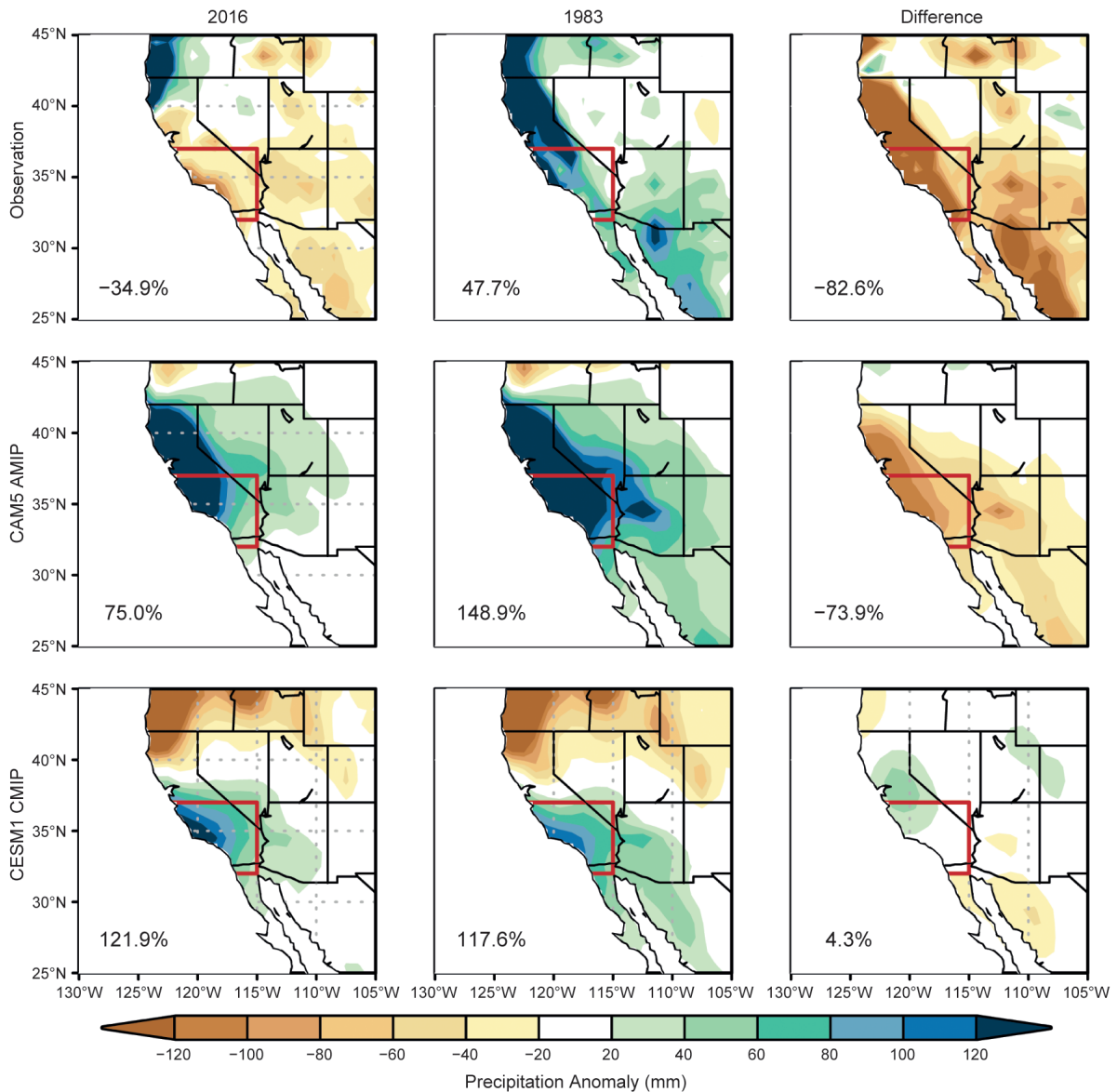
Fig. 10.1. Rows: Dec–Feb (DJF) total precipitation anomalies (mm) in observation (top), CAM5 AMIP (middle), and CESM1 (bottom) simulations. Shadings indicate difference between DJF of 2015/16 (left column), 1982/83 (middle column) and 1981–2010 climatological mean. Differences between the two strong El Niño winters are shown in right-side panels. Percentage values in each panel indicate departure of area mean of DJF total relative to observed and simulated 1981–2010 climatology of area mean, respectively. Red region denotes SCAL domain used for area averaging.

climatological SSTs were specified over the remaining world oceans. These experiments address how differences in the "flavor of El Niño" alone affected SCAL precipitation in 2016 versus 1983. Further, we address how SSTs over the "rest-of-the-world" affected SCAL precipitation by first calculating differences between the globally forced runs and the El Niño core-region runs, and then comparing these residual estimates for 2016 and 1983.

To test the effect of climate change on the response to strong El Niño, we construct composites of strong

El Niño events occurring around 1983 and 2016 by subsampling the 40-member CESM1 ensemble. Hurrell et al. (2013) demonstrate that the CESM1 realistically simulates the magnitude of the observed rise in global surface temperature during recent decades. Using a 15-year period centered in 1983 or 2016, we select all December–February warm events that exceed 1.5 times the standard deviation of the model's Niño3.4 SST variability (1981–2010 reference). This yields strong El Niño composites having about 30–40 members for each period. Our results are robust to

an alternate method in which El Niño occurrences are calculated relative to each 15-year climatology rather than from the single 1981–2010 climatology.

Results. a. Observations. Across all regions of California, less precipitation fell during winter (December–February) 2016 compared to 1983 (Fig. 10.1, top row). For SCAL (Fig. 10.1, red outline), 2016 precipitation was 35% below the 1981–2010 mean, compared to 48% above the mean in 1983. Owing to the positive skew of SCAL climatological winter rainfall, the 2016 total was only 22% below the climatological median. It was thus not particularly extreme when assessed in an unconditional framework. However, winter rainfall statistics derived from the CAM5 AMIP simulations indicate that the observed dryness was an extreme event when conditioned upon the particular global boundary forcing of strong El Niño (Fig. ES10.1b).

The immediate cause for the drastic distinction in SCAL rainfall between 2016 and 1983 is the difference in North Pacific atmospheric circulations. Both winters exhibit features of the well-known canonical El Niño teleconnection pattern (e.g., Horel and Wallace 1981). A key distinction, however, is that the North Pacific 200-hPa negative height anomaly is weaker and shifted farther north into the Gulf of Alaska during 2016 (Fig. 10.2, top row). The circulation difference between those two winters (Fig. 10.2, top right) consists of an anticyclonic anomaly across the central North Pacific which reduced the frequency of storms over SCAL during 2016.

b. Atmospheric model simulations. The ensemble mean of CAM5 experiments indicates a SST-forced wet signal over SCAL in 2016 (Fig. 10.1, middle row), consistent with aforementioned forecast guidance. The dryness in 2016 was therefore unlikely due to boundary forcing.
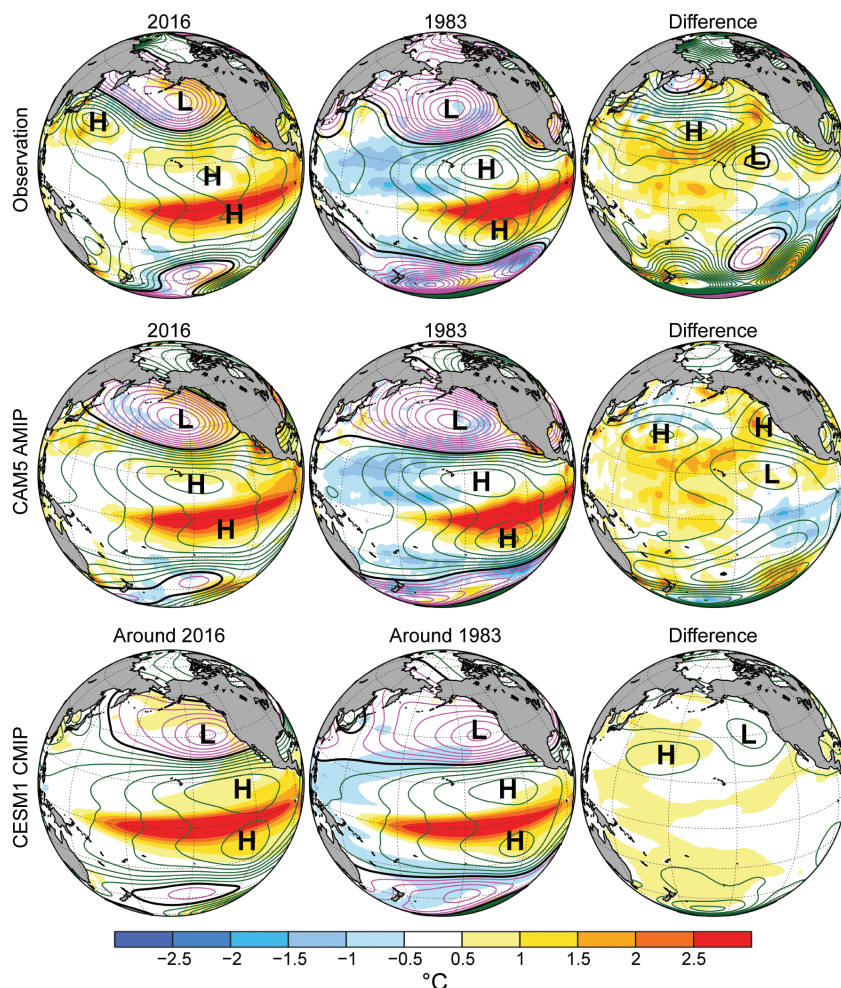

FIG. 10.2. As in Fig. 10.1, but for the 200-hPa geopotential height anomalies (gpm). Contour interval is 15 m for left and middle columns, and 10 m for right column. High and low anomaly centers are denoted by H and L, respectively. Colored shadings indicate SST anomalies (°C).

The magnitude of the CAM5 wet signal was diminished in 2016 when compared to 1983, however. Note especially that the simulated difference in ensemble mean California precipitation between these two winters is remarkably similar to the difference in observations. Also, comparison of the model probability density function (PDF) of SCAL precipitation in 2016 versus 1983 (Fig. ES10.1b) indicates increased likelihood for dryness in 2016; the two distributions are significantly different at the 5% level according to a Kolmogorov–Smirnov test. Nonetheless, the magnitude of observed dryness was a low probability within both ensembles.

The dynamical basis for this weaker SCAL wet signal in CAM5 is a weakened and northward displaced North Pacific low pressure in the model's circulation pattern during 2016 (Fig. 10.2, middle row). The

model, whose El Niño driven upper tropospheric wave train agrees well with observations (Fig. 10.2, top and middle rows), indicates that upper tropospheric heights are higher across the entire Pacific basin in 2016 compared to 1983. Importantly for SCAL rainfall, differences between the height patterns of the two events consist of an anomalous anticyclonic circulation across the mid-Pacific basin which steers storms northward in 2016 relative to 1983.

Results from the El Niño core-region experiments confirm that distinct El Niño flavors (e.g., stronger far east Pacific SST warmth in 1983 but stronger central Pacific SST warmth in 2016) did not cause the Pacific–North American differences in the fully forced CAM5 simulations. Rather, the principal climate sensitivity distinguishing these two strong El Niño winters arises from the rest-of-the-world boundary conditions. In 2016 relative to 1983, these drive widespread increases in Pacific basin heights whose main feature is an anticyclonic circulation across the mid-Pacific basin (Fig. ES10.2, bottom right).

c. Coupled model simulations. To understand the AMIP results in the context of climate change, we compare CESM1 strong El Niño impacts on western U.S. precipitation for 2016 and 1983 (Fig. 10.1, bottom row). No statistically significant difference in their El Niño-related composite rainfall occurs over SCAL, even though El Niño events circa 2016 are immersed in a warmer ocean. Consistent with a warmer ocean, CESM1 indicates that climate change increases upper level heights across the entire Pacific basin (Fig. 10.2, bottom row). Importantly, however, these height increases are relatively uniform across the Pacific; there is thus no meaningful shift in the model's El Niño-related teleconnection and hence little change in the SCAL winter precipitation. The PDF of CESM1 SCAL winter precipitation for El Niño events circa 2016 versus 1983 are statistically indistinguishable according to a Kolmogorov–Smirnov test (Fig. ES10.1c).

Conclusion. Based on transient coupled climate simulations, no transformation of El Niño teleconnections has occurred since 1983 that would materially alter the remote sensitivity of Southern California precipitation to strong El Niño forcing. Both composites of strong El Niño in CESM1 experiments circa 1983 versus 2016 show wet signals over SCAL, with no significant difference in the probability distributions for either extreme wet or extreme dry winters. We conclude that the failure of heavy rains in SCAL during the strong El Niño of 2016, compared to the flooding rains of 1983, does not constitute a climate change effect.

Our analysis of atmospheric simulations does indicate, however, that the actual global boundary forcing in 2016 (especially the rest-of-the-world boundary forcing outside of the El Niño core-region) was significantly less favorable for wet SCAL in 2016 than in 1983. Additional experiments are required to better understand the nature of these rest-of-world boundary conditions that operated in 2016. More research is especially needed to reconcile those conditions with plausible modes of internal natural variability (Berg and Hall 2015; Kumar and Chen 2016).

REFERENCES

Berg, N., and A. Hall, 2015: Increased interannual precipitation extremes over California under climate change. *J. Climate*, **28**, 6324–6334, doi:10.1175/JCLI-D-14-00624.1

Diaz, H., M. Hoerling, and J. Eischeid, 2001: ENSO variability, teleconnections, and climate change. *Int. J. Climatol.*, **21**, 1845–1862, doi:10.1002/joc.631.

Hoell, A., and Coauthors, 2016: Does El Niño intensity matter for California precipitation? *Geophys. Res. Lett.*, **43**, 819–825, doi:10.1002/2015GL067102.

Horel, J. D., and J. M. Wallace, 1981: Planetary-scale atmospheric phenomena associated with the Southern Oscillation. *Mon. Wea. Rev.*, **109**, 813–829.

Hurrell, J., J. Hack, D. Shea, J. Caron, and J. Rosinski, 2008: A new sea surface temperature and sea ice boundary dataset for the Community Atmosphere Model. *J. Climate*, **21**, 5145–5153, doi:10.1175/2008JCLI2292.1.

——, and Coauthors, 2013: The Community Earth System Model: A framework for collaborative research. *Bull. Amer. Meteor. Soc.*, **94**, 1339–1360, doi:10.1175/BAMS-D-12-00121.1.

Kalnay, E., and Coauthors, 1996: The NCEP/NCAR 40-year reanalysis project. *Bull. Amer. Meteor. Soc.*, **77**, 437–471.

Kay, J. E., and Coauthors, 2015: The Community Earth System Model (CESM) Large Ensemble project: A community resource for studying climate change in the presence of internal climate variability. *Bull. Amer. Meteor. Soc.*, **96**, 1333–1349, doi:10.1175 /BAMS-D-13-00255.1.

Kug, J.-S., S.-Il An, Y.-G. Ham, and I.-S. Kang, 2009: Changes in El Niño and La Niña teleconnection over North Pacific-America in the global warming simulations. *Theor. Appl. Climatol.*, **100**, 275–282, doi:10.1007/s00704-009-0183-0.

Kumar, A., and M. Chen, 2016: What is the variability in US west coast winter precipitation during strong El Niño events? *Climate Dyn.*, First online, doi:10.1007 /s00382-016-3485-9.

Meehl, G., and H. Teng, 2007: Multi-model changes in El Niño teleconnections over North America in a future warmer climate. *Climate Dyn.*, **29**, 779–790, doi:10.1007 /s00382-007-0268-3.

Neale, R. B., and Coauthors, 2012: Description of the NCAR Community Atmospheric Model (CAM5.0). NCAR Tech. Note NCAR/TN-486+STR, 289 pp. [Available online at www.cesm.ucar.edu/models/cesm1.0/cam/docs /description/cam5_desc.pdf.]

Schneider, U., and Coauthors, 2013: GPCC's new land surface precipitation climatology based on quality-controlled in situ data and its role in quantifying the global water cycle. *Theor. Appl. Climatol.*, **115**, 15–40, doi:10.1007 /s00704-013-0860-x.

Wang, S.-Y., W.-R Huang, H.-H. Hsu, and R. Gilles, 2015: Role of the strengthened El Niño teleconnection in the May 2015 floods over the Southern Great Plains. *Geophys. Res. Lett.*, **42**, 8140–8146, doi:10.10002/2015GL065211.

Zhou, Z.-Q., S.-P. Xie, X.-T. Zheng, Q. Liu, and H. Wang, 2014: Global warming-induced changes in El Niño teleconnections over the North Pacific and North America. *J. Climate*, **27**, 9050–9064, doi:10.1175 /JCLI-D-14-00254.1.

11. WAS THE JANUARY 2016 MID-ATLANTIC SNOWSTORM "JONAS" SYMPTOMATIC OF CLIMATE CHANGE?

Klaus Wolter, Martin Hoerling, Jon K. Eischeid, and Dave Allured

Model simulations indicate that anthropogenic climate change has made extreme snowstorms less likely over the mid-Atlantic United States. Empirical evidence shows no decline since 1901, with recent storms colder than before.

Introduction. The biggest winter storm of 2016 named "Jonas"[1] over the eastern United States hit the mid-Atlantic states around 23 January, dumping up to 1 m of snow from Virginia to New York (Fig. 11.1a)[2], inflicting around $1 billion (U.S. dollars) in damages and causing 55 fatalities[3],[4].

This motivated our exploratory inquiry about how heavy winter precipitation events overall, and heavy snowstorms in particular, have changed in the mid-Atlantic region due to long-term climate change. In the eastern United States, heavy rain- and snowstorms have become more frequent during recent decades (Kunkel et al. 2013; Lawrimore et al. 2014). Both El Niño (Smith and O'Brien 2001; Lawrimore et al. 2014) and the negative phase of the NAO (Hoerling et al. 2010; Seager et al. 2010) increase the odds of heavy snow in this region. Given these natural drivers together with the regional rarity of major snowstorms (Changnon et al. 2006), identifying human-induced contributions requires model experimentation, results of which are presented here to augment empirical diagnosis of historical data.

[1] http://nypost.com/2016/01/28/winter-storm-jonas-ranks-4th-worst-among-northeast-snowstorms/

[2] https://weather.com/storms/winter/news/winter-storm-jonas-record-snowstorm-new-york-city

[3] https://en.wikipedia.org/wiki/January_2016_United_States_blizzard

[4] www.washingtonpost.com/local/dc-politics/dcs-credit-card-was-shut-off-and-that-wasnt-the-worst-of-snowzilla-audit-finds/2017/01/11/5b84921a-d7f9-11e6-b8b2-cb5164beba6b_story.html?utm_term=.3c72de60003e&wpisrc=nl_localheads-draw6&wpmm=1

Data and methods. A database of 987 climate stations (GHCN-D) of daily precipitation records since 1901 (Wolter et al. 2016) is used to identify heavy daily precipitation (≥25.4 mm). In the mid-Atlantic, 19 stations (Fig. 11.1b) have nearly complete records of precipitation, snowfall, and temperature during December–March 1900/01 through 2015/16. We define heavy daily snow (≥15.2 cm) in conjunction with heavy daily precipitation. Average temperatures during heavy precipitation days are used to derive an empirical relation of rain/snow transition thresholds for this region, inspired by Collins et al. (2004) and Kienzle (2008).

A 30-member ensemble of historical AMIP-style simulations is conducted with the T159 resolution (~85 km) ECHAM5 atmospheric model (Roeckner et al. 2003). This so-called "factual" simulation—using observed boundary and external radiative forcings—is compared to a parallel 30-member ensemble of "counterfactual" simulations. Linear trends of observed post-1880 sea surface temperatures (SST) are removed from the full time-varying SST; sea ice conditions are set to an early twentieth century climatology; and radiative forcings are altered to their 1880 values in counterfactual runs, thus retaining interannual and decadal variations of boundary forcings related to internal variability (Seager and Hoerling 2014; Sun et al. 2017, manuscript submitted to *Wea. Climate Extremes*). Simulated daily precipitation and temperature are analyzed for the mid-Atlantic domain of Fig. 11.1b. Heavy daily precipitation events are identified as in observations, and simulated snowstorms are inferred using the empirical relation of rain–snow temperature thresholds derived from observations. We compare factual versus counterfactual statistics of heavy precipitation and snowstorms for 2001–16 to maximize the climate change signal. A model's ability to simulate realistic storm tracks is an important attribute when considering heavy snowstorms. In this regard, we note
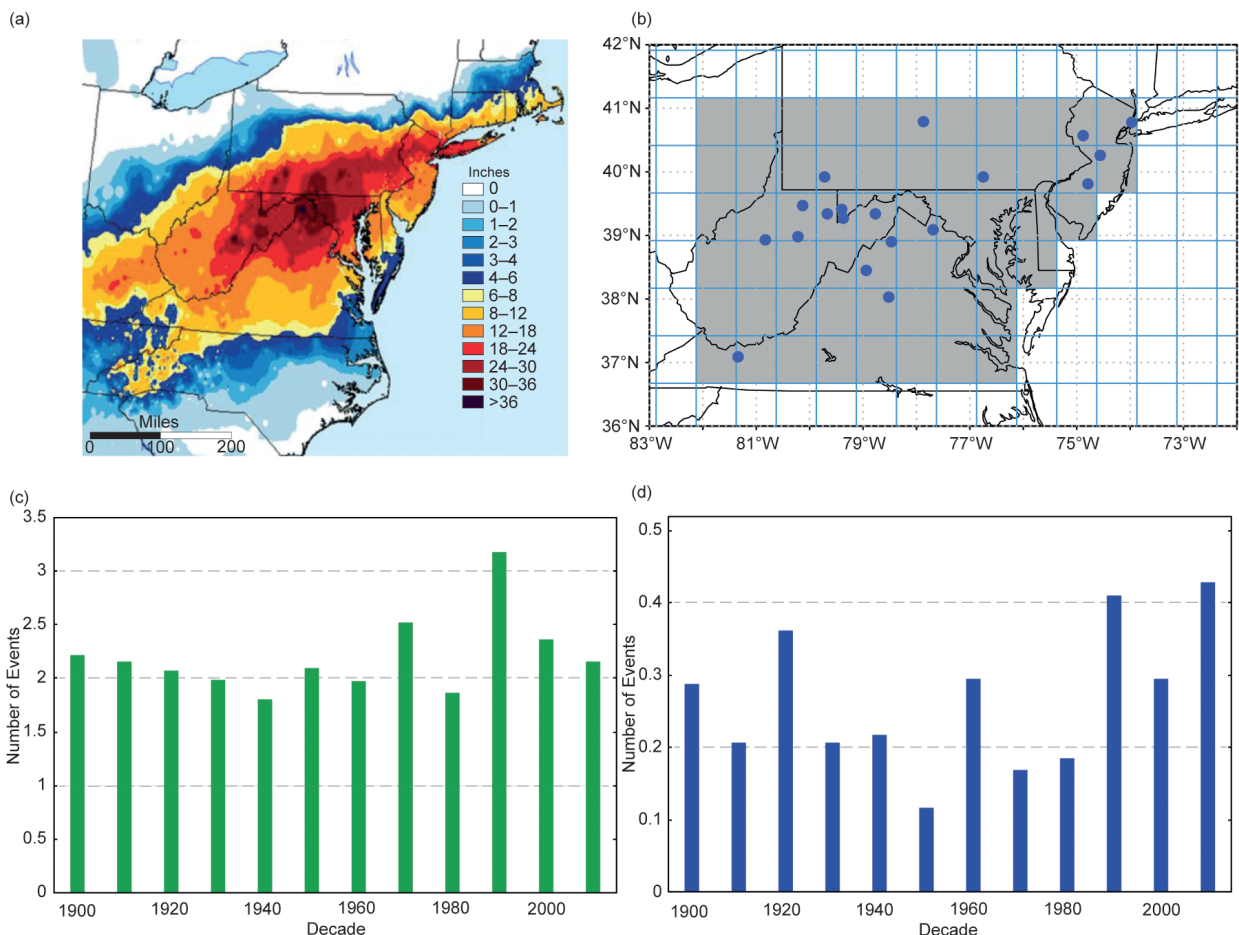
(a)

(b)

(c)

(d)

FIG. 11.1. (a) Jonas snowfall totals (inches); (b) 19 mid-Atlantic stations with 100yr+ precipitation records (Wolter et al. 2016) that also have more than 90% extant snowfall and temperature records during heavy precipitation days; gridding and shading refer to coverage by ECHAM5 for mid-Atlantic (~37°–41°N, ~74°–82°W); (c) Average annual counts of observed daily precipitation totals of 25.4 mm or higher from Dec–Mar 1900/01 through 2015/16 (last decade 2010/11 to 2015/16) for 19 mid-Atlantic stations; linear regression-based increase over 116 years: +20%; (d) As in (c) but for observed daily snowfall totals of 15.2 cm or higher (the number of usable stations varied from 16 to 19 per decade); linear regression-based increase over 116 years: +47%. [Source for (a): NWS Burlington.]

that storm tracks in the mid-Atlantic region are well represented in CMIP5 models with spatial resolution similar to that of our ECHAM5 experiments (Colle et al. 2015).

Results. (a) Empirical: Winter storm Jonas walloped our mid-Atlantic 19-station network: 12 stations reported daily totals of at least 23 cm of snow (25.4 mm of precipitation); see online supplement for more details.

Figure 11.1c documents the average number of heavy precipitation days per winter season and station on a decadal basis (overall average: 2.2). Figure 11.1d does the same for heavy snow days (average: 0.26). While both time series show an increase over the last 12 decades, their linear trends are not statistically significant due to large decadal variability. Nevertheless,

our results for the mid-Atlantic corroborate upward trends in heavy snowstorms since 1901 in the Northeast (Kunkel et al. 2013).

When binned by daily average temperatures (Tave; Table 11.1), heavy precipitation events above +2°C contain little snow [snow-to-rain ratio (S/R) < 1], while those below −6°C guarantee heavy snow days (S/R > 8). We calculated heavy snow water equivalent (SWE; 15.2 mm) days based on assuming that no snow fell above +2°C, all snow below −6°C, and linear fractions in-between. This is similar to Collins et al. (2004) who inferred snowfall in the NCAR CAM3 model using 0°C and −5°C for their all-rain and all-snow thresholds. For the 19 mid-Atlantic stations, a total of 518 calculated heavy SWE days correspond well to 538 observed heavy snow days since 1901.

Tave (°C)	#rain	#snow	%snow	<S/R>	%6+:1
≥6°C	1783	43	2.4%	0.05	0.1%
≥5/<6	372	33	8.1	0.17	0.7
≥4/<5	256	38	12.9	0.26	1.0
≥3/<4	324	67	17.1	0.36	1.5
≥2/<3	208	88	29.7	0.77	3.7
≥1/<2	203	127	38.5	1.21	5.8
≥0/<1	119	177	59.8	2.51	15.9
≥−1/<0	060	117	66.1	2.85	20.8
≥−2/<−1	036	173	82.8	4.06	30.6
≥−3/<−2	017	093	84.5	4.88	40.0
≥−4/<−3	018	094	83.9	5.48	45.6
≥−5/<−4	012	054	81.8	5.41	45.5
≥−6/<−5	005	031	86.1	7.28	61.1
<−6°C	003	117	97.5%	8.14	69.2%

Heavy snow counts show *no significant* change since 1901. Surprisingly, heavy snow days have become *significantly colder* (−2.55°C), in contrast with heavy rain-only days which have warmed slightly (+0.35°C; both in Fig. ES11.1).

(b) Model: Figure 11.2 shows results for the mid-Atlantic region from our model simulations. The Dec–Mar temperature difference between the factual and counterfactual experiments is +0.84°C (Fig. 11.2a) which is lower than the observed trend since 1900 (+1.1°C; Fig. ES11.2a). The corresponding precipitation difference for the same set of runs shows little change (+0.2%; Fig. 11.2b), compared to an observed decline of −4% (Fig. ES11.2b).

For each grid box and ensemble member, heavy precipitation events are extracted for Dec–Mar 2000/01 through 2015/16. Consistent with a wet bias of the model, the average number of such events is 3.7 per grid box in the factual case (Fig. 11.2c), high-er than the observed frequency per climate station (2.3; Fig. 11.1c). Model snowstorms are derived by applying the same algorithm to calculate SWE as for observed data. The number of simulated heavy snow days is 0.17 cases per winter and grid box in the factual case (Fig. 11.2d), *lower* than observed (0.34; Fig. 11.1d).

Given the large model sample size, we find statistically significant changes in the frequency of heavy precipitation and snow days as a consequence of long-term climate change. An *increase* in the average number of heavy precipitation days of 7.0% is 99% significant for the means, but not for the full distribution [Fig. 11.2c; Komolgorov–Smirnov (K–S) value of 0.13]. A *decrease* by 17.5% for the average number of heavy snow days (Fig. 11.2d) is significant (*t*-test: 99%; K–S = 0.07). Comparing the number of events per winter in factual versus counterfactual climates indicates that 68.5% of the factual precipitation seasons exceed the counterfactual median (3.5 events per winter; Fig. 11.2c), a 37% increase in the relative risk of heavy precipitation events. By contrast, for heavy snowstorms, only 24.1% of the factual model seasons exceed the counterfactual median (0.2 events per winter; Fig. 11.2d), a 52% decrease in the relative risk of heavy snowstorms. Thus, the modeled likelihood of experiencing a heavy snowstorm has decreased in recent decades, as a result of climate change alone.

Comparing the probability distributions of both factual and counterfactual runs shows a wide spread in outcomes for heavy precipitation and snow events (Fig. 11.2c,d). This suggests low confidence in detecting the forced signal from a single sample of historical data. Concerning the model's forced signal,
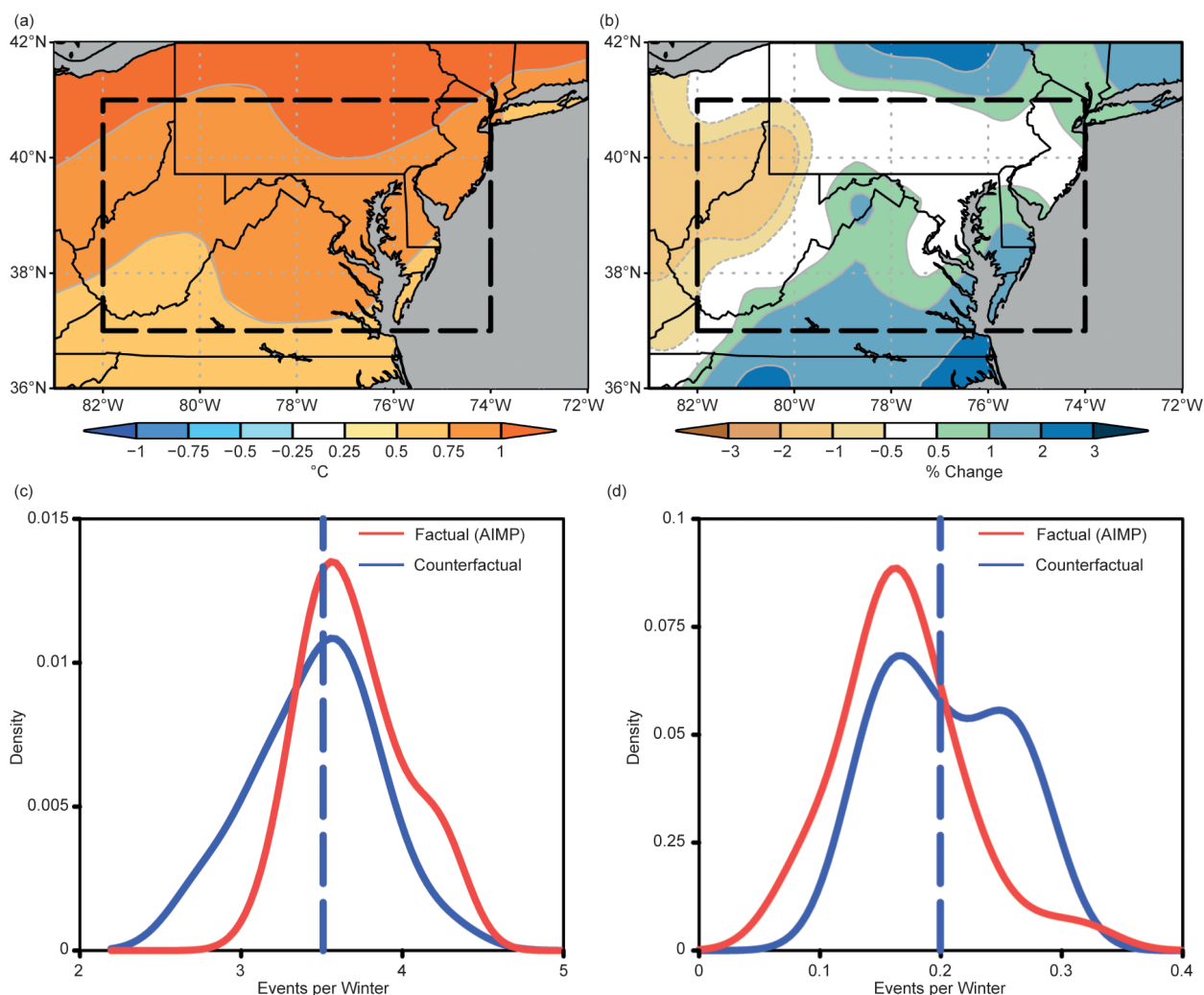
FIG. 11.2. ECHAM5 output for Dec–Mar 2000/01 through 2015/16. (a) Map of average change in seasonal temperatures (°C) of 30 factual runs compared to 30 counterfactual runs (+0.84°C) for mid-Atlantic (stippled outline); (b) As in (a) but for seasonal precipitation (+0.2%); (c) Probability distributions for mid-Atlantic region (57 grid boxes in Fig. 11.1b) for daily precipitation totals ≥ 25.4 mm, with median of 3.5 such events per season and grid box in counterfactual case (blue stippled vertical line); (d) As in (c) but for heavy snow events (SWE ≥ 15.2 mm), with median of 0.20 such events per counterfactual season and grid box. Probability distributions are nonparametric estimates of frequency distributions based on Kernel density and have been smoothed using Gaussian filter.

a key ingredient in its decrease of heavy snowstorms must be its increase in average temperature during modeled heavy precipitation days. More frequent heavy precipitation events alone—a plausible symptom of increased water vapor in a warmer climate (Hartmann et al. 2014)—would have implied more snowstorms. However, an increase in temperature more than countervailed the increase in moisture, yielding less heavy snowstorms.

Concluding remarks. Jonas was one of the most severe mid-Atlantic snowstorms of the last century (see http://nypost.com/2016/01/28/winter-storm-jonas -ranks-4th-worst-among-northeast-snowstorms/). We address how a class of such storms rather than Jonas itself are affected by anthropogenic climate change. Heavy snowstorm statistics derived from parallel climate experiments, one subjected to current climate conditions, the other subjected to conditions of the late nineteenth century, indicate a 52% decrease in the relative risk of experiencing a heavy snowstorm. Warmer temperatures dominated over the occurrence of more frequent heavy precipitation events in the model leading to fewer heavy snowstorms in the current climate. By contrast, the long-term observational record shows more heavy snowstorms in recent decades.

We reconcile these differences between the modeled and observed changes in heavy snowstorms by noting the large spread among the 30-members of ECHAM5 simulated mid-Atlantic snowstorm changes, implying low detectability of a change signal at this time. Heavy snowstorms are rare in the mid-Atlantic region, and their probability is affected by various natural drivers (El Niño, atmospheric blocking). Recent mid-Atlantic snowstorms were colder than those of the earlier twentieth century, contrary to a general winter warming trend in the region. It is plausible that internal variations in weather patterns responsible for mid-Atlantic snowstorms have dominated the observed increase. For instance, an eastward shift of storm tracks to slightly more offshore could cool the air mass during heavy precipitation events, allowing for heavy snow to fall over a wider reach of the mid-Atlantic (Changnon et al. 2008). In this regard, our results show a temperature increase of +0.3°C during model snowstorms, in contrast with the cooling trend in observed snowstorms since 1901 (−2.55°C), which may be due to natural decadal variations in storm tracks.

We further speculate that the wide observed range of temperatures during heavy snowstorms, many of them colder than −6°C, should allow for a continuation of at least some heavy snowstorm activity well into the future. This is consistent with O'Gorman's (2014) projection of only a slight decrease in the frequency of future extreme snowstorms compared to a much bigger decrease in seasonal snowfall totals for much of the northern midlatitudes. Meanwhile, the number of heavy mid-Atlantic snowstorms during the month of March has indeed declined compared to previous decades (Table ES11.1). Perhaps the future is showing its hand after all.

REFERENCES

Changnon, D., C. Merinsky, and M. Lawson, 2008: Climatology of surface cyclone tracks associated with large central and eastern U.S. snowstorms, 1950–2000. *Mon. Wea. Rev.*, **136**, 3193-3202, doi:10.1175/2008MWR2324.1.

Changnon, S. A., D. Changnon, and T. R. Karl, 2006: Temporal and spatial characteristics of snowstorms in the contiguous United States. *J. Appl. Meteor. Climatol.*, **45**, 1141–1155, doi:10.1175/JAM2395.1.

Colle, B. A., J. F. Booth, and E. K. M. Chang, 2015: A review of historical and future changes of extratropical cyclones and associated impacts along the U.S. east coast. *Curr. Climate Change Rep.,* **1**, 125-143, doi:10.1007/s40641-015-0013-7.

Collins, W. D., and Coauthors, 2004: Description of the NCAR Community Atmosphere Model (CAM3). NCAR Tech. Rep. NCAR/TN-464+STR, 226 pp. (Available online at www.ccsm.ucar.edu /models/atm-cam/docs/description/description.pdf.)

Hartmann, D. L., and Coauthors, 2014: Observations: Atmosphere and surface. *Climate Change 2013: The Physical Basis*. T. F. Stocker et al., Eds., Cambridge University Press, 159–254.

Hoerling, M., and Coauthors, 2010: Understanding the Mid-Atlantic snowstorms during the winter of 2009-2010. NOAA-ESRL, 16 pp. [Available online at www.esrl.noaa.gov/psd/csi/images /NOAA_AttributionTeam_SnowstormReport.pdf.]

Kienzle, S. W., 2008: A new temperature based method to separate rain and snow. *Hydrol. Process.*, **22**, 5067–5085, doi:10.1002/hyp.7131.

Kunkel, K. E., and Coauthors, 2013: Monitoring and understanding trends in extreme storms: State of knowledge. *Bull. Amer. Meteor. Soc.*, **94**, 499–514, doi:10.1175/BAMS-D-11-00262.1.

Lawrimore, J., T. R. Karl, M. Squires, D. A. Robinson, and K. E. Kunkel, 2014: Trends and variability in severe snowstorms east of the Rocky Mountains. *J. Hydrometeor.*, **15**, 1762–1777, doi:10.1175/JHM -D-13-068.1.

O'Gorman, P. A. 2014: Contrasting responses of mean and extreme snowfall to climate change. *Nature,* **512**, 416–418, doi:10.1038/nature13625.

Roeckner, E. K., and Coauthors, 2003: The atmospheric general circulation model ECHAM5. Part I: Model description. MPI Tech. Rep. 349, 127 pp. [Available online at www.mpimet.mpg.de/fileadmin /publikationen/Reports/max_scirep_349.pdf.]

Seager, R., and M. Hoerling, 2014: Atmosphere and ocean origins of North American droughts. *J. Climate,* **27,** 4581–4606, doi:10.1175/JCLI-D-13-00329.1.

——, Y. Kushnir, J. Nakamura, M. Ting, and M. Naik, 2010: Northern Hemisphere winter snow anomalies: ENSO, NAO, and the winter of 2009/10. *Geophys. Res. Lett.*, **37,** L14703, doi:10.1029/2010GL043830.

Smith, S. R., and J. J. O'Brien, 2001: Regional snowfall distributions associated with ENSO: Implications for seasonal forecasting. *Bull. Amer. Meteor. Soc.*, **82,** 1179–1191.

Wolter, K., M. Hoerling, J. K. Eischeid, and L. Cheng, 2016: What history tells us about 2015 U.S. daily rainfall extremes [in "Explaining Extreme Events of 2015 from a Climate Perspective"]. *Bull. Amer. Meteor. Soc.*, **97** (12), S9–S13, doi:10.1175/BAMS -D-16-0166.1.

12. ANTHROPOGENIC FORCINGS AND ASSOCIATED CHANGES IN FIRE RISK IN WESTERN NORTH AMERICA AND AUSTRALIA DURING 2015/16

Simon F. B. Tett, Alexander Falk, Megan Rogers, Fiona Spuler, Calum Turner, Joshua Wainwright, Oscar Dimdore-Miles, Sam Knight, Nicolas Freychet, Michael J. Mineter, and Caroline E. R. Lehmann

Extreme vapor pressure deficits (VPD) have been associated with enhanced wildfire risk. Using one model, we found for 2015/16 that human influences quintupled the risk of extreme VPD for western North America and increased the risk for extratropical Australia.

Introduction. In 2016, about 3.6 million hectares of land burned in the United States and Canada (NIFC 2017; NFD 2017). In Canada, a wildfire southwest of Fort McMurray, Alberta, caused the largest wildfire evacuation in Alberta's history and destroyed 2400 homes in 2016 (McConnell 2016). Abatzoglou and Williams (2016; AP16 from hereon) showed that anthropogenic climate change has increased forest fire activity in the western United States. This raises the question if anthropogenic forcing are increasing the risk of devastating events outside this region such as the Canadian Fort McMurray fire.

During the Australian summer of 2015/16, the country experienced high numbers of bushfires: the southwest and southeast of the country were most affected with more than 100000 hectares of vegetation burned in Tasmania (ABC News 2016a). Over the course of this summer, 408 residential and 500 non-residential buildings were destroyed nationwide. This fire season was moderately destructive with insured losses of about AUD $350 million (ABC News 2016b).

AP16 found for the western United States a strong link between the spring–summer vapor pressure deficit (VPD) and the annual burned area. In this paper, we build on this work using monthly average VPD as a proxy for fire risk during the summer of 2016 for extratropical Australia (October–February) and western North America (May–August) though

this link has not been directly established for either region. VPD is an absolute measure of the state of atmospheric moisture, specifically the difference between the saturation vapor pressure and the actual vapor pressure of the atmosphere (Seagar et al. 2015). Changes in VPD are associated with the drying of both live vegetation and litter fuels, and it is only when vegetation and litter fuels are sufficiently dry that fires can both ignite and spread (Bradstock 2010).

Methods. To estimate the effect of anthropogenic climate change on VPD in western North America and extratropical Australia, we compared three different ensembles of the HadAM3P atmosphere-only model (Massey et al. 2015), which has a resolution of $1.875° \times 1.25°$, with each other and the ERA-Interim (ERAI) reanalysis (Dee et al. 2011). The ensembles are:

- **Hist15–16**: Driven by observed sea surface temperatures (SST), sea ice coverage (SIC) as well as current concentrations of greenhouse gases and estimates of aerosol emissions (updated from Tett et al. 2013).
- **Nat15–16**: Driven by SST, SIC, greenhouse gases, and aerosol emissions as they are estimated to have been without human induced climate change with natural SST (Fig. ES12.1a) and SIC conditions described in the online supplement.
- **Historical:** Ensemble of 5 continuous simulations from December 1959 to November 2009 described by Tett et al. (2013).

Both Hist15–16 and Nat15–16 have 24 members, each using slightly different initial conditions, starting in December 2014 and ending in August 2016. We analyze the 12-month period September 2015 to

August 2016. VPD is defined as (Seager et al. 2015; Wallace and Hobbs 2006):

$$VPD = e_s - e \ \& \ e_s = \frac{e}{RH}$$

and, neglecting moisture mass in the atmosphere, can be rewritten as:

$$VPD = \frac{M_{dry\,air}}{M_{H_2O}} \, q \, p^* \left(\frac{1}{RH} - 1 \right) \qquad \text{Eq. (1)}$$

where $e(e_s)$ is the (saturated) vapor pressure, q the specific humidity, p^* the surface pressure, and RH the relative humidity near the surface.

We computed VPD in the HadAM3P simulations and ERAI reanalysis using Eq. (1) applied to gridded monthly mean data neglecting nonlinearity. For HadAM3P, q and RH were 1.5 meter values while for ERAI we interpolated q and RH from monthly mean pressure level data to the surface. We use as a reference period the 30 years 01 December 1979–30 November 2009 and VPD, q_{sat} (q/RH), q, and p^* were converted to anomalies against this period from the Historical or ERAI values.

The western North America (WNA) region was defined as in Giorgi and Francisco (2000; GF00), while we defined an extratropical Australian region (extAUS) as the GF00 AUS region south of 23.5°S. Fire does not occur in all places in the regions, so we defined a fire-mask to keep locations in our analysis where fire occurs. This mask was constructed from the MODIS CMG dataset using *Aqua* satellite measurements (Giglio et al. 2009) for 2003–16. Each $0.5° \times 0.5°$ grid box and climatological month, was defined as a fire grid box if the fraction of pixels with fire detected for 2003–16 was greater than 10^{-5} (Figs. ES12.1b–e show regions and fraction of fire pixels for January and July). The 10^{-5} is arbitrary and corresponds to roughly one detected fire pixel per month. Simulated (and reanalysis) VPD, q, RH, q_{sat} (q/RH), and p^* anomalies and normals were bilinearly interpolated to this grid from the model/reanalysis grid, data only kept at fire grid boxes, and then area
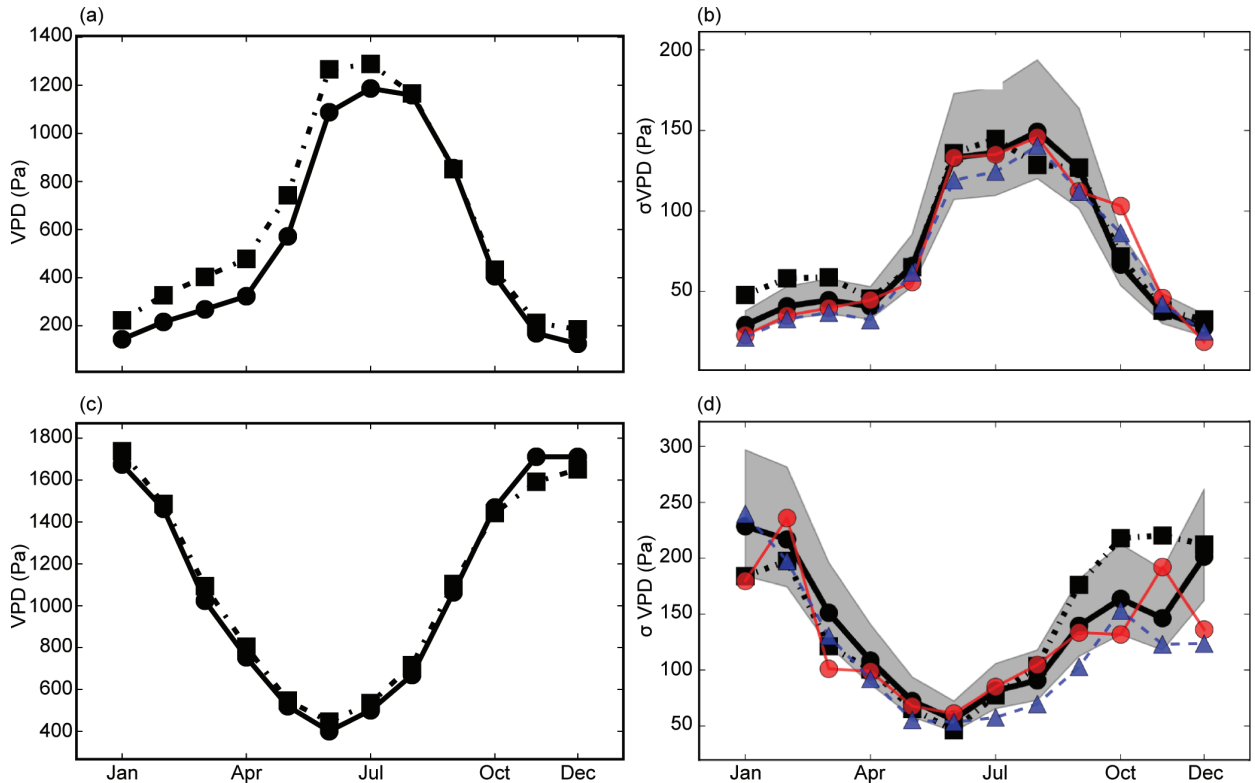

Fig. 12.1. VPD (Pa) comparison between ERAI (black dot-dashed, squares) and Historical (black lines, circles): (a),(c) 01 Dec 1979–Nov 2009 normals; (b),(d) std. dev. for WNA and extAUS, respectively. Gray shading indicates where reanalysis and Historical std. dev. are consistent (5%–95%). Std. dev for Sep 2105–Aug 2016 from Hist15–16 (red circles, lines) and Nat15–16 (blue triangles, dashed lines) are also shown in (b),(d). The x-axis on all plots shows climatological month (labels on bottom plots only).
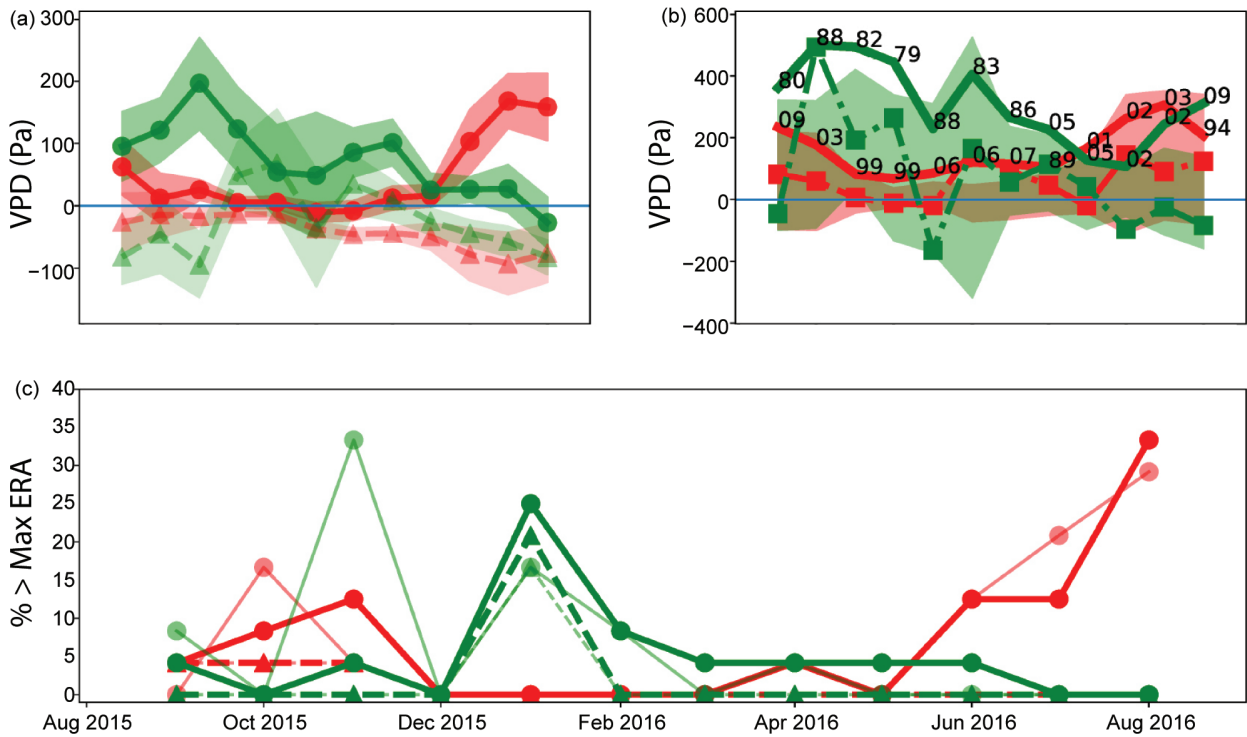
FIG. 12.2. (a) Ensemble-mean VPD anomalies (Pa) from Hist15–16 (circles) and Nat15–16 (triangles) for WNA (red) and extAUS (green). Shading shows ±2σ uncertainty. (b) Maximum VPD anomaly (Pa) for each climato-logical month [thick solid line and year (number) when max occurred] and anomaly for 15/16 (squares) from ERAI. Shading shows 5%–95% ranges from Hist15–16 ensemble with colors as (a). (c) Fraction (%) of Nat15–16 (dashed lines, triangles) and Hist15–16 (solid lines, circles) ensembles that exceeded 1979–2009 ERAI maximum VPD value for each month. Thin pale lines show same when anomalies scaled to correct for variance errors. All subplots use same common x-axis [values shown in (c)].

averaged over the two regions to produce time series. It is these time series that we subsequently analyze. Uncertainties on ensemble averages were computed by bootstrapping (Efron and Tibshirani 1994) over the ensemble members.

We define as a threshold for extreme events the ERAI maximum regional average VPD anomaly, for each calendar month, from the reference period cor-responding to a one-in-30-year event. To compute the risk of exceeding this threshold we compute, for each month, the fraction of the Nat15–16 and Hist15–16 anomalies that exceed it. We test sensitivity to vari-ance errors by scaling the Hist15–16 and Nat15–16 anomalies by the ratio of the monthly mean standard deviations from ERAI and Historical anomalies for the reference period.

Results. Model simulations are evaluated by comparing the Historical ensemble with ERAI. HadAM3P's VPD biases are small relative to the annual cycle though are negative for most of the year in WNA (Fig. 12.1a) with largest differences in June of −180 Pa. HadAM3P

VPD variance appears consistent with that of ERAI (Fig. 12.1b) though the model has significantly smaller variance than ERAI for January–March, and there is no strong evidence of an increase in variability due to human forcings.

For extAUS Historical mean, VPD is, apart from November and December, consistent with that from ERAI (Fig. 12.1c). In November and December biases peak at about +120 Pa. Variability from reanalysis and HadAM3P is broadly consistent though reanalysis variability during austral summer is generally larger than simulated in HadAM3P. For most of the year, ex-tAUS has larger variability in Hist15–16 and Histori-cal than in Nat15–16 (Fig. 12.1d). Mean VPD values peak in WNA in June–August while in extAUS they are largest during October–February. It is these com-ponents of the annual cycle we subsequently focus on.

We now compare ensemble means from Hist15–16 with Nat15–16. For WNA, differences between the two ensembles are significant throughout most of the year with largest differences in July and August 2016 (Fig. 12.2a). For extAUS the Hist15–16 (Nat15–16)

ensemble has positive (negative) anomalies for most of the period suggesting that human influences have increased VPD. However, during December 2015 and January 2016 Nat15–16 shows positive anomalies.

We compare the Hist15–16 ensemble anomalies with ERAI (Fig. 12.2b). For both regions Hist15–16 is broadly consistent with ERAI though extAUS in October 2015, and WNA in February 2016 are exceptions to this (Fig. 12.2b). ERAI VPD values for September 2015 to August 2016, though generally larger than Nat15–16, are not very exceptional with almost all values being smaller than the maximum 1979–2009 VPD value. Maximum ERAI anomalies occur throughout the reference period with no obviously preferred year (or decade).

We now investigate the probability, for both ensembles, of crossing the 1979–2009 threshold. In extAUS, only in January 2016 do any of the Nat15–16 members cross the ERAI threshold (Fig. 12.2c). In WNA, the threshold is exceeded once in each of September through November 2015. For extAUS, there is an approximate doubling of the probability of exceeding the thresholds for October–February with a probability of about 7% (4%) for Hist15–16 (Nat15–16). May 2016, when the Fort McMurray fires started, has near-zero anomaly for WNA in both ensembles and reanalysis suggesting that this event was not strongly linked to continental scale VPD changes, and no ensemble members cross the 30-year threshold (Fig. 12.2c) during this month. However, during June 16–August 16, we find several extreme VPD values in the Hist15–16 ensemble, and no such events in the Nat15–16 ensemble (Fig. 12.2c). The average probability of crossing the threshold during this period is 19%. Making a relative risk estimate is difficult when the probability of events in the natural world are small. Being very conservative we assume, with 24 ensemble members, that the probability of crossing the threshold in Nat15–16 is 4% (1/24) giving a risk ratio of about 5, though larger values are possible.

We tested the sensitivity of these results to correcting for variance errors and found little sensitivity in WNA, but the risk for extAUS changed to 12% (3%) for Hist15–16 (Nat15–16) suggesting a risk ratio of about 4. Being conservative and taking the risk of 1:30 events for Nat15–16 as 4% then the risk of extreme VPD events, in extAUS, has increased by 2–3 times.

Our estimation of risk ratios is dependent on HadAM3P and the boundary conditions used. HadAM3P compares well with the ERAI VPD climatology (Fig. 12.1a) and the reanalysis values for September 2015–August 2016 are largely contained within the Hist15–16 ensemble (Fig. 12.2a). We decompose the changes in VPD into changes in saturated humidity, surface pressure, relative humidity, and residual effects (see online supplement and Fig. ES12.2). We find that changes in saturated humidity (likely dominated by changes in temperature) and relative humidity (likely model sensitive) are the dominant drivers of VPD in both regions. In WNA, changes in q_{sat} make the largest contribution with a small enhancement by reductions in *RH*. In contrast, for extAUS changes in *RH* offset changes in q_{sat} suggesting some model sensitivity in that region. Overall, we conclude that for WNA that human influences have very considerably increased the risk of extreme VPD values in June–August 2016, though not for the Fort McMurray fire period in May. For extratropical Australia, we find a weaker human influence with a doubling of the risk of extreme VPD. Assuming wildfire in extAUS and WNA, like in the western United States, is related to VPD then human influences have considerably increased the risk of one-in-30-year wildfire events.

REFERENCES

ABC News, 2016a: *Major bushfires in Australia in 2015-2016 summer: Before and after.* ABC News [Australia] website, accessed 29 March 2017. [Available online at www.abc.net.au/news/2016-03-15/satellite-pictures-reveal-scale-of-summersbushfire-destruction/7232594.]

——, 2016b: *Catastrophic Summer events cost insurers more than $550 million, Insurance Council of Australia says*, ABC News [Australia] website, accessed 29 March 2017. [Available online at www.abc.net.au/news/2016-03-25/catastrophes-summer-costs-insurance-companies-more-than-550m/7276564.]

Abatzoglou, J. T., and A. P. Williams, 2016: Impact of anthropogenic climate change on wildfire across western US forests. *Proc. Natl. Acad. Sci. USA*, **113**, 11,770–11,775, doi:10.1073/pnas.1607171113.

Bradstock, R. A., 2010: A biogeographic model of fire regimes in Australia: Current and future implications. *Global Ecol. Biogeogr.*, **19**, 145–158, doi:10.1111/j.1466-8238.2009.00512.x.

Dee, D. P., and Coauthors, 2011: The ERA-Interim reanalysis: Configuration and performance of the data assimilation system. *Quart. J. Roy. Meteor. Soc.*, **137**, 553–597, doi:10.1002/qj.828.

Efron, B., and R. J. Tibshirani, 1994: *An Introduction to the Bootstrap.* CRC press, 456 pp.

Giglio, L., T. Loboda, D. P. Roy, B. Quayle, and C. O. Justice, 2009: An active-fire based burned area mapping algorithm for the MODIS sensor. *Remote Sens. Environ.*, 113, 408–420, doi:10.1016/j.rse.2008.10.006.

Giorgi, F., and R. Francisco, 2000: Uncertainties in regional climate change prediction: A regional analysis of ensemble simulations with the HADCM2 coupled AOGCM. *Climate Dyn.*, **16**, 169–192, doi:10.1007/PL00013733.

Massey, N., and Coauthors, 2015: weather@home—development and validation of a very large ensemble modelling system for probabilistic event attribution. *Quart. J. Roy. Meteor. Soc.*, **141**, 1528–1545, doi:10.1002/qj.2455.

McConnell, R., 2016: Fort McMurray is 'still alive,' fire chief says — but safety concerns linger. Canadian Broadcasting Corporation News, webstory. [Available at www.cbc.ca/news/canada/edmonton/fort-mcmurray-tour-notley-media-1.3572982, Date accessed 2017-03-29.]

NFD, 2017: National forest and forest management statistics. National Forestry Database [Canada], accessed 30 March 2017. [Available online at http://nfdp.ccfm.org/index_e.php.]

NIFC, [2017]: Total wildland fires and acres. National Interagency Fire Center [U.S.], accessed 29 March 2017. [Available at www.nifc.gov/fireInfo/fireInfo_stats_totalFires.html.]

Seager, R., A. Hooks, A. P. Williams, B. Cook, J. Nakamura, and N. Henderson, 2015: Climatology, variability, and trends in the U.S. vapor pressure deficit, an important fire-related meteorological quantity. *J. Appl. Meteor. Climatol.*, **54**, 1121–1141, doi:10.1175/JAMC-D-14-0321.1.

Tett, S. F. B., K. Deans, E. Mazza and J. Mollard, 2013: Are recent wet northwestern European summers a response to sea ice retreat? [in "Explaining Extreme Events of 2012 from a Climate Perspective"]. *Bull. Amer. Meteor. Soc.*, **94** (9), S32–S35.

Wallace, J., and P. Hobbs, 2006: *Atmospheric Science: An Introductory Survey.* 2nd ed. Academic Press, 483 pp.

13. A MULTIMETHOD ATTRIBUTION ANALYSIS OF THE PROLONGED NORTHEAST BRAZIL HYDROMETEOROLOGICAL DROUGHT (2012–16)

Eduardo S. P. R. Martins, Caio A. S. Coelho, Rein Haarsma, Friederike E. L. Otto,
Andrew D. King, Geert Jan van Oldenborgh, Sarah Kew, Sjoukje Philip,
Francisco C. Vasconcelos Júnior, and Heidi Cullen

Northeast Brazil experienced profound water shortages in 2016 due to a five-year drought. Using multiple methods, we could not find sufficient evidence that anthropogenic climate change increased drought risk.

Introduction. The northeast Brazil region (NEB, defined as the land area in 7°–21°S, 36°–47°W; Fig. 13.1a) has experienced a remarkable drought during the 5-year period between 2012–16 (Fig. 13.1c). The NEB encompasses the largest regional water supply system of Brazil, the São Francisco River Basin (SFRB), which is of great importance not solely for human consumption, but also for agricultural and hydropower production. During the 2012–16 drought, this system suffered major impacts due to water shortages affecting several sectors. Southern NEB experiences the wet season during austral summer and the dry season during austral winter. Central NEB has a semiarid climate with reduced precipitation, relative to the rest of Brazil, during all seasons. Northern NEB experiences the wet season during austral autumn and is predominantly dry during the other seasons. The region is prone to frequent droughts most often associated with El Niño (Ropelewski and Halpert 1987, 1989) and/or the positive (northward) anomalous sea surface temperature (SST) gradient between tropical north and south Atlantic (Moura and Shukla 1981). However, the beginning of the 2012–16 drought has been documented not to be associated to El Niño (Rodrigues and McPhaden 2014; Marengo et al. 2016).

The SFRB water system (composed of Três Marias, Sobradinho, and Itaparica reservoirs) reached in January 2016 just 5% of its volume capacity (Fig. 13.1b). Most important reservoirs across other regional states reached similar low levels, causing water shortages in several municipalities. In December 2016, one of the regional states (Ceará), registered 39 collapsed (empty) reservoirs out of 153 monitored reservoirs. Another 42 reached the inactive volume, with waters solely accessible when installing dedicated pumping systems. In addition, 96 out of the 184 Ceará municipalities experienced water supply interruption. To reduce northern basin vulnerability, a long-lasting project dating back to colonial times, was implemented: the São Francisco diversion project a large-scale interbasin water transfer to the driest NEB portion, bringing southern SFRB water to northern states. Remaining issues to be addressed are the impacts of prolonged droughts on the project sustainability and the potential impact the diversion may have in increasing water demand in the northern basins.

This water crisis is not solely due to the evolving state of the physical system but is also aggravated by various federal and state system structural problems affecting drought monitoring/forecasting, vulnerability assessment, mitigation, and response planning. The crisis is therefore profoundly exacerbated by drought management deficiencies. Both exposure and vulnerability (due to population growth and increased water demand) remain high and can be further intensified with frequent disregard of long-term view in short- and medium-term decisions.

This study investigates possible changes in the hydrometeorological hazard, comprising the accumulated precipitation, the difference between precipitation and evaporation ($P–E$), and its potential impact on two SFRB reservoirs inflows (Q). A drought as-

sessment solely based on meteorological aspects is not sufficient to inform public decisions. The combination of the physical event, vulnerability, and exposure of millions of people living in rural and urban areas represent the true impact (Field et al. 2012).

Data and methods. This paper performs an assessment and attribution analysis of the 2016 NEB drought event through a multimethod investigation of 12-month (January to December 2016) and multiyear (2012–16) accumulated precipitation, water balance

(P–E), and 12-month hydrological flow (Q). The methods include:

(i) Estimation of return periods for the 2016 and 2012–16 drought events based on historical records (1900–2016). Return periods were obtained by inverting the fit of annual accumulation of monthly mean precipitation to a Gaussian distribution that scales with the smoothed global mean surface temperature (GMST). Global warming is factored in by allowing the Gaussian fit to be a function of the (low-pass filtered) GMST. It is assumed that the scale parameter
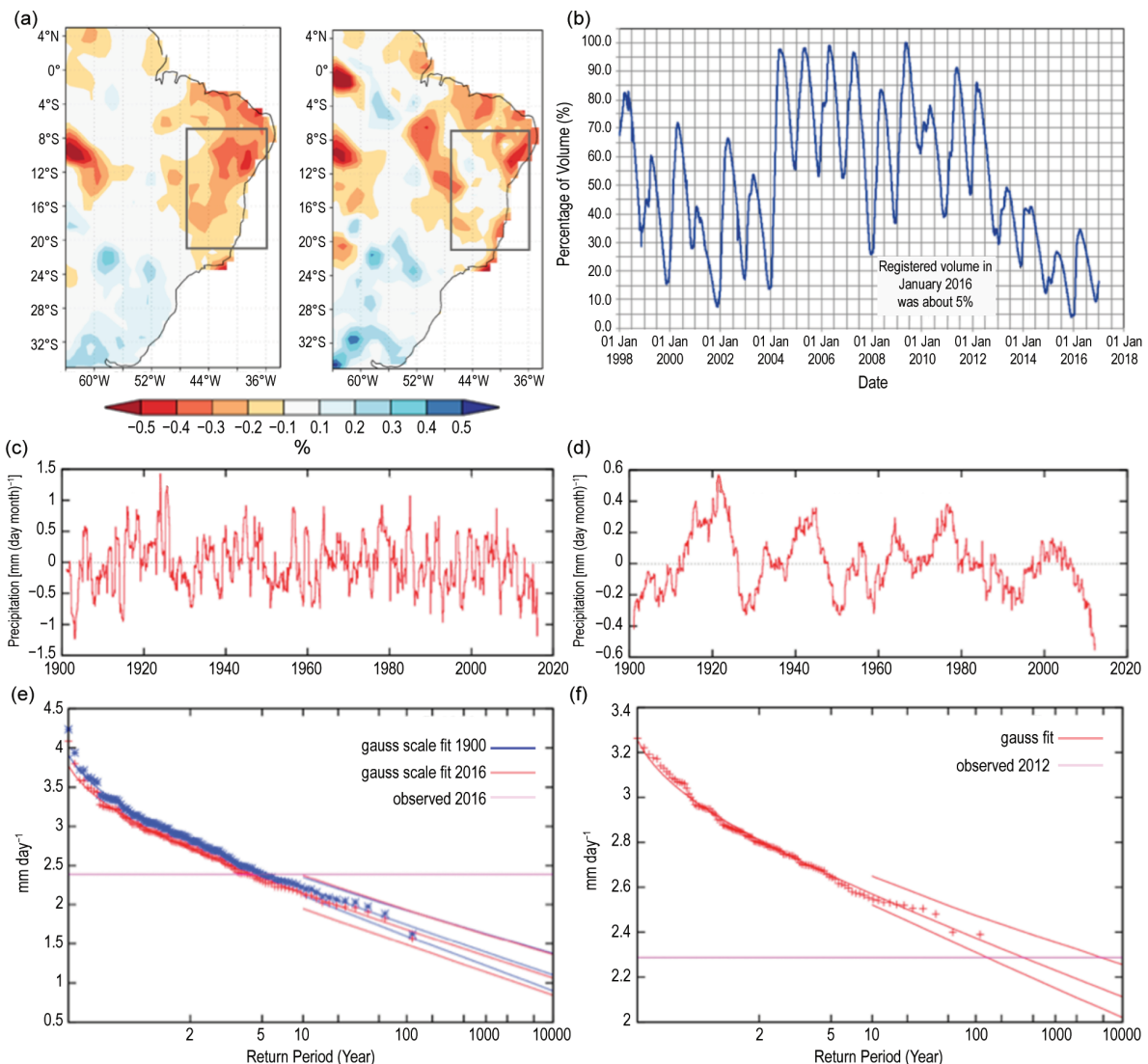

FIG. 13.1. (a) Relative precipitation anomalies for Jan 2012–Dec 2016 (left) and Jan–Dec 2016 (right) as a percentage of the 1941–2010 climatology (Source: GPCC); **(b)** São Francisco River Basin equivalent reservoir water volume (%) since 1998; **(c)** 12-month running mean of precipitation anomalies averaged over land grid points within the area 7°–21°S, 36°–47°E. Base period 1941–2010; **(d)** Same as (c), but for 5-year running mean; **(e)** Return period curve obtained by inverting the fit of annual sum of monthly mean precipitation to a Gaussian distribution that scales with the smoothed global mean surface temperature. Observations (pink) are shown twice: scaled to the 2016 climate (red) and to the 1900 climate (blue); **(f)** As in (e), but now for 5-year sum and no trend.

(i.e., the standard deviation) scales with the position parameter (i.e., the mean) of the Gaussian fit. This observational analysis is based on the GPCC-V7 analysis up to 2013 (Global Precipitation Climatology Centre; Schneider et al. 2014), and the GPCC monitoring V5 analysis for 2014–16, designed to be compatible with each other.

(ii) Estimation of the change in drought risk for this event by comparing model simulations of the current climate with simulations of the climate in a "world that might have been" if the atmospheric composition through greenhouse gas emissions had not been changed. We use the distributed computing framework—*weather@home*—to run the Met Office Hadley Centre atmosphere-only general circulation model HadAM3P (Massey et al. 2015) to simulate precipitation and *P–E* in two different ensembles representing: 1) observed climate conditions of 2016, and 2) counterfactual conditions under preindustrial greenhouse gas forcings and 11 different SST estimates without human influence (Schaller et al. 2014).

(iii) A similar procedure as in (ii) but instead using coupled multimodel ensemble simulations (CMIP5; Taylor et al. 2012) and the SST-forced HadGEM3-A model (Christidis et al. 2013).

(iv) Downscaling HadAM3P precipitation and evaporation using a hydrological model (Lopes et al. 1981) for estimating flows for both High (Três Marias) and Medium (Sobradinho) São Francisco hydrographic regions.

Results. Drought conditions were observed over NEB during 2012–15 and continued into 2016 for most of the region (Fig. 13.1a). Figures 13.1c,d show NEB 12-month and 5-year running mean time series, respectively. While the severity of the 2012–16 drought is evident, no historical trend is discernible in either of the series. The return period for the 2016 drought is about 4 years [95% confidence interval (CI): 2–9 years (Fig. 13.1e)]; however the continuous 2012–16 drought has a return period of 350 years [95% CI: at least 135 years (Fig. 13.1f)], characterizing this drought as exceptional. There is no autocorrelation in the series, so the 5-year drought is a combination of 1-year droughts. Note that with 100 years of this data, only trend changes that exceed a roughly twofold increase or decrease in probability can be detected.

The NEB annual mean precipitation *weather@home* analysis (Fig. 13.2a) shows that low precipitation extremes have become slightly less likely due to anthropogenic forcing: what would have been a 1-in-4-year precipitation deficit event like the 2016

event has become approximately a 1-in-6-year event with a risk ratio of 0.70 (95% CI: 0.55–0.84). The *P–E* analysis (Fig. 13.2d) also indicates a reduction in drought risk. For future precipitation projections under a 2°C scenario (Mitchell et al. 2017), the picture is different (not shown) with a marked increase in low precipitation extremes in consistency with the CMIP5 analysis below.

Our CMIP5 analysis used eight climate models passing our evaluation test of satisfactorily capturing the observed NEB annual precipitation anomalies distribution (see online supplementary material). Using these models we compared the likelihood of 1- and 5-year precipitation deficits comparable to the 2016 and 2012–16 events, respectively (Figs. 13.2b,e). Our multimodel analysis indicates that climate change has increased the probability of such prolonged low precipitation events, although there is high uncertainty on the magnitude of that influence (Fig. 13.2i). In future, precipitation deficits like 2016 or the last five years are projected to be even more likely. There is also no detectable change in *P–E* due to human-induced climate change (Fig. 13.2c,f) presumably because the increase in evaporation cancels the increase in precipitation. The HadGEM3-A analysis indicates reduced risk for low precipitation events due to anthropogenic forcing, with even higher uncertainty than CMIP5 (Figs. 13.2i).

The comparison of the probability density functions (PDF) for 2016 annual flow under preanthropogenic (counterfactual ensemble) and current emissions (actual ensemble) for both SFRB regions (Figs. 13.2g,h) reveals slightly reduced risk of extreme low flow as observed in 2016 due to anthropogenic forcing.

Conclusions. The observational analysis confirmed that droughts are common over NEB, but prolonged droughts comparable to the current one are exceptional, as highlighted by the impressive return period for the 2012–16 drought of at least 135 years.

The *weather@home* simulations indicated that anthropogenic climate change is not contributing to increased risk of single-year droughts over NEB, which is in line with the hydrological analysis that also did not indicate increased risk for extreme low flow. This is consistent with the observational analysis that did not indicate a trend toward drier conditions up to now as an association with global mean temperature (see Fig. ES13.1e). Despite the CMIP5 analysis indicating increased likelihood of 1- and 5-year precipitation deficits over NEB due

to anthropogenic forcing, an uncertainty analysis of the 1-year precipitation risk ratio results shows that the evidence is weighted toward natural climate variability as the principle driver, as summarized in Fig. 13.2i. Most CIs include the risk ratio equal to 1 indicating that no change in drought risk can be detected or attributed. Our multimethod analysis suggests that there is not enough evidence that anthropogenic climate change increased drought risk. In future projections under strong radiative forcing, both *weather@home* and CMIP5 indicate increased risk for extremely dry events.

The 2012–16 drought might also have been prolonged by a positive hydrological cycle feedback. The possibility of a positive feedback between precipitation and soil moisture and the existence of multiple equilibria was theoretically suggested by D'Andrea et al. (2006). Oyama and Nobre (2003) and Hirota et al. (2011) investigated this feedback for NEB showing that land surface and vegetation changes could induce tipping points and multiple equilibria. A similar investigation focused on the 2012–16 event could help advance the understanding of the mechanisms associated to the observed drought.
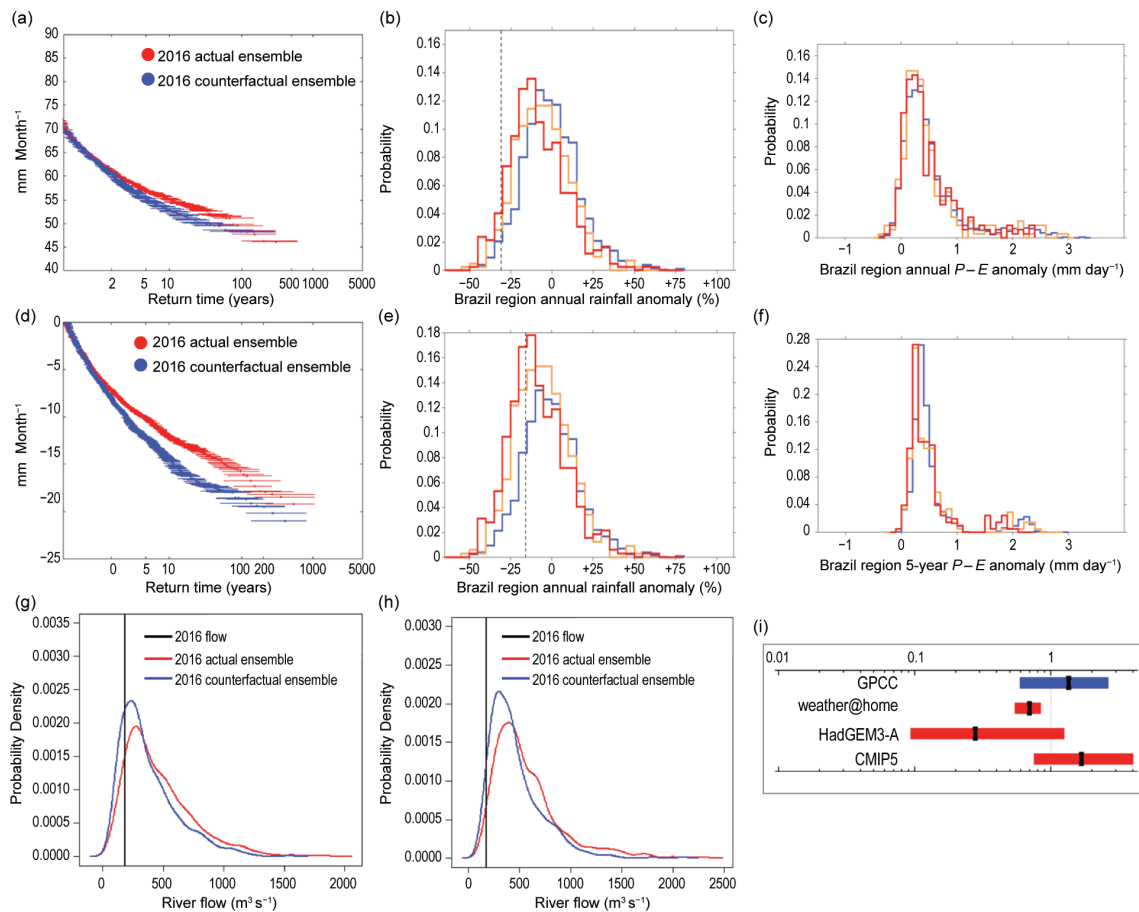

FIG. 13.2. (a) Return period curve obtained by inverting the empirical distribution fit of total precipitation averaged over NEB land grid points for the year 2016 in HadAM3P; (b) PDF of annual precipitation anomalies (from a 1961–90 historical climatology) averaged over NEB land grid points in climate simulations under natural influences only (blue), all-forcings (orange) and projected forcings under the RCP8.5 scenario in 2050 (red). The dashed line shows the observed 2016 anomaly; (c) Same as (b), but for annual *P–E* anomalies; (d) Return period curve of 12-month mean *P–E* (for the year 2016) averaged over NEB land grid points in HadAM3P; (e) Same as (b), but for 5-year precipitation anomalies. The dashed line shows the observed 2012–16 anomaly; (f) Same as (e), but for 5-year *P–E* anomalies; (g) High São Francisco (Três Marias); (h) Medium São Francisco (Sobradinho) annual flow PDF for 2016 estimated using HadAM3P simulations; (i) Risk ratio and 95% CIs (represented by the horizontal thick bars) for annual precipitation accumulation in GPCC, *weather@home*, HadGEM3-A, and CMIP5. HadGEM3-A experiments were performed for the European Climate Extremes: Interpretation and Attribution (EUCLEIA) project by the Met Office. A risk ratio larger (smaller) than 1 indicates a trend toward more (less) severe droughts.

Government responses to the past and present droughts have common characteristics that severely prevent drought risk mitigation through improved response and relief, long-term resilience building, and adaptation measures (Martins et al. 2016). This is particularly true for the multiyear drought (2012–16) analyzed in this paper.

REFERENCES

Christidis, N., P. A. Stott, A. A. Scaife, A. Arribas, G. S. Jones, D. Copsey, J. R. Knight, and W. J. Tennant, 2013: A new HadGEM3-A-based system for attribution of weather- and climate-related extreme events. *J. Climate,* **9**, 2756–2783, doi:10.1175/JCLI-D-12-00169.1.

D'Andrea, F., A. Provenzale, R. Vautard, and N. De Noblet-Decoudré, 2006: Hot and cool summers: Multiple equilibria of the continental water cycle. *Geophys. Res. Lett.,* **33**, L24807, doi:10.1029/2006GL027972.

Field, C. B., and Coauthors, 2012: *Managing the Risks of Extreme Events and Disasters to Advance Climate Change Adaptation.* Cambridge University Press, 582 pp.

Hirota, M., M. Holmgren, E. H. Van Nes, and M. Scheffer, 2011: Global resilience of tropical forest and savanna to critical transitions. *Science,* **334**, 232–235, doi:10.1126/science.1210657.

Lopes, J. E. G., B. P. F. Braga Jr., and J. G. L. Conejo, 1981: Hydrological simulation: Application of a simplified model (in Portuguese). *Annals of III Brazilian Symposium on Water Resources (Fortaleza)/ABRH,* **2**, 42–62.

Marengo, J. A., R. R. Torres, and L. M. Alves, 2016: Drought in Northeast Brazil—past, present, and future. *Theor. Appl. Climatol.,* **129**, 1189–1200 doi:10.1007/s00704-016-1840-8.

Martins, E. S. P. R., F. J. C. Teixeira, J. G. L. Conejo, J. Machado, and A. D. Moura, 2016: Crisis, opportunity, and leadership. *Drought in Brazil: Proactive Management and Policy,* E. De Nys et al. Eds., CRC Press, 19–26.

Massey, N., and Coauthors, 2015: weather@home—development and validation of a very large ensemble modelling system for probabilistic event attribution. *Quart. J. Roy. Meteor. Soc.,* **141**, 1528–1545, doi:10.1002/q j.2455.

Mitchell, D., and Coauthors, 2017: Half a degree additional warming, projections, prognosis and impacts (HAPPI): Background and experimental design. *Geosci. Model Dev.,* **10**, 571–583, doi:10.5194/gmd-10-571-2017.

Moura, A. D., and J. Shukla, 1981: On the dynamics of droughts in Northeast Brazil: Observations, theory, and numerical experiments with a general circulation model. *J. Atmos. Sci.,* **38**, 2653–2675, doi:10.1175/1520-0469(1981)038<2653:OTDODI>2.0.CO;2.

Oyama, M. D., and C. A. Nobre, 2003: A new climate-vegetation equilibrium state for tropical South America. *Geophys. Res. Lett.,* **30**, 2199, doi:10.1029/2003GL018600.

Rodrigues, R. R., and M. J. McPhaden, 2014: Why did the 2011–2012 La Niña cause a severe drought in the Brazilian Northeast? *Geophys. Res. Lett.,* **41,** 1012–1018, doi:10.1002/2013GL058703.

Ropelewski, C. F., and M. S. Halpert, 1987: Global and regional scale precipitation patterns associated with the El Niño/Southern Oscillation. *Mon. Wea. Rev.,* **115,** 1606–1626, doi:10.1175/1520-0493(1987)115<1606:GARSPP>2.0.CO;2.

——, and ——, 1989: Precipitation patterns associated with the high index phase of the Southern Oscillation. *J. Climate,* **2**, 268–284, doi:10.1175/1520-0442(1989)002<0268:PPAWTH>2.0.CO;2.

Schaller, N., J. Sedláček, and R. Knutti, 2014: The asymmetry of the climate system's response to solar forcing changes and its implications for geoengineering scenarios. *J. Geophys. Res. Atmos.,* **119**, 5171–5184, doi:10.1002/2013JD021258.

Schneider, U., A. Becker, P. Finger, A. Meyer-Christoffer, M. Ziese, and B. Rudolf, 2014: GPCC's new land surface precipitation climatology based on quality-controlled in situ data and its role in quantifying the global water cycle. *Theor. Appl. Climatol.,* **115**, 15–40, doi:10.1007/s00704-013-0860-x.

Taylor, K. E., R. J. Stouffer, and G. A. Meehl, 2012: An overview of CMIP5 and the experiment design. *Bull. Amer. Meteor. Soc.,* **93**, 485–498, doi:10.1175/BAMS-D-11-00094.1.

14. ATTRIBUTION OF WINTERTIME ANTICYCLONIC STAGNATION CONTRIBUTING TO AIR POLLUTION IN WESTERN EUROPE

ROBERT VAUTARD, AUGUSTIN COLETTE, ERIK VAN MEIJGAARD, FREDERIK MELEUX, GEERT JAN VAN OLDENBORGH, FRIEDERIKE OTTO, ISABELLE TOBIN, AND PASCAL YIOU

Climate simulations suggest a potential increase in frequency of stagnant wintertime conditions that prevailed over northwestern Europe in December 2016: it is significant in one multimodel ensemble but not in two single-model ensembles.

Introduction. In December 2016, western European weather was dominated by persistent anticyclonic conditions (Fig. 14.1a) leading to dry and calm weather. At this time of year, solar radiation does not bring enough energy to develop a well-mixed boundary layer under such calm conditions. The resulting lack of dispersion led to several air pollution episodes in western Europe, as pollutants such as particulate matter (PM10) accumulated. PM10 concentrations reached very high values over the main European air pollution hotspots: the Po-Valley, eastern Europe, and the northern France, Benelux, southern United Kingdom region, which is the primary focus of the present study (marked as a rectangle in Fig. 14.1b).

December 2016 was also among the least windy winter months of the last three decades (Fig. 14.1c), as measured from observed wind speeds over 53 measurement stations in the high-emission area. The mean observed concentrations of PM10 in that area were 25.4 µg m^{-3} that is 55% above expected average of 16.4 µg m^{-3} accounting for the decadal decreasing trend (Fig. 14.1d). Traffic bans took place in several places such as in Paris (six ban days). The question as to whether climate change had a role in such an event was raised by the media.

Detecting a climate change signal in air pollution is difficult as other factors than climatic ones such as emission reduction policies that took place over the last two decades are important. However, several modeling studies showed potential effects of future climate change on particulate matter levels from individual (Carvalho et al. 2010; Colette et al. 2013; Hedegaard et al. 2008, 2013; Manders et al. 2012; Markakis et al. 2014) or ensemble simulations (Lacressonnière et al. 2016, 2017; Lemaire 2016). These studies characterized mean pollutant concentration changes, but potential changes in air pollution episode frequency did not receive much attention.

Air pollution results from emissions and several potential meteorological factors: lack of dispersion, lack of precipitation scavenging, and chemical reactions. We focus on one of the main weather factors, the lack of dispersion by horizontal wind. We hypothesize that December monthly winds (as shown among points in Fig. 14.1d) are strong drivers of air pollution as they are more anticorrelated with PM10 concentrations of Fig. 14.1d ($r = -0.75$) than monthly precipitations ($r = -0.51$) over the area and over the 2001–16 period. Shallow planetary boundary layers are also important, but long-term measurements and model assessments are lacking for attribution studies. Near-surface wind speeds are determined by the large-scale circulation, which forces the wind in the free atmosphere, and by surface roughness and stability, which modulate near-surface momentum fluxes. We examine whether human influence could have affected stagnation episodes at monthly time scales. This issue is of particular relevance as previous studies showed that more stagnant conditions are expected (Horton et al. 2014), as well as a decrease in mean wind speeds and wind power production (Tobin et al. 2016) in future decades in some areas of Europe, however not over the area under consideration.
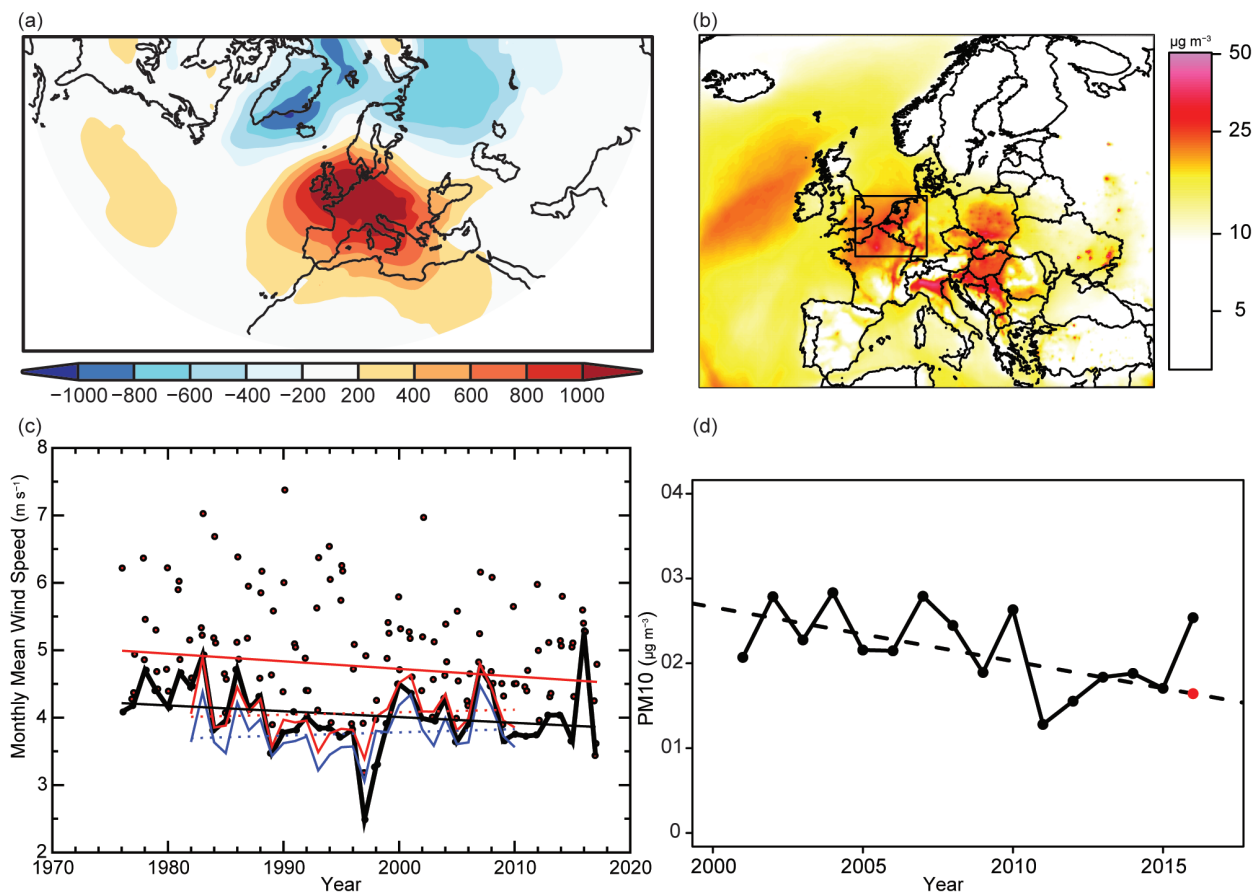
FIG. 14.1. (a) Mean sea level pressure anomaly (Pa) map for monthly average for Dec 2016; (b) PM10 (µg m⁻³) monthly mean over Dec 2016 in median ensemble of 7 chemistry–transport models of Copernicus Atmospheric Monitoring Service: Chimere, EMEP, Silam, Lotos-Euros, Mocage, Eurad, and Match (Marécal et al. 2015); (c) Dots: Nov to Mar monthly mean wind speed values (m s⁻¹) for each winter month as averaged over 53 ISD-Lite measurement stations within area under consideration; *Black heavy curve*: Winter minimum of observed monthly wind speeds; *Red curve*: Same as black curve using WFDEI winds, interpolated to station points with nearest neighbor method; *Blue curve*: Same as *Red* but using gridpoint average, over land grid points; straight lines: linear trends for all winter months (red) and the least windy month of each winter (black). To estimate offset between two types of averages and to estimate WFDEI-equivalent monthly wind speed from observations for Dec 2016; (d) Dec average of PM10 concentration (µg m⁻³) at about 50 background stations over selected area for 2001 to 2016 in EEA e-reporting air quality database. *Dotted line* indicates linear fit for 2001–15 period and *red dot*, estimated value for 2016, according to fit.

Over the last three decades, monthly surface wind speed observations exhibit a significant increase in stagnant wintertime monthly conditions (Fig. 14.1c), when considering all winter months ($p < 0.05$) but not when considering the least windy month. Such a trend may be part of the general "wind stilling" (Vautard et al. 2010; McVicar et al. 2012). Whether this can be linked with climate change is difficult to establish as other possible causes such as urbanization or forest growth may interfere.

Event definition and observations. The indicator used here to characterize stagnation is the minimum monthly mean wind speed in each winter month

(from November to February). The spatial wind speed average is done over the land area of high emission centers in western Europe, including the cities of Paris, London, Hamburg, the densely populated area of Benelux and the industrial Ruhr area (48°–54°N, 1°W–10°E; see Fig. 14.1b). Observations were taken from 53 cup anemometer measurements in the ISD-Lite archive (Smith et al. 2011), mostly coming from airport weather reports. The stations were selected to ensure sufficient time coverage (at least 30 years of 3-hourly values with presence over at least 20 days for each month and hour of the day). The 3-hourly Watch Forcing Data ERA Interim (WFDEI) gridded dataset (Weedon et al. 2014), which guarantees homogeneous

coverage, was also used to calibrate model simulations over the reference period 1981–2010. WFDEI consists in reinterpolated ERA-Interim reanalyses (Dee et al. 2011), with a higher resolution (0.5° × 0.5°) than native. There is a systematic difference of 0.3 m s⁻¹ between the average wind speed interpolated over the stations and the land gridpoint average for WFDEI (Fig. 14.1c). We will therefore assume that the actual value of the December 2016 mean wind speed over land grid points is 3.15 m s⁻¹, instead of the ISD-Lite observed value of 3.45 m s⁻¹.

Simulation ensembles. We use several ensembles of model simulations. First, the actual (observed SST forcing) and natural simulations (only natural forcings and anthropogenic signal removed from SSTs, sea–ice) of the HadGEM3-A model (Christidis et al. 2013; Vautard et al. 2017, manuscript submitted to *Climate Dyn.*) covering the period (1960–2013) with 15 members per ensemble are used. In order to focus on the latter part of the data, analyses were only made over the last 30 years (1984–2013). Second, we use 11 high-resolution (0.11°) climate projections from the EURO-CORDEX ensemble (Jacob et al. 2014), with 5 Global Climate Models (GCMs) downscaled by 6 Regional Climate Models (RCMs), that were available and downloaded at the time of the study. GCMs and RCMs are listed in the online supplement. For these ensembles, natural simulations were not available, but the anthropogenic forcing was assumed dominant in explaining the difference between two available climate periods (1971–2000 and 2001–30). We then compare the extreme value distributions from these time periods and a third future one (2031–60) in order to analyze the effect of forcing changes on low wind speeds. We also used a 16-member ensemble of KNMI-RACMO simulations (Royal Netherlands Meteorological Institute Regional Atmospheric Climate Model; Lenderink et al. 2014; de Vries et al. 2014; van den Hurk et al. 2015) downscaling different realizations of EC-EARTH simulations, with the same periods as for EURO-CORDEX for consistency.

Model evaluation. For each set of simulations, we first compared the distribution of the simulation with the indicator calculated from WFDEI. The comparison was made over the 1981–2010 reference period for EURO-CORDEX and HadGEM3-A (29 winters). In Fig. ES14.1, quantile–quantile plots of the distributions of the stagnation indicator calculated from model ensembles are shown. HadGEM3-A slightly underestimates wind speed, especially in

the lower tail of the distribution. In the EURO-CORDEX ensemble, the stagnation indicator is either underestimated or overestimated depending on the model used. The RACMO ensemble slightly overestimates the indicator values. In all cases, a simple multiplicative bias adjustment was applied using a single coefficient for the whole ensembles for HadGEM3-A and RACMO and a model-dependent coefficient for EURO-CORDEX. The bias-adjusted simulations distributions are in closer agreement with WFDEI (Fig. ES14.1).

Attribution. We use each model ensemble separately to estimate how human influence has altered the risk of winter monthly wind speed lower than observed in December 2016 (3.15 m s⁻¹). December 2016 is found to be a ~10-year event. For HadGEM3-A, actual and natural simulations do not show much difference in the extreme low wind speeds, despite a systematically higher probability in the natural than in the actual simulations for less extreme months (see Fig. 14.2a). In the EURO-CORDEX ensemble, wind speeds lower than Dec 2016 become more than twice as probable in the current climate than in the 1971–2000 climate [risk ratio = 2.4 (1.7–3.7); see Table ES14.1 and details of calculation of confidence intervals]. For the RACMO ensemble, there is a nonsignificant increase in frequency of low mean monthly wind speed [risk ratio = 1.3 (0.9–2.0)]. When combining the last two ensembles, using therefore 27 simulations, the risk ratio becomes 1.7 (1.3–2.3). The risk ratio [1.2 (1.0–1.5)] is lower but remains significant when taking all ensembles together, but this combined estimate requires prudence in interpretation as time periods differ and ensembles are of different nature. For RACMO and EURO-CORDEX, changes are also found for future periods (2031–60; see Figs. 14.2b,c and Table ES14.1). This is in agreement with the widening of the distribution as revealed by the change in variance of the indicator (Fig. ES14.2), more pronounced in future than current periods.

Discussion. An immediate potential candidate to explain changes in low winds speeds is the atmospheric flow and its potential changes. The high pressures of December 2016 are among the strongest as indicated by monthly mean sea level pressure (SLP) measured in De Bilt (Fig. 14.2d). However, no trend could be found in wintertime extreme monthly SLP or its variance, and only a weak correlation was found between monthly SLP and monthly winds (e.g., $r = -.39$ in December), excluding SLP as driving
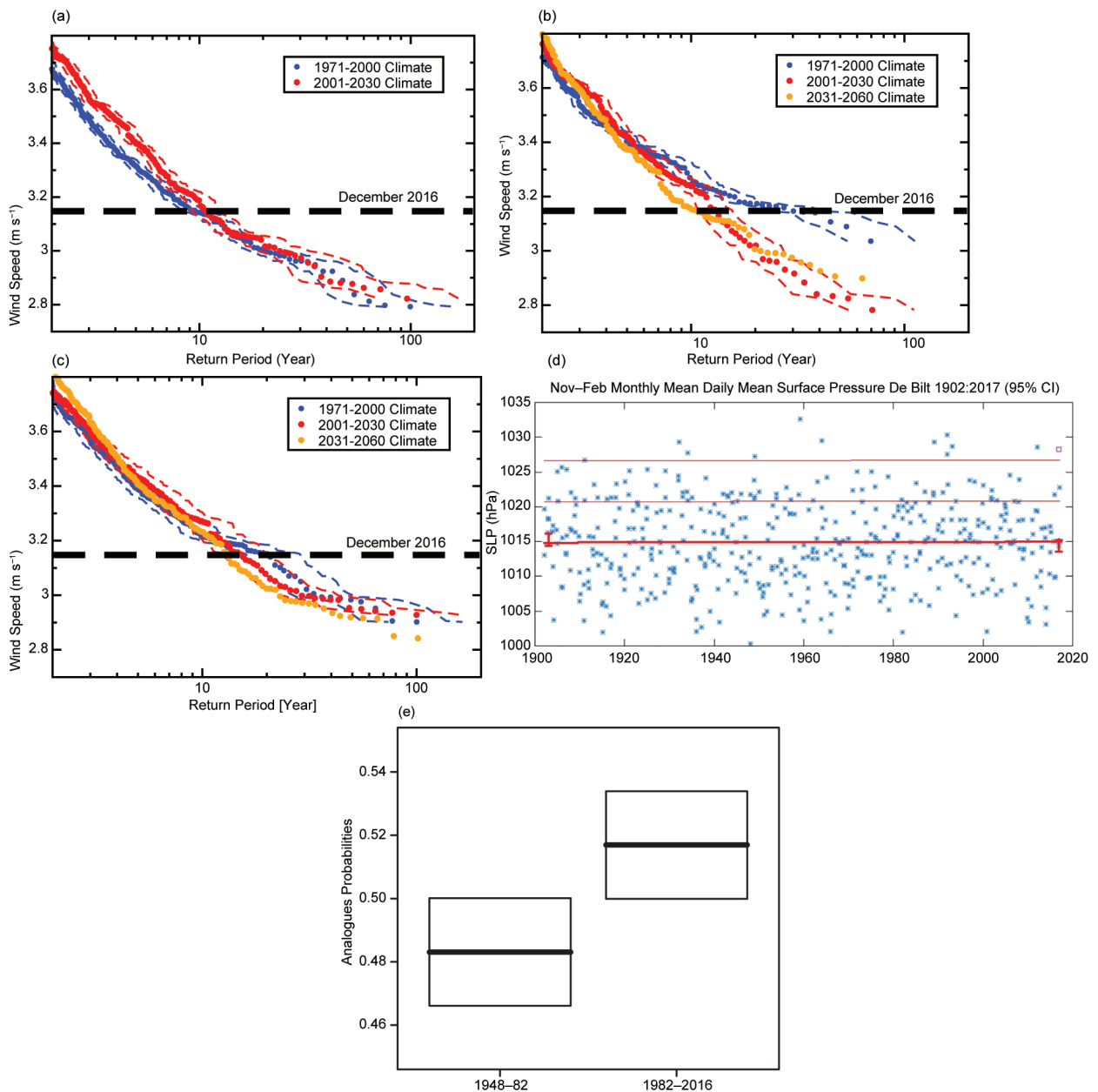
FIG. 14.2. Changes in return values (m s⁻¹) of stagnation indicator vs. return periods for different model ensembles: **(a) HadGEM3-A, (b) EURO-CORDEX ensemble, (c) RACMO–EC-EARTH ensemble. Dots represent median of binned running 11 consecutive sorted return period/values model values from 10 000 bootstrap estimations, together with 5%–95% confidence intervals (dashed lines). (d) Winter monthly SLP average (hPa) in De Bilt since 1900, together with average, average +1 standard deviation, average +2 std. dev.; Dec 2016 is shown as red square symbol. (e) Thick lines of plot show mean frequency of SLP analogues of 2016–17 winter in 1948–82 and 1983–2016 (until Mar 2016, not including current winter). Sampling distribution of probabilities is assessed with bootstrap test over winter days. Boxes are bootstrap confidence intervals [p − (p⁹⁵ − p), p − (p⁵ − p)].**

the wind changes. However, a large-scale pattern of moderate anticyclonic conditions may be more conductive to low winds than strong SLP values because geostrophic winds are due to pressure gradients and not pressure itself. To test whether changes in atmospheric weather patterns could be linked to increases in low wind speeds, we used the method of flow analogues (Yiou et al. 2013). We computed the 20 best analogues of daily SLP anomalies of winter 2016/17 from the NCEP reanalysis (Kalnay et al. 1996) by minimizing a Euclidean distance between daily SLP patterns over the North Atlantic

region (30°–70°N, 80°W–30°E). The empirical probability that analogues of winter 2016/17 are found in 1948–82 vs. 1983–2016 (excluding November and December 2016) has significantly increased by about 10% in the recent decades (Fig. 14.2e). Although such trend could contribute to the stagnation trend, we could not establish a clear causal link between these phenomena.

Other mechanisms than more frequent favorable atmospheric flows may be involved in explaining the increase in stagnant conditions in both observations and the EURO-CORDEX climate projections, such as changes in atmospheric stability or in the vertical wind profile. Surface roughness or aerosols could contribute to observed but not to simulated changes as in general they were kept fixed in most simulations. Changes in stability can also explain changes in turbulent fluxes. While calling for investigation, resolving these issues is clearly beyond the scope of this article. These results therefore call for prudence in interpretation and for further analyses.

REFERENCES

Carvalho, A., A. Monteiro, S. Solman, A. I. Miranda, and C. Borrego, 2010: Climate-driven changes in air quality over Europe by the end of the 21st century, with special reference to Portugal. *Environ. Sci. Policy*, **13**, 445–558, doi:10.1016/j.envsci.2010.05.001.

Christidis, N., P. A. Stott, A. A. Scaife, A. Arribas, G. S. Jones, D. Copsey, J. R. Knight, and W. J. Tennant, 2013: A new HadGEM3-A-based system for attribution of weather- and climate-related extreme events. *J. Climate*, **26**, 2756–2783, doi:10.1175/JCLI-D-12-00169.1.

Colette, A., and Coauthors, 2013: European atmosphere in 2050, a regional air quality and climate perspective under CMIP5 scenarios. *Atmos. Chem. Phys.*, **13**, 7451–7471, doi:10.5194/acp-13-7451-2013.

Dee, D. P., and Coauthors, 2011: The ERA-Interim reanalysis: Configuration and performance of the data assimilation system. *Quart. J. Roy. Meteor. Soc.*, **137**, 553–597, doi:10.1002/qj.828.

de Vries, H., G. Lenderink, and E. van Meijgaard, 2014: Future snowfall in western and central Europe projected with a high-resolution regional climate model ensemble. *Geophys. Res. Lett.*, **41**, 4294–4299, doi:10.1002/2014GL059724.

Hedegaard, G. B., J. Brandt, J. H. Christensen, L. M. Frohn, K. M. Hansen, and M. Stendel, 2008: Impacts of climate change on air pollution levels in the Northern Hemisphere with special focus on Europe and the Arctic *Atmos. Chem. Phys.*, **8**, 3337–3367, doi:10.5194/acp-8-3337-2008.

——, J. H. Christensen, and J. Brandt, 2013: The relative importance of impacts from climate change vs. emissions change on air pollution levels in the 21st century. *Atmos. Chem. Phys.*, **13**, 3569–3585, doi:10.5194/acp-13-3569-2013..

Horton, D. E., C. B. Skinner, D. Singh, and N. S. Diffenbaugh, 2014: Occurrence and persistence of future atmospheric stagnation events. *Nat. Climate Change*, **4**, 698–703, doi:10.1038/nclimate2272.

Jacob, D., and Coauthors, 2014: EURO-CORDEX: New high-resolution climate change projections for European impact research. *Reg. Environ. Change*, **14**, 563–578, doi:10.1007/s10113-013-0499-2.

Kalnay, E., and Coauthors, 1996: The NCEP/NCAR 40-year reanalysis project. *Bull. Amer. Meteor. Soc.*, **77**, 437–471, doi:10.1175/1520-0477(1996)077<0437:TNYRP>2.0.CO;2.

Lacressonnière, G., and Coauthors, 2016: Impacts of regional climate change on air quality projections and associated uncertainties. *Climatic Change*, **136**, 309–324, doi:10.1007/s10584-016-1619-z.

——, and Coauthors, 2017: Particulate matter air pollution in a +2°C warming world. *Atmos. Environ.*, **154**, 129–140, doi:10.1016/j.atmosenv.2017.01.037.

Lenderink, G., B. J. J. M. van den Hurk, A. M. G. Klein Tank, G. J. van Oldenborgh, E. van Meijgaard, H. de Vries, and J. J. Beersma, 2014: Preparing local climate change scenarios for the Netherlands using resampling of climate model output. *Environ. Res. Lett.*, **9**, 115008, doi:10.1088/1748-9326/9/11/115008.

Lemaire, V. E. P., A. Colette, and L. Menut, 2016: Using statistical models to explore ensemble uncertainty in climate impact studies: The example of air pollution in Europe. *Atmos. Chem. Phys.*, **16**, 2559–2574, doi:10.5194/acp-16-2559-2016.

Manders, A. M. M., E. van Meijgaard, A. C. Mues, R. Kranenburg, L. H. van Ulft, and M. Schaap, 2012: The impact of differences in large-scale circulation output from climate models on the regional modeling of ozone and PM. *Atmos. Chem. Phys.*, **12**, 9441–9458, doi:10.5194/acp-12-9441-2012.

Marécal, V., and Coauthors, 2015: A regional air quality forecasting system over Europe: The MACC-II daily ensemble production. *Geosci. Model Dev.*, **8**, 2777–2813, doi:10.5194/gmd-8-2777-2015.

Markakis, K., and Coauthors, 2014: Air quality in the mid-21st century for the city of Paris under two climate scenarios; from the regional to local scale. *Atmos. Chem. Phys.*, **14**, 7323–7340, doi:10.5194 /acp-14-7323-2014.

McVicar, T. R., and Coauthors, 2012: Global review and synthesis of trends in observed terrestrial near-surface wind speeds: Implications for evaporation. *J. of Hydrol.*, **416**, 182–205, doi:10.1016 /j.jhydrol.2011.10.024.

Smith, A., N. Lott, and R. Vose, 2011: The integrated surface database: Recent developments and partnerships. *Bull. Amer. Meteor. Soc.*, **92**, 704-708, doi:10.1175/2011BAMS3015.1.

Tobin, I., and Coauthors, 2016: Climate change impacts on the power generation potential of a European mid-century wind farms scenario. *Environ. Res. Lett.*, **11**, 034013, doi:10.1088/1748-9326/11/3/034013.

Van den Hurk, B. J. J. M., E. van Meijgaard, P. de Valk, K. J. van Heringen and J. Gooijer, 2015: Analysis of a compounding surge and precipitation event in the Netherlands. *Environ. Res. Lett.*, **10**, 35001, doi:10.1088/1748-9326/10/3/035001.

Vautard, R., J. Cattiaux, P. Yiou, J.-N Thepaut, and P. Ciais, 2010: Northern Hemisphere atmospheric stilling partly attributed to an increase in surface roughness. *Nat. Geosci.*, **3**, 756–761, doi:10.1038/ngeo979.

Weedon, G. P., G. Balsamo, N. Bellouin, S. Gomes, M. J. Best, and P. Viterbo, 2014: The WFDEI meteorological forcing data set: WATCH Forcing Data methodology applied to ERA-Interim reanalysis data. *Water Resour. Res.*, **50**, 7505–7514, doi.10.1002/2014WR015638.

Yiou, P., T. Salameh, P. Drobinski, L. Menut, R. Vautard, and M. Vrac, 2013: Ensemble reconstruction of the atmospheric column from surface pressure using analogues. *Climate Dyn.*, **41**, 1333–1344, doi:10.1007 /s00382-012-1626-3.

15. ANALYSIS OF THE EXCEPTIONALLY WARM DECEMBER 2015 IN FRANCE USING FLOW ANALOGUES

Aglaé Jézéquel, Pascal Yiou, Sabine Radanovics, and Robert Vautard

December 2015 in France was an extreme of circulation and temperature. Both circulation and climate change partly explain the 4°C anomaly. We found no link between climate change and circulation.

The event. The December 2015 average temperature broke a record in France, with an anomaly of +4.1°C (Fig. 15.1a) with respect to the 1949–2015 climatology. The linear trend of average December temperature (red in Fig. 15.1a) is not significant (p-value > 0.05), as regional temperature variability is high in winter. Such a positive temperature anomaly has impacts on the vegetation cycle (the French press covered this topic in the daily newspaper *Le Monde*[1]). It also affects local economies (e.g., tourism in ski resorts). The temperature anomaly was concomitant with a zonal atmospheric circulation over western Europe (Fig. 15.1b), directing mild subtropical air masses toward France. We found that the mean monthly SLP (sea level pressure) anomaly over the black box of Fig. 15.1b is also a record high for the NCEP reanalysis. Such a circulation type generally leads to warm temperatures over France (Yiou and Nogaj 2004).

In this paper, we seek to address three questions: How much does the circulation anomaly explain the temperature anomaly during December 2015 in France? What is the influence of climate change on the occurrence of the circulation anomaly? How does the distribution of temperature conditional to the atmospheric circulation evolve with climate change? We hence perform a *conditional attribution* exercise (NASEM 2016, p. 30), with a circulation that is fixed to the observation of December 2015. This estimates the thermodynamic contribution of climate change on the increase of temperature (Vautard et al. 2016; Yiou et al. 2017).

---

[1] http://abonnes.lemonde.fr/biodiversite/article/2015/12/30/la
-nature-deboussolee-par-un-hiver-tres-doux_4839801
_1652692.html?xtmc=temperature&xtcr=1

Flow analogues and the role of circulation. We evaluated the link between the SLP anomalies over the black box in Fig. 15.1b and temperature in France using the method of flow analogues (e.g., Yiou et al. 2017). We considered the French national temperature index supplied by Météo France (Soubeyroux et al. 2016). This daily index is computed as the average of 30 stations distributed over France and starts in 1949. We use temperature anomalies with respect to a daily seasonal cycle obtained by spline smoothing (cf. Yiou et al. 2008). The circulation proxy is the SLP from the National Centers for Environmental Predictions (NCEP) reanalysis, between 1949 and 2015. For each day of December 2015, we identified the 30 best analogues of SLP (with a Euclidean distance) from 1949 to 2015 on the domain delimited by the black rectangle in Fig. 15.1b. Jézéquel et al. (2017) showed that the results on analogues are qualitatively insensitive to the number of analogues (between 5 and 30 analogues). We simulate daily sequences of SLP by randomly picking one of the 30 best analogues within the NCEP dataset for each day. The repetition of this random selection (with replacements) builds an ensemble of *uchronic* months. Those *uchronic* months reproduce the SLP anomaly of December 2015 (see Figs. ES15.1a–d). We then compute monthly averages for December of the national temperature index. We hence obtain *uchronic* French seasonal anomalies of temperature for December. We iterated this process 10^4 times in order to produce *uchronic* probability distributions of monthly mean temperatures (see Jézéquel et al. 2017 for more details). This *uchronic* distribution of temperatures represents the ensemble of temperatures that could have been expected for the circulation observed in December 2015. We compared the *uchronic* distribution of temperature anomalies to a distribution built from randomly picked December days. In Fig. 15.1c, the *control* experiment corresponds to a monthly average of the daily temperature anomalies from the 10^4 random samples without conditioning on the atmospheric circulation. In order to take
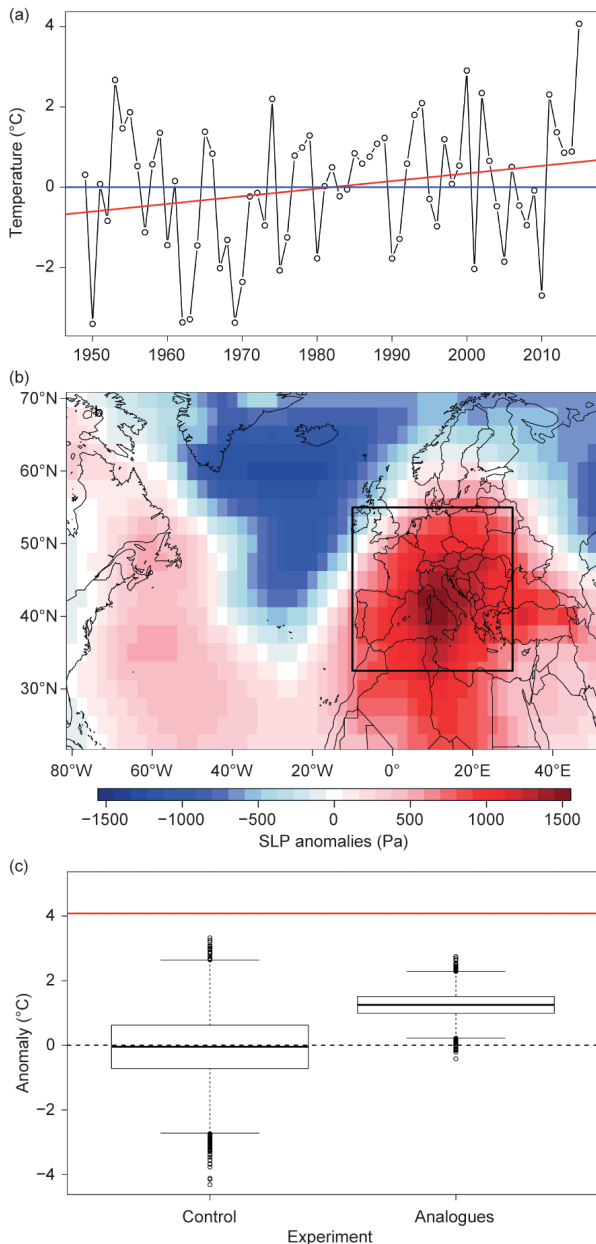
FIG. 15.1. (a) Evolution of French national temperature index (°C) for Dec between 1949 and 2015. Red line is (nonsignificant) linear trend. (b) SLP anomalies for Dec 2015 relative to 1949–2015 average of NCEP Reanalysis I dataset (Kalnay et al. 1996). (c) Comparison of *uchronic* monthly seasonal anomalies of national index distribution for randomly picked days (*control*) and randomly picked analogues. Red line is observed temperature anomaly (+4°C). Three lines composing box plots are, respectively, from bottom to top, 25th (p25), median (p50), and 75th percentile (p75) of *uchronic* temperature anomaly distribution. Value of upper whiskers is min [1.5 × (p75 – p25) + p50, max (temperature anomaly)]. Value of lower whiskers is its conjugate. Circles represent values that are outside of whiskers.

into account the dependence between consecutive days in the *Control* distribution, we calculated the monthly means using only every third day (Jézéquel et al. 2017).

We find that the SLP partly explains the monthly temperature anomaly in France during December 2015 (Fig. 15.1c). The median of the *uchronic* temperature anomaly distribution is 1.3°C (i.e., ~30% of the anomaly). The other ~70% of the anomaly could be explained by other factors (e.g., snow cover feedback). This positive anomaly demonstrates the link between the synoptic situation and the anomaly of temperature in France and justifies the choice of a conditional attribution approach.

Role of climate change. In order to estimate the role of climate change, we rely on the CESM1 model large ensemble, CESM–LENS (Kay et al. 2015). We use 30 members for both surface temperature and SLP using historical runs between 1951 and 2005 and RCP8.5 between 2006 and 2100. We reconstitute the French national temperature index from the surface temperature using the coordinates of the 30 stations used to calculate the index. Kay et al. (2015) showed that CESM–LENS reproduces reasonably well features of the Northern Hemisphere atmospheric circulation. An analysis of the SLP distances between those observed during December 2015 and CESM simulations indicates that they are not statistically different from the NCEP reanalysis (Fig. ES15.1e). We hence consider that this model does not yield biases that prevent its use for the purpose of this study.

We estimate the influence of climate change on the circulation pattern leading to December 2015 by computing the probability distributions of distances between SLP anomalies among all the December days in both NCEP and CESM and the closest day of December 2015 (Fig. 15.2a). We keep only the distances below the 5th percentile of the distribution, in order to focus on the days with SLP anomalies closest to those observed in December 2015. For each December, we count the number of days below this threshold for each ensemble member (NCEP and CESM). If the circulation that prevailed in December 2015 became more frequent with time, then a trend should be detected in this number of days. We detect no such trend. Therefore it is not possible to conclude there is an impact of climate change on the atmospheric circulation itself.

We then estimate the temperature anomaly for a similar event in terms of synoptic circulation without climate change, and in future climate change sce-
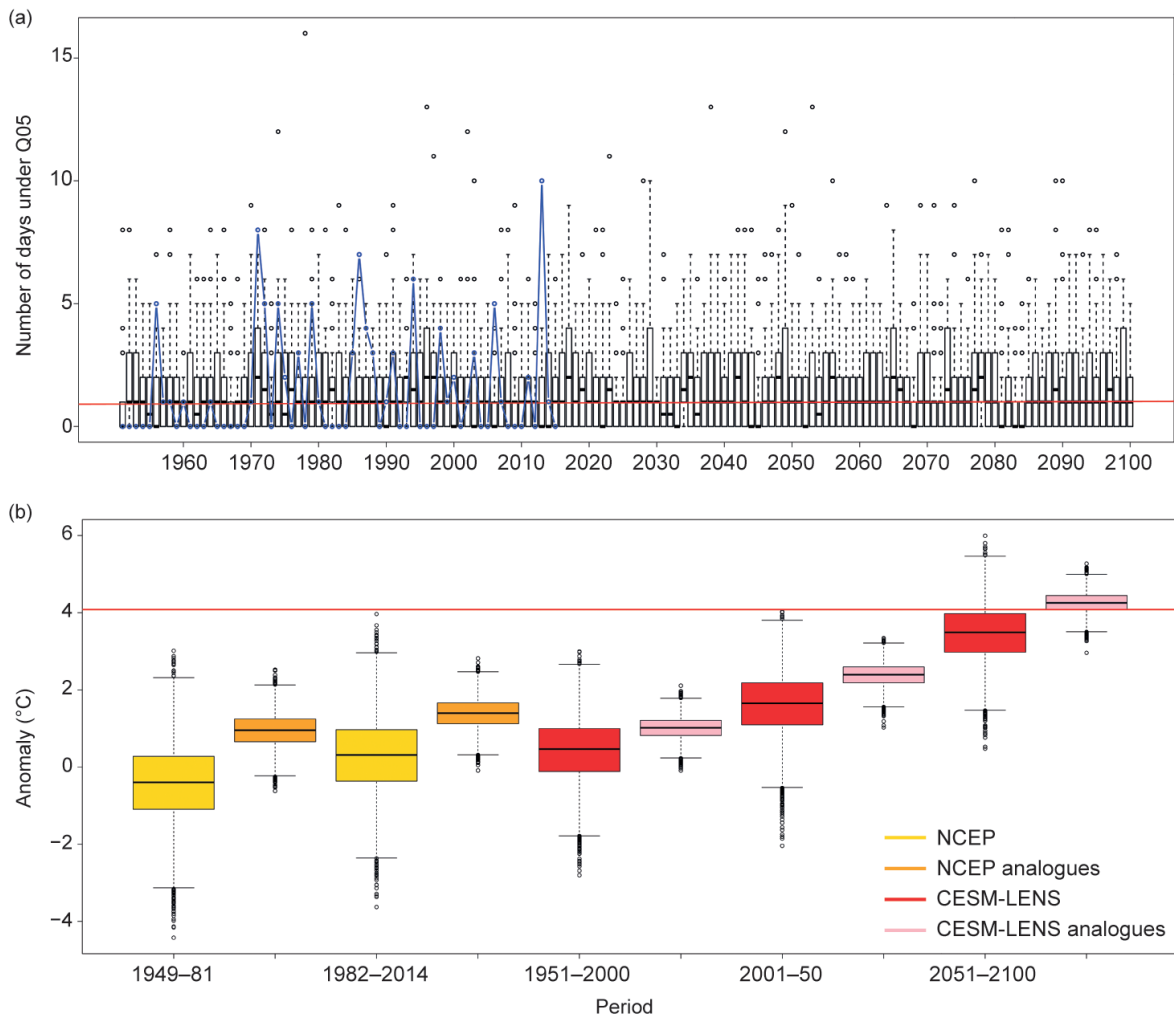
(a)

(b)

Fig. 15.2. (a) Number of days per year with SLP distances below 5th percentile of distribution of daily distances to closest December 2015 day. Box plots show dispersion of CESM ensemble members. Blue lines-dots are values for NCEP reanalysis. Red line is (nonsignificant) linear trend of median of CESM ensemble members. (b) Box plots of control distributions (respectively *uchronic* distributions) of anomalies of national temperature index relative to observed climatology of this index between 1948 and 2015, in yellow (orange) using NCEP and in red (pink) using CESM–LENS subsets.

narios by computing analogues of circulation from different periods of observations and CESM simulations. We analyzed the *uchronic* temperature anomalies constructed with analogues of the December 2015 flows from two time periods of the NCEP dataset. We compared an early subset of 33 years (1949–1981) to a more recent one (1982–2014). The two gold box plots in Fig. 15.2b represent those two experiments. We detected a difference of 0.4°C between the two distributions, in contrast with the monthly temperature trend for 1949–2015 displayed in Fig. 15.1c, which is not significant. However, it is not possible to attribute this difference of temperature to climate change, as it could also relate to interdecadal variability, especially for very small subsets of 33 years, whose length was imposed by the NCEP reanalysis length.

In order to study the relative influences of climate change and variability, we rely on CESM–LENS. We study three periods of 50 years: 1951–2000, 2001–50, and 2051–2100. Using 30 members, we have 1500 years of data for each subperiod from which we can calculate the analogues (which correctly represent the observed SLP anomaly as displayed in Figs. ES15.1a–d). This reduces the uncertainty related to the quality of the analogues we picked. The three pink box plots in Fig. 15.2b represent the *uchronic* distributions for SLP analogues picked from CESM–LENS. The three red box plots represent the *control* distributions for the same subperiods. We observe that the December 2015 anomaly of temperature was never reached before 2000. It is still not reached for 2001–50 under the RCP8.5 scenario. For the second half of the twenty-

first century, the temperature anomaly is expected to exceed 4°C for the same synoptic situation. The observed anomaly is still warmer than the median of the *control* distribution. A caveat of this study is that we only used one model, which could have biases especially in the future.

Conclusion. The month of December 2015 set a record temperature in France. The zonal circulation that prevailed over western Europe during the whole month accounts for ~30% or 1.3°C of the temperature anomaly. No trend was found in the atmospheric circulation patterns themselves (Fig. 15.2a). For this given circulation, our analysis shows that the observed temperature is never reached in the second half of the twentieth century (Fig. 15.2b), and the model is unable to reach it even during the first half of the twenty-first century. However, the December temperature observed in 2015 is projected to be exceeded in the second half of the twenty-first century under the same synoptic situation. Cattiaux et al. (2010) found with a similar analysis that the cold winter of 2009/10 would have been colder if not for climate change. Our analysis of December 2015 is a warm counterpart to that study. We find a 1.4°C difference between the median of the *uchronic* temperatures of the second half of the twentieth century and the first half of the twenty-first century and an additional 1.9°C for the second half of the twenty-first century. We find approximately the same differences between *control* distribution medians, which means that the trend conditional to the circulation equals the unconditional trend.

REFERENCES

Cattiaux, J., R. Vautard, C. Cassou, P Yiou, V. Masson-Delmotte, and F. Codron, 2010 : Winter 2010 in Europe: A cold extreme in a warming climate. *Geophys. Res. Lett.*, **37**, L20704, doi:10.1029/2010GL044613.

Jézéquel, A., P. Yiou, and S. Radanovics, 2017: Role of circulation in European heatwaves using flow analogues. *Climate Dyn.*, First Online, doi:10.1007/s00382-017-3667-0.

Kay, J. E., and Coauthors, 2015: The Community Earth System Model (CESM) large ensemble project: A community resource for studying climate change in the presence of internal climate variability. *Bull. Amer. Meteor. Soc.*, **96**, 1333–1349, doi:10.1175/BAMS-D-13-00255.1.

Kalnay, E., and Coauthors, 1996: The NCEP/NCAR 40-year reanalysis project. *Bull. Amer. Meteor. Soc.*, **77,** 437–471, doi:10.1175/1520-0477(1996)077<0437:TNYRP>2.0.CO;2

NASEM, 2016: *Attribution of Extreme Weather Events in the Context of Climate Change*. National Academies Press, 165 pp., doi:10.17226/21852.

Soubeyroux, J.-M., G. Ouzeau, M. Schneider, O. Cabanes, and R. Kounkou, 2016 : Les vagues de chaleur en France: Analyse de l'été 2015 et évolutions attendues en climat futur (in French). *La Météorologie*, **94**, 45–51, doi:10.4267/2042/60704.

Vautard R., P. Yiou, F. Otto, P. Stott, N. Christidis, G. J. van Oldenborgh and N. Schaller, 2016: Attribution of human-induced dynamical and thermodynamical contributions in extreme weather events. *Environ. Res. Lett.*, **11**, 114009, doi:10.1088/1748-9326/11/11/114009.

Yiou, P., and M. Nogaj, 2004: Extreme climatic events and weather regimes over the North Atlantic: When and where? Geophys. Res. Lett., **31***, L07202, doi:10.1029/2003GL019119.

——, K. Goubanova, Z. X. Li, and M. Nogaj, 2008: Weather regime dependence of extreme value statistics for summer temperature and precipitation. *Nonlin. Processes Geophys.*, **15**, 365–378, doi:10.5194/npg-15-365-2008.

——, A. Jézéquel, P. Naveau, F. E. L. Otto, R. Vautard, and M. Vrac, 2017: A statistical framework for conditional extreme event attribution. *Adv. Stat. Climatol. Meteor. Oceanogr.*, **3**, 17–31, doi:10.5194/ascmo-3-17-2017.

16. WARM WINTER, WET SPRING, AND AN EXTREME RESPONSE IN ECOSYSTEM FUNCTIONING ON THE IBERIAN PENINSULA

Sebastian Sippel*, Tarek S. El-Madany*, Mirco Migliavacca, Miguel D. Mahecha, Arnaud Carrara,
Milan Flach, Thomas Kaminski, Friederike E. L. Otto, Kirsten Thonicke,
Michael Vossbeck, and Markus Reichstein

A warm winter 2015/16 followed by a wet spring enabled exceptionally high ecosystem gross primary productivity on the Iberian Peninsula. Climate-ecosystem model simulations show warming winters and increased CO_2 availability benefit ecosystem productivity, but no increase in spring precipitation.

Introduction. The Iberian Peninsula (IP) experienced unusual meteorological conditions in winter and spring 2015/16 (WS15/16) with a warm winter followed by wet conditions in late winter and spring (Figs. 16.1a–c). The unusual succession of these events coincided with an extremely positive anomaly in vegetation productivity on local and regional scales over the IP with unusually high regional vegetation greenness (Figs. 16.1d–f; a proxy for ecosystem productivity) and high crop yields (JRC MARS Bulletins 2016, https://ec.europa.eu/jrc/en/research-topic/crop-yield-forecasting).

Climatic changes can affect the intensity and frequency of extreme events (Seneviratne et al. 2012), and these changes are widely recognized to impose substantial impacts on terrestrial ecosystems (Reichstein et al. 2013). However, interpreting and quantifying climate-induced ecosystem impacts such as the vegetation productivity on the IP in WS15/16 remains challenging as continuous site-level measurements that span over a decade are generally rare, and even the longest site measurements are only available for the last 25 years (http://fluxnet.fluxdata.org/data/fluxnet2015-dataset/).

While long-term climatic changes impose fundamental impacts on terrestrial ecosystems (Parmesan and Yohe 2003; Walther et al. 2002), cause–effect chains under climatic extremes are often highly nonlinear (Frank et al. 2015) and typically include instantaneous and lagged effects (Arnone et al. 2008). Ecosystem responses to climate extremes are specific to the ecosystem type affected (Teuling et al. 2010), depend on nutrient status, ecosystem health, and pre-exposure; and extreme climatic events can lead to little ecosystem responses while moderate events can trigger large responses. Similarly, ecosystem responses can be mitigated or amplified across seasons (Wolf et al. 2016). For example, higher spring carbon uptake due to higher spring temperatures could compensate for carbon losses under drought conditions over the contiguous United States in summer 2012 (Wolf et al. 2016).

To improve our understanding of extreme responses of ecosystem productivity, the concept of compound events is particularly useful. A compound event is a combination, or in our case succession, of events in which the single drivers are not necessarily extreme themselves but lead to an extreme impact (Field et al. 2012; Leonard et al. 2014). A warm winter followed by wet spring in a Mediterranean ecosystem is one example of a compound event in which single drivers (winter temperature and spring precipitation) are not record-breaking extremes themselves, but this favorable combination of meteorological variables can lead to highly positive impacts on ecosystem productivity if other stressors are absent. In particular, for the ecosystem studied, other stressors could include, but are not limited to, short but intense cold spells in
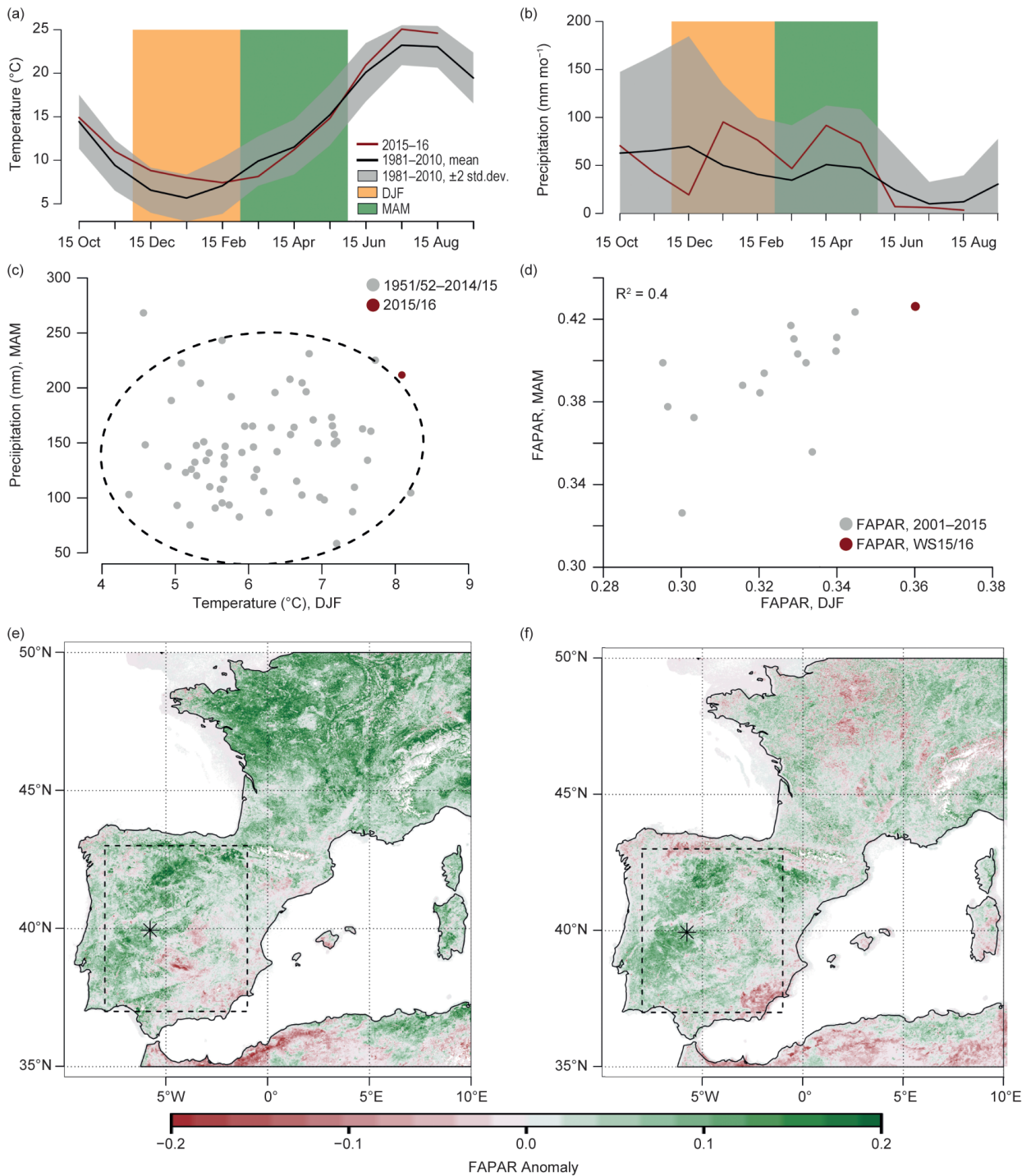
* S.S. and T.S.E.-M contributed equally to the manuscript.

FIG. 16.1. (a),(b) Time series of (a) temperature (°C) and (b) precipitation (mm month⁻¹) over IP in 2015/16 (gray shading indicates ±2σ range, w.r.t. 1981–2010). (c),(d) Scatter plot of (c) winter temperature (°C) and spring precipitation (mm month⁻¹), and (d) winter and spring fraction of FAPAR. Ellipse denotes quantile of 95% in multivariate normal distribution (Santos-Fernández 2012). (e),(f) Map of relative anomaly in FAPAR in (e) winter and (f) spring 2015/16 w.r.t. 2001–16 (black dot indicates study site Majadas del Tietar; rectangle denotes model domain).

winter, moisture stress carried over from previous seasons, fires, pests, or legacy effects thereof.

In this paper, we: 1) analyze the extreme ecosystem productivity anomaly of WS15/16 at the regional scale

and with site-level measurements, including a process interpretation, and 2) assess, based on an ensemble of process-oriented ecosystem model simulations, how the odds of extremely positive vegetation productivity events [measured in gross primary productivity (GPP) and net ecosystem productivity (NEP)] in winter and spring are changing in response to climate change.

Winter 2015/16 and spring 2016: Meteorological drivers and extreme ecosystem impacts. REGIONAL-SCALE ANALYSIS OF VEGETATION PRODUCTIVITY. Strong and persistent anticyclonic conditions prevailed from November to mid-January over the Mediterranean basin, leading to the advection of very mild air into the IP and, in fact, into large parts of western Europe. For example, December 2015 was among the warmest months ever recorded in a range of European countries, such as Spain (2nd; Fig. 16.1a; www.aemet.es /documentos/es/serviciosclimaticos/vigilancia _clima/resumenes_climat/mensuales/2015/res _mens_clim_2015_12.pdf), France (1st; http://actualite .lachainemeteo.com/actualite-meteo/2015-12-26 -06h09/decembre-2015---historiquement-chaud-et -sec-29466.php), and Germany (1st; www.dwd.de /DE/presse/pressemitteilungen/DE/2015/20151230 _deutschlandwetter_dezember_news.html), among others; and combined December and January temperatures exceeded the previous IP area-average record value by 0.72°C in the EOBS—dataset (Haylock et al. 2008). In late winter, however, the synoptic situation changed with temperatures returning to near normal, and abundant above-average precipitation over the IP continuing from January through May (Fig. 16.1c). Hence, high winter temperatures were followed by high late winter and spring precipitation, exceeding a bivariate 95th percentile (Fig. 16.1c; see online supplement for details).

Continuously high temperatures during winter enable better functioning of plant enzymes used in the photosynthetic machinery (Sage and Kubien 2007) and prevent plants from damage through cold stress. The availability of water during spring prevents soils from drying out and the plants from experiencing drought stress. The 2015/16 meteorological conditions thus provided the basis for the highest area averaged IP fraction of absorbed photosynthetically active radiation (FAPAR, a proxy for ecosystem productivity observed from space that is related to the state and greenness of vegetation canopies; Gobron et al. 2010) in both winter and spring (Fig. 16.1d), using the Tip–FAPAR dataset (Pinty et al. 2011) in the MODIS era (2001–16); and positive FAPAR anomalies

prevailed in both seasons across most of the IP except its southeastern parts (Figs. 16.1e,f).

A correlation analysis of concurrent and lagged meteorological variables and FAPAR at the seasonal time scale shows that IP FAPAR (as a regional-scale ecosystem productivity proxy) is mainly temperature-limited in winter, which gradually transcends toward water limitation in spring (Table ES16.1). While we focus only on the individual 2015/16 event, in fact out of the four years (i.e., 25% of the 16-year FAPAR record) that showed the highest December–May IP FAPAR, all four years were among the warmest 30% of IP winters in the EOBS—dataset, and three out of four among the wettest 30% of IP springs (and all four within the wettest 35% of springs on record). Nonetheless, FAPAR in IP ecosystems is also sensitive to precipitation in the previous season both in winter and spring (Table ES16.1), which highlights the role of lagged effects. Hence, the dependence on contemporaneous meteorological conditions should not be mistaken as the sole driver of positive ecosystem productivity events.

SITE-SCALE ANALYSIS OF VEGETATION PRODUCTIVITY. In Spain, 2.16 million hectares of the vegetation used for livestock production consists of a mosaic of at least 20% oak woodlands plus grass- and shrublands, so-called dehesas. Over a quarter of this vegetation type is located in Extremadura (Campos et al. 2013) in which the study site, Majadas del Tietar (39.9415°N, −5.7734°E), is located (Casals et al. 2009).

The site was established in 2003 with meteorological measurements and eddy covariance flux measurements of energy, water vapor, and carbon dioxide, thus a 13-year record is available for analysis.

At site-level, the meteorological variables largely mirrored the regional-scale patterns, that is high temperatures in winter (2.5°C above site average in winter) and wet conditions in spring [57 mm (~25%) above site average precipitation in spring]. During the warm winter and wet spring, GPP exceeded the respective seasonal averages by 29 grams of carbon (gC) m^{-2} month^{-1} (~45%) and 43 gC m^{-2} month^{-1} (~30%). In addition, ecosystem respiration (Reco, the release of carbon by the ecosystem), is coupled to temperature and also increased during the warm winter by 29 gC m^{-2} month^{-1} (70%) as compared to the average winter. The absence of water stress during the wet spring 2016 also led to increased Reco by 40 gC m^{-2} month^{-1} (42%; Fig. ES16.1). Therefore, despite the fact that ecosystem productivity was high in WS15/16 as measured by FAPAR (Figs. 16.1e,f;
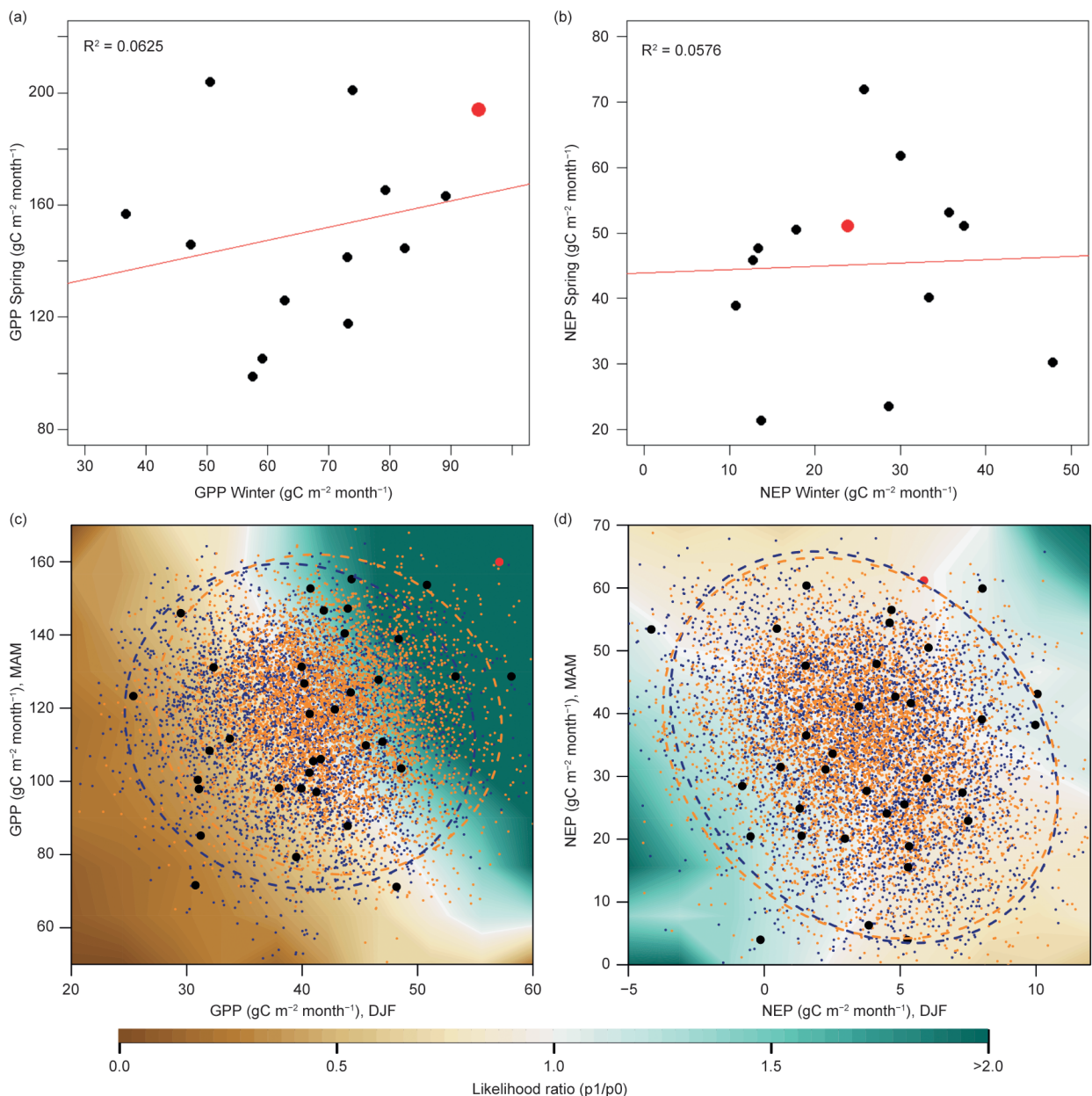
Fɪɢ. 16.2. (a) GPP and (b) NEP in winter and spring 2015/16 at Majadas del Tietar w.r.t. earlier years. (c),(d) Area-averaged ensemble ecosystem model simulations over the IP for (c) GPP and (d) NEP for earlier (1986–95, blue dots) and more recent (2001–10, orange dots) period; ellipses indicate bivariate 95% quantile. Black dots indicate LPJmL simulations driven by ERA-Interim for 1979–2015 (means adjusted); red dot is 2016. Background colors illustrate relative changes in event occurrence probabilities between earlier and more recent period (i.e., PR = p_{recent}/p_{early}) derived from multivariate normal distribution fitted to both model simulation periods individually. Units for GPP and NEP are gC m^{-2} month^{-1}.

Pearson correlation between FAPAR and GPP$_{site}$, R$_{Dec-May}$ = 0.84), the simultaneous increase of GPP and Reco meant that NEP (the net sequestration of carbon) was not unusually high (Fig. 16.2b). This means, that an increase in ecosystem productivity does not necessarily lead to the ecosystem functioning as a larger carbon sink.

How do climatic changes affect regional-scale ecosystem productivity extremes? We provide an estimate of changes in the likelihood of ecosystem productivity extremes such as in 2015/16 based on a process-oriented ecosystem model over the time period of 1986–2010. To do so, we evaluate an ensemble of process-oriented ecosystem model simulations over

the IP (500 members in each year in 1986–2010), using the Lund–Potsdam–Jena managed Land (LPJmL) ecosystem model (Bondeau et al. 2007; Sitch et al. 2003). The simulations are driven by (i) a bias corrected regional climate model ensemble (Massey et al. 2015), and (ii) ERA-Interim reanalysis data (Dee et al. 2011) as a transient simulation reflecting observed meteorology (Pearson correlation between FAPAR and $GPP_{LPJmL–ERAI}$, $R_{Dec–May} = 0.83$). Further, the ecosystem model is run in two setups, that is, in standard mode with transient (i.e., observed) CO_2 concentrations, and a second setup with CO_2 values held constant at 1986 values ($CONSTCO_2$) in order to isolate direct CO_2 effects on ecosystem functioning. The climate model is driven by observed sea surface temperatures in the *weather@home* setup (Massey et al. 2015). A detailed methodological description of the HadRM3P–LPJmL ensemble approach is available in Sippel et al. (2017) and is summarized in the online supplement.

Overall, the ecosystem model simulations driven by ERA-Interim indicate that 2015/16 had been an extreme event in regional-scale GPP consistent with site-scale measurements (Fig. 16.2c), and to a lesser degree in NEP (Fig. 16.2d), which differs from site observations that do not indicate anomalous conditions. Contrasting the bivariate distribution of an earlier (1986–95) and a more recent period (2001–10) reveals that the odds for high winter GPP associated with high spring GPP have indeed increased, and the model indicates that the odds for an event similar to 2015/16 have more than doubled (Fig. 16.2c). These changes can be attributed to higher winter temperatures, consistent with anthropogenic climate change, in combination with CO_2 fertilization effects in the ecosystem model. Long-term meteorological observations show a strong trend in winter temperatures over the IP (Fig. ES16.2), which is reproduced by the climate model that drives the ecosystem model (both for the 2001–10 vs. 1986–95 decade, but also if the 2001–10 decade is compared to a hypothetical preindustrial 2001–10 ensemble; see Fig. ES16.2 and online supplement text for details). In contrast, there is no significant trend in IP spring precipitation neither in observations nor in the climate model (Fig. ES16.2). Thus increased odds for high spring GPP events that follow high winter GPP events (Fig. 16.2c) cannot be attributed to changes in spring precipitation. Instead, the increased odds in high spring GPP events arise from direct CO_2 effects in the ecosystem model, because these changes disappear in the $CONSTCO_2$ scenario (cf. Fig. ES16.3 and Fig. 16.2c). However,

crucially, the ecosystem model ensemble simulations also indicate that net ecosystem carbon sequestration, that is after ecosystem respiration is accounted for, has not increased (Fig. 16.2d). This might be due to the fact that higher temperatures are associated with increased Reco (as consistently observed at site scale in Majadas in 2015/16).

Conclusion. Our study shows that the 2015/16 positive GPP anomaly on the Iberian Peninsula, which was enabled by a compound warm winter and wet spring event, is indeed consistent with recent observed climate change, as diagnosed in site and regional scale observations and model simulations. While the increase in winter GPP can be attributed to increasing temperatures, the increase in spring GPP cannot be attributed to changes in spring precipitation, but these changes result from increased CO_2 fertilization. However, these warming and CO_2-induced effects are largely canceled in terms of net ecosystem carbon sequestration in 2015/16, as carbon uptake and release intensified in tandem, which is consistent with expectations in a changing climate as indicated by the ecosystem model ensemble. This study presents and discusses a novel inquiry into the attribution of ecosystem impacts to extreme climate events and the underlying drivers. However, because it uses only one combination of climate–ecosystem models, and a relatively short observational record, its conclusions should be regarded as contingent on these limitations.

REFERENCES

Arnone, J. A., and Coauthors, 2008: Prolonged suppression of ecosystem carbon dioxide uptake after an anomalously warm year. *Nature*, **455,** 383–386, doi:10.1038/nature07296.

Bondeau, A., and Coauthors, 2007: Modelling the role of agriculture for the 20th century global terrestrial carbon balance. *Global Change Biol.*, **13**, 679–706, doi: 10.1111/j.1365-2486.2006.01305.x.

Campos, P., L. Huntsinger, J. L. Oviedo, P. F. Starrs, M. Díaz, R. B. Standiford, and G. Montero, Eds., 2013: *Mediterranean Oak Woodland Working Landscapes.* Landscape Series, Vol. 16, Springer, 508 pp.

Casals, P., C. Gimeno, A. Carrara, L. Lopez-Sangil, and M. J. Sanz, 2009: Soil CO_2 efflux and extractable organic carbon fractions under simulated precipitation events in a Mediterranean Dehesa. *Soil Biol. Biochem.*, **41**, 1915–1922, doi:10.1016/j.soilbio.2009.06.015.

Dee, D. P., and Coauthors, 2011: The ERA-Interim reanalysis: configuration and performance of the data assimilation system. *Quart. J. Roy. Meteor. Soc.*, **137,** 553–597, doi:10.1002/qj.828.

Field, C. B., and Coauthors, Eds., 2012: *Managing the Risks of Extreme Events and Disasters to Advance Climate Change Adaptation.* Cambridge University Press, 582 pp. [Available online at www.ipcc-wg2.gov/SREX/images/uploads/SREX-All_FINAL.pdf.]

Frank, D. A., and Coauthors, 2015: Effects of climate extremes on the terrestrial carbon cycle: Concepts, processes and potential future impacts. *Global Change Biol.*, **21**, 2861–2880, doi:10.1111/gcb.12916.

Gobron, N., A. Belward, B. Pinty, and W. Knorr, 2010: Monitoring biosphere vegetation 1998–2009. *Geophys. Res. Lett.*, **37**, L15402, doi:10.1029/2010GL043870.

Haylock, M. R., N. Hofstra, A. M. G. K. Tank, E. J. Klok, P. D. Jones, and M. New, 2008: A European daily high-resolution gridded data set of surface temperature and precipitation for 1950–2006. *J. Geophys. Res.*, **113**, D20119, doi:10.1029/2008JD010201.

Leonard, M., and Coauthors, 2014: A compound event framework for understanding extreme impacts. *Wiley Interdiscip. Rev.: Climate Change*, **5**, 113–128, doi:10.1002/wcc.252.

Massey, N., and Coauthors, 2015: weather@ home—development and validation of a very large ensemble modelling system for probabilistic event attribution. *Quart. J. Roy. Meteor. Soc.*, **141**, 1528–1545, doi:10.1002/qj.2455.

Parmesan, C., and G. Yohe, 2003: A globally coherent fingerprint of climate change impacts across natural systems. *Nature*, **421**, 37–42, doi:10.1038/nature01286.

Pinty, B., and Coauthors, 2011: Exploiting the MODIS albedos with the Two-stream Inversion Package (JRC-TIP): 2. Fractions of transmitted and absorbed fluxes in the vegetation and soil layers. *J. Geophys. Res.*, **116**, D09106, doi:10.1029/2010JD015373.

Reichstein, M., and Coauthors, 2013: Climate extremes and the carbon cycle. *Nature*, **500**, 287–295, doi:10.1038/nature12350.

Sage, R. F., and D. S. Kubien, 2007: The temperature response of C_3 and C_4 photosynthesis. *Plant, Cell Environ.*, **30,** 1086–1106, doi:10.1111/j.1365-3040.2007.01682.x.

Santos-Fernández, E., 2012: *Multivariate Statistical Quality Control Using R.* SpringerBriefs in Statistics, Vol. 14, Springer, 127 pp.

Seneviratne, S. I., and Coauthors, 2012: Changes in climate extremes and their impacts on the natural physical environment. *Managing the Risks of Extreme Events and Disasters to Advance Climate Change Adaptation,* C. B. Field et al., Eds., Cambridge Univeristy Press, 109–230.

Sippel, S., and Coauthors, 2017: Contrasting and interacting changes in simulated spring and summer carbon cycle extremes in European ecosystems. *Environ. Res. Lett.*, **12**, 075006, doi:10.1088/1748-9326/aa7398.

Sitch, S., and Coauthors, 2003: Evaluation of ecosystem dynamics, plant geography and terrestrial carbon cycling in the LPJ dynamic global vegetation model. *Global Change Biol.*, **9**, 161–185.

Teuling, A. J., and Coauthors, 2010: Contrasting response of European forest and grassland energy exchange to heatwaves. *Nat. Geosci.*, **3**, 722–727, doi:10.1038/ngeo950.

Walther, G. R., and Coauthors, 2002: Ecological responses to recent climate change. *Nature*, **416**, 389–395, doi:10.1038/416389a.

Wolf, S., and Coauthors, 2016: Warm spring reduced carbon cycle impact of the 2012 US summer drought. *Proc. Natl. Acad. Sci. USA*, **113**, 5880–5885, doi:10.1073/pnas.1519620113.

17. ANTHROPOGENIC INTENSIFICATION OF SOUTHERN AFRICAN FLASH DROUGHTS AS EXEMPLIFIED BY THE 2015/16 SEASON

Xing Yuan, Linying Wang, and Eric F. Wood

Flash drought over southern Africa was tripled during the last 60 years mainly due to anthropogenic climate change, and it was intensified during 2015/16 in the midst of heat waves.

Introduction. Droughts are mainly driven by natural climate variability. They usually evolve slowly and persist for a few months to decades. Anthropogenic climate change, however, not only increases the likelihood of local and regional droughts, but also alters their characteristics (Sheffield and Wood 2008; Dai 2013; Trenberth et al. 2014). For instance, the soil moisture drought during growing seasons is often accompanied by heat waves, resulting in a type of drought that has a rapid onset and short duration (from a few days to 1–2 months), but high intensity and devastating impacts, which is recently termed "flash drought" (Hoerling et al. 2014; Mo and Lettenmaier 2015; Yuan et al. 2015; Wang et al. 2016). During November–April of 2015/16, most parts of southern Africa (SA; 10°–40°E, 10°–35°S) experienced a rainy season–long drought. Within the seasonal drought, heat waves occurred suddenly, which caused a severe flash drought characterized by soil moisture deficit and heat waves at the beginning of December. The flash drought was then terminated by a rainfall event in early January. The South African Weather Service announced that 32 daily temperature records were broken in South Africa with the highest reaching 45°C. Millions of people were affected by famine, disease, and water shortages. The SA drought is basically associated with the 2015/16 strong El Niño (Nicholson and Entekhabi 1986; Reason and Jagadheesha 2005; Yuan et al. 2013; Ratnam et al. 2014; Hoell et al. 2015)

and possibly altered by Indian Ocean sea surface temperature variability (Reason 2001; Washington and Preston 2006; Manatsa et al. 2011; Hoell et al. 2016), but the warming climate may also play an important role. This study will investigate the 2015/16 SA flash drought in the context of a changing climate during 1948–2016, and detect the anthropogenic influences.

Data and methods. Daily precipitation and surface air temperature hybrid reanalysis–observational datasets at 0.25° resolution during 1948–2008 were obtained from Princeton's African drought monitoring and forecasting system (PADMF; Sheffield et al. 2014; Yuan et al. 2013). They were extended to 2016 by using NOAA's Climate Prediction Center (CPC) global 0.5° analysis of daily gauge measurements of precipitation (Chen et al. 2008) and ERA-Interim reanalysis of surface air temperature (Dee et al. 2011). Both CPC precipitation and ERA-Interim temperature were interpolated into 0.25° and were adjusted to match the climatology of the PADMF forcing data. The 500-hPa geopotential height data was also obtained from ERA-Interim reanalysis.

The Variable Infiltration Capacity (VIC; Liang et al. 1996) land surface hydrological model, which was calibrated against streamflow observations from over 800 Global Runoff Data Centre gauges before being implemented in the PADMF system (Yuan et al. 2013), was used in this study to estimate soil moisture. Driven by the meteorological forcings mentioned above, the VIC model was run from 1948 to 2016 over SA with default initial conditions, and the model states at the end of the run were used as initial conditions on 1 January 1948 for another 69-year simulation. Soil moisture from the second round simulation was used for the flash drought analysis.

Daily surface air temperature and soil moisture were aggregated into pentad-mean values for each 0.25° grid cells over SA during the growing seasons

(October–March). For each grid and each pentad, a flash drought is defined as pentad-mean surface air temperature anomaly is larger than one standard deviation, the percentile of target pentad-mean soil moisture is lower than 40%, and the soil moisture percentile of target pentad is at least 10% lower than the preceding pentad. A common view of droughts is a condition of land surface soil moisture deficits that accumulates gradually, while the third criterion of flash drought guarantees a remarkable swiftness. If two or more consecutive flash drought pentads happen one after another, they will be treated as a single drought event. The selection of the thresholds will be discussed below.

Daily precipitation and surface air temperature simulations from 13 atmosphere–ocean coupled general circulation models (CGCMs; see Table ES17.1 for the model list) provided by the Coupled Model Intercomparison Project Phase 5 (CMIP5; Taylor et al. 2012) were used in this study. Actually simulations of 30 CMIP5 models that combined anthropogenic and natural forcings (ALL) were used to drive the VIC land surface hydrological models, and 13 of them were selected according to their performance for flash drought changes, as well as data availability for the simulations that only considered natural forcing (NAT) or be controlled to preindustrial situations (CTL). CMIP5 simulated daily surface air temperature and CMIP5/VIC simulated daily soil moisture were used to identify flash drought events with or without anthropogenic forcings. In this study, CMIP5 NAT experiments covered the period 1950–2012, and CMIP5 ALL experiments were extended to 2016 by using model simulations under the representative concentration pathways (RCP) 4.5 emission scenario during 2006–16, which is a common way to extend the ALL experiments (Sun et al. 2014). The optimal fingerprint method (Allen and Stott 2003) was used to detect the anthropogenic influence on the change in flash drought over SA. In this study, the regression was conducted over 1961–2012 for two-signal ALL-NAT (ANT) and NAT analysis on non-overlapping 3-year averages of SA areal mean flash drought events by using the total least squares method.

Results. Figure 17.1a shows that extremely high regional mean temperature anomaly (2.85 standard deviations higher than the climatological mean) occurred during December 2015–January 2016, which was ranked as the highest since 1948. Meanwhile, there was also a severe rainfall deficit (one standard deviation lower than the climatology), although not the most severe in

the history. Based on Mann–Kendall nonparametric trend analysis, it is found that both the decreasing trend in precipitation (−28.6 mm decade^{-1}) and increasing trend in temperature (+0.062°C decade^{-1}) are significant during 1948–2016, with statistical significances of $p < 0.05$ and $p < 0.01$, respectively. At the end of November 2015, there were deficits in the precipitation and soil moisture, but temperature was normal (Fig. 17.1b). However, the extremely high temperature anomaly (higher than one standard deviation) occurred at the beginning of December 2015 and lasted until the second pentad of January 2016, with precipitation lower than climatology by more than half standard deviation, and soil moisture percentile lower than 5% for a large area of SA (Figs. 17.1c–e). From the third pentad of January 2016, the rainfall events terminated the heat wave and alleviate the soil dryness to some extent (Fig. 17.1f).

It is possible that the dry soil triggered the heat waves (Mueller and Seneviratne 2012) and sustained them for the flash drought with such a long duration. Moreover, recent study found that the variability in Botswana High has a close relationship with rainfall and temperature anomalies over SA (Driver and Reason 2017). Figure 17.1a shows that the 500 hPa geopotential height averaged over the region has a positive correlation with temperature ($r = 0.71$) and a negative correlation with precipitation ($r = −0.38$), both are statistically significant. During 2015/16 austral summer, the height is almost 3 standard deviations higher than normal (Fig. 17.1a), which is also responsible for the drought and heat conditions.

Figure ES17.1a shows that the eastern part of SA (which is more humid) has a higher chance to experience flash drought than the western part. Other thresholds for the soil moisture percentile (e.g., 30%, 50%) and declining rate (e.g., 5% decline between two pentads) were tested, and similar spatial patterns were obtained with different magnitudes (Figs. ES17.1b,c). On average, flash drought events over SA increased by 220% from 1961 to 2016, with a significance level of $p < 0.01$ (black lines in Fig. 17.2a). The CMIP5/VIC ensemble simulations driven by all forcings (ALL) successfully captured this upward trend with $p < 0.01$ (red lines in Fig. 17.2a), but those with natural only forcing (NAT) had a very small upward trend (blue lines in Fig. 17.2a). This suggests that anthropogenic climate change is mainly responsible for the increasing flash drought over SA. The simulations of surface air temperature change are more reliable than those for soil moisture and precipitation (Figs. 17.2b,c), indicating the major source of uncertainty in detecting
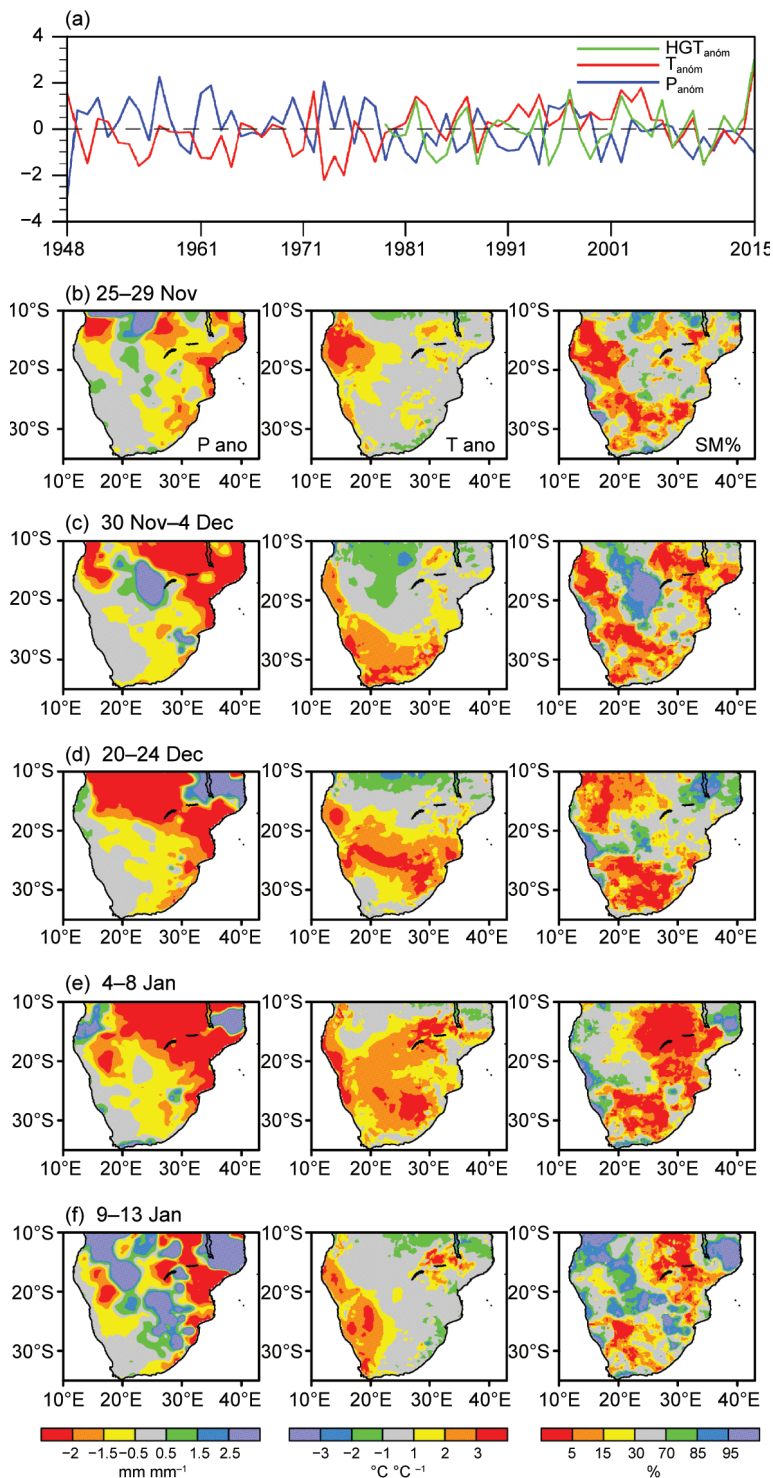
FIG. 17.1. (a) Interannual variations of standardized Dec–Jan mean precipitation (blue), temperature (red) and 500-hPa geopotential height (green) anomalies averaged over southern Africa (10°–40°E, 10°–35°S) during 1948–2016. (b)–(f) Flash drought snapshots of standardized pentad-mean precipitation (left; mm mm^{-1}) and surface air temperature (middle; °C °C^{-1}) anomalies and soil moisture percentiles (right; %) during Dec–Jan 2015/16. Precipitation and temperature anomalies were divided by std. dev. of the 1961–2012 climatology.

and attributing flash drought change is the soil moisture variation.

The best estimates of scaling factors show that both the anthropogenic and natural signals are detectable with p < 0.01 (Fig. 17.2e). As the NAT simulations do not have discernible upward trend in flash drought (Fig. 17.2a), the observed increasing flash drought over SA is mainly attributable to anthropogenic forcing (Fig. 17.2e). Therefore, although the recent strong El Niño as well as the high pressure anomaly have caused the 2015/16 drought conditions over SA, the warming climate may quite likely be responsible for the increasing likelihood of such severe flash drought.

Conclusions. A flash drought characterized by severe heat waves and soil moisture deficit hit southern Africa (SA) during December–January 2015/16, which raises the attention of flash drought risk over semihumid and semiarid regions. Similar to other parts of the world (Mazdiyasni and AghaKouchak 2015; Wang et al. 2016), there is a substantial increase in concurrent droughts and heatwaves in SA, with flash drought increased by 220% from 1961 to 2016. Although both the anthropogenic and natural signals are detectable in attributing the flash drought changes, the anthropogenic influence is mainly responsible for the increasing flash drought over SA. In the midst of heat waves, the risk of flash drought over SA is very likely to increase in the future.
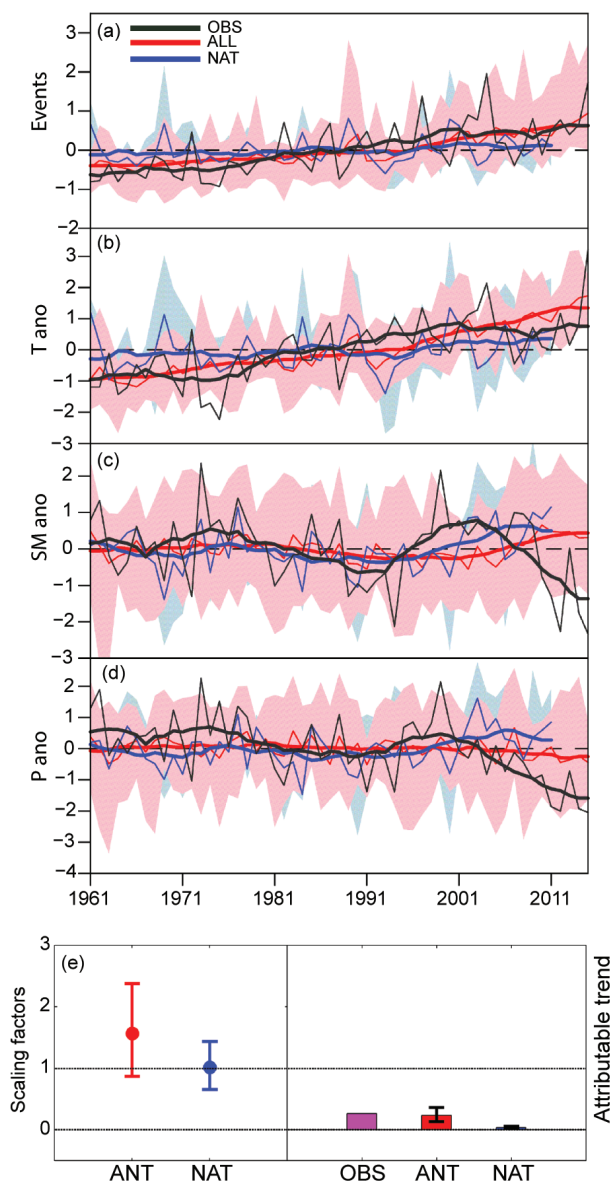
Fig. 17.2. Observed and simulated anomalies of (a) flash drought events (Events), (b) surface air temperature (T), (c) soil moisture (SM), and (d) precipitation (P) averaged over SA. Results from each CMIP5/VIC simulation were first standardized before constructing the ensemble mean ALL (red lines) and NAT (blue lines). The offline VIC simulations (black lines) were also standardized. (a)–(d) The thick lines are 10-year running means, and the pink and cyan shading display the ranges of ALL and NAT simulations respectively. (e) Best estimates of the scaling factors (left axis) and attributable increasing trend (right axis) from two-signal (ANT = ALL-NAT and NAT) analyses of SA flash drought for the period of 1961–2012. Error bars indicate their corresponding 5%–95% uncertainty ranges estimated via Monte Carlo simulations.

the Public Interest (GYHY201506001), CAS Key Research Program of Frontier Sciences (QYZDY-SSW-DQC012), and Thousand Talents Program for Distinguished Young Scholars.

REFERENCES

Allen, M. R., and P. A. Stott, 2003: Estimating signal amplitudes in optimal fingerprinting. Part I: Theory. *Climate Dyn.*, **21**, 477–491, doi:10.1007/s00382-003-0313-9.

Chen, M., W. Shi, P. Xie, V. B. S. Silva, V. E. Kousky, R. W. Higgins, and J. E. Janowiak, 2008: Assessing objective techniques for gauge-based analyses of global daily precipitation. *J. Geophys. Res.*, **113**, D04110, doi:10.1029/2007JD009132.

Dai, A., 2013: Increasing drought under global warming in observations and models. *Nat. Climate Change*, **3**, 52–58, doi:10.1038/nclimate1633.

Dee, D. P., and Coauthors, 2011: The ERA-Interim reanalysis: Configuration and performance of the data assimilation system. *Quart. J. Roy. Meteor. Soc.*, **137**, 553–597, doi:10.1002/qj.828.

Driver, P., and C. J. C. Reason, 2017: Variability in the Botswana High and its relationship with rainfall and temperature characteristics over southern Africa. *Int. J. Climatol.*, **37**, 570–581, doi:10.1002/joc.5022.

Hoell, A., C. Funk, T. Magadzire, J. Zinke, and G. Husak, 2015: El Niño–Southern Oscillation diversity and Southern Africa teleconnections during Austral Summer. *Climate Dyn.*, **45**, 1583–1599, doi:10.1007/s00382-014-2414-z.

——, ——, J. Zinke, and L. Harrison, 2016: Modulation of the Southern Africa precipitation response to the El Niño Southern Oscillation by the subtropical Indian Ocean Dipole. *Climate Dyn.*, **48**, 2529–2540, doi:10.1007/s00382-016-3220-6.

Hoerling, M. P., J. Eischeid, A. Kumar, R. Leung, A. Mariotti, K. Mo, S. Schubert, and R. Seager, 2014: Causes and predictability of the 2012 Great Plains drought. *Bull. Amer. Meteor. Soc.*, **95**, 269–282, doi:10.1175/BAMS-D-13-00055.1.

Liang, X., E. F. Wood, and D. P. Lettenmaier, 1996: Surface soil moisture parameterization of the VIC-2L model: Evaluation and modifications. *Global Planet. Change*, **13**, 195–206, doi:10.1016/0921-8181(95)00046-1.

Manatsa, D., C. H. Matarira, and G. Mukwada, 2011: Relative impacts of ENSO and Indian Ocean dipole/zonal mode on east SADC rainfall. *Int. J. Climatol.*, **31**, 558–577, doi:10.1002/joc.2086.

Mazdiyasni, O., and A. AghaKouchak, 2015: Substantial increase in concurrent droughts and heatwaves in the United States. *Proc. Natl. Acad. Sci. USA*, **112**, 11 484–11 489, doi:10.1073/pnas.1422945112.

Mo, K. C., and D. P. Lettenmaier, 2015: Heat wave flash droughts in decline. *Geophys. Res. Lett.*, **42**, 2823–2829, doi:10.1002/2015GL064018.

Mueller, B., and S. I. Seneviratne, 2012: Hot days induced by precipitation deficits at the global scale. *Proc. Natl. Acad. Sci. USA*, **109**, 12 398–12 403, doi:10.1073/pnas.1204330109.

Nicholson, S., and D. Entekhabi, 1986: The quasi-periodic behavior of rainfall variability in Africa and its relationship to the southern oscillation. *Arch. Meteor. Geophys. Bioclimatol. A.*, **34**, 311–348, doi:10.1007/BF02257765.

Ratnam, J. V., S. K. Behera, Y. Masumoto, and T. Yamagata, 2014: Remote effects of El Niño and Modoki events on the austral summer precipitation of southern Africa. *J. Climate*, **27**, 3802–3815, doi:10.1175/JCLI-D-13-00431.1.

Reason, C. J. C., 2001: Subtropical Indian Ocean SST dipole events and southern African rainfall. *Geophys. Res. Lett.*, **28**, 2225–2227, doi:10.1029/2000GL012735.

——, and D. Jagadheesha, 2005: A model investigation of recent ENSO impacts over southern Africa. *Meteor. Atmos. Phys.*, **89**, 181–205, doi:10.1007/s00703-005-0128-9.

Sheffield, J., and E. F. Wood, 2008: Projected changes in drought occurrence under future global warming from multi-model, multi-scenario, IPCC AR4 simulations. *Climate Dyn.*, **31**, 79–105, doi:10.1007/s00382-007-0340-z.

——, and Coauthors, 2014: A drought monitoring and forecasting system for sub-Sahara African water resources and food security. *Bull. Amer. Meteor. Soc.*, **95**, 861–882, doi:10.1175/BAMS-D-12-00124.1.

Sun, Y., X. Zhang, F. W. Zwiers, L. Song, H. Wan, T. Hu, H. Yin, and G. Ren, 2014: Rapid increase in the risk of extreme summer heat in Eastern China. *Nat. Climate Change*, **4**, 1082–1085, doi:10.1038/nclimate2410.

Taylor, K. E., R. J. Stouffer, and G. A. Meehl, 2012: An overview of CMIP5 and the experiment design. *Bull. Amer. Meteor. Soc.*, **93**, 485–498, doi:10.1175/BAMS-D-11-00094.1.

Trenberth, K. E., A. Dai, G. van der Schreier, P. D. Jones, J. Barichivich, K. R. Briffa, and J. Sheffield, 2014: Global warming and changes in drought. *Nat. Climate Change*, **4**, 17–22, doi:10.1038/nclimate2067.

Wang, L., X. Yuan, Z. Xie, P. Wu, and Y. Li, 2016: Increasing flash droughts over China during the recent global warming hiatus. *Sci. Rep.*, **6**, 30571, doi:10.1038/srep30571.

Washington, R., and A. Preston, 2006: Extreme wet years over southern Africa: Role of Indian Ocean sea surface temperatures. *J. Geophys. Res.*, **111**, D15104, doi:10.1029/2005JD006724.

Yuan, X., E. F. Wood, N. W. Chaney, J. Sheffield, J. Kam, M. Liang, and K. Guan, 2013: Probabilistic seasonal forecasting of African drought by dynamical models. *J. Hydrometeor.*, **14**, 1706–1720, doi:10.1175/JHM-D-13-054.1.

——, Z. Ma, M. Pan, and C. Shi, 2015: Microwave remote sensing of short-term droughts during crop growing seasons. *Geophys. Res. Lett.*, **42**, 4394–4401, doi:10.1002/2015GL064125.

18. ANTHROPOGENIC ENHANCEMENT OF MODERATE-TO-STRONG EL NIÑO EVENTS LIKELY CONTRIBUTED TO DROUGHT AND POOR HARVESTS IN SOUTHERN AFRICA DURING 2016

Chris Funk, Frank Davenport, Laura Harrison, Tamuka Magadzire, Gideon Galu, Guleid A. Artan, Shraddhanand Shukla, Diriba Korecha, Matayo Indeje, Catherine Pomposi, Denis Macharia, Gregory Husak, and Faka Dieudonne Nsadisa

A 40-member CESM LE ensemble indicates that climate change likely increased the intensity of the 2015/16 El Niño, contributing to further decreases in SA precipitation, crop production and food availability.

Introduction. In December–February (DJF) of 2015/16, a strong El Niño (Niño-3.4 SST >29°C) contributed to a severe drought over southern Africa (SA; Funk et al. 2016). A 9-million ton cereal deficit resulted in 26 million people in need of humanitarian assistance (SADC 2016). While SA rainfall has a well-documented negative teleconnection with Niño-3.4 SSTs (Hoell et al. 2015, 2017; Jury et al. 1994; Lindesay 1988; Misra 2003; Nicholson and Entekhabi 1987; Nicholson and Kim 1997; Reason et al. 2000; Rocha and Simmonds 1997), the link between climate change and El Niño remains unclear (Christensen et al. 2013) due to the large natural variability of ENSO SSTs (Wittenberg 2009), uncertainties surrounding measurements and trends (Solomon and Newman 2012), intermodel differences in ENSO representation and feedbacks (Guilyardi et al. 2012; Kim et al. 2014), and difficulties associated with quantifying ENSO strength (Cai et al. 2015).

Figure 18.1a highlights observational uncertainties (Compo and Sardeshmukh 2010; Solomon and Newman 2012) using four datasets: ERSSTv4 (Huang et al. 2015), HadISST (Rayner et al. 2003), Kaplan SST (Kaplan et al. 1998), and Hurrell (Hurrell et al. 2008). These products differ substantially in their representation of cool events and Niño-3.4 variance. Two SST products indicate significant upward trends; two SST products do not. These data have been standardized to remove systematic differences in variance.

Focusing just on the behavior of moderate–strong El Niño events (MSENEs), we can produce more robust (first order) statistics by comparing the means of the top ten warmest Niño-3.4 events between 1921–80 and the top six warmest events between 1981–2016. Rather than using a set SST threshold, MSENEs are defined as 1-in-6-year warm events. This provides a simple nonparametric approach that takes advantage of the well understood quasi-periodic nature of ENSO to identify MSENEs across multiple models and simulations. Modest changes in the number of events (say, 1-in-7 or 1-in-5) produced modest increases and decreases in El Niño temperatures, but did not substantially change the results.

We begin our analysis in 1921 (because ship data before 1921 is limited), and divide the remaining 96 years into two time periods with relatively weak and strong radiative forcing, respectively. Examining changes in MSENE means (horizontal lines in Fig. 18.1a), we find that all the observational datasets identify significant increases (Fig. ES18.1 examines ERSSTv4 errors). Note that we are not explicitly examining changes in ENSO variance, ENSO means, or Niño-3.4 SST trends, but only Niño-3.4 magnitudes
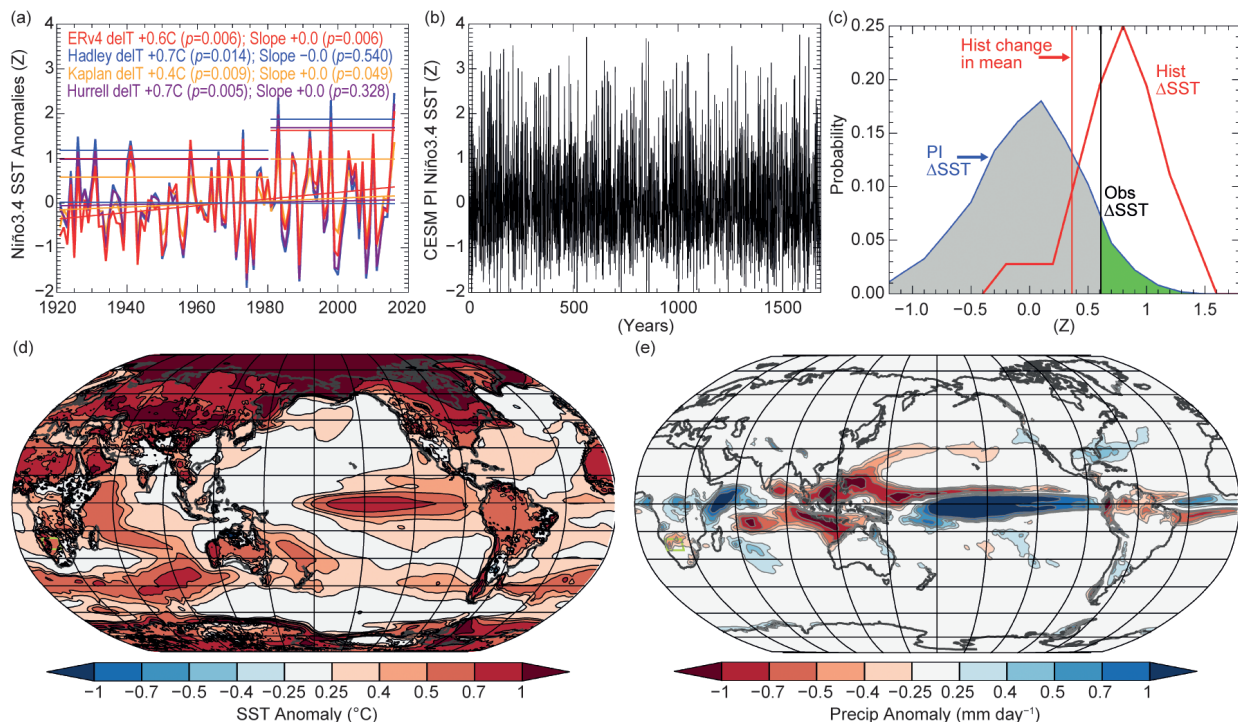
Fig. 18.1. (a) Observed NINO3.4 SST (Z) from four sources, trend lines, and changes in 1-in-6-year maximum Niño-3.4 seasons. **(b)** 1700 years of DJF Niño-3.4 SSTs (Z) from the CESM1 PI simulation. **(c)** PI and Historic distributions of changes in 1-in-6-year maximum NINO3.4 SST. Gray/green shading denotes likelihood given PI conditions. **(d),(e)** Composites of CESM Historic simulation SST (°C) and precipitation (mm day⁻¹), respectively, for the top 1-in-6 1981–2016 NINO3.4 SST seasons and the top 1921–80 seasons. These are based on the mean of 6 × 40 events and 10 × 40 events.

during MSENEs. We will use a 40-member ensemble of simulations from the CESM1 Large Ensemble (LE) project (Kay et al. 2015) to contrast SA rainfall during MSENEs based on historic simulations forced with greenhouse gasses and aerosols with simulated precipitation under preindustrial (PI) conditions.

ENSO exhibits large natural variations in amplitude (Wittenberg 2009). Figure 18.1b shows Niño-3.4 SST from 1700 years of CESM LE PI simulations. Even without climate change, we find Niño-3.4 SST anomalies greater than +3°Z (where Z denotes a standardized anomaly), sometimes occurring in sequence. To derive a PI sampling distribution that mimics Fig. 18.1a, we calculate 10 000 sample changes in 1-in-6-year maximum SST, based on sequential periods of 60 and 36 years, drawn from the 1700 year CESM1 PI simulation. Large changes can occur through nonanthropogenic processes (Fig. 18.1c). We use this PI distribution to assess the likelihood of the observed ~+0.61° ± 0.18°C temperature difference for MSENEs in the two composites. Such a change would be possible but *very unlikely* under PI conditions (only 7% of the PI simulations warmed this much). While

unlikely, such an event is certainly plausible in a world without climate change.

Using 40 simulations from the CESM LE experiment, we can also derive a PDF of 1981–2016 versus 1921–80 El Niño SSTs (Fig. 18.1c). An animation of these individual simulations can be found at https://tinyurl.com/Niño3-4-sims-gif. Contrasting the variance of the 1981–2016 historic versus PI Niño-3.4 CESM LE SST time series, we find a substantial (55%) increased in variance (from 1.23°C² to 1.91°C², $p = 0.0001$). Not all simulations produced an increase, and the PI and historical PDFs overlap substantially. Overall, however, we find a substantial (+0.75°C average change) and significant ($p = 0.0001$, d.f. 638) increase in MSENE Niño-3.4 SST, which appears to be only partially explained by a shift in the overall mean between 1921–80 and 1981–2016 (+0.36°C). The 95% confidence intervals of this estimated change are large 0.0 to +1.3°C. Under PI conditions, the observed +0.61°C warming would be *very unlikely* ($p = 6\%$). Based on the historical climate change PDF, warming of +0.61°C or more would be *likely*. A 53-member multimodel ensemble also shows substantial and

significant Niño-3.4 SST increases). This 53-member multimodel ensemble indicates that 1981–2016 MSENEs would be +0.58°C warmer.

These results appear consistent with recent model analyses showing an increase in the frequency of strong El Niño events with greenhouse warming (Cai et al. 2015) and 1920–2040 ENSO amplitude (Kim et al. 2014), and reconstructions of paleo-ENSO variance at centennial (Li et al. 2013; McGregor et al. 2013) and millennial (Cobb et al. 2003) time scales. Figures 18.1d, e show changes in the CESM1 historic El Niño SST and precipitation; the CESM simulations indicate substantial increases in zonal and meridional SST gradients and equatorial rainfall anomalies, both of which are features of stronger ENSO forcing (Cai et al. 2015). CAM5 simulations based on observed SSTs show similar precipitation changes (Fig. ES18.2).

SA and Niño-3.4 rainfall analysis. This section examines SA and NINO3.4 precipitation from CESM LE PI and historical precipitation simulations[1]. Figure 18.2a shows the SA and NINO3.4 precipitation PDFs associated with MSENEs. Precipitation increases in Niño-3.4 excites equivalent barotropic Rossby wave trains (Hoskins and Karoly 1981) that increase the frequency of SA drought (Hoell et al. 2015). The risk ratio for strong Niño-3.4 precipitation events (>1Z-score, or standardized anomaly) was 181%. The risk ratio is the ratio of the event probability in the real

world and 'natural' world without climate change influences (Easterling et al. 2016).

The PDFs of SA rainfall indicate substantial uncertainty, underscoring the complexity of SA rainfall, internal atmospheric variability, and the partial influence of ENSO, which describes about ~50% of the SA rainfall variance (Funk et al. 2016). Both the PI and historic ensembles have substantial spread, but the historic PDF is shifted to the left, indicating an increased chance of droughts during El Niño events. The risk ratio for droughts less than −1Z is 160%. A two-sample *t*-test indicates a very significant change (−0.6Z, $p = 0.0001$), with 95% confidence intervals of −0.4Z to −0.8Z. Given the inherent complexities in ENSO and a limited observational record to place the 2015/16 event in a broader historical context, we cannot be sure that SSTs in the Niño-3.4 region during recent MSENEs were not higher due to internal variability (noise). Still, utilizing tools like the CESM LE project, we can conclude that there is a likely shift towards higher Niño-3.4 SSTs and precipitation, and lower SA rainfall outcomes in the later MSENEs compared to earlier ones and that this is related to anthropogenic forcing. Examining the probabilities of the observed −1.7Z rainfall deficit based on the PI and historic distributions, we find that a drought of this severity would be possible but very unlikely under PI conditions (probability ~9%) and unlikely under historic conditions (probability ~20%).

Food security analysis—southern Africa. We relate changes in SA rainfall to changes in crop production. The major sources of uncertainty in this assessment

[1]We use a box for SA that is slightly to the west (19°–25°S, 15°–25°E) of the region used Funk et al. 2016, because rainfall simulations from the atmospheric component of the CESM1 (CAM5) displace the SA ENSO teleconnection slightly to the west (Fig. ES18.2).
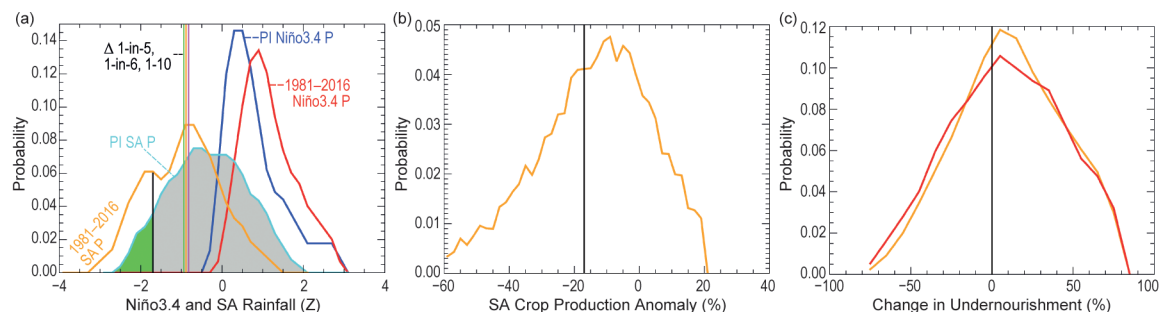

FIG. 18.2. (a) Precipitation attribution results. Standardized CESM SA and Niño-3.4 MSENE precipitation (Z) PDFs for PI and 1981–2016 Historic ensembles. Historic MSENE ensemble was based on 15% of 40 simulations for 36 years (216 El Niño events). Also shown are results based on 10% and 20%. PI ensemble used 15% of 1680 years (252 El Niño events). Green and gray shading indicates the probability of the observed −1.7Z drought occurring within the PI distribution. (b) Bootstrapped distribution of SA crop production anomalies (%), based on the PI and Historic SA precipitation distributions from (a), and the slope coefficient sampling distribution. Anomalies based on 2008–13 averages. (c) PDFs of changes in undernourishment (%) in Zimbabwe and Malawi, based on (b) and an FAO percent undernourished estimation procedure.

are 1) the uncertainty associated with SA rainfall changes, and 2) uncertainty in the relationship between SA rainfall and crop production. A regression between detrended 1981–2016 southern African[2] crop production and SA rainfall exhibited a significant but modest relationship (slope = +13.5% per 1Z, $R^2 = 0.42$), with a considerable standard error (3.7% per Z). To capture these uncertainties, we use a Monte Carlo sampling strategy based on 10 000 samples. For each sample we drew one CESM SA rainfall value out of the 240 1981–2016 El Niño samples ($R_{1981-2016}$), one rainfall outcome from the 280 PI SA El Niño rainfall values (R_{PI}), and one regression slope value (S) from a normal distribution with a mean of 13.5 and a standard deviation of 3.7. A production change value was then estimated as ($R_{1981-2016} - R_{PI}$)S. This was repeated 10 000 times. As shown in Fig. 18.2b these estimates exhibit a high degree of uncertainty. The 95% confidence intervals range from −48% to 21%, with a median impact of −11%. The observed 2016 production anomaly was −17%. Seventy-four percent of these estimates were below normal, suggesting that it was *likely* that anthropogenic SA rainfall reductions also reduced SA crop production. Repeating this analysis for 1-in-10 and 1-in-5-year El Niño events produced similar results. It should be noted that the CAM5/CESM models tend to displace the SA rainfall anomalies to the west, indicating that the models do not perfectly capture the regional climatology. Observational studies, however, have produced results consistent with those presented here (Funk et al. 2016; Hoell et al. 2015; Ratnam et al. 2014).

Focusing on Zimbabwe and Malawi, large countries that rely on local production, we estimate changes in the undernourished population by translating production losses (Fig. 18.2b) into changes in the percent of the population estimated to be undernourished (FAO 2008). The broad uncertainty in production impacts translates into a wide spread of possible changes in undernourishment (Fig. 18.2c). These results indicate a median increase of the percent undernourished population to be 15% in Zimbabwe and 18% in Malawi, but the uncertainty surrounding these estimates is very high.

Conclusion. While the high natural variability of Niño-3.4 SSTs and the complexities surrounding both ENSO and climate change and ENSO/SA teleconnections make analyzing ENSO/SA/climate change difficult, the large CESM LE ensemble provides an exciting new resource. These simulations suggest that the recent increases in MSENE Niño-3.4 SST would be possible but *unlikely* under PI conditions and *likely* in historic climate change conditions. The CESM1 simulations suggest that some of this warming (+0.36°C) is associated with a trend towards warmer Niño-3.4 conditions, but we find additional warming that may be associated with an amplification of strong ENSO responses (Cai et al. 2015) and east Pacific precipitation (Cai et al. 2015). Contrasts between PI and historic SA and Niño-3.4 El Niño precipitation events show *likely* decreases and increases, respectively. Contributions to increased crop deficits are also found to be likely, but with a large spread of possible outcomes. While the large number of available CESM and CAM5 simulations allowed us to examine in depth responses in a single atmospheric model, more research with more models will be needed to validate the results. It should also be noted that this study has not focused on the future average climate; we are not suggesting that the future average climate will look more El Niño-like. It should also be noted that while observational analyses support stronger SA drought signals during strong canonical El Niño events (Hoell et al. 2015; Ratnam et al. 2014), Indian Ocean SST patterns also influence regional precipitation (Goddard and Graham 1999; Hoell et al. 2017); these influences have not been factored into this analysis.

---

[2] South Africa, Lesotho, Swaziland, Botswana, Zambia, Mozambique, Malawi, and Zimbabwe.

REFERENCES

Cai, W., and Coauthors, 2015: ENSO and greenhouse warming. *Nat. Climate Change.*, **5**, 849–859, doi:10.1038/nclamite2743.

Christensen, J. H., and Coauthors, 2013: Climate phenomena and their relevance for future regional climate change. *Climate Change 2013: The Physical Science Basis*, T. Stocker et al., Eds., Cambridge University Press, 1217–1308.

Cobb, K. M., C. D. Charles, H. Cheng, and R. L. Edwards, 2003: El Niño/Southern Oscillation and tropical Pacific climate during the last millennium. *Nature*, **424**, 271–276, doi:10.1038/nature01779.

Compo, G. P., and P. D. Sardeshmukh, 2010: Removing ENSO-related variations from the climate record. *J. Climate*, **8**, 1957–1978, doi:10.1175/2009JCLI2735.1.

Easterling, D. R., K. E. Kunkel, M. F. Wehner, and L. Sun, 2016: Detection and attribution of climate extremes in the observed record. *Wea. Climate Extremes*, **11**, 17–27, doi:10.1016/j.wace.2016.01.001.

FAO, 2008: FAO Methodology for the Measurement of Food Deprivation: Updating the minimum dietary energy requirements. United Nations Food and Agriculture Organization. [Available online at www.fao.org/fileadmin/templates/ess/documents /food_security_statistics/metadata/undernourishment _methodology.pdf.]

Funk, C., L. Harrison, S. Shukla, A. Hoell, D. Korecha, T. Magadzire, G. Husak, and G. Galu, 2016: Assessing the contributions of local and east Pacific warming to the 2015 droughts in Ethiopia and southern Africa [in "Explaining Extreme Events of 2015 from a Climate Perspective"]. *Bull. Amer. Meteor. Soc.*, **97** (12), S75–S80, doi:10.1175/BAMS-D-16-0167.1.

Goddard, L., and N. E. Graham, 1999: Importance of the Indian Ocean for simulating rainfall anomalies over eastern and southern Africa. *J. Geophys. Res.*, **104**, 19,099–19,116, doi:10.1029/1999JD900326.

Guilyardi, E., H. Bellenger, M. Collins, S. Ferrett, W. Cai, and A. Wittenberg, 2012: A first look at ENSO in CMIP5. *CLIVAR Exchanges No.58*, **17** (1), 29–32.

Hoell, A., C. Funk, T. Magadzire, J. Zinke, and G. Husak, 2015: El Niño–Southern Oscillation diversity and southern Africa teleconnections during austral summer. *Climate Dyn.*, **45**, 1583–1599, doi:10.1007 /s00382-014-2414-z.

——, ——, J. Zinke, and L. Harrison, 2017: Modulation of the Southern Africa precipitation response to the El Niño Southern Oscillation by the subtropical Indian Ocean dipole. *Climate Dyn.*, **48**, 2529–2540, doi:10.1007/s00382-016-3220-6.

Hoskins, B. J., and D. J. Karoly, 1981: The steady linear response of a spherical atmosphere to thermal and orographic forcing. *J. Atmos. Sci.*, **38**, 1179–1196, doi:10.1175/1520-0469(1981)038<1179:TSLROA>2 .0.CO;2.

Huang, B., and Coauthors, 2015: Extended reconstructed sea surface temperature version 4 (ERSST. v4). Part I: upgrades and intercomparisons. *J. Climate*, **28**, 911–930, doi:10.1175/JCLI-D-14-00006.1.

Hurrell, J. W., J. J. Hack, D. Shea, J. M. Caron, and J. Rosinski, 2008: A new sea surface temperature and sea ice boundary dataset for the Community Atmosphere Model. *J. Climate*, **21**, 5145–5153, doi:10.1175/2008JCLI2292.1.

Jury, M., C. Mc Queen, and K. Levey, 1994: SOI and QBO signals in the African region. *Theor. Appl. Climatol.*, **50**, 103–115,doi:10.1007/BF00864907.

Kaplan, A., M. A. Cane, Y. Kushnir, A. C. Clement, M. B. Blumenthal, and B. Rajagopalan, 1998: Analyses of global sea surface temperature 1856–1991. *J. Geophys. Res.*, **103**, 18,567–18,589, doi:10.1029/97JC01736.

Kay, J., and Coauthors, 2015: The Community Earth System Model (CESM) large ensemble project: A community resource for studying climate change in the presence of internal climate variability. *Bull. Amer. Meteor. Soc.*, **96**, 1333–1349, do:10.1175/BAMS-D-13-00255.1.

Kim, S. T., W. Cai, F.-F. Jin, A. Santoso, L. Wu, E. Guilyardi, and S.-I. An, 2014: Response of El Niño sea surface temperature variability to greenhouse warming. *Nat. Climate Change*, **4**, 786–790, doi:10.1038 /nclimate2326.

Li, J., and Coauthors, 2013: El Niño modulations over the past seven centuries. *Nat. Climate Change*, **3**, 822–826, doi:10.1038/nclimate1936.

Lindesay, J., 1988: South African rainfall, the Southern Oscillation and a Southern Hemisphere semi-annual cycle. *J. Climatol.*, **8**, 17–30, doi:10.1002 /joc.3370080103.

McGregor, S., A. Timmermann, M. England, O. E. Timm, and A. Wittenberg, 2013: Inferred changes in El Niño–Southern Oscillation variance over the past six centuries. *Climate Past*, **9**, 2269–2284, doi:10.5194/cp-9-2269-2013.

Misra, V., 2003: The influence of Pacific SST variability on the precipitation over southern Africa. *J. Climate*, **16**, 2408–2418, doi:10.1175/2785.1.

Nicholson, S. E., and D. Entekhabi, 1987: Rainfall variability in equatorial and southern Africa: Relationships with sea surface temperatures along the southwestern coast of Africa. *J. Appl. Meteor.*, **26**, 561–578, doi:10.1175/1520-0450(1987)026<0561 :RVIEAS>2.0.CO;2.

——, and J. Kim, 1997: The relationship of the El Niño-Southern Oscillation to African rainfall. *Int. J. Climatol.*, **17**, 117–135.

Ratnam, J. V., S. K. Behera, Y. Masumoto, and T. Yamagata, 2014: Remote effects of El Niño and Modoki events on the austral summer precipitation of southern Africa. *J. Climate*, **27**, 3802–3815, doi:10.1175/JCLI-D-13-00431.1.

Rayner, N., D. E. Parker, E. B. Horton, C. K. Follard, L. V. Alexander, D. P. Rowell, E. C. Kent, and A. Kaplan, 2003: Global analyses of sea surface temperature, sea ice, and night marine air temperature since the late nineteenth century. *J. Geophys. Res.*, **108**, 4407, doi:029/2002JD002670.

Reason, C., R. Allan, J. Lindesay, and T. Ansell, 2000: ENSO and climatic signals across the Indian Ocean basin in the global context: Part I, Interannual composite patterns. *Int. J. Climatol*, **20**, 1285–1327.

Rocha, A., and I. Simmonds, 1997: Interannual variability of south-eastern African summer rainfall. Part I: Relationships with air-sea interaction processes. *Int. J. Climatol.*, **17**, 235–265.

SADC, 2016: SADC Regional Vulnerability Assessment and Analysis Synthesis Report 2016: State of Food Insecurity and Vulnerability in the Southern African Development Community. Southern African Development Community, 65 pp. [Available online at www.sadc.int/documents-publications /show/4720.]

Solomon, A., and M. Newman, 2012: Reconciling disparate twentieth-century Indo-Pacific ocean temperature trends in the instrumental record. *Nat. Climate Change*, **2**, 691–699, doi:10.1038/nclimate1591.

Wittenberg, A. T., 2009: Are historical records sufficient to constrain ENSO simulations? *Geophys. Res. Lett.*, **36**, L12702, doi:10.1029/2009GL038710.

19. CLIMATE CHANGE INCREASED THE LIKELIHOOD OF THE 2016 HEAT EXTREMES IN ASIA

Yukiko Imada, Hideo Shiogama, Chiharu Takahashi, Masahiro Watanabe,
Masato Mori, Youichi Kamae, and Shuhei Maeda

*The 2016 extreme warmth across Asia would not have been possible without climate change.
The 2015/16 El Niño also contributed to regional warm extremes over Southeast Asia
and the Maritime Continent.*

Introduction. Analyses of the observed monthly temperature record from the Goddard Institute for Space Studies (GISS) Surface Temperature Analysis (GISTEMP; Hansen et al. 2010) indicate that the total area that experienced extreme warmth over the global land surface in 2016 was record-breaking, exceeding the previous highest record in 2010 (Fig. 19.1a, fraction of area that experiences extremely high temperature). This frequent occurrence of warm events is particularly remarkable over the Asian region (Fig. 19.1a). Many parts of Southeast Asia, southern India, and northern Eurasia experienced extremely high temperature by the end of 2016 (Fig. 19.1b). In India, at least 580 people were killed by the heat waves from March to May (India's government; European Commission). The record-breaking high temperature had been persistent more than 10 months in the Maritime Continent. In Thailand, the heat wave also caused a new record for energy consumption because of the nationwide usage of air conditioners (Gecker and Chuwiruch 2016).

Generally, Southeast Asia experiences warm and dry conditions during El Niño, being in the region of anomalously downward motion associated with the weakened Walker Circulation. Also, the global surface warms up with a lag of several months following

an El Niño event through persistent changes in atmospheric circulation (Trenberth et al. 2002). In this report, we investigate to what extent the 2016 extreme warmth across Asia was attributable to anthropogenic warming or to the major El Niño episode in 2015/16.

Many studies have concluded that heat waves over the global land area have become more frequent due to human-induced global warming (e.g., Jones et al. 2008; Christidis and Stott 2014; Shiogama et al. 2016). To separate the influences of anthropogenic warming and natural variability on the 2016 heat events in Asia, we analyzed large ensembles of atmospheric general circulation model (AGCM) simulations with and without anthropogenic warming and ENSO effects.

Methods. We performed several 100-member ensemble experiments of 2016 (initialized on 1 June 2009 and continuously updated every year) using the AGCM of MIROC5 (T85L40, Watanabe et al. 2010): 1) ALL: All-forcing run integrated by the historical sea surface temperature (SST) and sea ice (HadISST dataset, Rayner et al. 2003) and historical anthropogenic and natural forcing agents. 2) NAT1 and NAT2: Natural forcing runs by removing 1870–2012 linear trends of the observed SST and sea ice (NAT1, Christidis and Stott 2014), and by removing the estimates of anthropogenic changes in SST and sea ice based on the Coupled Model Intercomparison Project Phase 5 (CMIP5) historical experiments (NAT2, Stone 2013). See Shiogama et al. (2014) for details of ALL and NAT. 3) ALLnoENSO: Same as ALL but ENSO-related variability was eliminated by removing the observed SST anomaly regressed to the Niño-3.4 SST anomaly (Takahashi et al. 2016) in order to examine the impact of the extreme El Niño in 2015/16. The SST patterns removed in NAT1, NAT2, and ALLnoENSO are shown in Figure ES19.1. The long-term historical run, ALL-LNG (1949–2016), which also uses observed SST and sea ice as specified forcings, is also
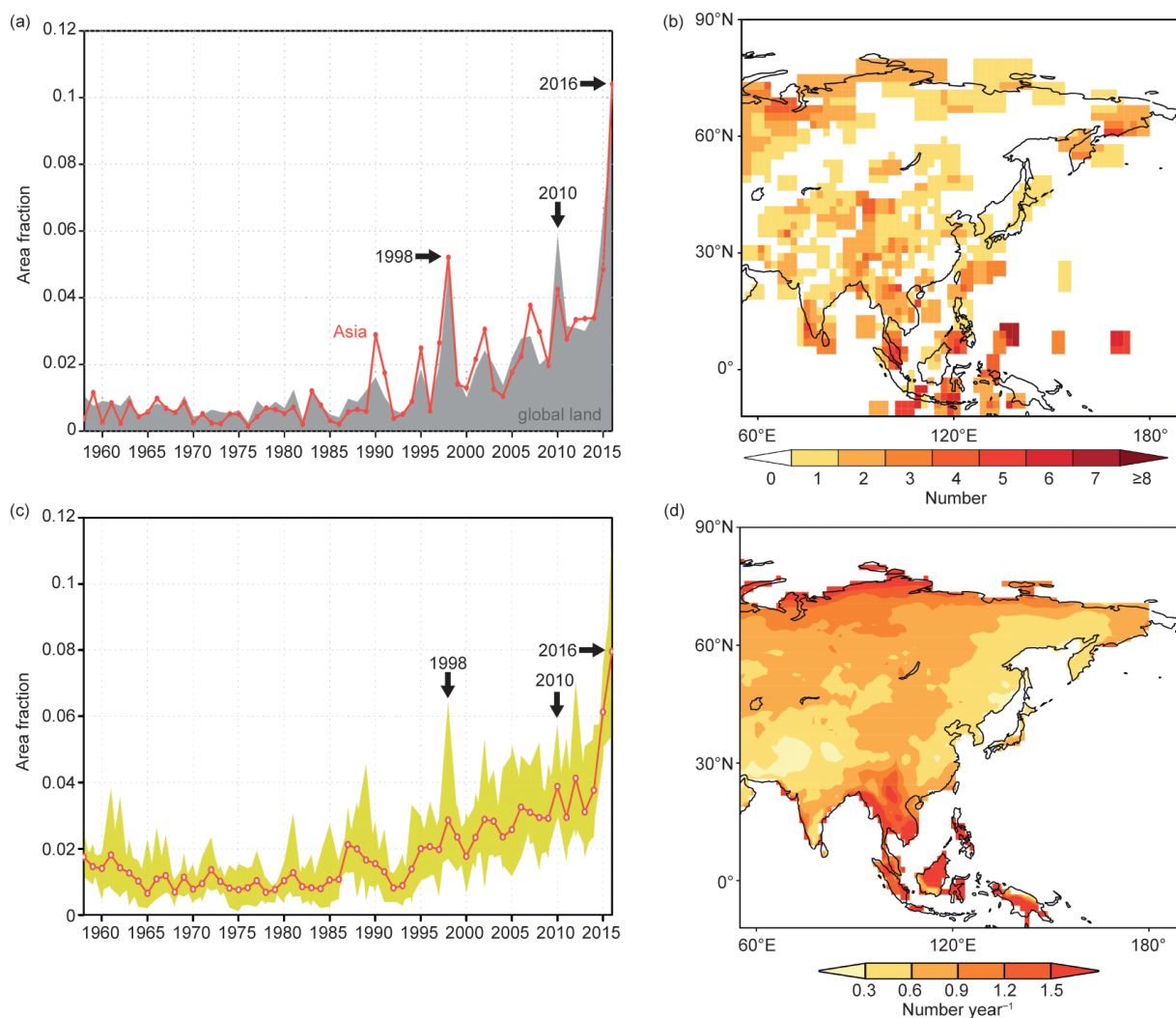
FIG. 19.1. (a) Time series of area fraction with extreme warmth, defined as total land surface area with extreme warmth (exceeding 2 std. dev.) divided by total area of available grid points, based on GISTEMP dataset. Global land surface (gray shaded) and Asian region (10°S–90°N, 55°E–170°W) (red) are shown. (b) Map of number of monthly warm events in 2016. (c) Same as Asian time series of (a) but ensemble mean values (red line) and range (shaded) of 10 member simulations of ALL-LNG are shown. (d) Same as (b) but for result from 2016 ensemble simulations of ALL, where number of monthly warm events was divided by 100 (number of members) to get annual value number per year. Values exceeding 99% confidential level by Student's *t* test are plotted.

conducted with 10-member ensembles for validation and to define a threshold of warm events. We used the monthly observation data from GISTEMP for land surface temperature.

For each land–surface grid point, annual time series of the total number of months exceeding a threshold are calculated. The thresholds for the observation and simulations are defined by two standard deviations of surface air temperature from 1951 to 2016 for GISTEMP and ALL-LNG, respectively. We assessed relative contributions of human influence and ENSO to the frequent occurrences of extreme warmth in terms of the fraction of attributable risk

(FAR; Allen 2003), defined as $1 - (P_0 / P_1)$, where P_1 and P_0 are threshold exceedances computed with the ALL and NAT/ALLnoENSO simulations, respectively. The threshold is defined as a 99-percentile value of area fraction estimated by the kernel method (Silverman 1986; Kimoto and Ghil 1993); 0.103 for the observation and 0.065 for the simulations (the ALL-LNG simulation underestimates the extreme values of the area fraction).

Results. Figure 19.1c depicts the modeled time series of the fraction: area-weighted total number of grid points experiencing extremely high temperature
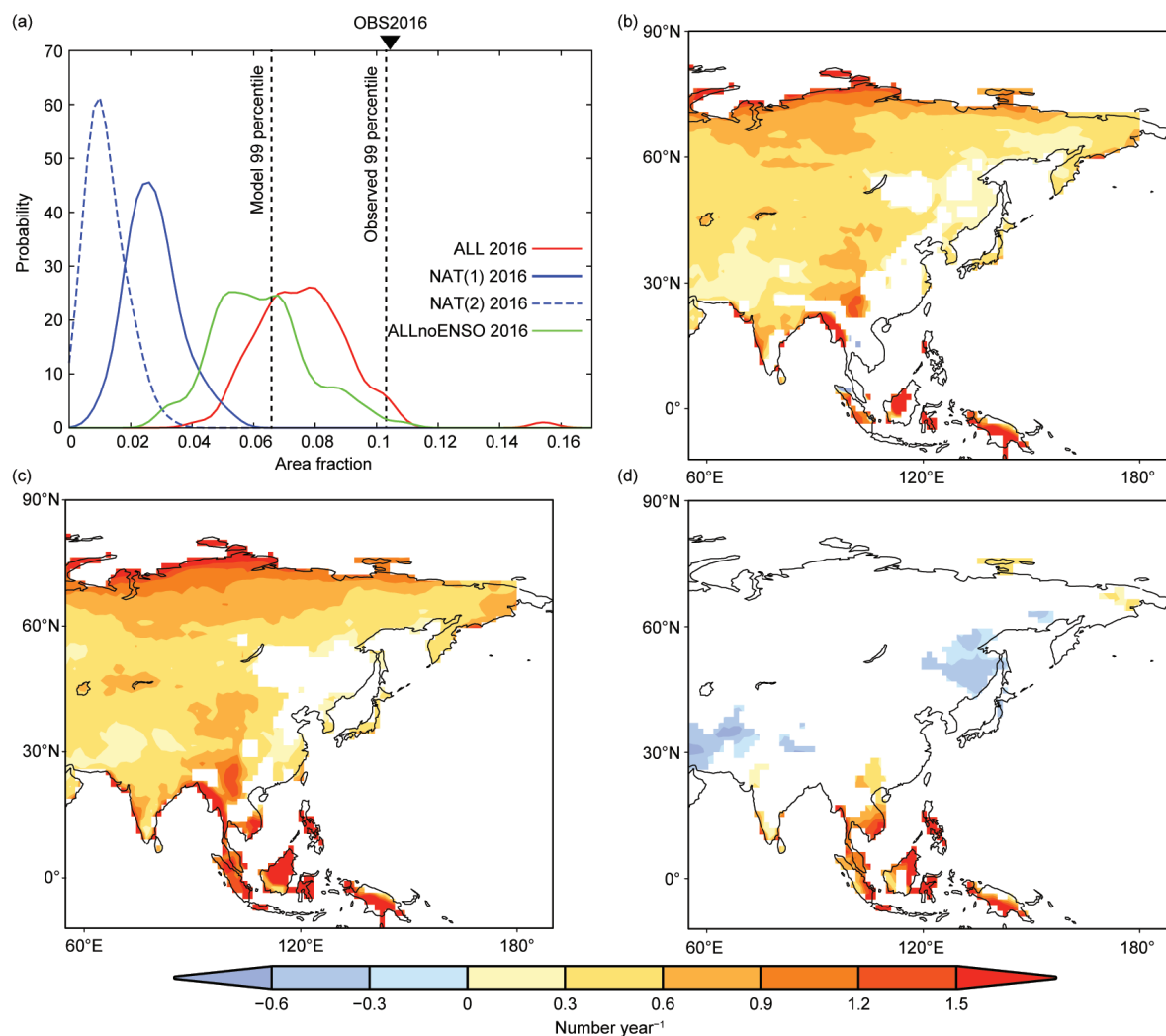
FIG. 19.2. (a) PDFs of annual area fraction of extreme warmth over Asian region in 2016 for ALL (red), NAT1 (blue, solid), NAT2 (blue, broken), and ALLnoENSO (green) estimated by kernel method (Silverman 1986; Kimoto and Ghil 1993). (b) Map of difference in frequency of extreme warmth (per year) between ALL and NAT1 (ALL minus NAT1). Extreme warmth is defined as monthly temperatures that exceed 2 std. dev. of 1951–2016 average. (c),(d) Same as (b) but for ALL minus NAT2 and ALL minus ALLnoENSO, respectively. In (b)–(d), values exceeding 99% confidential level by Student's t test are plotted.

divided by the total number of available grid points (hereinafter, referred to as "area fraction") over the Asian region from the ALL-LNG runs. The ALL-LNG model captures peaks of the area fraction occurring after large El Niño events (1998, 2010, and 2016) and the most frequent occurrence of warmth in 2016 (Fig. 19.1c). The model also captures the general trend of the observations. Owing to the large ensembles, a simulated event frequency map based on the 100-member ALL simulations (Fig. 19.1d) depicts continuous distribution, and reproduces the concentration of the events in Southeast Asia, southern India, and northern Eurasia.

Next, we constructed probability density functions (PDFs) of the area fraction of extreme warmth over

the Asian region in 2016 using the ALL, NAT1, NAT2, and ALLnoENSO simulations (Fig. 19.2a). The results indicate that anthropogenic forcing leads to a marked increase in the event occurrence although there is a certain degree of uncertainty induced by the different estimations of anthropogenic changes in SST and sea ice between NAT1 and NAT2. Compared with this, the impact of ENSO is weaker but substantially increases the area fraction of extreme warmth.

The effects of the anthropogenic warming and ENSO on the occurrence of extreme warmth are evaluated from the difference between ALL and NAT, and ALL and ALLnoENSO, respectively. Again, extreme warmth months are defined as monthly temperatures that exceed 2 standard deviations of

the 1951–2016 average from the ALL-LNG run. The spatial maps of frequency change due to anthropogenic forcing (Figs. 19.2b,c) indicate that the frequent occurrence of warm events across Asia shown in Fig. 19.1d can be attributable to the anthropogenic effect in most regions except narrow parts of East Asia and the Indochina peninsula. On the other hand, the ENSO-induced frequency change (Fig. 19.2d) shows increased incidence particularly over Southeast Asia. The positive frequency anomalies of extreme warmth over Southeast Asia appeared during the months from January to May in 2016 (not shown) and seem to be attributable to the warmer Indian Ocean SSTs and descending anomalies over the Maritime Continent during that period associated with the continued big El Niño since the 2015 winter (the ENSO-related SST transition in 2016 is shown in Fig. ES19.1c). Note that, in our simple concurrent regression method, lagged influence of ENSO on the East Asian summer climate (the so-called Indian Ocean capacitor effect; Xie et al. 2009, 2016) cannot be taken into account. In 2016, however, the major Indian Ocean warming occurred in the beginning of the year, which is partly captured in the concurrent regression method (Fig. ES19.1c), and the lagged impact of ENSO was relatively small in the summer.

From the observed record, the occurrence rate of extreme area fraction in 2016 can be estimated at less than 1% in the long-term climate (the observed area fraction of 2016 is greater than the 99-percentile threshold). The ALL simulations, however, indicate that the 2016 condition raised the level of the occurrence rate up to 75.9%. On the other hand, the occurrence rate is 0.000%, 0.000%, and 41.1% for NAT1, NAT2, and ALLnoENSO, respectively. The estimated FARs are 1.000, 1.000, and 0.458, respectively. These results suggest that the frequent occurrence of extreme warmth across Asia in 2016 would never have happened without the anthropogenic warming, and the ENSO condition also partly contributed to the increase in the probability particularly over the Philippines, the Maritime Continent, and Southeast Asia.

Several studies demonstrated that the magnitude of the attributable signal can change substantially depending on the model used (e.g., Bellprat and Doblas-Reyes 2016). It is also known that the atmosphere-only model experiments lack air–sea interactions and overestimate the role of SST (e.g., Barsugli and Battisti 1998). To evaluate the impact from these drawbacks, we analyzed the results of fully-forced 20-member historical AGCM simulations conducted by ESRL-CAM5 (available at www.esrl.noaa.gov/psd/repository/alias/facts/), and also, 5-member historical (ALL) and natural (NAT) CMIP5 simulations conducted by MIROC5 (atmospheric components are exactly the same as the model used in this study). The linear trends of the historical simulations from 1958 to 2016 are 0.0569% per year of area fraction for the ALL-LNG run (Fig. 19.1c), 0.0590% per year for the ESRL-CAM5 AGCM simulations (Fig. ES19.2a), and 0.0764% per year for the coupled GCM of MIROC5 (Fig. ES19.2c). The sensitivity to different AGCM is relatively small between MIROC5 and CAM5 AGCMs. On the other hand, the difference between MIROC5 AGCM and CGCM suggests that the air–sea interaction might have some impacts on the occurrence of extreme warmth over Asia.

Conclusions. All of the risk of the extremely high temperatures over Asia in 2016 can be attributed to anthropogenic warming. In addition, the ENSO condition made the extreme warmth two times more likely to occur. It is found that anthropogenic warming contributed to raising the level of event probability almost everywhere, although the 2015/16 El Niño contributed to a regional increase of warm events over the Maritime Continent, the Philippines, and Southeast Asia, but had little significant contribution elsewhere in Asia.

REFERENCES

Allen, M. R. 2003: Liability for climate change. *Nature*, **421**, 891–892, doi:10.1038/421891a.

Barsugli, J. J., and D. S. Battisti, 1998: The basic effects of atmosphere–ocean thermal coupling on midlatitude variability. *J. Atmos. Sci.*, **55**, 477–493.

Bellprat, O., and F. Doblas-Reyes, 2016: Attribution of extreme weather and climate events overestimated by unreliable climate simulations. *Geophys. Res. Lett.*, **43**, 2158–2164, doi:10.1002/2015GL067189.

Christidis, N., and P. A. Stott, 2014: Change in the odds of warm years and seasons due to anthropogenic influence on the climate. *J. Climate*, **27**, 2607–2621, doi:10.1175/JCLI-D-13-00563.1.

Gecker, J., and N. Chuwiruch, 2016: Thailand is used to hot Aprils, but not this hot! Bangkok AP news, Accessed 11 August 2017. [Available online at https://apnews.com/42c7c080f86644168102ceeea105ddd0/thailand-used-hot-aprils-not-hot].

Hansen, J., R. Ruedy, M. Sato, and K. Lo, 2010: Global surface temperature change. *Rev. Geophys.*, **48**, RG4004, doi:10.1029/2010RG000345.

Jones, G. S., P. A. Stott, and N. Christidis, 2008: Human contribution to rapidly increasing frequency of very warm Northern Hemisphere summers. *J. Geophys. Res.*, **113**, D02109, doi:10.1029/2007JD008914.

Kimoto, M., and M. Ghil, 1993: Multiple flow regimes in the Northern Hemisphere winter. Part I: Methodology and hemispheric regimes. *J. Atmos. Sci.*, **50**, 2625–2643.

Rayner, N. A., Parker, E. B. Horton, C. K. Folland, L. V. Alexander, D. P. Rowell, E. C. Kent, and A. Kaplan, 2003: Global analyses of sea surface temperature, sea ice, and night marine air temperature since the late nineteenth century. *J. Geophys. Res.*, **108**, 4407, doi:10.1029/2002JD002670.

Shiogama, H., M. Watanabe, Y. Imada, M. Mori, Y. Kamae, M. Ishii, and M. Kimoto, 2014: Attribution of the June–July 2013 heat wave in the southwestern United States. *SOLA*, **10**, 122–126, doi:10.2151/sola.2014-025.

——, and Coauthors, 2016: Attributing historical changes in probabilities of record-breaking daily temperature and precipitation extreme events. *SOLA*, **12**, 225–231, doi:10.2151/sola.2016-045.

Silverman, B. W., 1986: *Density Estimation for Statistics and Data Analysis*. Chapman and Hall, 175 pp.

Stone, D. A., 2013: Boundary conditions for the C20C Detection and Attribution project: The ALL-Hist/est1 and NAT-Hist/CMIP5-est1 scenarios. International CLIVAR C20C+ Detection and Attribution Project, 18 pp. [Available online at http://portal.nersc.gov/c20c/input_data/C20C-DandA_dSSTs_All-Hist-est1_Nat-Hist-CMIP5-est1.pdf.]

Takahashi, C., M. Watanabe, H. Shiogama, Y. Imada, and M. Mori, 2016: A persistent Japanese heat wave in early August 2015: Roles of natural variability and human-induced warming [in "Explaining Extreme Events of 2015 from a Climate Perspective"]. *Bull. Amer. Meteor. Soc.*, **97** (12), S107–S112, doi:10.1175/BAMS-D-16-0157.1.

Trenberth, K., J. M. Caron, D. P. Stepaniak, and S. Worley, 2002: Evolution of El Niño–Southern Oscillation and global atmospheric surface temperatures. *J. Geophys. Res.*, **107** (D8), doi:10.1029/2000JD000298.

Watanabe, M., and Coauthors, 2010: Improved climate simulation by MIROC5: Mean states, variability, and climate sensitivity. *J. Climate*, **23**, 6312–6335, doi:10.1175/2010JCLI3679.1.

Xie S.-P., K. Hu, J. Hafner, H. Tokinaga, Y. Du, G. Huang, and T. Sampe, 2009: Indian Ocean capacitor effect on Indo–western Pacific climate during the summer following El Niño. *J. Climate*, **22**, 730–747, doi:10.1175/2008JCLI2544.1.

——, Y. Kosaka, Y. Du, K. Hu, J. S. Chowdary, and G. Huang, 2016: Indo–western Pacific ocean capacitor and coherent climate anomalies in post-ENSO summer: A review. *Adv. Atmos. Sci.*, **33**, 411–432, doi:10.1007/s00376-015-5192-6.

20. EXTREME RAINFALL (R20MM, RX5DAY) IN YANGTZE–HUAI, CHINA, IN JUNE–JULY 2016: THE ROLE OF ENSO AND ANTHROPOGENIC CLIMATE CHANGE

Qiaohong Sun and Chiyuan Miao

Both the 2015/16 strong El Niño and anthropogenic factors contributed to the June–July 2016 extreme precipitation (R20mm, RX5day) in Yangtze–Huai, China. Combined, they increased the risk of the event tenfold.

Introduction. In June–July 2016, the Yangtze–Huai region (27.5°–35°N, 107.5°–123°E) in China experienced a deluge of extreme rainfall, especially in the middle and lower reaches of the Yangtze River Basin (Fig. ES20.1a). The extreme rainfall caused widespread severe flooding, waterlogging, and landslides in the Yangtze–Huai region.

We examined changes in the characteristics of rainfall for the June–July period, including the number of days with very heavy precipitation (daily precipitation ≥ 20 mm; R20mm) and the maximum 5-day precipitation amount (RX5day). In this study, we estimated the probability that the changes in extreme rainfall were due to El Niño or to anthropogenic climate change.

Data and methods. We used observed daily precipitation data for the period 1957–2016, obtained from the National Meteorological Information Center of the China Meteorological Administration. The dataset is constructed from over 2400 station observations across China at a resolution of 0.5° × 0.5° (Shen et al. 2010). We calculated R20mm and RX5day (Sillmann et al. 2013) to estimate the characteristics of extreme precipitation in June–July. We conducted a lag–lead correlation between the June–July extreme precipitation and the December–February (DJF) ENSO index during the preceding winter. The DJF oceanic Niño index (ONI, 3-month running mean of ERSST.v4 SST anomalies in the Niño-3.4 region), based on centered 30-year base periods updated every 5 years, was used as an indicator of the ENSO.

Simulations from six climate models involved in phase 5 of the Coupled Model Intercomparison Project (CMIP5; Taylor et al. 2012) that adequately capture climate variability in the Yangtze–Huai region were used to attribute the June–July extreme precipitation over Yangtze–Huai (see Table ES20.1). We used simulations for the period 1912–2005 with natural forcing and all forcings. We obtained the simulated RX5day and R20mm data from the Canadian Centre for Climate Modelling and Analysis (www.cccma.ec.gc.ca/data/climdex/index.shtml). Data from NCEP/NCAR Reanalysis 1 were used to depict large-scale atmospheric circulation. We used several statistical techniques to assess the severity and causes of the extreme precipitation:

1) To estimate the univariate return period, we used the generalized extreme value (GEV) distribution for parametric fitting. We used the Kolmogorov–Smirnov (K–S) goodness-of-fit test to verify the distribution (Wilks 2006). The return periods (R) for RX5day and R20mm were estimated from the GEV distribution and defined as $R = 1 / [1 − F(x)]$, where $F(x)$ is the cumulative probability of June–July RX5day or R20mm in 2016. Then, after using the Akaike Information Criterion (AIC; Akaike 1974) to identify the most appropriate copula function (smallest AIC), the T-copula function was used to estimate the probability of concurrence of high RX5day and R20mm.

2) To assess the influence of the 2015/16 El Niño on the 2016 extreme precipitation, we used the non-stationary GEV distribution with the ENSO index in the preceding winter as a covariate. The location parameter of the GEV distribution was linearly regressed to the DJF ENSO index (Sun et al. 2017; Zhang et al. 2010). Then, the probability ratios ($PR = P_1/P_2$) were used to estimate the influence of ENSO. P_1 and P_2 represent the probabilities of exceeding the June–July RX5day threshold in two different scenarios. P_1

AFFILIATIONS: Sun and Miao—State Key Laboratory of Earth Surface Processes and Resource Ecology, Geographical Science, Beijing Normal University, Beijing, China

was estimated from the GEV distribution with the parameter fit to the winter 2015/16 ENSO index; P_2 was calculated from the GEV distribution fitted to the ENSO index from the neutral years.

3) To quantify the human-induced changes in the odds of extreme events, we employed the fraction of attributable risk (FAR = $1 - P_2/P_1$) and the corresponding probability ratios (Fischer and Knutti 2015; Stott et al. 2005). We estimated the anthropogenic influence by setting P_1 to be the probability of exceeding the 2016 RX5day in the all-forcings scenarios, with P_2 being the equivalent for the natural-forcing scenarios. To estimate the influence of El Niño conditions during the preceding winter on the June–July extreme precipitation, we calculated the probability ratio (PR) with P_1 from the El Niño all-forcings simulations and P_2 from the neutral all-forcings simulations. The sample method (90% of samples were randomly selected for each time) was performed 1000 times per period to estimate the PR uncertainty.

Results A. Observed 2016 June–July extreme rainfall in historical context. The regional averages for the 2016 June–July RX5day (127.04 mm) and R20mm (7.91 days) were the third highest since records began in 1957, with 45.1% and 47. 9% growth relative to the baseline period (1961–90), respectively (Fig. 20.1a). 2016–like RX5day and R20mm events occur in the present climate in the Yangtze–Huai region approximately every 116 years (95% confidence level: 45–2947 years) and 51 years (95% confidence level: 25–234 years), respectively, but the concurrency of the two events was close to being a 1-in-181-year event (Fig. 20.1a). The maximum changes in RX5day were concentrated in the middle and lower reaches of the Yangtze River Basin, where there were positive anomalies greater than 100% (Fig. 20.1b). More regions were affected by severe precipitation in 2016 compared with the baseline period, as demonstrated by the distinct rightward shift in the 2016 histogram for RX5day (Fig. 20.1b). Successive days of heavy precipitation were mainly concentrated in late June and early July. The water levels in five main hydrological stations surpassed the alert level for long durations, triggering widespread, severe flooding in the middle and lower reaches of the Yangtze River Basin (Fig. ES20.2).

Results B. Attribution to El Niño and anthropogenic influences. The 2015/16 El Niño was one of the strongest on record, comparable to the 1972/73 event (L'Heureux et al. 2017). The ENSO index during the preceding winter was significantly correlated ($p < 0.05$) with the June–July extreme precipitation and flooding in the Yangtze–Huai region (Fig. 20.1c), and the correlation map has field significance ($p < 0.05$) as suggested by the field significance test (Livezey and Chen 1983; Fig. ES20.1b). The risk of occurrence of the 2016 extreme precipitation event was increased by the preceding winter El Niño, with a 1.5- to 4-fold increase in risks relative to preceding neutral conditions for most areas in the Yangtze–Huai region (Fig. 20.1d). Comparing precipitation extremes between the preceding El Niño and neutral seasons in the all-forcings simulations, we found that about 72% of the risk of the June–July 2016 RX5day could be attributed to the influence of El Niño, indicating that the El Niño event produced a greater than threefold increase in the likelihood of the extreme precipitation event (Figs. ES20.2a,b). The western Pacific subtropical high (WPSH) generally shifts southward and has a westward extension during El Niño decay (Huang and Wu 1989; Wang et al. 2000), which is conducive to water-vapor transmission to the Yangtze–Huai region and the induction of persistent heavy precipitation in the Yangtze River Basin (Figs. 20.1e,f). The circulation systems in June–July of 1998 and 2016 were characterized by a stronger than normal WPSH with its high ridge extending more westward. The high ridge of the WPSH in 2016 was slightly eastward compared to that in 1998 owing to some inconsistences of sea surface temperature patterns (L'Heureux et al. 2017); however, the intensity of the WPSH in 2016 was slightly stronger than that in 1998. An anomalous anticyclone dominated over the northwestern Pacific in the lower troposphere and induced intensified water vapor transport from the western Pacific to the Yangtze–Huai region (Yuan et al. 2017); this transport was linked to the occurrence of extreme precipitation.

We compared the likelihood of occurrence of the 2016 June–July RX5day event in different CMIP5 experiments. When the 2016 June–July RX5day was marked as the threshold, precipitation extremes like those experienced during June–July 2016 in the Yangtze–Huai region were 35% more likely because of anthropogenic climate change. This is equivalent to an approximately 1.5-fold (5%–95% uncertainty range: 0.6–4.7) increase in the probability of occurrence owing to anthropogenic influences. The compound effects of both anthropogenic climate change and the preceding strong El Niño can explain 91% (5%–95% uncertainty range: 66%–99%) of the risk of such event conditional on the preceding winter El Niño state between all-forcings and natural-forcing simulations. That is, anthropogenic climate change
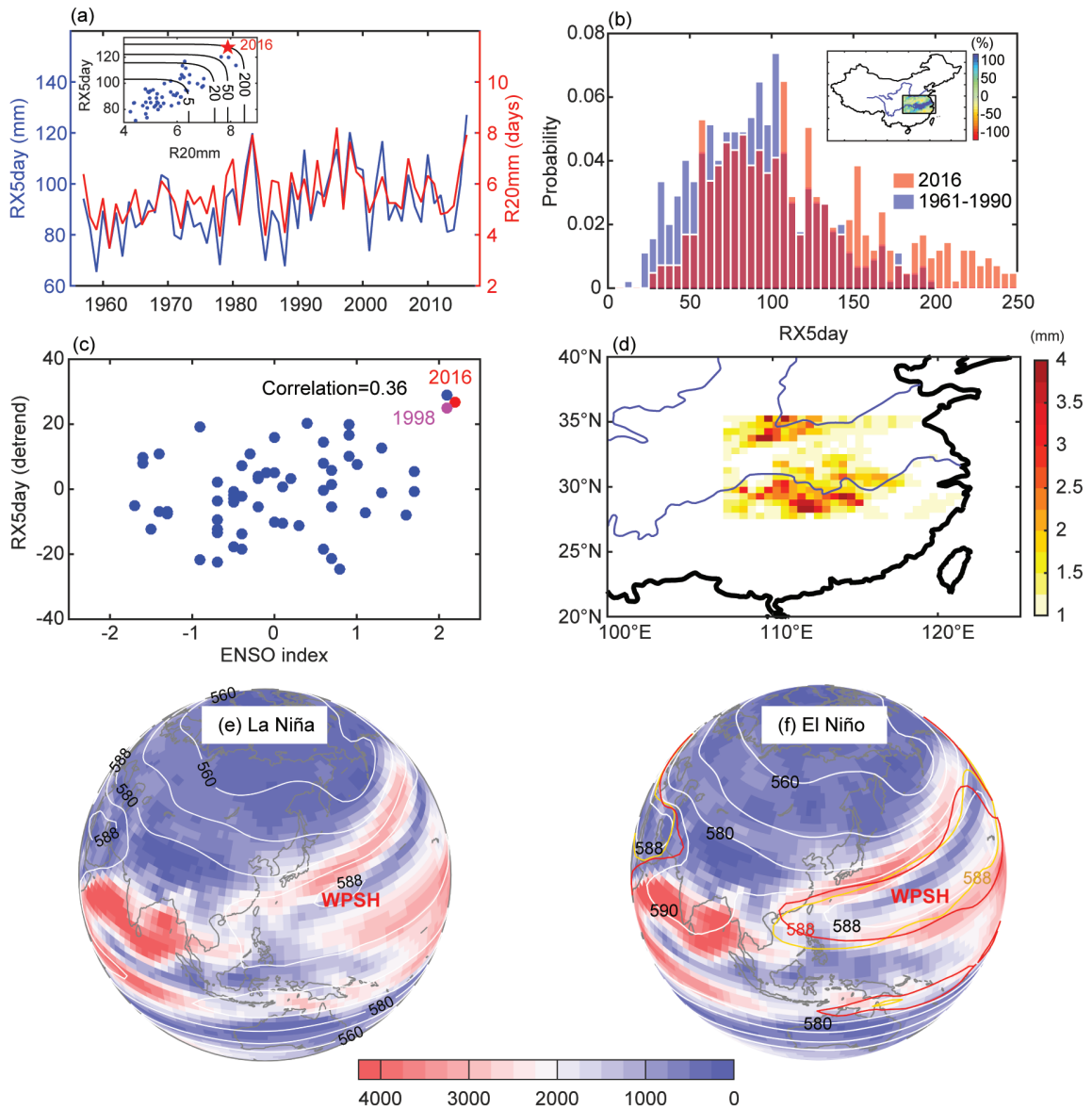
FIG. 20.1. (a) Time series for Jun–Jul RX5day (blue) and R20mm (red) over the Yangtze–Huai region (area in black box in Fig. ES20.1a) for the period 1957–2016. Embedded figure shows bivariate return periods for concurrent RX5day and R20mm. (b) Standardized histograms of RX5day values over Yangtze–Huai region in 2016 (red) and in baseline period (1961–90; blue). Embedded figure shows spatial distribution of percentage change (%) in Jun–Jul RX5day in 2016 relative to mean RX5day during baseline period (1961–90). (c) ENSO index during preceding winter and area-averaged Jun–Jul RX5day were significantly correlated at 95% confidence level (r = 0.365). (d) Spatial distribution of probability ratio, with preceding winter ENSO index as covariate, representing difference in probability of 2016 RX5day event occurring during decaying El Niño conditions versus during neutral conditions. (e),(f) Mean Jun–Jul integrated water-vapor flux g m⁻¹ s⁻¹ of layer from surface to 300 hPa and 500 hPa geopotential height on (white contours) for (e) five strongest La Niña years and (f) five strongest El Niño years. Red and orange contour lines in (f) are for 588 dagpm in Jun–Jul 2016 and 1998, respectively.

and El Niño together resulted in a tenfold increase in the risk of this extreme event (Fig. 20.2b).

Conclusions. Model and observational analyses showed that the extreme precipitation event that occurred in June–July 2016 in the Yangtze–Huai region of China, featuring high intensity and frequency of precipitation, was strongly correlated with the preceding 2015/16 El Niño conditions and with anthropogenic factors. The El Niño conditions during the preceding winter strongly increased the probability of summer extreme precipitation over the Yangtze–Huai region
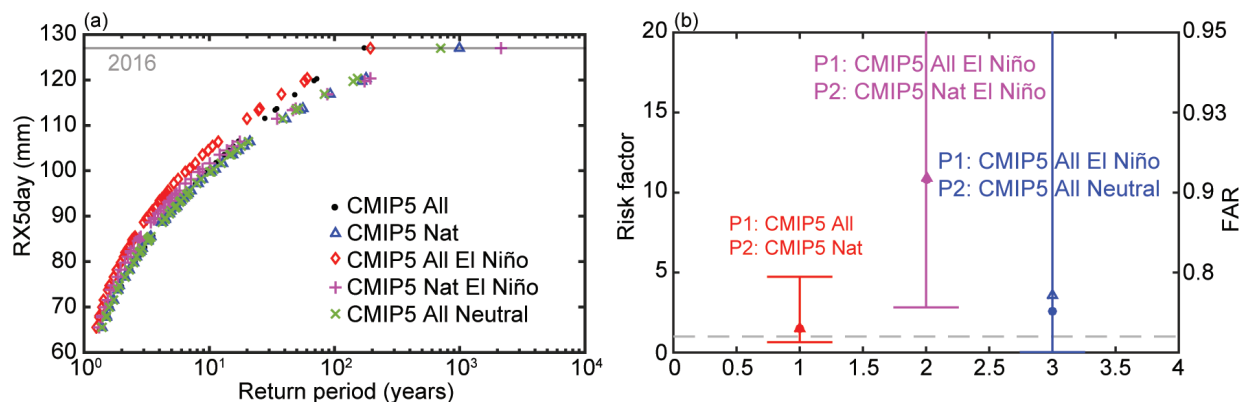
FIG. 20.2. (a) Return period plots for Jun–Jul RX5day under various modeling scenarios. Horizontal line represents 2016 RX5day. **(b)** Corresponding probability ratios and FAR calculated using different scenario combinations for P_1 and P_2, as indicated. Estimates of probability ratios were calculated using a bootstrapping approach (resampling the distributions 1000 times with replacement); bars show the interquartile range (5th–95th percentiles); dots and triangles show median values and best estimates, respectively.

via an enhancement and westward extension of the WPSH. The models showed a 35% contribution of anthropogenic factors to the 2016 extreme precipitation. Together, anthropogenic climate change and El Niño may result in a tenfold increase in the risk of occurrence of this extreme event. The frequency of extreme El Niño events are projected to increase with a warming climate (Cai et al. 2014), which may induce more frequent and more severe episodes of extreme precipitation in the future.

REFERENCES

Akaike, H., 1974: A new look at the statistical model identification. *IEEE Trans. Automat. Contr.*, **19**, 716–723, doi: 10.1109/TAC.1974.1100705.

Cai, W., and Coauthors, 2014: Increasing frequency of extreme El Niño events due to greenhouse warming. *Nat. Climate Change*, **4**, 111–116, doi:10.1038/nclimate2100.

Fischer, E. M., and R. Knutti, 2015: Anthropogenic contribution to global occurrence of heavy-precipitation and high-temperature extremes. *Nat. Climate Change*, **5**, 560–564, doi:10.1038/nclimate2617 .

Huang, R., and Y. Wu, 1989: The influence of ENSO on the summer climate change in China and its mechanism. *Adv. Atmos. Sci.*, **6**, 21–32, doi:10.1007/BF02656915.

L'Heureux, M., and Coauthors, 2017: Observing and predicting the 2015/16 El Niño. *Bull. Amer. Meteor. Soc.*, **98**, 1363–1382, doi:10.1175/BAMS-D-16-0009.1

Livezey, R. E., and W. Chen, 1983: Statistical field significance and its determination by Monte Carlo techniques. *Mon. Wea. Rev.*, **111**, 46–59, doi:10.1175/1520-0493(1983)111<0046:SFSAID>2.0.CO;2.

Shen, Y., A. Xiong, Y. Wang, and P. Xie, 2010: Performance of high-resolution satellite precipitation products over China. *J. Geophys. Res.*, **115**, D02114, doi:10.1029/2009JD012097.

Sillmann, J., V. V. Kharin, X. Zhang, F. W. Zwiers, and D. Bronaugh, 2013: Climate extremes indices in the CMIP5 multimodel ensemble: Part 1. Model evaluation in the present climate. *J. Geophys. Res.*, **118**, 1716–1733, doi:10.1002/jgrd.50203.

Stott, P. A., D. A. Stone, and M. R. Allen, 2005: Human contribution to the European heatwave of 2003. *Nature*, **436**, 610–614, doi:10.1038/nature03089.

Sun, Q., C. Miao, Y. Qiao, and Q. Duan, 2017: The non-stationary impact of local temperature changes and ENSO on extreme precipitation at the global scale. *Climate Dyn.*, online, doi:10.1007/s00382-017-3586-0.

Taylor, K. E., R. J. Stouffer, and G. A. Meehl, 2012: An overview of CMIP5 and the experiment design. *Bull. Amer. Meteor. Soc.*, **93**, 485–498, doi:10.1175/BAMS -D-11-00094.1.

Wang, B., R. G. Wu, and X. H. Fu, 2000: Pacific-East Asian teleconnection: How does ENSO affect East Asian climate? *J. Climate*, **13**, 1517–1536, doi:10.1175/1520-0442(2000)013<1517:PEATHD >2.0.CO;2.

Wilks, D. S., 2006: *Statistical Methods in the Atmospheric Sciences.* 2nd ed. International Geophysics Series, Vol. 91, Elsevier, 627 pp.

Yuan, Y., H. Gao, W. Li, Y. Liu, L. Chen, B. Zhou, and Y. Ding, 2017: The 2016 summer floods in China and associated physical mechanisms: A comparison with 1998. *J. Meteor. Res.*, **31**, 261–277, doi:10.1007 /s13351-017-6192-5.

Zhang, X., J. Wang, F. W. Zwiers, and P. Ya. Grois-man, 2010: The influence of large-scale climate variability on winter maximum daily precipitation over North America. *J. Climate*, **23**, 2902–2915, doi:10.1175/2010JCLI3249.1.

21. ATTRIBUTION OF THE JULY 2016 EXTREME PRECIPITATION EVENT OVER CHINA'S WUHAN

CHUNLÜE ZHOU, KAICUN WANG, AND DAN QI

Human-induced warming and El Niño may have substantially increased the probability of the occurrence of such events as the July 2016 extreme precipitation over China's Wuhan.

Introduction. From 30 June to 6 July 2016 Wuhan City, which has approximately ten million residents, received a record-breaking weekly rainfall of 574 mm, reaching a maximum of 1087.2 mm in the downtown areas. This intense rainfall resulted in a disastrous flood that killed 237 people, left 93 people missing, and caused at least $22 billion in damage (U.S. dollars), making it the second most expensive weather-related natural disaster in China's history.

The 2016 Wuhan extreme precipitation was a part of Mei-yu rain (called Baiu in Japan), which has been shown to become particularly heavy in the summer following an El Niño event (Huang et al. 2000; Lin and Lu 2009; Jin et al. 2016). Two ENSO-related processes were proposed to explain this phenomena: 1) the persistent western North Pacific anticyclonic anomaly in the lower troposphere due to the ENSO-related wind–evaporation–SST feedback (Wang et al. 2000; Lau and Weng 2001; Lim and Kim 2007; Chou et al. 2009; Jin et al. 2016; Zhang et al. 2016), and 2) the southward displacement of the Asian jet stream in the upper troposphere due to the increasing meridional temperature gradient and the thermal wind balance that are forced by the ENSO-related warming in the tropical troposphere (Seager et al. 2003; Lin and Lu 2009; Lin 2010). Both processes can transport more moisture to the middle–lower valley of the Yangtze River and induce more precipitation extremes.

The meridional propagation of the Mei-yu front can be quantified by the pattern of R7x (defined as the wettest period over seven consecutive summer days; Fig. 21.1a). The Mei-yu front is typically located over the south coast of China in May, propagates north

to the Yangtze River basin by June and to northern China by July, and retreats in August with the end of the East Asian monsoon (Chang et al. 2000).

Using the R7x from the observed and simulated precipitation data, this study tried to answer two questions: 1) How extreme is the 2016 Wuhan extreme precipitation in historical context? 2) What are the relative impacts of the recent El Niño event and human-induced warming on the precipitation extreme?

Data and methods. The latest daily precipitation from 1961 to 2016 at ~2400 meteorological stations (Fig. ES21.1) were used in this study. To better show the spatial variability of precipitation, the hourly precipitation in 2016 at ~50 000 auto weather stations in China were used in Fig. 21.1a. These datasets have undergone a series of quality control tests including outlier identification, internal consistency checks, and spatial and temporal consistency checks (Ren et al. 2010; Shen and Xiong 2016).

The Niño-3.4 index derived from HadISST over the region (5°S–5°N, 170°–120°W; Rayner et al. 2003) was calculated for December–February (DJF). Model data were extracted from the CMIP5 archive (Taylor et al. 2011). We evaluated their performance in capturing the observed variabilities of precipitation and the DJF Niño-3.4 index via a Kolmogrov–Smirnoff test ($p > 0.05$; failure to reject the null hypothesis that the modeled precipitation has the same distribution as the observed). The simulations with standard deviations greater than 1.47°C (1.5σ) in the Niño-3.4 index were excluded, because the overestimated ENSO variability can result in its spurious relationship with the East Asia summer rainfall (Fu et al. 2013).

To separate the influences of the El Niño and La Niña events, we further evaluated and selected the all-forcing (ALL) simulations with a significantly positive relationship ($p < 0.1$) between the detrended precipitation and DJF Niño-3.4 time series. The years with the DJF Niño-3.4 index above (below) 0.98°C
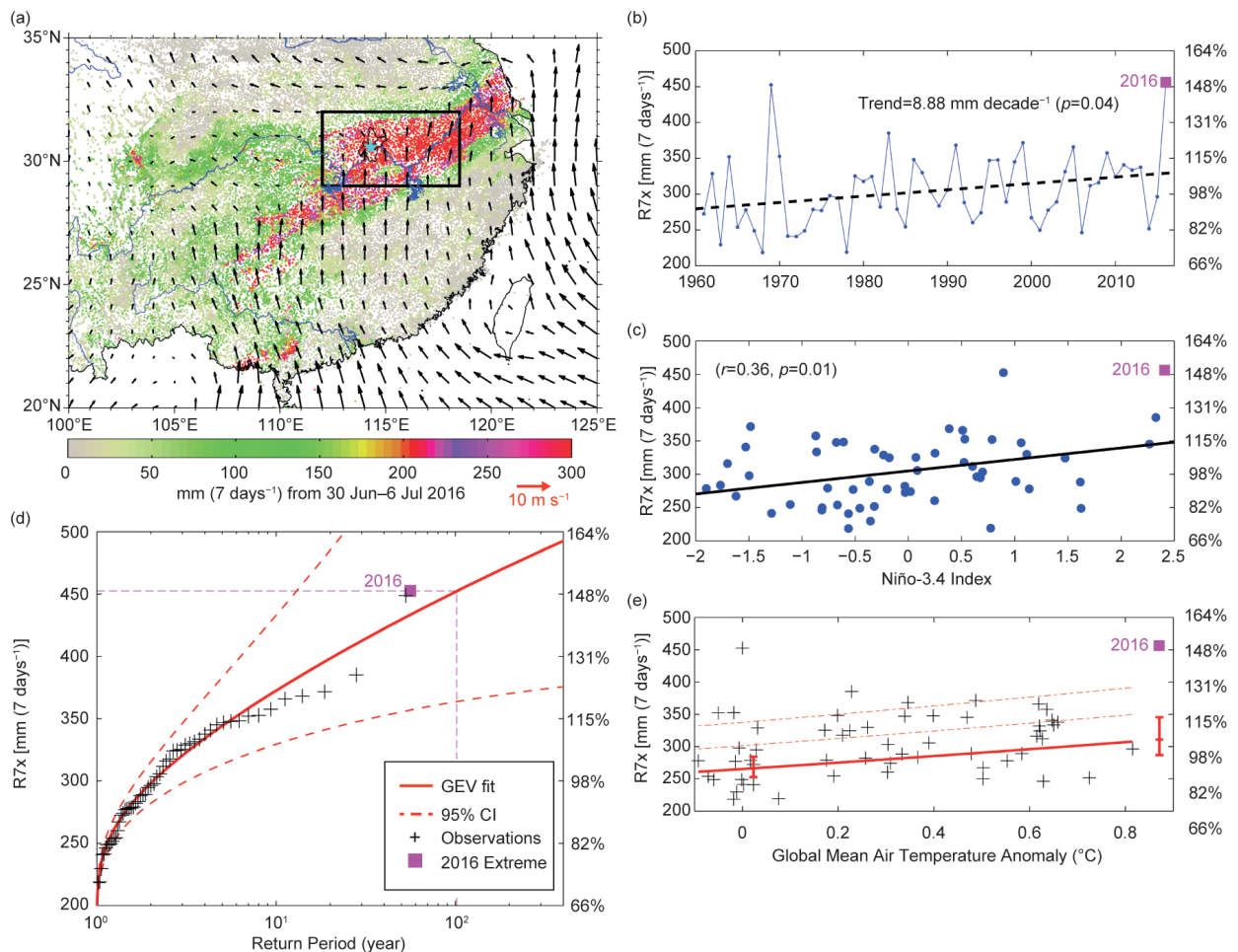
FIG. 21.1. (a) Spatial pattern in precipitation accumulation (R7x, in station dots) and 10-m wind field (in black arrows) during 2016 Wuhan extreme precipitation (30 Jun to 6 Jul 2016). Cyan pentagram shows Wuhan City, China. Blue lines indicate first-class rivers in China. Black rectangle denotes study region (29°–32°N, 112°–118°E). (b) Time series of R7x for black boxed region. 2016 is marked in pink square. (c) R7x for black box region during 1961–2016 is illustrated with DJF Niño-3.4 index. Right axis denotes normalized value (1961–2016 average of R7x). Correlation coefficient is 0.36 (*p* < 0.01), which is almost same as that from detrended series (0.37, *p* < 0.01). (d) GEV fit (in red line) of R7x with 95% confidence intervals (dashed lines). (e) Scaled GEV fit of R7x in which location parameter (thick red line) and scale parameter (difference between red lines) depend exponentially on global mean air temperature anomaly with ratio of two parameters being constant.

(1σ) in the observation and model simulations were regarded to be El Niño (La Niña) years (Black and Karoly 2016; King et al. 2016; Lehner et al. 2016). As a result, 13% (11%) of the years from the twelve models were selected (Table ES21.1).

These CMIP5 models provide 35 simulations with all-forcings (ALL) and natural forcings only (NAT). The ALL runs were extended through 2016 with the Representative Concentration Pathways (RCP) 8.5, because the projected greenhouse gas forcing of RCP8.5 is more consistent with present values than other RCPs (Peters et al. 2013). Values of R7x were estimated with fewer simulations, as three of the models did not provide the necessary daily rainfall data.

We further used model data from a pair of multidecadal ensemble experiments using the latest Met Office HadGEM3-A-based attribution system (N216 L85, 0.83° × 0.56° resolution; Christidis et al. 2013). This attribution system adopts the latest operational dynamical core (Wood and Stainforth 2010) and land surface model (JULES; Best et al. 2011), as well as an updated set of forcings consistent with the CMIP5 generation (Jones et al. 2011). Additionally, this attribution system comprises two sets of 15 stochastic physics experiments spanning the period 1960–2015, one set with all-forcings and the other with natural forcings only. The observed sea surface temperature and sea ice data from HadISST provided a better

estimation of the boundary conditions for the two sets of runs (Christidis et al. 2013).

For consistency with our observational analysis, the model data are area-averaged over the study region (29°–32°N, 112°–118°E; Fig. 21.1a). In addition to R7x, we also did the analysis for monthly (July) precipitation. We applied several statistical techniques to assess the 2016 Wuhan extreme precipitation:

1) A Kolmogorov–Smirnoff test (K–S) was conducted to determine how well the distributions of the simulated precipitation and Niño-3.4 index matched the observed distribution.

2) Both the generalized extreme value (GEV; Schaller et al. 2016) and scaled GEV (van der Wiel et al. 2017) were performed to fit the observed precipitation. In the scaled GEV fit, the location and scale parameters depend exponentially on the global mean air temperature anomaly with the ratio of the two parameters being constant (van der Wiel et al. 2017; more details in the online supplement). The scaled GEV can reflect the influence of global warming on the odds of precipitation extremes. Only the GEV was conducted to fit the modeled precipitation here. Their uncertainties (5%–95%) were estimated with a 1000-member bootstrap.

3) The fraction of attributable risk (FAR = $1 - P_{NAT}/P_{ALL}$) method (Stone and Allen 2005) was used to ascertain the influence of anthropogenic climate change. Bootstrapping (with replacement) was performed 1000 times to estimate the FAR uncertainty.

4) The scaling factors of the simulated extreme precipitation to best match the observations by two-signal analyses of the optimal fingerprinting (OF) method were estimated to evaluate the impact of anthropogenic climate change (Hegerl et al. 1997; Allen and Stott 2003; Ribes et al. 2013). The observed precipitation was regressed onto the multimodel mean precipitation response to NAT and anthropogenic forcings (ANT = ALL − NAT) simultaneously (Wan et al. 2015). A total of 114 chunks, each 55 years long, were obtained from 12 preindustrial control simulations to estimate internal variability (Table ES21.1). Uncertainty ranges (5%–95%) for the scaling factors were evaluated via Monte Carlo simulations. The signal of human-induced warming is considered detected if the scaling factor is significantly greater than zero (Min et al. 2011).

Results. Figure 21.1a illustrates the rainbelt of R7x related to the northward propagation of the Mei-yu front, originating from the South China Sea. Fol-

lowing the 2015/16 strong El Niño event, the study region received a record-breaking average R7x of 456.28 mm. The R7x exhibits a significantly positive correlation with the DJF Niño-3.4 index ($r = 0.36$, $p = 0.01$; Fig. 21.1c).

The R7x over this region shows a significant increasing trend of 8.88 mm decade⁻¹ (Fig. 21.1b). Therefore, we considered the covariance of R7x and global warming and found the location parameter of the scaled GEV for the observed R7x exhibits an upward trend (Fig. 21.1e). A GEV fit of the observed R7x denotes that the 2016 Wuhan extreme precipitation was close to a 1-in-106-year event (Fig. 21.1d). Under the global mean air temperature of 1961, the precipitation extreme like the 2016 Wuhan extreme precipitation (normalized value of 149.69%) is a 1-in-272-year event (Fig. 21.2a). However, it becomes a 1-in-28-year event when the observations are shifted up with global mean air temperature of 2016 (Fig. 21.2a).

To assess the influence of human-induced warming, we compared the changes in the likelihood of the R7x anomaly from the ALL and NAT runs (Fig. 21.2a). Given the El Niño events, 64% [95% confidence intervals (CI): 45%–71%; 26% (95% CI: 20%–39%) for the HadGEM3-A-based system] of the attributable risk of such an event as the 2016 Wuhan extreme precipitation is attributed to human-induced warming (Figs. 21.2a and ES21.3a). Given the La Niña events, such events do not occur in NAT scenarios (as indicated by all the green squares below the observed 2016), whose intense precipitation tail agrees well with that scaled with the global mean air temperature of 1961 (Fig. 21.2a). However, such events do exist in La Niña years in the ALL simulations (Fig. 21.2a).

Compared with the likelihood of the R7x anomaly between El Niño and La Niña events in the ALL simulations, we found a 144% [(95% CI: 119%–182%); 216% (95% CI: 192%–253%) for the HadGEM3-A-based system] increase in the likelihood of such an extreme event in El Niño years (Figs. 21.2a and ES21.3a).

Furthermore, the best estimate of scaling factor of the R7x for anthropogenic forcings is 0.92 (CI: 0.08–1.91; 0.86 with CI 0.18–1.63 in the HadGEM3-A-based system), as derived via two-signal analyses (Figs. 21.2b and ES21.2), suggesting the robustness of detectable human influence on the increasing likelihood for such an event as the 2016 Wuhan extreme precipitation. However, the signal of the natural forcings cannot be detected using the OF method (Fig. 21.2b), likely due to its mixture of the El Niño and La Niña years.

We found that the scaling factors of the R7x for anthropogenic forcings are comparable for the CMIP5 models and the HadGEM3-A-based system via the use of OF method. However, the different attributable risks of such an event as the 2016 Wuhan extreme precipitation to anthropogenic climate change are derived by the FAR method, which may be due to various sensitivities of extreme precipitation to El Niño events between the CMIP5 models and the HadGEM3-A-based system.
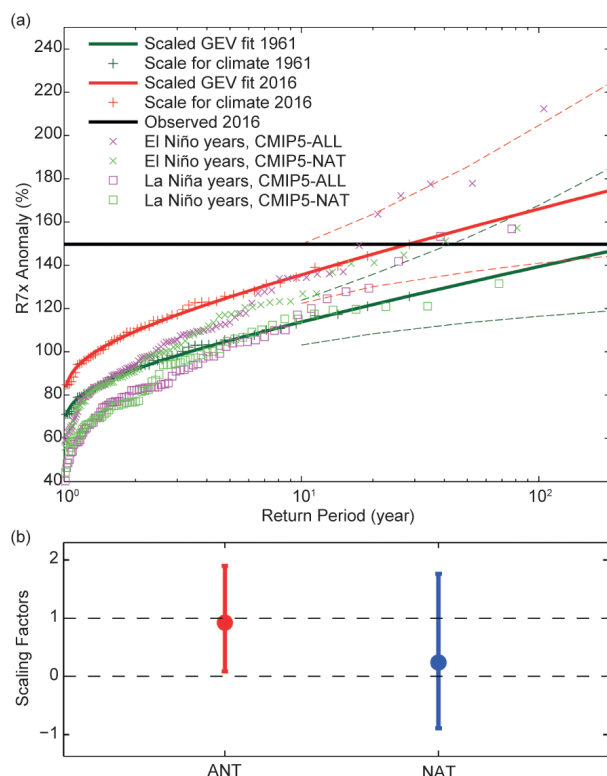

FIG. 21.2. (a) Return period (unit: year) of normalized R7x (1961–2016 average of R7x) from observations and models participating in CMIP5 under different conditions, including ALL and NAT simulations. Pink (green) crosses/squares are in El Niño/La Niña years from ALL (NAT) simulations. Observed R7x is fitted with scaled GEV in which location and scale parameters depend exponentially on global mean air temperature. Red line indicates fit of R7x scaled with global mean air temperature of 2016; dark green line indicates same but for global mean air temperature of 1961. Dashed lines indicate 95% CI. Observations are also plotted twice: one shifted up with trend to 2016 and other shifted down to 1961. GEV is fitted to modeled precipitation. Horizontal black line denotes observed value in 2016. (b) Best estimates of scaling factors of R7x using two-signal analysis of optimal fingerprint method. The 5%–95% uncertainties are estimated by Monte Carlo simulations.

Conclusions and discussion. Our analysis based on R7x indicates that the record-breaking extreme precipitation event of 2016 in China's Wuhan is a 1-in-28-year event in the climate of 2016. It is a 1-in-272-year event in the climate of 1961. CMIP5-based FAR analyses suggest that approximately 60% of the risk of such an event can be attributed to human-induced warming. El Niño has substantially increased the likelihood of such an event as the 2016 Wuhan extreme precipitation by 144%. This study helps to advance our understanding of the role of human-induced warming and El Niño in intense precipitation over East Asia.

If monthly (July) precipitation was used as the index of such an event (normalized value of 260.07% in 2016), 75% [(95% CI: 54%–86%); 21% (95% CI: 17%–29%) for the HadGEM3-A-based system] of the risk can be attributed to human-induced warming using the CMIP5 models (Figs. ES21.3b and ES21.4a), which is consistent with the results based on R7x (Figs. 21.2a and ES21.3a). However, such events do not occur during La Niña years, and anthropogenic forcings make monthly precipitation extremes occur infrequently (Figs. ES21.3b and ES21.4a). Additionally, the signal of human-induced warming in monthly precipitation was significantly detected by the optimal fingerprinting method in the CMIP5 models (Fig. ES21.3c), but not in the HadGEM3-A-based system (Fig. ES21.4b).

We found that the FAR of such events due to human-induced warming in the CMIP5 models is higher than those in the HadGEM3-A-based system, but the increases in the likelihoods of such events in El Niño years compared to those in the La Niña years are smaller in the CMIP5 models than those in the HadGEM3-A-based system. Both the CMIP5 and HadGEM3-A-based system adopt consistent anthropogenic forcings. However, the CMIP5 coupled models have large uncertainties in the modeling of internal variability, and CMIP5 models might be more sensitive to anthropogenic forcings than the HadGEM3-A-based system. The HadGEM3-A-based system tends to better capture the influence of ENSO due to the use of the observed sea ice and sea surface temperature, the latest operational dynamical core (Wood and Stainforth 2010) and its land surface model (Best et al. 2011). Despite all this, the HadGEM3-A-based system does not adopt a fully coupled atmosphere–ocean system, which may introduce some uncertainty when deriving the scaling factor.

REFERENCES

Allen, M., and P. Stott, 2003: Estimating signal amplitudes in optimal fingerprinting, Part I: Theory. *Climate Dyn.*, **21**, 477–491, doi:10.1007/s00382-003 -0313-9.

Best, M., and Coauthors, 2011: The Joint UK Land Environment Simulator (JULES), model description–Part 1: Energy and water fluxes. *Geosci. Model Dev.*, **4**, 677–699, doi:10.5194/gmd-4-677-2011.

Black, M. T., and D. J. Karoly, 2016: Southern Australia's warmest October on record: The role of ENSO and climate change [in "Explaining Extreme Events of 2015 from a Climate Perspective"]. *Bull. Amer. Meteor. Soc.*, **97**, S118–S121, doi:10.1175/BAMS -D-16-0124.1.

Chang, C.-P., Y. Zhang, and T. Li, 2000: Interannual and interdecadal variations of the East Asian summer monsoon and tropical Pacific SSTs. Part I: Roles of the subtropical ridge. *J. Climate*, **13**, 4310–4325, doi:10.1175/1520-0442(2000)013<4310:IAIVOT >2.0.CO;2.

Chou, C., L.-F. Huang, J.-Y. Tu, L. Tseng, and Y.-C. Hsueh, 2009: El Niño impacts on precipitation in the western North Pacific–East Asian sector. *J. Climate*, **22**, 2039–2057, doi:10.1175/2008JCLI2649.1.

Christidis, N., P. A. Stott, A. A. Scaife, A. Arribas, G. S. Jones, D. Copsey, J. R. Knight, and W. J. Tennant, 2013: A new HadGEM3-A-based system for attribution of weather- and climate-related extreme events. *J. Climate*, **26**, 2756–2783, doi:10.1175 /JCLI-D-12-00169.1.

Fu, Y., R. Lu, H. Wang, and X. Yang, 2013: Impact of overestimated ENSO variability in the relationship between ENSO and East Asian summer rainfall. *J. Geophys. Res. Atmos.*, **118**, 6200–6211, doi:10.1002 /jgrd.50482.

Hegerl, G. C., K. Hasselmann, U. Cubasch, J. F. B. Mitchell, E. Roeckner, R. Voss, and J. Waszkewitz, 1997: Multi-fingerprint detection and attribution analysis of greenhouse gas, greenhouse gas-plus-aerosol and solar forced climate change. *Climate Dyn.*, **13**, 613–634, doi:10.1007/s003820050186.

Huang, R., Z. Renhe, and Z. Qingyun, 2000: The 1997/98 ENSO cycle and its impact on summer climate anomalies in East Asia. *Adv. Atmos. Sci.*, **17**, 348–362, doi:10.1007/s00376-000-0028-3.

Jin, D., S. N. Hameed, and L. Huo, 2016: Recent changes in ENSO teleconnection over the western Pacific impacts the eastern China precipitation dipole. *J. Climate*, **29**, 7587–7598, doi:10.1175/JCLI-D-16-0235.1.

Jones, C., and Coauthors, 2011: The HadGEM2-ES implementation of CMIP5 centennial simulations. *Geosci. Model Dev.*, **4**, 543–570, doi:10.5194/gmd -4-543-2011.

King, A. D., G. J. van Oldenborgh, and D. J. Karoly, 2016: Climate change and El Niño increase likelihood of Indonesian heat and drought [in "Explaining Extreme Events of 2015 from a Climate Perspective"]. *Bull. Amer. Meteor. Soc.*, **97** (12), S113–S117, doi:10.1175/BAMS-D-16-0164.1.

Lau, K.-M., and H. Weng, 2001: Coherent modes of global SST and summer rainfall over China: An assessment of the regional impacts of the 1997–98 El Niño. *J. Climate*, **14**, 1294–1308, doi:10.1175/1520 -0442(2001)014<1294:CMOGSA>2.0.CO;2.

Lehner, F., A. P. Schurer, G. C. Hegerl, C. Deser, and T. L. Frölicher, 2016: The importance of ENSO phase during volcanic eruptions for detection and attribution. *Geophys. Res. Lett.*, **43**, 2851–2858, doi:10.1002/2016GL067935.

Lim, Y.-K., and K.-Y. Kim, 2007: ENSO impact on the space–time evolution of the regional Asian summer monsoons. *J. Climate*, **20**, 2397–2415, doi:10.1175 /JCLI4120.1.

Lin, Z.-D., 2010: Relationship between meridional displacement of the monthly East Asian jet stream in the summer and sea surface temperature in the tropical central and eastern Pacific. *Atmos. Oceanic Sci. Lett.*, **3**, 40–44, doi:10.1080/16742834.2010.11446840.

——, and R. Lu, 2009: The ENSO's effect on eastern China rainfall in the following early summer. *Adv. Atmos. Sci.*, **26**, 333–342, doi:10.1007/s00376-009 -0333-4.

Min, S.-K., X. Zhang, F. W. Zwiers, and G. C. Hegerl, 2011: Human contribution to more-intense precipitation extremes. *Nature*, **470**, 378–381, doi:10.1038/nature09763.

Peters, G. P., and Coauthors, 2013: The challenge to keep global warming below 2°C. *Nat. Climate Change*, **3**, 4–6, doi:10.1038/nclimate1783.

Rayner, N., D. E. Parker, E. B. Horton, C. K. Folland, L. V. Alexander, D. P. Rowell, E. C. Kent, and A. Kaplan, 2003: Global analyses of sea surface temperature, sea ice, and night marine air temperature since the late nineteenth century. *J. Geophys. Res.*, **108**, 4407, doi:10.1029/2002JD002670.

Ren, Z. H., and Coauthors, 2010: Quality control procedures for hourly precipitation data from automatic weather stations in China (in Chinese with English abstract). *Meteor. Mon.*, **36**, 123–132.

Ribes, A., S. Planton, and L. Terray, 2013: Application of regularised optimal fingerprinting to attribution. Part I: method, properties and idealised analysis. *Climate Dyn.*, **41**, 2817–2836, doi:10.1007/s00382-013-1735-7.

Schaller, N., and Coauthors, 2016: Human influence on climate in the 2014 southern England winter floods and their impacts. *Nat. Climate Change*, **6**, 627–634, doi:10.1038/nclimate2927.

Seager, R., N. Harnik, Y. Kushnir, W. Robinson, and J. Miller, 2003: Mechanisms of hemispherically symmetric climate variability. *J. Climate*, **16**, 2960–2978, doi:10.1175/1520-0442(2003)016<2960:MOHSCV>2.0.CO;2.

Shen, Y., and A. Xiong, 2016: Validation and comparison of a new gauge-based precipitation analysis over mainland China. *Int. J. Climatol.*, **36**, 252–265, doi:10.1002/joc.4341.

Stone, D. A., and M. R. Allen, 2005: The end-to-end attribution problem: From emissions to impacts. *Climate Change*, **71**, 303–318, doi:10.1007/s10584-005-6778-2.

Taylor, K. E., R. J. Stouffer, and G. A. Meehl, 2011: An overview of CMIP5 and the experiment design. *Bull. Amer. Meteor. Soc.*, **93**, 485–498, doi:10.1175/BAMS-D-00094.1.

van der Wiel, K., and Coauthors, 2017: Rapid attribution of the August 2016 flood-inducing extreme precipitation in south Louisiana to climate change. *Hydrol. Earth Syst. Sci.*, **21**, 897–921, doi:10.5194/hess-21-897-2017.

Wan, H., X. Zhang, F. Zwiers, and S.-K. Min, 2015: Attributing northern high-latitude precipitation change over the period 1966-2005 to human influence. *Climate Dyn.*, **45**, 1713–1726, doi:10.1007/s00382-014-2423-y.

Wang, B., R. Wu, and X. Fu, 2000: Pacific–East Asian teleconnection: How does ENSO affect East Asian climate? *J. Climate*, **13**, 1517–1536, doi:10.1175/1520-0442(2000)013<1517:PEATHD>2.0.CO;2.

Wood, L., and A. Stainforth, 2010: ENDGame Formulation v3.01. Met Office [United Kingdom] paper.

Zhang, W., H. Li, M. F. Stuecker, F.-F. Jin, and A. G. Turner, 2016: A new understanding of El Niño's impact over East Asia: Dominance of the ENSO combination mode. *J. Climate*, **29**, 4347–4359, doi:10.1175/JCLI-D-15-0104.1.

22. DO CLIMATE CHANGE AND EL NIÑO INCREASE LIKELIHOOD OF YANGTZE RIVER EXTREME RAINFALL?

Xing Yuan, Shanshan Wang, and Zeng-Zhen Hu

Anthropogenic climate change has increased the risk of 2016 Yangtze River extreme summer rainfall by 17%–59%, and the increase could reach 37%–91% in El Niño years.

Introduction. In June–July 2016, a barrage of extreme rainfall hit the middle and lower reaches of Yangtze River in eastern China, which caused severe urban inundations in large cities such as Wuhan and Nanjing, and resulted in direct economic loss of 70 billion RMB (about $10 billion U.S. dollars). Similar to the 1998 Yangtze River extreme rainfall, the 2016 extreme rainfall coincided with the decaying phase of 2015/16 super El Niño through Pacific–East Asian teleconnection which enhanced the west Pacific subtropical high (WPSH) and weakened the East Asia summer monsoon (EASM), resulting in an anomalously anticyclonic circulation pattern over the northwestern Pacific that brought lots of atmospheric moisture from the Pacific to the Yangtze River (Wang et al. 2000; Yuan et al. 2017). A possible mechanism for the lag-impact of El Niño/Southern Oscillation (ENSO) on East Asia summer climate is the Indo–western Pacific Ocean capacitor (IPOC), where the North Indian Ocean warming after El Niño plays an important role (Xie et al. 2016). The spatial distribution of the 2016 extreme rainfall, however, is different from that in 1998 with a northward shift of the ENSO-forced teleconnection (Figs. 22.1e,f), which raises the question of whether the climate change and El Niño increase the likelihood of Yangtze River extreme rainfall. This paper will examine the 2016 extreme rainfall in a historical context, and investigate the effects of anthropogenic climate change and natural climate variability (e.g., ENSO) on the likelihood of the extreme rainfall.

Data and methods. Daily rainfall observations from 2474 China Meteorological Administration (CMA) stations provided by CMA National Meteorological Information Center (NMIC) were interpolated into 0.25-degree grid cells during June–July of 1951–2016 by using the inverse quadratic distance weighting method (Yuan et al. 2016). Detecting the human influence on precipitation change is a grand challenge especially at regional or local scales (Hu et al. 2003; Zhang et al. 2007). Therefore, daily rainfall at 0.25-degree grid cells were averaged over the middle and lower reaches of Yangtze River (27°–34°N, 110°–123°E) for a more robust analysis. The area-averaged maximum 10-day rainfall amounts (RX10day) during each June–July, which is a good indicator for flooding, was selected to represent the extreme rainfall over Yangtze River. The generalized extreme value (GEV) distribution was used to fit the extreme rainfall distribution and to estimate the return period in this study.

To analyze the ENSO impact on the extreme rainfall, the extended reconstructed sea surface temperature version 4 (ERSSTv4; Huang et al. 2014) monthly data during 1854–2016 was used as SST observations in this study. An El Niño event was defined as the mean Niño-3.4 (5°S–5°N, 120°–170°W) SST anomaly during preceding December–February (DJF) exceeding 0.95°C (1σ) of the Niño-3.4 SST time series; a La Niña event was defined by a mean SST anomaly of less than −0.95°C. Note that the same criterion (> 0.95°C) was also applied for the model simulations for the ENSO identification.

Daily rainfall and SST simulations from 14 atmosphere–ocean coupled general circulation models (CGCMs; see Table ES22.1 for the model list) provided by the Coupled Model Intercomparison Project Phase
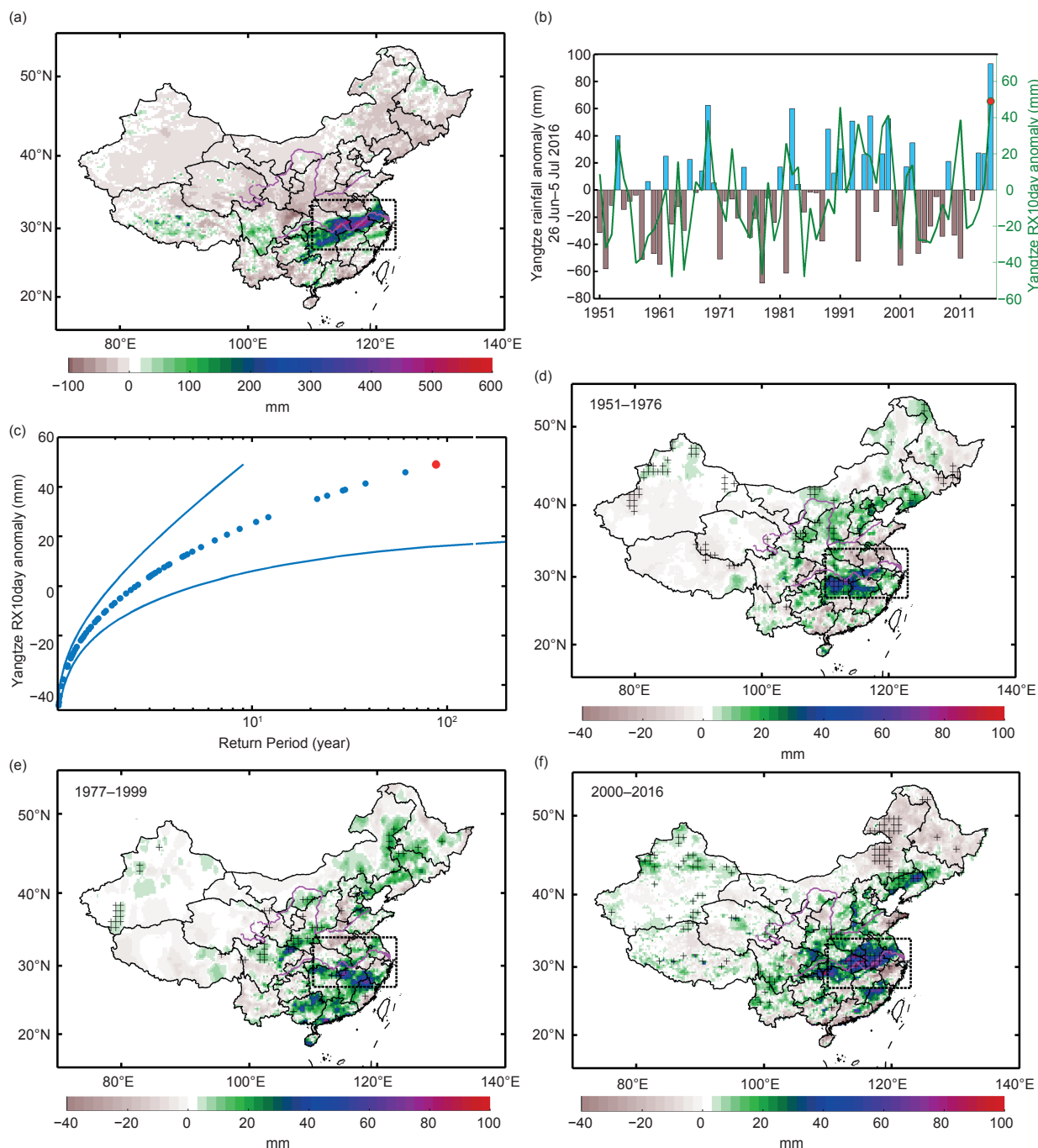
Fig. 22.1. (a) Rainfall anomaly (colors; mm) in 26 Jun–5 Jul 2016 relative to 1981–2010 climatology in CMA/NMIC observations. (b) Time series of 10-day accumulated rainfall anomaly (bar plot; mm) of 26 Jun–5 Jul averaged over middle and lower reaches of Yangtze River [27°–34°N, 110°–123°E; dashed box in (a)] and Yangtze River RX10day anomaly during Jun–Jul (green line; mm). (c) Return period (years) and 95% CI for RX10day anomaly; red dot represents 2016. (d)–(f) Regressed RX10day anomaly (colors; mm) against Niño-3.4 SST in the preceding DJF during 1951–76, 1977–99, and 2000–16, respectively; stippling indicates a 90% confidence level ($p < 0.1$).

5 (CMIP5; Taylor et al. 2012) were used in this study. For each CGCM, several pairs of realizations driven by all (ALL) and natural only (NAT) forcings during 1950–2005 were used. A number of evaluation tests were carried out to identify models: 1) as compared with observation, variability of both simulated consecutive 10-day rainfall averaged over middle and lower Yangtze River and DJF Niño-3.4 SST should pass the Kolmogorov–Smirnov test with $p < 0.05$; 2) standard deviations of model simulated Niño-3.4 SST

should be less than 1.43°C (1.5σ of observed Niño-3.4 SST); and 3) both ALL and NAT experiments should produce a positive correlation between DJF Niño-3.4 and June–July RX10day. After evaluation, six CMIP5 models with 12 realizations (red bold in Table ES22.1) were selected to determine the effects of anthropogenic climate change and ENSO on the Yangtze River extreme rainfall. The fraction of attributable risk (FAR; Stott et al. 2004) method that compares the event tail probabilities (P) between CMIP5/NAT and CMIP5/ALL simulations (FAR = $1-P_{NAT}/P_{ALL}$), was used to assess the contribution of anthropogenic climate change. For instance, a value of FAR = 0.5 suggests that the risk of an extreme event is doubled over natural conditions due to anthropogenic climate change. Bootstrapping was performed 1000 times to estimate the FAR uncertainty.

Results. Figure 22.1a shows the spatial distribution of 10-day accumulated rainfall anomaly during 26 June–5 July in 2016. Extreme rainfall was found to have occurred over the middle and lower reaches of Yangtze River, with anomaly exceeding 300–400 mm within 10 days. Moreover, the area-averaged 10-day rainfall anomaly in 2016 is ranked as the first during recent 66 years (1951–2016) according to the CMA/ NMIC observations (bar plot in Fig. 22.1b). Figure 22.1c shows that the RX10day extreme rainfall index in 2016 is also ranked as the first during 1951–2016, with a return period of 88 years (>8 years at 95% confidence level).

The Yangtze River extreme rainfall occurred in the context of the 2015/16 super El Niño. Actually there were statistically significant correlations between Yangtze River extreme summer rainfall and preceding Niño-3.4 index. Figure ES22.1 shows that the RX10day index during summer positively correlated with the Niño-3.4 index in the preceding cold seasons, with the highest correlation for DJF Niño-3.4 index. To assess the El Niño impacts spatially, the RX10day at each 0.25-degree grid cell were regressed against Niño-3.4 index during preceding DJF (Wu et al. 2003). Figures 22.1d–f show the regressed RX10day for the periods of 1951–76, 1977–99, and 2000–16, respectively, where the ENSO forced teleconnection pattern shifts from southeastern China to the middle and lower reaches of Yangtze River after 2000, resulting in a pattern (Fig. 22.1f) that is similar to the 2016 extreme rainfall (Fig. 22.1a). This suggests the northward shift of the ENSO forced teleconnection may increase the risk of extreme rainfall over Yangtze River. The cause of the shift is still unclear, and one

possibility is the decadal internal variability, such as interdecadal Pacific oscillation (IPO). For example, Song and Zhou (2016) found that the IPO plays a dominant role in the decadal variation of the relationship between ENSO and East Asian summer monsoon during the twentieth century.

Figure ES22.1 also shows that although the correlation is statistically significant, it is actually very weak (less than 0.25). This implies that other factors, such as sea–ice, land surface processes, stratosphere, and unforced internal variability due to the chaos of the weather, may play a role. Moreover, Gao et al. (2014) argued that only a small fraction of monthly precipitation in eastern China is predictable. He et al. (2016) also indicated that only about 18% of the interannual variation of rainfall over East Asian land can be explained by SST. Tropical Indian and Pacific Oceans each account for approximately 6% of the total variance of rainfall. These studies document the dominant role of atmospheric internal dynamical processes in variation of East Asian summer rainfall. In fact, Sterl et al. (2007) showed that changes in the strength of ENSO teleconnection could be very small and only detectable on centennial time scales.

To explore the causality of the risk change, CMIP5 model simulations with ALL and NAT-only forcings were used. Similar to other CGCM applications (Yuan and Wood 2013; Wang et al. 2017), CMIP5 models seem to overrepresent the ENSO–seasonal mean rainfall teleconnection (not shown) and under-represent the ENSO–extreme rainfall teleconnection (Fig. ES22.2). Models' simulations on the teleconnection pattern, however, can be improved to some extent with the consideration of anthropogenic forcings (Fig. ES22.2), suggesting that anthropogenic climate change may play an important role in influencing the likelihood of the Yangtze River extreme rainfall.

Therefore, the probability density functions (PDFs) for RX10day of CMIP5 model simulations, were calculated by fitting GEV distributions. The FAR for the RX10day heavier than the 2016 case is 0.38 (±0.21), with the return period decreased from 72 years [95% confidence interval (CI): 34–238 years] to 45 years (CI: 24–120 years) under the influence of the anthropogenic climate change (Fig. 22.2a). For the results during El Niño years (Fig. 22.2b), there is a more robust difference between the simulations with and without anthropogenic forcings, with FAR changed to 0.64 (±0.27). Figure 22.2b also shows that an extreme rainfall event like that in 2016 is most likely to occur in El Niño years with ALL forcings (red square), and least likely in La Niña years without
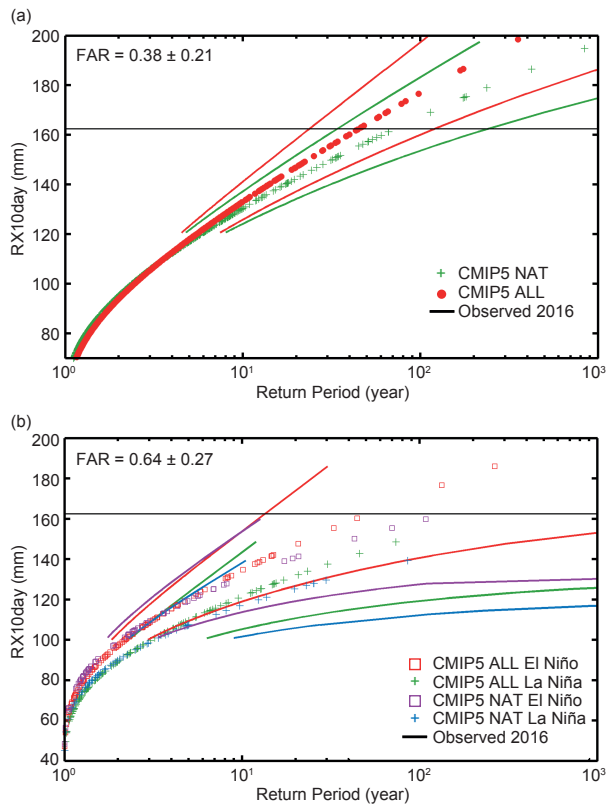
Fig. 22.2. (a) Return periods for Yangtze River RX10day anomaly from CMIP5 simulations under ALL and NAT forcings during 1950–2005. (b) As in (a), but during El Niño or La Niña years (see text for definitions).

anthropogenic forcings (blue plus). The results for El Niño years without anthropogenic forcings (purple square) and La Niña years with all forcings (green plus) are between them. Under ALL forcing conditions, El Niño years increase the likelihood of having extreme rainfall from La Niña years by 416% (±200%).

Conclusions. Extreme rainfall hit the middle and lower reaches of Yangtze River during the summer of 2016, where the anomaly exceeded 300–400 mm within 10 days, ranking as the heaviest 10-day rainfall since 1951. In fact, the observed ENSO-extreme rainfall teleconnection shows a northward shift after 2000 and may increase the risk of extreme rainfall over the Yangtze River, although such northward shift of the teleconnection is compatible with natural variability. By using CMIP5 model simulations, it is found that the likelihood of Yangtze River extreme rainfall such as that occurring in 2016 has increased by about 38% (±21%) due to anthropogenic climate change, and the likelihood can be increased by 64% (±27%) in El Niño years. There are large uncertainties, however, both because of complicated causes of Yangtze River ex-

treme rainfall, and the deficiencies in current CMIP5 models in representing ENSO, ENSO-teleconnection, and extreme rainfall processes.

REFERENCES

Gao, Z., Z.-Z. Hu, B. Jha, S. Yang, J. Zhu, B. Shen, and R. Zhang, 2014: Variability and predictability of Northeast China climate during 1948–2012. *Climate Dyn.*, **43**, 787–804, doi:10.1007/s00382-013-1944-0.

He, C., B. Wu, C. Li, A. Lin, D. Gu, Z. Zheng, and T. Zhou, 2016: How much of the interannual variability of East Asian summer rainfall is forced by SST? *Climate Dyn.*, **47**, 555–565, doi:10.1007/s00382-015-2855-z.

Hu, Z.-Z., S. Yang, and R. Wu, 2003: Long-term climate variations in China and global warming signals. *J. Geophys. Res.*, **108**, 4614, doi:10.1029/2003JD003651.

Huang, B., and Coauthors, 2014: Extended reconstructed sea surface temperature version 4 (ERSST.v4): Part I. Upgrades and intercomparisons. *J. Climate*, **28**, 911–930, doi:10.1175/JCLI-D-14-00006.1.

Song, F., and T. Zhou, 2015: The crucial role of internal variability in modulating the decadal variation of the East Asian summer monsoon–ENSO relationship during twentieth century. *J. Climate*, **28**, 7093–7107, doi:10.1175/JCLI-D-14-00783.1.

Sterl, A., G. J. van Oldenborgh, W. Hazeleger, and G. Burgers, 2007: On the robustness of ENSO teleconnections. *Climate Dyn.*, **29**, 469–485, doi:10.1007/s00382-007-0251-z/.

Stott, P. A., D. A. Stone, and M. R. Allen, 2004: Human contribution to the European heatwave of 2003. *Nature*, **432**, 610–614, doi:10.1038/nature03089.

Taylor, K. E., R. J. Stouffer, and G. A. Meehl, 2012: An overview of CMIP5 and the experiment design. *Bull. Amer. Meteor. Soc.*, **93**, 485–498, doi:10.1175/BAMS-D-00094.1.

Wang, B., R. Wu, and X. Fu, 2000: Pacific–East Asian teleconnection: How does ENSO affect East Asian climate? *J. Climate*, **13**, 1517–1536, doi:10.1175/1520 -0442(2000)013<1517:PEATHD>2.0.CO;2.

Wang, S., X. Yuan, and Y. Li, 2017: Does a strong El Niño imply a higher predictability of extreme drought? *Sci. Rep.*, **7**, 40741, doi:10.1038/srep40741.

Wu, R., Z.-Z. Hu, and B. P. Kirtman, 2003: Evolution of ENSO-related rainfall anomalies in East Asia. *J. Climate*, **16**, 3742–3758, doi:10.1175/1520 -0442(2003)016<3742:EOERAI>2.0.CO;2.

Xie, S.-P., Y. Kosaka, Y. Du, K. Hu, J. S. Chowdary, and G. Huang, 2016: Indo–western Pacific Ocean capacitor and coherent climate anomalies in post-ENSO summer: A review. *Adv. Atmos. Sci.*, **33**, 411–432, doi:10.1007/s00376-015-5192-6.

Yuan, X., and E. F. Wood, 2013: Multimodel seasonal forecasting of global drought onset. *Geophys. Res. Lett.*, 40, 4900–4905, doi:10.1002/grl.50949.

——, F. Ma, L. Wang, Z. Zheng, Z. Ma, A. Ye, and S. Peng, 2016: An experimental seasonal hydrological forecasting system over the Yellow River basin-Part 1: Understanding the role of initial hydrological conditions. *Hydrol. Earth Syst. Sci.*, **20**, 2437–2451, doi:10.5194/hess-20-2437-2016.

Yuan, Y., H. Gao, W. Li, Y. Liu, L. Chen, B. Zhou, and Y. Ding, 2017: The 2016 summer floods in China and associated physical mechanisms: A comparison with 1998. *J. Meteor. Res.*, **31**, 216–277, doi:10.1007 /s13351-017-6192-5.

Zhang, X., F. W. Zwiers, G. C. Hegerl, F. H. Lambert, N. P. Gillett, S. Solomon, P. A. Stott, and T. Nozawa, 2007: Detection of human influence on twentieth-century precipitation trends. *Nature*, **448**, 461–466, doi:10.1038/nature06025.

23. HUMAN INFLUENCE ON THE RECORD-BREAKING COLD EVENT IN JANUARY OF 2016 IN EASTERN CHINA

Cheng Qian, Jun Wang, Siyan Dong, Hong Yin, Claire Burke,
Andrew Ciavarella, Buwen Dong, Nicolas Freychet,
Fraser C. Lott, and Simon F. B. Tett

Anthropogenic influences are estimated to have reduced the likelihood of an extreme cold
event in midwinter with the intensity equal to or stronger than the record of 2016
in eastern China by about two-thirds.

Introduction. A strong cold surge occurred during 21–25 January 2016 affecting most areas of China, especially eastern China (Fig. 23.1a). Daily mean temperatures dropped by up to 10°C–18°C within this event at individual stations in this region (CMA 2017) and broke daily minimum temperature (T_{min}) records at many stations (Fig. 23.1b). The area averaged anomaly of T_{min} over the region (20°–44°N, 100°–124°E) for this pentad was −4°C (−2.2 standard deviations) relative to the 1961–90 normal. This was the lowest temperature recorded, for 21–25 January, since modern meteorological observations started in 1960 (Fig. 23.1c). According to press reports (CMA 2017), 1.18 billion people were in the area where daily mean temperatures fell by more than 6°C within this event. On 24 January, the snowline even reached Guangzhou and the Pearl River Delta in southern China. This was the lowest latitude recorded since 1951. A sharp temperature drop, low temperatures, and associated freezing rain and snow caused widespread disruptions to transport, power supply, and public services, and damage to agriculture in southern China (http://mt.sohu.com/20160210 /n437184257.shtml; last accessed 19 March 2017).

Cold extremes have been gaining wide attention in many parts of midlatitude Eurasia and North America in recent years (e.g., Mori et al. 2014; Trenary et al. 2016; McCusker et al. 2016). It is controversial whether they are related to Arctic warming. Some studies suggested that greenhouse-gas-induced global and Arctic warming may enhance the meandering of the jet stream thus increasing the probability of cold extremes in certain regions (Francis and Vavrus 2015), and that the Arctic warming in the Barents–Kara Seas is closely connected to the cooling in eastern Asia (Kug et al. 2015) and robust Arctic sea–ice influence on recent increases in Eurasian cold winters (Mori et al. 2014). However, other studies have suggested that the Arctic warming does not cause midlatitude cooling (e.g., McCusker et al. 2016; Sun et al. 2016).

Given the impact of this cold event in China and the controversy whether Asian midlatitude cold surges are becoming more likely as a consequence of Arctic warming, it is compelling to investigate how much anthropogenic forcing agents have affected the probability of cold events with an intensity equal to or larger than the January 2016 extreme event. We use the Met Office Hadley Centre system for attribution of extreme weather and climate events (ACE; Christidis et al. 2013; Burke and Stott 2017) and station observations to investigate the effect of anthropogenic forcings on the likelihood of such a cold event.

Data. We used observational data for T_{min} from 744 national Reference Climatic and Basic Meteorological Stations from the China National Meteorological Information Centre for the period 1960–2016. From 1960 to 2013, the updated temperature dataset
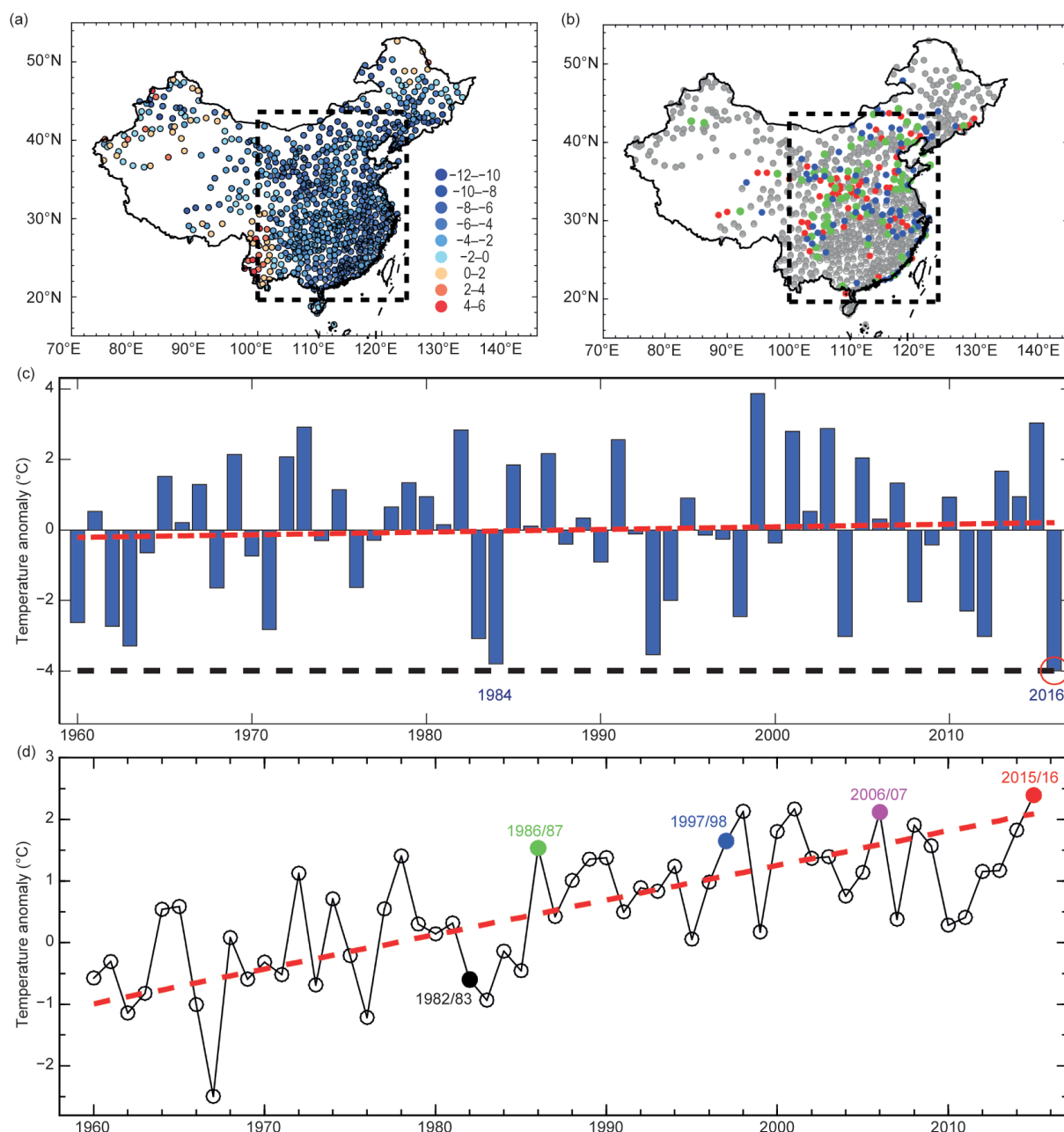
Fɪɢ. 23.1. (a) Observed pentad T_{min} anomalies (°C; relative to 1961–90 climatology) for 21–25 Jan 2016. Dashed box indicates study region (20°–44°N, 100°–124°E); (b) Colored dots represent stations that in 2016 recorded coldest (red), second coldest (green) and third coldest (blue) pentad T_{min} for any 21–25 Jan since 1960; (c) Time series of area-weighted average 21–25 pentad T_{min} anomaly °C over study region for 1960–2016. Red line shows linear trend of 0.078°C decade^{-1}; (d) Averaged winter T_{min} anomalies °C and corresponding linear trend over 1960/61–2015/16 in target region. Labeled dots show El Niño years

developed by Li et al. (2015) is used. This dataset was homogenized using the Multiple Analysis of Series for Homogenization (MASH) method (Szentimrey 1999) and was improved in terms of physical consistency among diurnal temperature records (Li et al. 2015), such that the temperature observations were quality-controlled and adjusted for most nonclimatic biases due to the changes in the local observing system, such as station relocation. After 2013, it is updated directly from those stations that have continuous records to January 2016.

We used simulations of the Hadley Centre Global Environmental Model version 3 Global Atmosphere 6.0 (HadGEM3-GA6; Walters et al. 2017) at N216

resolution. Daily outputs of T_{min} at approximately $0.56° × 0.83°$ horizontal resolution are used. Fifteen members of the historical (all forcing) 1961–90 period (histClim) are compared with observations to estimate the model bias. Two ensembles of 525 members with and without anthropogenic forcings are provided for January 2016 to estimate the risk of such a cold event. One of these ensembles (histALL) uses historical anthropogenic and natural forcings and is an extension of the previous 15-member histClim runs. The other ensemble (histNAT) uses natural forcings only and is a continuation of a historical natural ensemble of 15 members, complementary to the histClim runs. Beyond the initial conditions of this continuation, the only difference between each of the 525 members in these experiments is the stochastic physics seed, and they are therefore considered equivalent. The boundary conditions for the histNAT experiments (see online supplement) are the same as in previous experiments using an earlier version of Met Office attribution system (Christidis et al. 2013).

Methods. For each station, the observed daily T_{min} anomaly relative to 1961–90 was calculated, from which the pentad-mean T_{min} anomaly for 21–25 January (PT_{min}) of each year was computed. These PT_{min} were gridded into $2° × 2°$ grid boxes for the region (20°–44°N, 100°–124°E) by simply averaging the available station data within a $2° × 2°$ grid box. This region was chosen because the PT_{min} had a large negative anomaly in most stations of this region (Fig. 23.1a). We also calculated the regional average winter (December–February, DJF) T_{min} anomalies over the region.

To make observations and simulations comparable, the following steps were adopted: 1) For both histALL and histNAT ensembles, daily anomalies (relative to 1961–90 normal for histClim) were computed removing any constant model bias; 2) PT_{min} for 2016 in histALL and histNAT runs were calculated and a land–sea mask applied; 3) These masked anomalies were regridded to the same $2° × 2°$ grid boxes as the observations using linear interpolation and masked by the observational gridded data; 4) Gridded observations were then masked by this simulated data; 5) The area-weighted average PT_{min} of both the observations (Fig. 23.1c) and the 525 histALL and histNAT runs were then computed.

To estimate the attributable risk (Stott et al. 2004, 2016) of such an extreme cold event in midwinter, area-weighted average T_{min} anomalies of 9 non-overlapping pentads from the coldest period in the climatology (1 January to 15 February) from the 525 histALL and histNAT runs were calculated and fitted to probability distribution functions (PDFs). Goodness-of-fit was tested for Gaussian and generalized extreme value (GEV) distributions. The GEV fit was found to be the most appropriate (Fig. ES23.1) and return periods of an event like the one in 2016 were estimated from this GEV fit. The shape, scale, and location parameters of the GEV fit for histALL (histNAT) runs are −0.28, 2.35, and −0.21 (−0.31, 2.25, and −1.39), respectively.

Results. Figure 23.1a shows that during this extreme cold event, most stations in eastern China recorded negative PT_{min}, with the largest negative anomalies below −4°C. The PT_{min} broke the historical low temperature records for the same pentad at more than twenty stations, and many more recorded the second and third coldest pentad since 1960 (Fig. 23.1b). The linear trend in the regional average PT_{min} ($RAPT_{min}$; Fig. 23.1c) is 0.078°C decade⁻¹ with 95% confidence interval (−0.26, 0.45), which is not statistically significant. This trend slope and significance testing is based on the nonparametric Sen's slope and Mann–Kendall test taking into account the first-order autocorrelation estimated by an iterative method (Wang and Swail 2001; WS2001). The 2016 $RAPT_{min}$ is the coldest 21–25 January in the record, which started 1960, beating the previous record in 1984 (Fig. 23.1c). Figure 23.1d shows that this cold event occurred in a background of the warmest winter T_{min} since 1960, showing a warming trend of 0.56 (−0.05, 1.0054) °C decade⁻¹ estimated also by WS2001, and that El Niño tends to be associated with warm winters (four-out-of-five El Niño years since 1982).

Figure 23.2a shows an overall mean shift toward warmer anomalies in histALL relative to histNAT indicating that human influences have reduced the risk of extreme cold events. To estimate the attributable risk ratio, we defined a threshold of −4°C based on the observed $RAPT_{min}$ for 2016. The probability (P0) of an event equal to or colder than this threshold in midwinter in histNAT is 6.8%, whereas in histALL (P1) it is only 2.3%. The risk ratio (P1/P0) is approximately 34%, which suggests that human influences have reduced the risk of such an extreme cold event by about 66%. We estimated the uncertainty of P1/P0 by resampling the PDF 1000 times (Pall et al. 2011). Results show that P1/P0 lies between 31.1% and 37.8% (one standard deviation), suggesting that human influences reduced the probability of such a cold event by approximately two
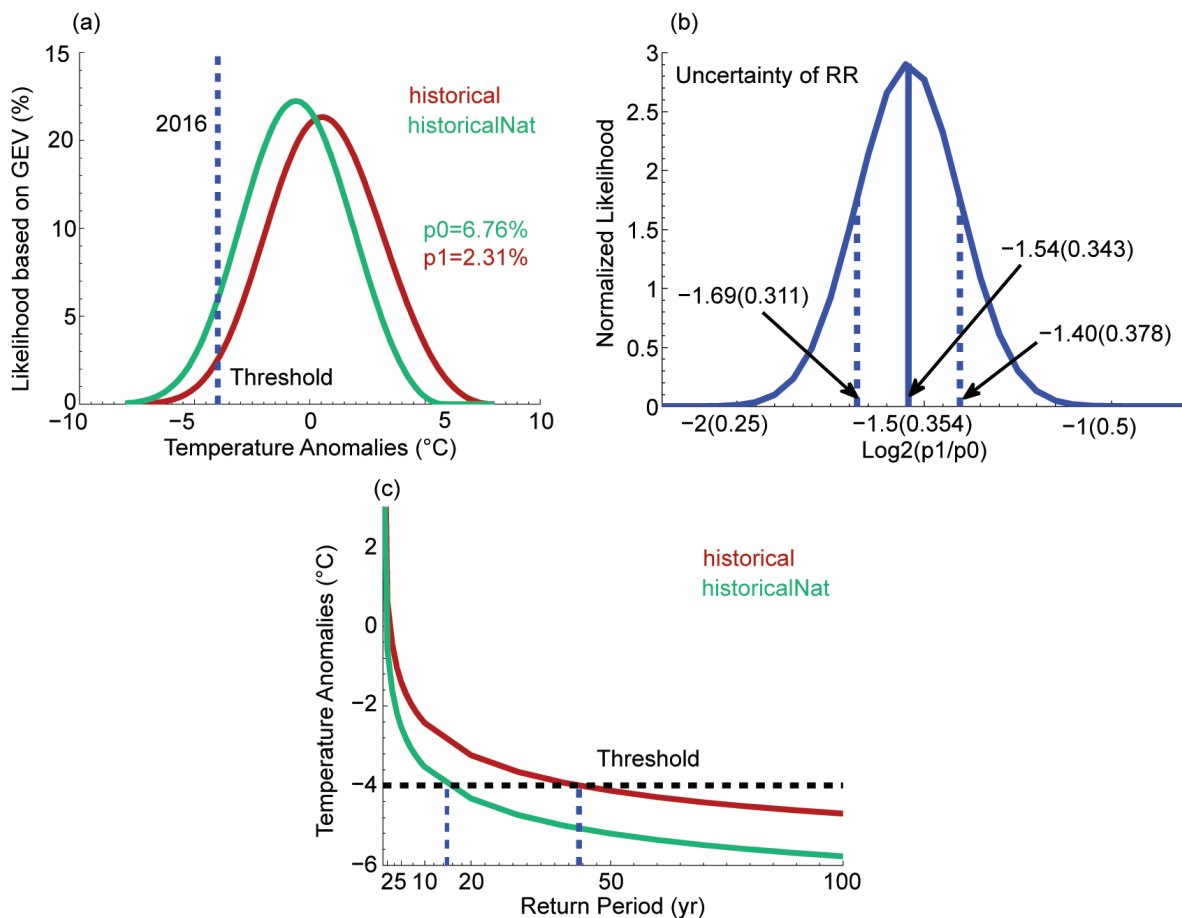
Fig. 23.2. (a) GEV distribution fit to 9 × 525 regional average pentad T_{min} anomalies °C during midwinter 2016 in eastern China from histALL simulations (red line; with anthropogenic and natural forcings) and that from histNAT simulations (green line; only with natural forcings). Dashed line indicates threshold, which is regional average pentad T_{min} anomaly of 21–25 Jan 2016 in observations. **(b)** Uncertainty in attributable risk ratio of such extreme cold event due to anthropogenic influences. Dashed lines indicate one standard deviation. **(c)** Return period (years) of extreme cold event with intensity equal or larger than extreme cold event of Jan 2016 in eastern China in histALL (red line) and histNAT simulations (green line). Black dashed line indicates threshold used in (a).

thirds (Fig. 23.2b). The estimated return period of RAPT$_{min}$ like January 2016 is one-in-15 years with only natural forcings while it is extended to one-in-43 years with anthropogenic forcings (Fig. 23.2c).

Conclusions and discussion. Cold winters in China are expected to become rarer in a warming climate. By employing high quality station observations and model simulations, we estimate that anthropogenic influences have reduced the occurrence probability of an extreme cold event with the intensity equal to or stronger than the record in 2016 by approximately two-thirds. Conversely, if there were no anthropogenic influences, the probability of an extreme cold pentad in 2016 would be more than double. The return period of such a record cold event is estimated to have been extended by about 28 years due to human

influences. Our results are in line with McCusker et al. (2016) and Sun et al. (2016) and agree with Trenary et al. (2016) that despite severe cold surges and record-breaking extreme cold-day occurrences during 2016, winters have become warmer. Our results also imply that even under human-induced warming, extreme cold events can still occur as a result of natural variability, such as Arctic Oscillation, which was believed to be responsible for the reporting event (Cheung et al. 2016).

REFERENCES

Burke, C., and P. Stott, 2017: Impact of anthropogenic climate change on the East Asian summer monsoon. *J. Climate*, **30**, 5205–5220, doi:10.1175/JCLI-D-16-0892.1.

Cheung, H. H. N., W. Zhou, M. Y. T. Leung, C. M. Shun, S. M. Lee, and H. W. Tong, 2016: A strong phase reversal of the Arctic Oscillation in midwinter 2015/2016: Role of the stratospheric polar vortex and tropospheric blocking. *J. Geophys. Res. Atmos.*, 121, 13,443–13,457, doi:10.1002/2016JD025288.

Christidis, N., P. A. Stott, A. A. Scaife, A. Arribas, G. S. Jones, D. Copsey, J. R. Knight, and W. J. Tennant, 2013: A new HadGEM3-A-based system for attribution of weather- and climate-related extreme events. *J. Climate*, **26**, 2756–2783, doi:10.1175/JCLI-D-12-00169.1.

CMA, 2017: China Climate Bulletin 2016. China Meteorological Administration.

Francis, J. A., and S. J. Vavrus, 2015: Evidence for a wavier jet stream in response to rapid Arctic warming, *Environ. Res. Lett.*, **10**, 014005, doi:10.1088/1748-9326/10/1/014005.

Kug, J.-S., J.-H. Jeong, Y.-S. Jang, B.-M. Kim, C. K. Folland, S.-K. Min, and S.-W. Son, 2015: Two distinct influences of Arctic warming on cold winters over North America and East Asia. *Nat. Geosci.*, **8**, 759–762, doi:10.1038/ngeo2517.

Li, Z., Z. W. Yan, and H. Y. Wu, 2015: Updated homogenized Chinese temperature series with physical consistency. *Atmos. Oceanic. Sci. Lett.*, **8**, 17–22, doi:10.3878/AOSL20140062.

McCusker, K. E., J. C. Fyfe, and M. Sigmond, 2016: Twenty-five winters of unexpected Eurasian cooling unlikely due to Arctic sea-ice loss. *Nat. Geosci.*, **9**, 838–842, doi:10.1038/ngeo2820.

Mori, M., M. Watanabe, H. Shiogama, J. Inoue, and M. Kimoto, 2014: Robust Arctic sea-ice influence on the frequent Eurasian cold winters in past decades. *Nat. Geosci.*, **7**, 869–873, doi:10.1038/NGEO2277.

Pall, P., T. Ainu, D. A. Stone, P. A. Stott, T. Nozawa, A. G. J. Hilberts, D. Lohmann, and M. R. Allen, 2011: Anthropogenic greenhouse gas contribution to flood risk in England and Wales in autumn 2000. *Nature*, **470**, 382–386, doi:10.1038/nature09762.

Stott, P. A., D. A. Stone, and M. R. Allen, 2004: Human contribution to the European heatwave of 2003. *Nature*, **432**, 610–614, doi:10.1038/nature03089.

——, and Coauthors, 2016: Attribution of extreme weather and climate-related events. *Wiley Interdisc. Rev.: Climate Change*, **7**, 23–41, doi:10.1002/wcc.380.

Sun, L., J. Perlwitz, and M. Hoerling, 2016: What caused the recent "warm Arctic, cold continents" trend pattern in winter temperatures? *Geophys. Res. Lett.*, **43**, 5345–5352, doi:10.1002/2016GL069024.

Szentimrey, T., 1999: Multiple analyses of series for homogenization (MASH). *Proc. of the Second Seminar for Homogenization of Surface Climatological Data*, WMO-TD-962, Budapest, Hungary, WMO, 27–46.

Trenary, L., T. DelSole, M. K. Tippett, and B. Doty, 2016: Extreme eastern U.S. winter of 2015 not symptomatic of climate change [in "Explaining Extreme Events of 2015 from a Climate Perspective"]. *Bull. Amer. Meteor. Soc.*, **97** (12), S31–S35, doi:10.1175/BAMS-D-16-0156.1.

Walters, D., and Coauthors, 2017: The Met Office Unified Model Global Atmosphere 6.0/6.1 and JULES Global Land 6.0/6.1 configurations. *Geosci. Model Dev.*, **10**, 1487–1520, doi:10.5194/gmd-10-1487-2017.

Wang, X. L., and V. R. Swail, 2001: Changes of extreme wave heights in Northern Hemisphere oceans and related atmospheric circulation regimes. *J. Climate*, **14**, 2204–2221, doi:10.1175/1520-0442(2001)014<2204:COEWHI>2.0.CO;2.

24. ANTHROPOGENIC INFLUENCE ON THE EASTERN CHINA 2016 SUPER COLD SURGE

Ying Sun, Ting Hu, Xuebin Zhang, Hui Wan, Peter Stott, and Chunhui Lu

Human influence decreased the probability of a cold surge occurrence in China.

Introduction. A super cold surge during the winter of December 2015 to February 2016 was widely reported by Chinese media. This cold surge originated from the Siberian High and swept across the country on 21–25 January 2016, bringing very strong winds and a large and sudden fall in temperature. During the cold surge, air temperatures dropped more than 12°C over 18% of the country and by 6°C over more than 80% of the country. More than 95% of the country experienced frigid winter weather with minimum temperatures below 0°C (Jiang et al. 2016). Record-breaking minimum temperatures were reported at many observing stations, with temperature at −46.8°C observed in the Inner Mongolia autonomous region. The lives of more than one billion people were affected by this cold surge. Snowfall occurred in Guangzhou, the capital city in one of the southernmost provinces in China—the first ever snow event since the meteorological observing station was established. Extreme weather brought by the cold surge, such as heavy snowfall, freezing rain, and frost, caused significant impacts on transportation and electricity transmission systems, and on agriculture and human health (CMA 2017).

One would naturally expect a reduction in cold extremes as a result of global warming. Nevertheless, some studies have suggested that Arctic amplification of warming and Arctic sea ice loss may have contributed to the so-called "warm Arctic–cold Eurasia" pattern over the past few decades (e.g., Cohen et al. 2014; Mori et al. 2014). It has therefore been speculated that continued Arctic sea ice loss would cause more cold extremes in the continental midlatitudes. This does not seem to be the case in the United States where very cold winters have become less likely due to global warming (Wolter et al. 2015; Trenary et al. 2016). In China, a few recent studies have shown that the decrease in the intensity and frequency of cold extremes can be attributed to human influence (Yin et al. 2016; Lu et al. 2016) although the attribution of cold surge events has not yet been resolved. Here we examine a related question with regard to long-term change in extreme cold surges, such as the 2015 winter cold surge in eastern China, and possible causes of the change.

Data and methods. We use the gridded daily minimum temperature available from the China National Meteorological Information Center. The data is on a 0.5° × 0.5° grid and is based on the homogenized daily temperatures at 2419 stations (Cao et al. 2016). These data were converted to 2° × 2° resolution prior to subsequent analyses. As the cold surge mainly affected the eastern part of China that is within the East Asian monsoon region, we focus on three large north–south regions, including Northern China (NC; 36°–46°N, 104°–124°E), the lower Yangtze River Valley (YRV; 28°–36°N, 104°–124°E) and Southern China (SC; 18°–28°N, 104°–124°E). These regions are marked by the red boxes in Fig. 24.1a. We use the lowest regional average of daily minimum 2-m temperatures (TNn) in winter months (December–February) to represent the severity of a large-scale cold air outbreak. The regional averages were obtained by area weighting the gridded data available within each region. Regional anomalies of TNn relative to 1961–90 average are retained for the subsequent analyses.

Daily minimum temperatures simulated by the climate models participating in the Coupled Model Intercomparison Project Phase 5 (CMIP5) are also used. This includes 62 simulations from 16 models forced with the combined effect of anthropogenic and natural external forcings (ALL) and 26 simulations from 6 models forced with the natural external forcings only
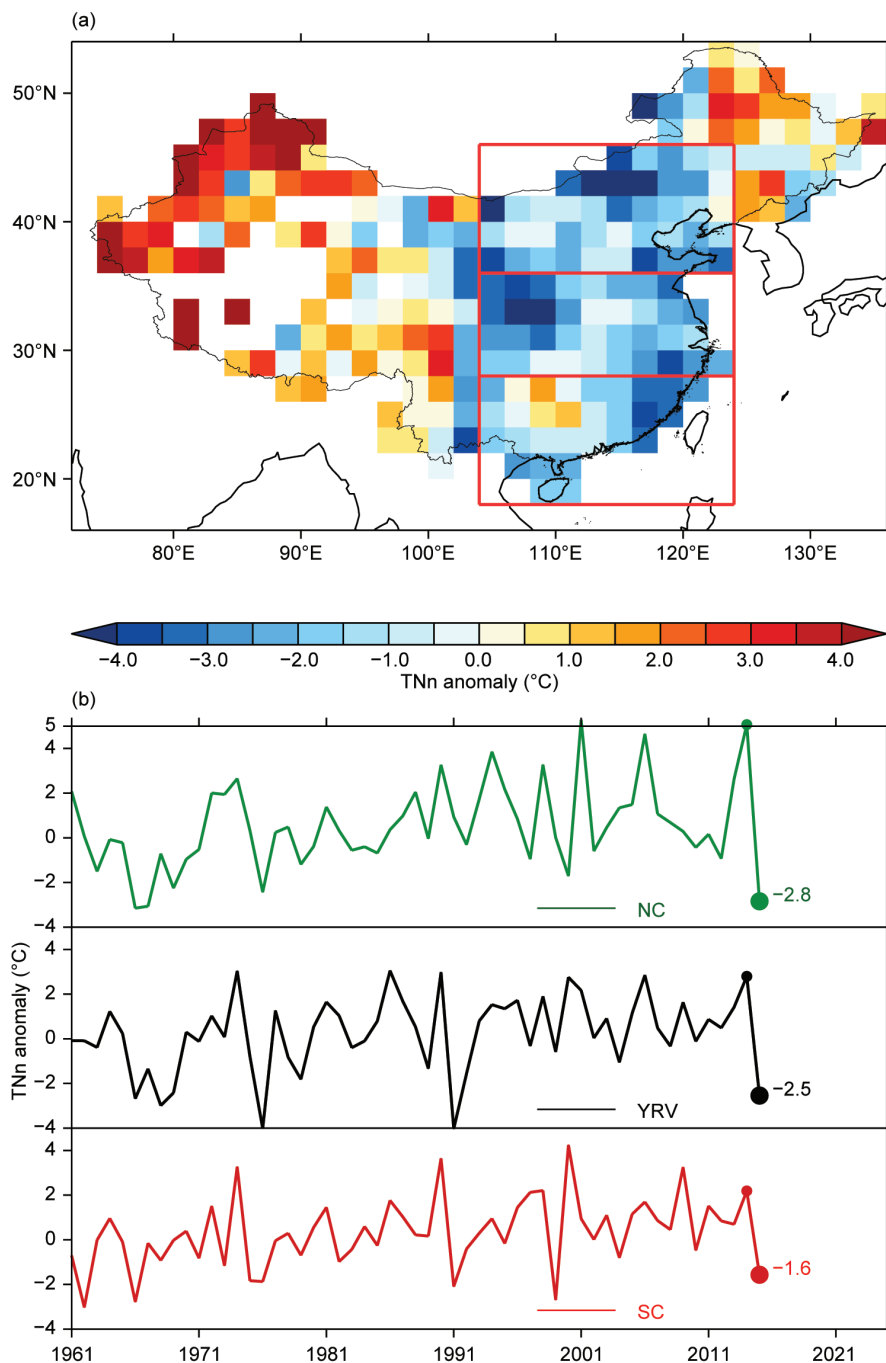
FIG. 24.1. (a) 2015/16 winter TNn anomalies (°C). Boxes indicate NC, YRV, and SC regions; see text for coordinates. (b) Time series of winter regional mean TNn anomalies (°C) in NC (green), YRV (black), and SC (red). The numbers indicate anomalies for 2015/16 winter.

Our method is similar to Sun et al. (2014); it involves the detection and attribution analysis and estimate of relative risk of an event in the world with or without human influence. For the detection and attribution analysis, we consider spatial averages of daily minimum temperature over a large region which has a strong temporal persistence. Because of this, the minimum values sampled from area average daily minimum temperature over a winter have a symmetric probability distribution rather than an extreme value distribution. We therefore apply the total least square (TLS) method (Allen and Stott 2003) to regress the observations onto ALL and NAT signals computed as multimodel ensemble means of the relevant simulations. The regression is conducted on space–time series of 3-winter non-overlapping mean series for winters 1961/62 through 2011/12 over the three spatial domains. The use of a 3-winter mean series is a compromise for reducing temporal dimension as well as variability but still retaining climate response to volcanic forcing. The co-variance matrix required for solving the regression problem is based on regularized co-variance matrix described in Ribes et al. (2013) as this estimator is more robust. The regression coefficient is called the scaling factor, indicating the magnitude that simulated signal must be scaled to best match the observations. A signal is detected if the 90% confidence interval (CI) of the corresponding scaling factor is above zero. To estimate relative risk, we first multiply the ALL and the NAT signals by the

(NAT). These simulations are used to estimate the model response to ALL and NAT forcings respectively. Pre-industrial control simulations from 28 models are also used in the estimation of natural variability. Details about the simulations and procedures for processing the model data are given in Table ES24.1 and the other online supplement material.

corresponding scaling factors to obtain the observation-constrained best estimates of ALL and NAT response in winters 2013/14–2015/16. We use ensemble mean of RCP4.5 simulation to represent ALL signal in winters 2013/14–2015/16 (red dots in Figs. 24.2a–c). The NAT experiments end in 2012, so we simply use the NAT signal for winters 2009/10–2011/12 for winters 2013/14–2015/16 (blue dots in Figs. 24.2a–c). This is justified since there was no major difference in the levels of volcanic activity between the two three-year periods. The scaling factors are obtained from the two-signal detection analysis in which observations are regressed simultaneously to ALL and NAT signals. We then add the preindustrial control simulations to these best estimates to reconstruct extreme temperature series representative of the 2015/16 winter climate in the world with or without human influence. The probabilities of a cold surge of the magnitude of the 2015/16 winter event in the world with (*p1*) or without (*p0*) anthropogenic influence are the percentages of times when temperature anomalies are at or below the observed 2015/16 winter value in the relevant series. The relative risk or risk ratio (RR) is defined as RR = *p1/p0*. The CI of the risk ratio was estimated from 1000 random samples of scaling factors assuming the scaling factors follow normal distributions.

Results. Figure 24.1a shows the TNn anomalies in the 2015/16 winter. Negative anomalies were observed in most areas of eastern China (east of 105°E), with the largest anomalies below −3.5°C appearing in central and northern China. This strong negative anomaly is in sharp contrast with continuous warming in winter mean temperature in recent decades (MOST 2016). In fact, the 2015/16 winter mean temperature was slightly higher than the 1971–2000 average (CMA 2017). The coldest TNn for the 2015/16 winter occurred during this cold surge (21–25 January 2016) in most stations (not shown). The anomalies of winter minimum regional mean daily minimum temperature in the three regions NC, YRV, and SC (Fig. 24.1b) were

−2.8°C, −2.5°C, and −1.6°C, respectively. They were ranked as the 3rd, 5th, and 7th coldest since 1961 for the respective regions.

Figures 24.2a–c show the observed and the simulated 3-winter mean non-overlapping series. The observed TNn has increased at the rates of 0.43°C decade⁻¹, 0.35°C decade⁻¹, and 0.41°C decade⁻¹ for NC, YRV, and SC, respectively, during 1961/62 winter through 2011/12 winter. The linear trends (dashed lines) in the simulated responses to ALL forcing are 0.25°C decade⁻¹, 0.17°C decade⁻¹, 0.15°C decade⁻¹, respectively, indicating that the models may have underestimated the observed changes. The NAT trends are 0.10°C decade⁻¹, 0.11°C decade⁻¹,
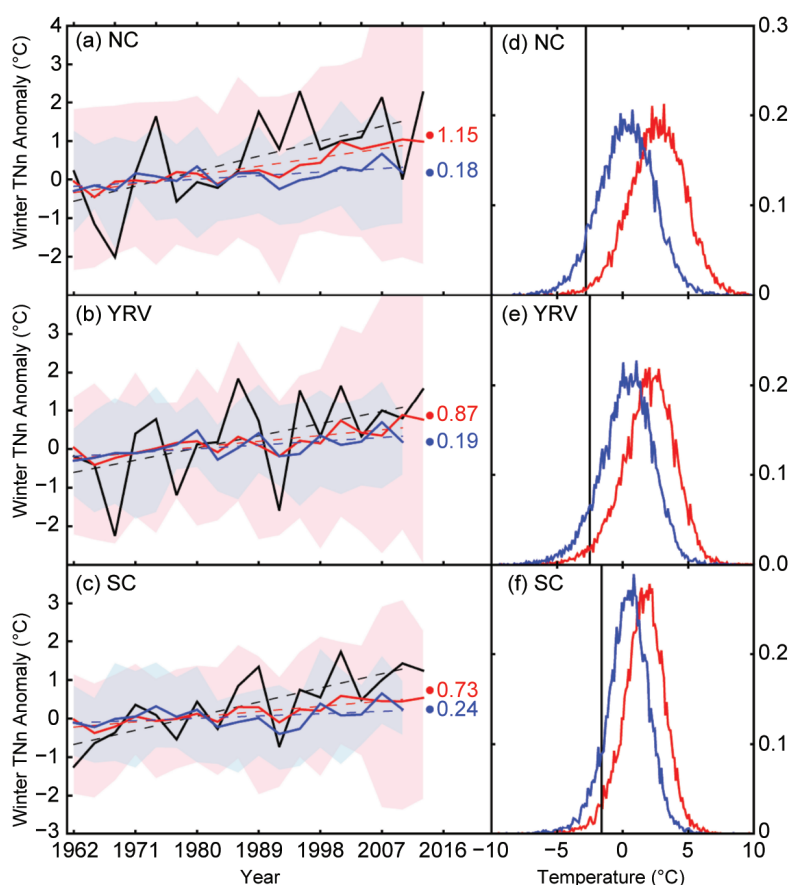
FIG. 24.2. The 3-year winter mean non-overlapping TNn anomalies (°C) from the observations (black) and model simulations under ALL (red) and NAT (blue) forcings for (a) NC, (b) YRV, and (c) SC regions. Red and blue lines indicate multimodel ensemble mean. Dashed lines show long term trends. Reconstructions of the 3-year winter mean for ALL forcings in winters 2013/14–2015/16 and NAT forcings in winters 2009/10–2011/12 are marked with red (ALL) and blue (NAT) dots and numbers. Pink and blue shadings show the 5%–95% ranges of the individual model simulations from ALL and NAT experiments, respectively. Histograms of the winter minimum regional mean TNn anomalies (°C) for (d) NC, (e) YRV, and (f) SC, under NAT (blue) ALL (red) forcing. The black lines indicate the 2015/16 winter anomalies.

0.07°C decade^{-1}, respectively, suggesting a possibility for NAT forcing to contribute to the observed warming. Note however that models may have overestimated NAT response since CMIP5 underestimates volcanic aerosols for the 21st century (Santer et al. 2014). The scaling factors for anthropogenic forcing (ANT) and NAT are 2.45 (90% CI: 1.07–4.17) and 1.52 (90% CI: −0.68–3.47), respectively, in the two-signal detection analysis in which observed series is regressed to ALL and NAT simultaneously. This means that the observed changes in extreme winter temperature are mainly due to anthropogenic forcing. Natural external forcing may have contributed to observed trend but its contribution is not significantly different from zero. The observed TNn has a standard deviation of 1.91°C, 1.70°C, 1.54°C in NC, YRV, and SC, respectively. The best estimate of reconstructed series with both anthropogenic and natural forcings has a standard deviation of 2.28°C (90% CI: 1.64°–2.93°C), 2.16°C (90% CI: 1.47°–2.86°C), 1.74 °C (90% CI: 1.16°–2.31°C), respectively. The fact that the observed variability is slightly smaller but also generally comparable to that in the reconstructed series indicates that it is possible to produce a credible estimate of the probability of extreme temperature based on reconstructed series.

As shown in Figs. 24.2d–f, the empirical probability density of TNn shifts towards warmer temperatures in the world under anthropogenic influence in all three regions, meaning that anthropogenic influence decreased the probability of cold surge. Table 24.1 summarizes the results. External forcing may have warmed TNn by 2.6°C, 2.0°C, and 1.6°C in NC, YRV, and SC, respectively, by 2015. That is to say, the 2015/16 winter cold surge would have been much stronger without anthropogenic induced warming.

The risk ratio for the event of 2015/16 winter magnitude is 0.11, 0.27, 0.31 for NC, YRV, and SC, respectively, meaning that the anthropogenic influence may have respectively reduced the occurrence of such a cold event by 89% (90% CI: 54%–98%), 73% (90% CI: 37%–90%), and 69% (90% CI: 30%–86%).

Conclusions and discussion. The magnitude of winter cold surge has not increased in Eastern China. It has decreased due to anthropogenic influence. This is consistent with earlier findings of Yin et al. (2016) and Lu et al. (2016), who found that cold extremes in China have decreased due to anthropogenic influence. The recent super cold surge of Eastern China that occurred 21–25 January 2016 would have been much stronger if there was no human-induced warming. Alternatively, the occurrence for a cold surge with the magnitude of the 2015/16 winter event has been much reduced due to anthropogenic influence. Note that our quantification of anthropogenic influence on cold surge involves the comparison between ALL and NAT responses. As different sets of models are used in such a comparison, the results would also be impacted by this aspect of modeling uncertainty. Additionally, results can also be sensitive to the subsets of selected models because uncertainty in signal estimation becomes larger with a much-reduced number of simulations.

TABLE 24.1. Possible human influence on the cold surge like the 2016 January event.			
TNn	**NC**	**YRV**	**SC**
Observed TNn anomaly	−2.8°C	−2.5°C	−1.6°C
Warming attributable to ALL forcing	2.6°C	2.0°C	1.6°C
Return period in a world without human influence	14 years (90% range 10–19 years)	12 years (90% range 9–15 years)	9 years (90% range 6–14 years)
Return period in a world with human influence	131 years (90% range 21–914 years)	42 years (90% range14–144 years)	28 years (90% range 8–97 years)
Risk ratio (RR)	0.11 (90% range 0.02–0.46)	0.27 (90% range 0.10–0.63)	0.31 (90% range 0.14–0.70)

REFERENCES

Allen, M., and P. Stott, 2003: Estimating signal amplitudes in optimal fingerprinting. Part I: Theory. *Climate Dyn.*, **21**, 477–491, doi:10.1007/s00382-003-0313-9.

Cao, L., Y. Zhu, G. Tang, and Z. Yan, 2016: Climatic warming in China according to a homogenized data set from 2419 stations. *Int. J. Climatol.*, **39**, 4384–4392, doi:10.1002/joc.4639.

CMA, 2017: *China Climate Bulletin 2016*. China Meteorological Administration, 50 pp.

Cohen, J., and Coauthors, 2014: Recent Arctic amplification and extreme mid-latitude weather. *Nat. Geosci.*, **7**, 627–637, doi:10.1038/ngeo2234.

MOST (Ministry of Science and Technology), 2016: *Third National Assessment Report on Climate Change* (in Chinese). China Science Press, 976 pp.

Jiang, Q., X. K. Ma, and F. Wang, 2016: Analysis of the January 2016 atmospheric circulation and weather (in Chinese). *Meteor. Mon.*, **42**, 514–520, doi:10.7519/j.issn.1000-0526.2016.04.16.

Lu, C., Y. Sun, H. Wan, X. B. Zhang, and H. Yin, 2016: Anthropogenic influence on the frequency of extreme temperatures in China. *Geophys. Res. Lett.*, **43**, 6511–6518, doi:10.1002/2016GL069296.

Mori, M., M. Watanabe, H. Shiogama, J. Inoue, and M. Kimoto, 2014: Robust Arctic sea-ice influence on the frequent Eurasian cold winters in past decades. *Nat. Geosci.*, **7**, 869–873, doi:10.1038/ngeo2277.

Ribes, A., S. Planton, and L. Terray, 2013: Application of regularised optimal fingerprinting to attribution. Part I: Method, properties and idealised analysis. *Climate Dyn.*, **41**, 2817–2836, doi:10.1007/s00382-013-1735-7.

Santer, B. D., and Coauthors, 2014: Volcanic contribution to decadal changes in tropospheric temperature. *Nat. Geosci.*, **2**, 185–189, doi:10.1038/ngeo2098.

Sun, Y., and Coauthors, 2014: Rapid increase in the risk of extreme summer heat in Eastern China. *Nat. Climate Change*, **4**, 1082–1085, doi:10.1038/nclimate2410.

Trenary, L., T. DelSole, M. K. Tippett, and B. Doty, 2016: Extreme eastern U.S. winter of 2015 not symptomatic of climate change [in "Explaining Extreme Events of 2015 from a Climate Perspective"]. *Bull. Amer. Meteor. Soc.*, **97** (12), S31–S35, doi:10.1175/BAMS-D-16-0156.1.

Wolter, K., M. Hoerling, J. K. Eisheid, G. J. van Oldenborgh, X.-W. Quan, J. E. Walsh, T. N. Chase, and R. M. Dole, 2015: How unusual was the cold winter of 2013/14 in the upper Midwest? [in ''Explaining Extreme Events of 2014 from a Climate Perspective'']. *Bull. Amer. Meteor. Soc.*, **96** (12), S10–S14, doi:10.1175/BAMS-D-15-00126.1.

Yin, H., Y. Sun, H. Wan, X. Zhang, and C. Lu, 2016: Detection of anthropogenic influence on the intensity of extreme temperatures in China. *Int. J. Climatol.*, **37**, 1229–1237, doi:10.1002/joc.4771.

25. THE HOT AND DRY APRIL OF 2016 IN THAILAND

Nikolaos Christidis, Kasemsan Manomaiphiboon, Andrew Ciavarella, and Peter A. Stott

The record temperature of April 2016 in Thailand would not have occurred without the influence of both anthropogenic forcings and El Niño, which also increased the likelihood of low rainfall.

Introduction. April is typically one of the hottest months in Thailand, marking the end of the dry season and the onset of monsoon rains. April heat reached unprecedented levels in 2016 (NASA 2016) and exacerbated the adverse socio-economic impacts from a prolonged drought that started in early 2015 and persisted until mid-2016, evidently favored by the presence of a strong El Niño (Singhrattna et al. 2005). The severe drought affected 41 Thai provinces, had devastating effects on major crops, such as rice and sugar cane, and incurred a total loss in the agricultural production of about half a billion U.S. dollars (Ministry of Agriculture and Cooperatives; MOAC 2016). Moreover, the extreme heat culminating in the April heat wave resulted in an estimated six-fold increase in heatstroke cases relative to 2014 (Ministry of Public Health; MOHP 2017), while record-breaking peak electricity demand was also reported (Electricity Generating Authority of Thailand; EGAT 2016), and extensive forest fires ravaged the country (Forest Fire Control Division; FFCD 2017).

This work considers possible drivers of the exceptionally high temperature and low rainfall over land in the region of Thailand (5°–20°N, 95°–110°E) in April 2016. We concentrate on the effect of anthropogenic forcings and the El Niño Southern Oscillation (ENSO), investigating how they influence the occurrence of extremes similar to 2016. The study focuses on the month of April when the heat peaked. In that month, temperatures in excess of 44°C set new records in some regions, and the severe weather and its impacts were extensively reported in the national press. Although our study does not consider the drought in which the event was embedded, or its

hydrological impacts, we examine streamflow data from the Royal Irrigation Department of Thailand for the country's two main river basins (see online-supplemental material), as this provides a context for the April event. For each month since 1950, normalized streamflow values are computed from the station data as the mean flow during the year ending at that month. The resulting streamflows reveal that in both basins the drought was greatly intensified after mid-2015. At least 7 months leading up to April 2015 ranked in the top ten since the 1950s in terms of severity (Figs. 25.1a,b; only recent years plotted for clarity).

Methods. We define extreme events using thresholds (Stott et al. 2016) and identify hot and dry events as those instances when the temperature rises above and the rainfall falls below the 2016 observed values. Our analysis sets out to answer three attribution questions: 1) How does anthropogenic climate change modify the likelihood of hot and dry events under the 2016 El Niño conditions?; 2) What would the anthropogenic effect on the likelihood be under any ENSO conditions?; and 3) How does ENSO affect the likelihood of extreme events in the current climate, already influenced by anthropogenic forcings? Local surface processes which may drive or amplify heat waves are better studied with regional and hydrological models, and their effect is not explicitly addressed here. Regional temperature and rainfall time series constructed with the CRUTEM4 (Jones et al. 2012) and GPCC (Schneider et al. 2014) datasets show that April 2016 was the hottest (Fig. 25.1c) and fourth driest (Fig. 25.1d) since 1900. Using these observations, we demonstrate the clear influence of ENSO on temperature and rainfall by grouping the data in consecutive bins and computing the mean Southern Oscillation Index in the years corresponding to each bin (Figs. 25.1e,f). El Niño favors warmer and drier conditions, so the markedly strong El Niño in 2015–16 (L'Heureux et al. 2017) is expected to have made a considerable contribution to the extreme conditions in April 2016.
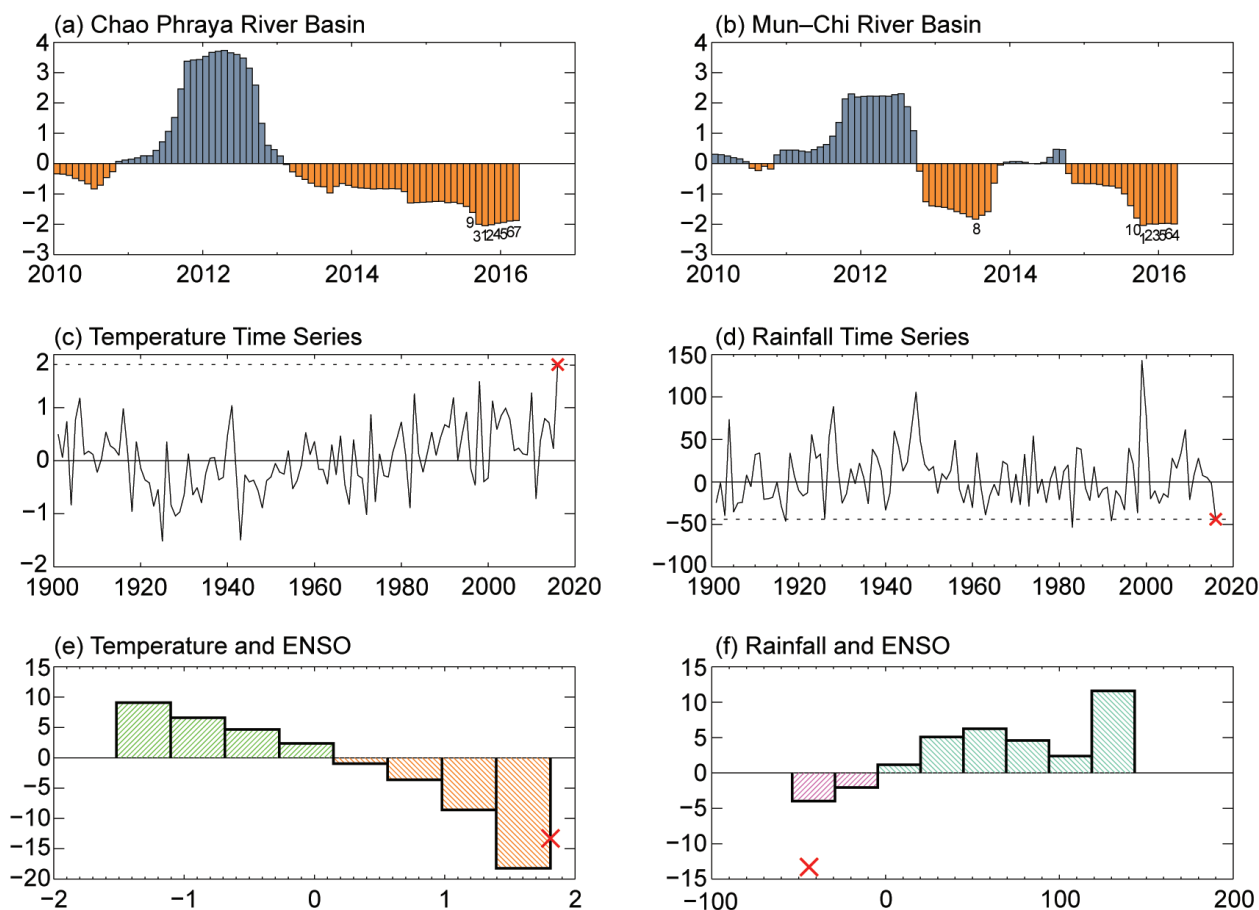
Fɪɢ. 25.1. Normalized monthly running sums (12-months back-totaled) of streamflow constructed with data from stations located in two major Thai river basins: (a) Chao Phraya and (b) Mun-Chi. Only recent years are plotted for clarity; last record is Mar 2016. Months with streamflows among the ten lowest are marked. (c),(d) Time series of the Apr mean temperature (°C) and rainfall (mm) in the region of Thailand from observations. (e),(f) Histograms showing the mean Southern Oscillation index (SOI) in years corresponding to different temperature and rainfall data bins. (c)–(f) Red asterisk marks year 2016 and all anomalies are relative to 1961–90.

Our analysis uses the Hadley Centre event attribution system (Christidis et al. 2013), which provides ensembles of simulations with the HadGEM3-A model for the actual climate with all external forcings included ("factual" experiment) and a hypothetical natural climate without the effect of human influence ("counterfactual" experiment). The system was recently upgraded to high resolution (N216 and 85 vertical levels; Ciavarella et al. 2017, *manuscript submitted to Wea. Climate Extremes*). Observed oceanic conditions were prescribed in the factual simulations using the HadISST dataset (Rayner et al. 2003). A model-based estimate of the ocean's warming calculated as the average across 51 simulations from 19 coupled models that provided data to the CMIP5 archive (http://portal.nersc.gov /c20c/experiment.html) was subtracted from the observations in the counterfactual simulations and

the sea–ice was adjusted accordingly (Christidis et al. 2013). The system provides ensembles of 525 simulations of March–May 2016 for each experiment, which include strong El Niño conditions through the prescribed boundary conditions. We also use shorter, 15-member ensembles of factual and counterfactual simulations over the period 1960–2015 and extract the last 15 years to approximate the near present-day climate. For each experiment, we extract the month of April and compute the monthly and regional mean temperature and rainfall. This yields samples of 525 months per variable and experiment for year 2016 and 225 months for the recent past (years 2001–15). With these we subsequently construct temperature and rainfall distributions and estimate the probability of a hot or dry April using our pre-specified thresholds and the return period, calculated as the reverse of the probability. Extreme probabilities are derived

with the generalized Pareto distribution and their uncertainties with a Monte Carlo bootstrap procedure (Christidis et al. 2013). Model evaluation assessments were also carried out (see online supplemental material), which suggest that HadGEM3-A represents well the climatological distribution of April temperature and rainfall in the region and also provides realistic probability estimates for extreme events.

Results. First, the effect of anthropogenic forcings under the observed El Niño conditions is examined. Temperature and rainfall distributions are constructed from the model simulations of April 2016 (Figs. 25.2a,b). The thresholds used to define extreme events are also marked on the distribution plots. The modeled rainfall data were bias corrected to have the same mean as the observations in the period 1961–90. The temperature threshold is set to be 3.3 standard deviations above the modeled climatological mean, as estimated from observations for April 2016. Human influence (i.e., the overall effect of anthropogenic emissions of well-mixed greenhouse gases, aerosols and ozone, as well as land-use changes) is shown to increase the chances of both dry and hot events. The associated reduction in the return time of extremes is shown in Fig. 25.2c. The likelihood of extremely low rainfall is estimated to increase by a factor of 2 (best estimate). However, the anthropogenic effect on temperature is far more pronounced, and we find that April temperatures as high as in 2016 cannot occur in the natural climate, even under the influence of a strong El Niño. The joint probability of hot and dry
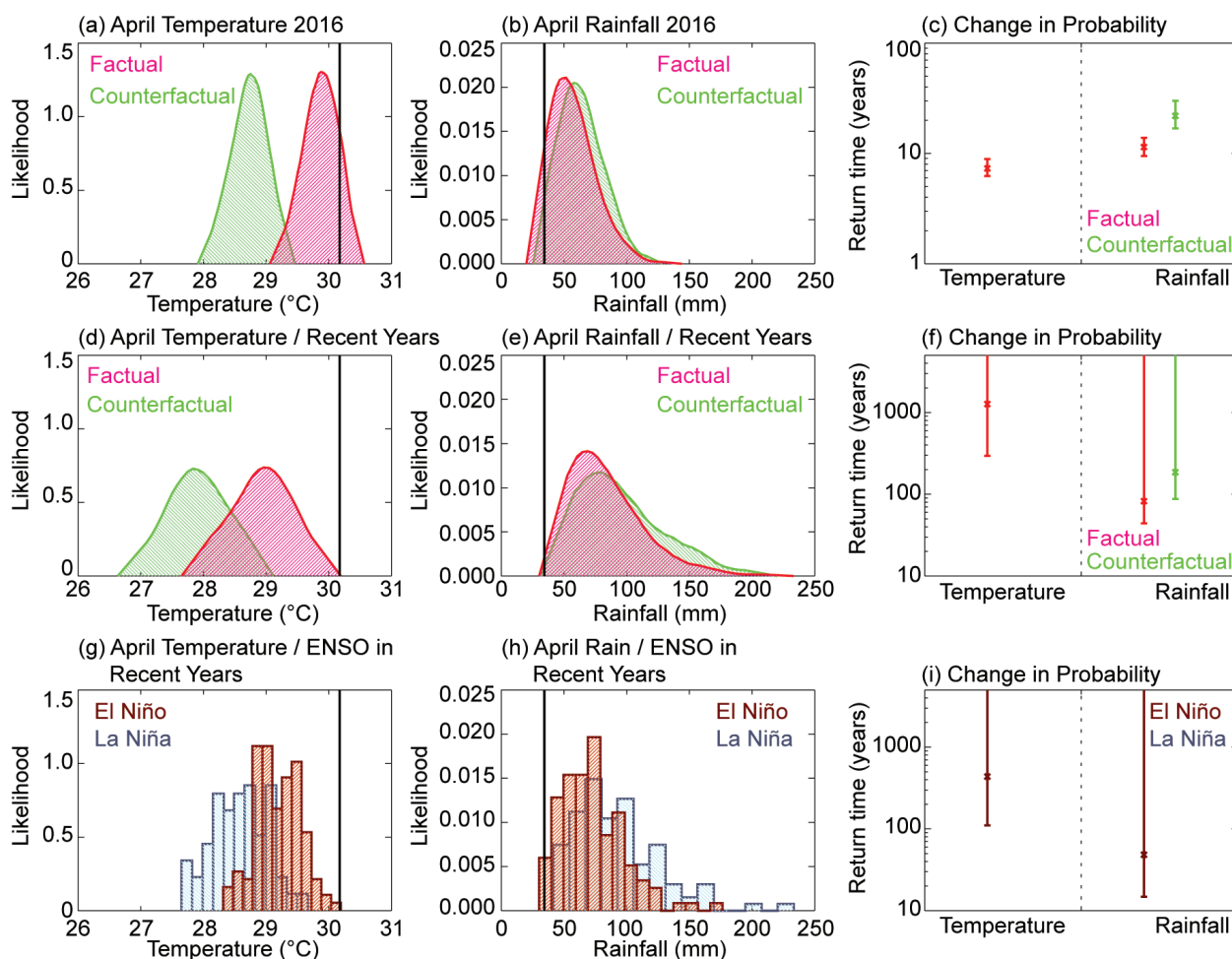
Fig. 25.2. Normalized distributions of the April mean temperature (°C) and rainfall (mm) in the region of Thailand with (red) and without (green) anthropogenic climate change constructed with HadGEM3-A data for (a),(b) 2016 and (d),(e) 2001–15. Distributions are also shown for El Niño (dark red) and La Niña (blue) conditions in (g),(h) recent years. Year 2016 is marked by the vertical line. (c), (f), and (i) illustrate estimates of the return times of extreme events corresponding to different model experiments or ENSO phases. The best estimate (50th percentile) is marked by a cross and the 5%–95% uncertainty range by whiskers.

events occurring simultaneously is also computed, and it is estimated that in the factual climate the return time is 105 years (5%–95% range: 53–263 years), while in the counterfactual world the likelihood is too small to be accurately estimated. Our results are to some extent affected by a known caveat arising from the uncertainty in the counterfactual boundary conditions (Christidis and Stott 2014; Solomon and Newman 2012), sometimes sampled by using several estimates of the oceanic warming from individual models. A computationally cheaper approach would be using improved boundary conditions derived from observations (Christidis and Stott 2014; Seager and Hoerling 2014). In this work, we use boundary conditions from a multimodel ensemble instead, which should (to some extent) alleviate errors from individual models.

The anthropogenic effect on extreme events irrespective of the ENSO phase is investigated next, based on the temperature and rainfall distributions for the recent past (Figs. 25.2d,e). Although human influence increases the likelihood of extremes, their probabilities are much smaller (Fig. 25.2f). We again find that the NAT experiment cannot reproduce the extreme April heat of 2016, which is also rare in the actual climate (Fig. 25.2d), but becomes more likely in years with a strong El Niño (Fig. 25.2a).

Finally, the influence of the ENSO phase on the likelihood of extremes in the current climate is also examined. We partition the simulated, near present-day data between positive and negative ENSO phases and construct the distributions for the two phases (Figs. 25.2g,h). As expected, El Niño conditions increase the chances of extreme events, which are not found to occur in La Niña years. The chance of extreme temperature events is small even under El Niño conditions (Fig. 25.2i), but apparently increases during stronger episodes (Fig. 25.2a).

Conclusions. Our analysis demonstrates that anthropogenic climate change results in a clear shift of the April temperature distribution toward warmer conditions and a more moderate, albeit distinct, shift of the rainfall distribution toward drier Aprils in Thailand. The synergy between anthropogenic forcings and a strong El Niño was crucial to the breaking of the temperature record in 2016, which our results suggest would not have occurred if one of these factors were absent. Rainfall as low as in 2016 is found to be extremely rare in La Niña years. The joint probability for hot and dry events similar to April 2016 is found to be relatively small (best estimate of about 1%), which

implies that in addition to the drivers examined here, other possible causes could have also played a role, like moisture availability and transport (especially in the context of the prolonged drought), atmospheric circulation patterns, and the effect of other non-ENSO modes of unforced variability.

REFERENCES

Christidis, N., P. A. Stott, A. Scaife, A. Arribas, G. S. Jones, D. Copsey, J. R. Knight, and W. J. Tennant, 2013: A new HadGEM3-A-based system for attribution of weather and climate-related extreme events. *J. Climate*, **26**, 2756–2783, doi:10.1175 /JCLI-D-12-00169.1.

——, and ——, 2014: Change in the odds of warm years and seasons due to anthropogenic influence on the climate. *J. Climate*, **27**, 2607-2621, doi: 10.1175 /JCLI-D-13-00563.1.

EGAT, 2016: Record breaking of peak electricity load for seventh time in 2016 by accumulated heat (in Thai). Electricity Generating Authority of Thailand. [Available online at www.egat.co.th/index .php?option=com_content&view=article&id=1491 :press-20160511-01&catid=31&Itemid=208.]

FFCD, 2017: Forest fire occurrence statistics (in Thai). Forest Fire Control Division, Department of National Park, Wildlife and Plant Conservation, Thailand. [Available online at www.dnp.go.th /forestfire/2546/firestatistic%20Th.htm.]

Jones, P. D., D. H. Lister, T. J. Osborn, C. Harpham, M. Salmon, and C. P. Morice, 2012: Hemispheric and large-scale land surface air temperature variations: An extensive revision and an update to 2010. *J. Geophys. Res.*, **117**, D05127, doi:10.1029/2011JD017139.

L'Heureux, M., and Coauthors, 2017: Observing and predicting the 2015-16 El Niño. *Bull. Amer. Meteor. Soc.*, **98**, 1363–1382, doi:10.1175/BAMS-D-16-0009.1.

MOAC, 2016: Daily reports of drought situations and mitigation (in Thai). National Operation Center of Drought Response and Mitigation for 2015/2016, Ministry of Agriculture and Cooperatives, Thailand. [Available online at www.moac.go.th /drought.]

MOPH, 2017: Health Data Center Services (in Thai). Ministry of Public Health, Thailand. [Available online at http://hdcservice.moph.go.th.]

NASA, 2016: Heat wave hits Thailand, India: Natural Hazards. [Available online at http://earthobservatory.nasa.gov/NaturalHazards/view.php?id=87981.]

Rayner, N. A., D. E. Parker, E. B. Horton, C. K. Folland, L. V. Alexander, D. P. Rowell, E. C. Kent, and A. Kaplan, 2003: Global analyses of sea surface temperature, sea ice, and night marine air temperature since the late nineteenth century. *J. Geophys. Res.*, **108**, 4407, doi:10.1029/2002JD002670.

Schneider, U, A. Becker, P. Finger, A. Meyer-Christoffer, M. Ziese, and B. Rufolf, 2014: GPCC's new land surface precipitation climatology based on quality-controlled in situ data and its role in quantifying the global water cycle. *Theor. Appl. Climatol.*, **115**, 15–40, doi:10.1007/s00704-013-0860-x.

Seager, R., and M. Hoerling, 2014: Atmosphere and ocean origins of North American droughts. *J. Climate*, **27**, 4581–4606, doi: 10.1175/JCLI-D-13-00329.1.

Singhrattna, N., B. Rajagopalan, K. Krishna Kumar, and M. Clark, 2005: Interannual and interdecadal variability of Thailand summer monsoon season. *J. Climate*, **18**, 1697–1708, doi:10.1175/JCLI3364.1.

Solomon, A., and M. Newman, 2012: Reconciling disparate twentieth-century Indo-Pacific ocean temperature trends in the instrumental record. *Nat. Climate Change*, **2**, 691–699, doi:10.1038/nclimate1591.

Stott, P. A., and Coauthors, 2016: Attribution of extreme weather and climate-related events. *Wiley Interdiscip. Rev: Climate Change*, **7**, 23–41, doi: 10.1002/wcc.380.

26. THE EFFECT OF INCREASING CO_2 ON THE EXTREME SEPTEMBER 2016 RAINFALL ACROSS SOUTHEASTERN AUSTRALIA

Pandora Hope, Eun-Pa Lim, Harry Hendon, and Guomin Wang

The effect of increasing atmospheric CO_2 on the extreme September 2016 rainfall across southeastern Australia was minimal, with changes in circulation and static stability driving a tendency towards drier conditions.

Introduction. In 2016 Australia experienced extreme, widespread rainfall, with flooding and wild weather impacting some agriculture and power generation. It was particularly wet through winter and into early spring, with the wettest September for eastern Australia ever recorded (Bureau of Meteorology 2016a,b; King 2017; Fig. 26.1d).

Extreme rainfall on a range of time scales is expected to become more extreme in a warmer world (e.g., Allan and Soden 2008; Held and Soden 2006) particularly at subdaily time scales (Westra et al. 2014), but also on daily (CSIRO and Bureau of Meteorology 2015) and monthly time scales (Watterson et al. 2016). Observed trends toward higher intensity rainfall have been found in many regions around the globe (Westra et al. 2013). While thermodynamic arguments alone might suggest that rainfall will increase in a warmer world, the circulation will also respond due to a range of factors (Bony et al. 2013; Colman and McAvaney 1997; He and Soden 2016; Johnson and Xie 2010; Seager et al. 2010; Vecchi et al. 2006), generally working to reduce rainfall in the subtropics.

In Australia, while there is some indication that the intensity of subhourly rainfall is increasing (Chen et al. 2013; Westra and Sisson 2011), the signal is not clear on daily or longer time scales (Gallant et al. 2012).

However, attribution studies of extreme events can elucidate the role of increasing levels of atmospheric CO_2 on extreme rainfall. The extreme rainfall across eastern Australia in September 2016 provides an excellent case study to help understand how increasing CO_2 is influencing extreme rainfall in Australia.

The event. Across central and eastern Australia, many regions had their highest September rainfall on record in 2016, resulting in the wettest September for eastern Australia ever recorded with an average of 84.0 mm, 8.9 mm greater than the previous record and more than three times the mean. It was the wettest September on record for New South Wales and the Northern Territory, as well as for the Murray–Darling basin (MDB) in southeastern Australia, Australia's "food-bowl" (Fig. 26.1d).

In this study, we focus on the important agricultural MDB region, which covers most of the noncoastal southeast, and a particular two-week period, [15–28 September] when various climate features were skillfully predicted by the Australian Bureau of Meteorology's dynamical forecast system, POAMA2, which is the base model for this investigation. For the MDB, these two weeks in 2016 were the second wettest on record (compared to all 15–28 September periods) with a sum of 49.3 mm of rain, for comparison with model results, the anomaly was +2.8 mm day^{-1}, compared to the 2000–14 average of 0.7 mm day^{-1}. Thus these two weeks in September 2016 provide an excellent example of an extreme rainfall episode to examine the influence from increasing levels of CO_2.

At the time in 2016, all of the key climate drivers of eastern Australian rainfall were in a state that would favor wet conditions (e.g., Lim et al. 2016). The Indian Ocean Dipole (IOD) of September 2016 was strongly negative (Lim and Hendon 2017), with its eastern node the second warmest on record (ERSSTv4 data; www.bom.gov.au/climate/enso/wrap-up/archive/20161011.archive.shtml). Also, the September 2016 Southern Oscillation Index (SOI) was strongly positive (13.5; www.bom.gov.au/climate/current/soihtm1.shtml)
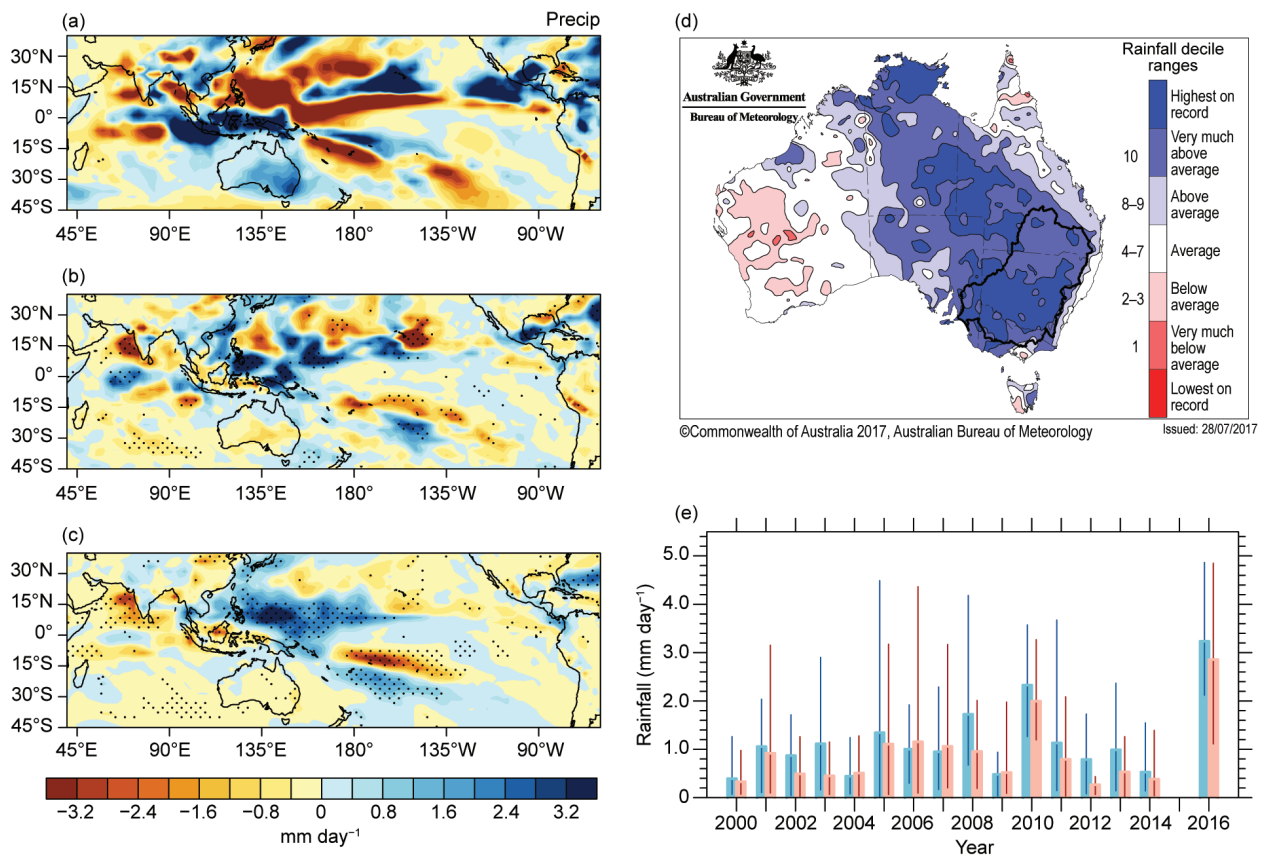
Fɪɢ. 26.1. (a) Forecast rainfall anomaly (mm day⁻¹) from 2000–14 climatology) for 15–28 Sep 2016, using 11 members of model version a. (b) Difference between 2016 forecast rainfall (mm day⁻¹) under current levels of CO_2 (401.03 ppm; www .esrl.noaa.gov/gmd/ccgg/trends/data.html) and 1960 CO_2 levels (315 ppm), using 11 members of model versions a,b,c (33 total). (c) Climatological rainfall difference (mm day⁻¹) for current minus low CO_2 levels, using 11 members of model version a. Stippling in (b) and (c) indicates significant differences (10% level). (d) Outline of MDB region, over rainfall deciles for Sep 2016 (relative to 1901–2016), and (e) ensemble mean rainfall forecast (mm day⁻¹) time series for last two weeks of Sep under current (red bars) and low CO_2 (blue bars) conditions for MDB region. Lines show ensemble spread across 11 members.

and Niño-3.4 was at near-La Niña levels, depending on the definition (Lim and Hendon 2017). SAM was strongly positive in the first three weeks of September 2016 but weakened later in the month (www.cpc.ncep .noaa.gov/products/precip/CWlink/daily_ao_index /aao/aao.shtml). The intensity of the IOD negative was found to be important for the high rainfall across Australia in 2016 (King 2017). In this study, we particularly focus on the factors that contribute to local rainfall generation including high humidity, unstable conditions, and favorable circulation.

Method. POAMA2 is the operational seasonal forecast system of the Australian Bureau of Meteorology (Wang et al. 2005). It has the BAM3 atmospheric model, (T47, L17; Colman et al. 2005), ACOM2 ocean model (Schiller et al. 2002) with a resolution of 2° longitude and a telescoping meridional resolution of

0.5° equatorward of 8° latitude, gradually increasing to 1.5° near the poles and 25 levels.

POAMA2 forecasts are initialized with realistic atmosphere, land, and ocean conditions that are generated from separate atmosphere/land surface (Hudson et al. 2011) and ocean (Yin et al. 2011) data assimilation systems. Sea–ice and ozone are set to their respective climatological annual cycles. Ensembles of 11 are produced using perturbed initial conditions with a coupled breeding technique (Hudson et al. 2013). Three versions of the model (called a, b, c) are used to increase the ensemble to 33 members. Model versions a and c differ in their boundary layer physics, and b is the flux-corrected version (Cottrill et al. 2013).

Thirty-three-member ensemble forecasts were initialized on 8 September with realistic atmosphere (including observed CO_2 concentration), ocean, and

land conditions, and verified for 15–28 September 2016. POAMA2 generally captures September rainfall in the MDB well (Langford and Hendon 2013), and these two particular weeks were chosen because not only was the rainfall forecast well (Fig. 26.1a), but the important, strong negative IOD and associated circulation were also forecast very well (Figs. ES26.1a,d). A second, "low CO_2", 33-member ensemble forecast was initialized with the same initial conditions, but with the influence of the last 55 years of CO_2 increase removed following Hope et al. (2016) and Wang et al. (2016). The CO_2 signal removed from the initial conditions was calculated for the ocean first (D_{ocean}), being the difference of the last five years of two sets of 30-year, free-running simulations with atmospheric CO_2 set to 1960 (315 ppm) or 2014 (~400 ppm) values. The anomalies D_{atmos} and D_{land} were calculated from the restart files valid at the end of two-month forecasts initialized with either observed initial conditions or those with D_{ocean} removed, and corresponding levels of atmospheric CO_2.

Two sets of hindcasts were generated for the period 2000–14 to compute the two climatologies that represent the climate states with current and low CO_2 using the same experimental method as described above, but only using version a of POAMA2 (Fig. 26.1e), resulting in 165 forecasts. The climatological pattern of change in SSTs (Fig. ES26.1c) aligns with the observed warming seen across the globe in the CMIP5 climate models, with particular alignment to those forced with only greenhouse gases (Bindoff et al. 2013).

To determine how increasing levels of CO_2 alter rainfall through circulation changes, we analyze the components of the moisture budget as done in Seager et al. (2010). They propose that the changes in the moisture budget due to increasing CO_2 are caused thermodynamically by changes in specific humidity and dynamically by changes in circulation. The thermodynamic and dynamic contributions are further separated into advective and divergent components. In our analysis for the last two weeks of September 2016, we found that the change in the moisture budget due to the change of wind divergence largely explained the forecast pattern of rainfall change produced under differing levels of CO_2. Therefore, we focus on the moisture transport by the CO_2-induced change of wind divergence.

Did increased atmospheric CO_2 alter the rainfall amount? The ensemble mean forecast 2016 rainfall anomaly under current levels of CO_2 (Fig. 26.1a)

shows wet conditions across all of Australia. The area mean forecast anomaly for the model MDB region (25°–40°S, 140°–156°E) is +2.1 mm day^{-1}, similar to the observed anomaly of +2.7 mm day^{-1}, and the wettest in the modeled climatology (red bar at 2016 in Fig. 26.1e). Other forecast features align with observed conditions, including the heavy rain and the high sea surface temperatures (Fig. ES26.1a) to the north of Australia associated with the negative IOD, weak La Niña, and the pressure anomalies associated with positive SAM (http://poama.bom.gov.au/).

The rainfall forecast under low levels of CO_2 is slightly higher than under current levels of CO_2, thus the forecast rain under current conditions minus that under 1960 CO_2 levels (Fig. 26.1b) is slightly drier over most of the continent. The difference over the MDB region is −0.35 mm day^{-1}. The impact of CO_2 on the 2016 forecasts resembles the underlying rainfall change due to the last 55 years of CO_2 increase as shown by the September 2000–14 climatological difference in current minus low CO_2 rainfall (Figs. 26.1c,e), confirming that our 2016 experiments capture the modeled canonical response to changing CO_2 levels. This analysis suggests that the rainfall might have been even greater without increased levels of CO_2, although the difference is not statistically significant (at 10% level).

We next briefly explore whether there was a shift in the intensity of the daily rainfall. The frequency distributions of predicted daily rainfall intensities for both 2016 (Fig. ES26.2a) and the climatology (Fig. ES26.2b) do differ between forecasts under current or low CO_2 conditions. We see a greater proportion of days with very little rainfall (0–1.5 mm day^{-1}) and reduced proportion of days with moderate rainfall (2–5 mm day^{-1}) under current CO_2 levels. There are no discernible differences in the tails of the distributions of either the predicted event or the climatologies (Fig. ES26.2). The structure of this shift might mean that under current conditions, greater energy is required to instigate rainfall, but this could be pursued in a further study.

Did increased CO_2 alter the physical processes responsible for the rainfall? To better understand the regional physical processes responsible for the high rainfall in 2016 and their response to CO_2, we consider the forecast changes in available moisture, the circulation, and the atmospheric stability. The forecast 2016 precipitable water was extremely high over north and eastern Australia (Fig. 26.2a), moisture convergence over eastern Australia was strong (Fig. 26.2b: note
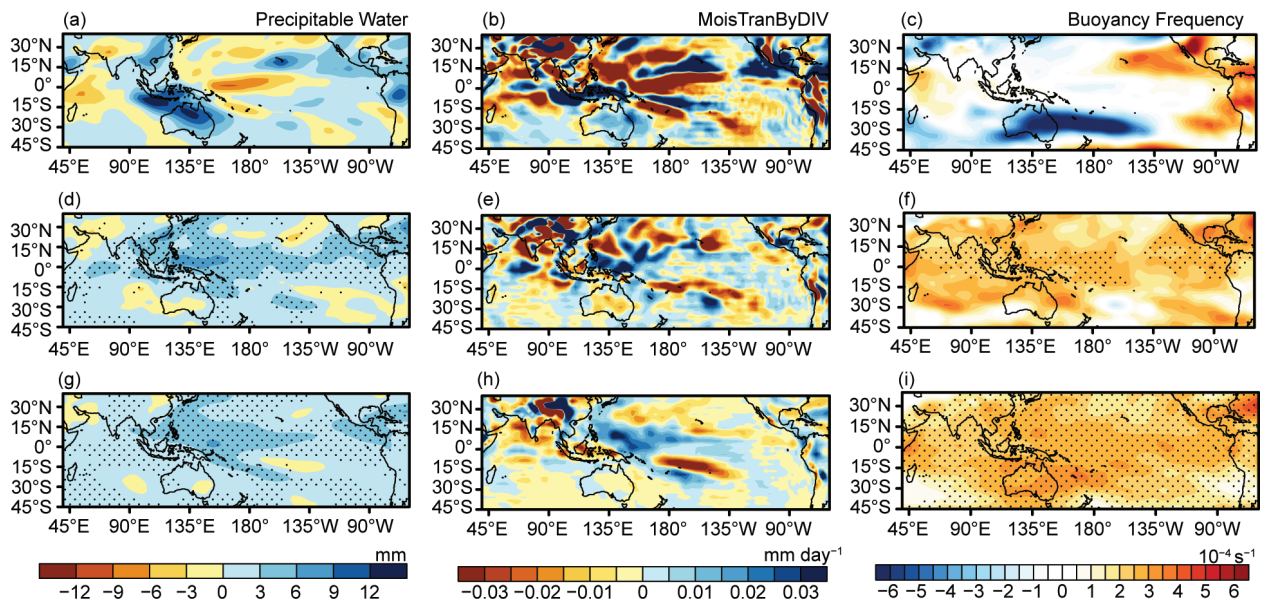
FIG. 26.2. (a) Precipitable water anomaly (mm), (b) moisture transport by divergence of anomalous winds (mm day^{-1}), and (c) midlevel (700–300 hPa) atmospheric stability as shown by buoyancy term, N (s^{-1}) of 15–28 Sep 2016 forecast anomaly (from 2000–14 climatology) (top panels). (d)–(f) Same as (a)–(c) but of difference in 2016 forecast with current and 1960 CO_2 conditions (middle panels). (g)–(h) The same as (a)–(c) but of climatological difference for current minus 1960 CO_2 levels. Stippling in left and right panels indicates statistically significant differences (10% level).

units of mm day^{-1}), and static stability was decreased as evidenced by large negative anomalies of midlevel atmospheric buoyancy (N) extending across Australia (Fig. 26.2c).

For these weeks in September, the influence resulting from the last 55 years of increasing CO_2 acted to increase the forecast precipitable water through most of the tropics including northern Australia (Fig. 26.2d), but there was little change over the MDB region. This is consistent with the current minus low CO_2 climatological difference (2000–14) in precipitable water (Fig. 26.2g). From the moisture budget analysis of the 2016 forecasts, the CO_2-induced change of moisture transport by wind divergence led to drying over southeast Australia, more so than in the climatological difference (Fig. 26.2h). Higher static stability was also simulated across Australia with increasing levels of CO_2 in 2016 (Fig. 26.2f), though this shift was weaker than that in the climatological difference (Fig. 26.2i). CMIP5 ALL-forcing historical simulations for 1960–2010 show atmospheric responses indicative of increased static stability, with a stronger warming trend in the upper troposphere (~0.35°C decade^{-1}) than in the lower troposphere (~0.27°C decade^{-1}) in the region of 20°S–20°N (Bindoff et al. 2013), which is weaker but still consistent with the temperature response in

POAMA2 experiments shown here, possibly as these are forced with the CO_2 change only.

Concluding remarks. A drier future is projected for the MDB in September at the end of the century by most climate models (CSIRO and Bureau of Meteorology, 2015; Hope et al. 2015), and results suggest that increasing levels of CO_2 over the last 55 years have already led to circulation and stability changes that would promote slightly drier conditions than in the 1960s, even for an extreme, two-week rainfall event. This study highlights the influence of changing levels of CO_2 alone, perhaps thus aligning more strongly with expected future changes and historical trends in models forced only with greenhouse gases compared to those attribution methods or models with all forcings (Bindoff et al. 2013).

REFERENCES

Allan, R. P., and B. J. Soden, 2008: Atmospheric warming and the amplification of precipitation extremes. *Science*, **321**, 1481–1484, doi:10.1126/science.1160787 .

Bindoff, N. L., and Coauthors, 2013: Detection and attribution of climate change: From global to regional. *Climate Change 2013: The Physical Science Basis*, T. F. Stocker et al., Eds., Cambridge University Press, 867–952.

Bony, S., G. Bellon, D. Klocke, S. Sherwood, S. Fermepin, and S. Denvil, 2013: Robust direct effect of carbon dioxide on tropical circulation and regional precipitation. *Nat. Geosci.*, **6**, 447–451, doi:10.1038/ngeo1799.

Bureau of Meteorology, 2016a: Special Climate Statement 57: Extensive early June rainfall affecting the Australian east coast. Bureau of Meteorology, 20 pp. [Available online at www.bom.gov.au/climate/current/statements/scs57.pdf.]

——, 2016b: Special Climate Statement 58: Record September rains continue wet period in much of Australia. Bureau of Meteorology, 31 pp. [Available online at www.bom.gov.au/climate/current/statements/scs58.pdf.]

Chen, Y.-R., B. Yu, and G. Jenkins, 2013: Secular variation in rainfall intensity and temperature in estern Australia. *J. Hydrometeor.*, **14**, 1356–1363, doi:10.1175/JHM-D-12-0110.1.

Colman, R. A., and B. J. McAvaney, 1997: A study of general circulation model climate feedbacks determined from perturbed sea surface temperature experiments. *J. Geophys. Res.*, **102**, 19383–19402, doi:10.1029/97JD00206.

——, and Coauthors, 2005: BMRC atmospheric model (BAM) version 3.0: Comparison with mean climatology. BMRC Research Rep. 108, Bureau of Meteorology Research Centre, 32 pp.

Cottrill, A., and Coauthors, 2013: Seasonal forecasting in the Pacific using the coupled model POAMA-2. *Wea. Forecasting*, **28**, 668–680, doi:10.1175/WAF-D-12-00072.1.

CSIRO and Bureau of Meteorology, 2015: *Climate Change in Australia: Projections for Australia's NRM Regions*. CSIRO and Bureau of Meteorology, Australia, 216 pp. [Available online at www.climatechangeinaustralia.gov.au/en/publications-library/technical-report/.]

Gallant, A. J. E., A. S. Kiem, D. C. Verdon-Kidd, R. C. Stone, and D. J. Karoly, 2012: Understanding climate processes in the Murray-Darling basin for natural resources management. *Hydrol. Earth Syst. Sci.*, **16**, 2049–2068, doi:10.5194/hess-16-2049-2012.

He, J., and B. J. Soden, 2016: A re-examination of the projected subtropical precipitation decline. *Nat. Climate Change*, **7**, 53–57, doi:10.1038/nclimate3157.

Held, I. M., and B. J. Soden, 2006: Robust responses of the hydrological cycle to global warming. *J. Climate*, **19**, 5686–5699, doi:10.1175/JCLI3990.1.

Hope, P., and Coauthors, 2015: Seasonal and regional signature of the projected southern Australian rainfall reduction. *Aust. Meteor. Oceanogr. J.*, **65**, 54–71. [Available online at www.bom.gov.au/jshess/docs/2015/hope1.pdf.]

——, G. Wang, E.-P. Lim, E.-P., H. H. Hendon, and J. M. Arblaster, 2016: What caused the record-breaking heat across Australia in October 2015? [in "Explaining Extreme Events of 2015 from a Climate Perspective"]. *Bull. Amer. Meteor. Soc.*, **97** (12), S122–S126, doi:10.1175/BAMS-D-16-0142.1.

Hudson, D., O. Alves, H. H. Hendon, and G. Wang, 2011: The impact of atmospheric initialisation on seasonal prediction of tropical Pacific SST. *Climate Dyn.*, **36**, 1155–1171, doi:10.1007/s00382-010-0763-9.

——, A. G. Marshall, Y. Yin, O. Alves, and H. H. Hendon, 2013: Improving intraseasonal prediction with a new ensemble generation strategy. *Mon. Wea. Rev.*, **141**, 4429–4449, doi:10.1175/MWR-D-13-00059.1.

Johnson, N. C., and S.-P. Xie, 2010: Changes in the sea surface temperature threshold for tropical convection. *Nat. Geosci.*, **3**, 842–845, doi:10.1038/ngeo1008.

King, A., 2017: Natural variability not climate change drove the record wet winter in southeast Australia. *Bull. Amer. Meteor. Soc.*, **99** (1), S139–S143, doi:10.1175/BAMS-D-0087.1.

Langford, S., and H. H. Hendon, 2013: Improving reliability of coupled model forecasts of Australian seasonal rainfall. *Mon. Wea. Rev.*, **141**, 728–741, doi:10.1175/MWR-D-11-00333.1.

Lim, E.-P., and H. H. Hendon, 2017: Causes and predictability of the negative Indian Ocean dipole and its impact on La Niña during 2016. *Sci. Rep.*, **7**, 12619, doi:10.1038/s41598-017-12674-z.

——, ——, J. M. Arblaster, C. Chung, A. F. Moise, P. Hope, G. Young, and M. Zhao, 2016: Interaction of the recent 50 year SST trend and La Nina 2010: Amplification of the Southern Annular Mode and Australian springtime rainfall. *Climate Dyn.*, **47**, 2273–2291, doi:10.1007/s00382-015-2963-9.

Schiller, A., J. S. Godfrey, P. C. McIntosh, G. A. Meyers, N. R. Smith, O. Alves, G. Wang, and R. Fiedler, 2002: A new version of the australian community ocean model for seasonal climate prediction. CSIRO Marine Research Rep. 240, 82 pp., doi:10.4225/08/585c1671163bd.

Seager, R., N. Naik, N., and G. A. Vecchi, 2010: Thermodynamic and dynamic mechanisms for large-scale changes in the hydrological cycle in response to global warming. *J. Climate*, **23**, 4651–4668, doi:10.1175/2010JCLI3655.1.

Vecchi, G. A., B. J. Soden, A. T. Wittenberg, I. M. Held, A. Leetmaa, and M. J. Harrison, 2006: Weakening of tropical Pacific atmospheric circulation due to anthropogenic forcing. *Nature*, **441**, 73–76, doi:10.1038/nature04744.

Wang, G., O. Alves, and N. Smith, 2005: BAM3.0 tropical surface flux simulation and its impact on SST drift in a coupled model. BMRC Research Rep. 107, 30 pp.

——, P. Hope, E.-P. Lim, H. H. Hendon, and J. M. Arblaster, 2016: Three methods for the attribution of extreme weather and climate events. Bureau of Meteorology Res. Rep. 018, 31 pp. [Available online at www.bom.gov.au/research/publications/researchreports/BRR-018.pdf.]

Watterson, I. G., Z.-W. Chua, and P. K. Hope, 2016: Extreme monthly rainfall over Australia in a changing climate. *J. South. Hemisphere Earth Syst. Sci.*, **66**, 402–423, doi:10.22499/3.6604.003.

Westra, S., and S. A. Sisson, 2011: Detection of non-stationarity in precipitation extremes using a max-stable process model. *J. Hydrol.*, **406**, 119–128, doi:10.1016/j.jhydrol.2011.06.014.

——, L. V. Alexander, and F. W. Zwiers, 2013: Global increasing trends in annual maximum daily precipitation. *J. Climate*, **26**, 3904–3918, doi:10.1175/JCLI-D-12-00502.1.

——, and Coauthors, 2014: Future changes to the intensity and frequency of short-duration extreme rainfall. *Rev. Geophys.*, **52**, 522–555, doi:10.1002/2014RG000464.

Yin, Y., O. Alves, and P. R. Oke, 2011: An ensemble ocean data assimilation system for seasonal prediction. *Mon. Wea. Rev.*, **139**, 786–808, doi:10.1175/2010MWR3419.1.

27. NATURAL VARIABILITY NOT CLIMATE CHANGE DROVE THE RECORD WET WINTER IN SOUTHEAST AUSTRALIA

ANDREW D. KING

Warmth in the east Indian Ocean increased the likelihood of the record wet July–September in southeast Australia by at least a factor two. The role of climate change was minimal.

Introduction. In July–September 2016, southeast Australia suffered from record-breaking wet conditions (Fig. 27.1a). This three-month wet period featured several significant extratropical low pressure systems culminating in a major system crossing the region that resulted in a power blackout across South Australia. While this wet period had many negative consequences, including multiple flood events, it also provided much-needed rainfall for farmers in a region of Australia home to a large volume of the country's food supply.

The 2016 wet extreme is not part of a trend towards wetter conditions (Fig. 27.1a). The event was associated with large quantities of moisture being advected from the eastern Indian Ocean, a region that was experiencing well-above average sea surface temperatures (Fig. 27.1b). This moisture interacted with extratropical weather systems crossing the south of the country (Bureau of Meteorology 2017). There was lower surface pressure than normal over southeast Australia (Fig. 27.1c), reflecting an equatorward movement in the storm track, and the moisture content of the atmosphere was higher than normal (Fig. 27.1d) in July–September 2016.

This study examines the roles of both human-induced climate change and natural climate variability in this event. The influences of these two factors on the circulation patterns conducive to unusually wet seasons and moisture availability are considered.

Data and methods. The observed precipitation anomalies (1961–90 baseline) are derived from the Australian Water Availability Project product (AWAP; Jones

et al. 2009). Over regions of the continent with relatively dense station coverage, like southeast Australia (SEA; 33°–45°S, 135°–155°E), AWAP performs well in capturing extreme rainfall variability and trends (King et al. 2013). The sea surface temperatures (SSTs) over the east Indian Ocean (EIO) region (0°–20°S, 90°–120°E) were extracted from HadISST (Rayner et al. 2003), and anomalies were also calculated from 1961–90. For both SEA rainfall and EIO SSTs the anomalies are calculated from the area-averaged time series for the July–September (JAS) period.

The mean sea level pressure (MSLP) and total column water vapor (TCWV) anomalies associated with the 2016 event were both calculated from the ERA-Interim reanalysis (Dee et al. 2011) with a 1981–2000 baseline period. The MSLP and TCWV anomalies were also calculated from the SEA-region area-average, over both land and sea grid boxes, whereas the rainfall anomalies were for land-only boxes. To estimate trends in these indices over a longer period, the ERA-20C reanalysis (Poli et al. 2016), which extends back to 1900, was used.

To assess the influence of anthropogenic climate change and natural climate variability from the EIO region, CMIP5 models (Taylor et al. 2012) were used. Simulations under both natural and anthropogenic forcings for the past (historical; 1860–2005) and future (RCP8.5; 2006–2100), and model simulations including only natural forcings (historicalNat; 1860–2005) were analyzed. Sixteen climate models, with at least three historical simulations, were analyzed initially (Table ES27.1). After evaluation (see online supplement information), nine of 16 CMIP5 models remained for further analysis (Table ES27.1).

The role of climate change was estimated through calculating the change in likelihood of wet JAS periods like 2016 (using a threshold of +30% rainfall anomaly) between the current world (2006–26 in RCP8.5 simulations) and a natural world (1901–2005 in historicalNat simulations). This is a relatively weak
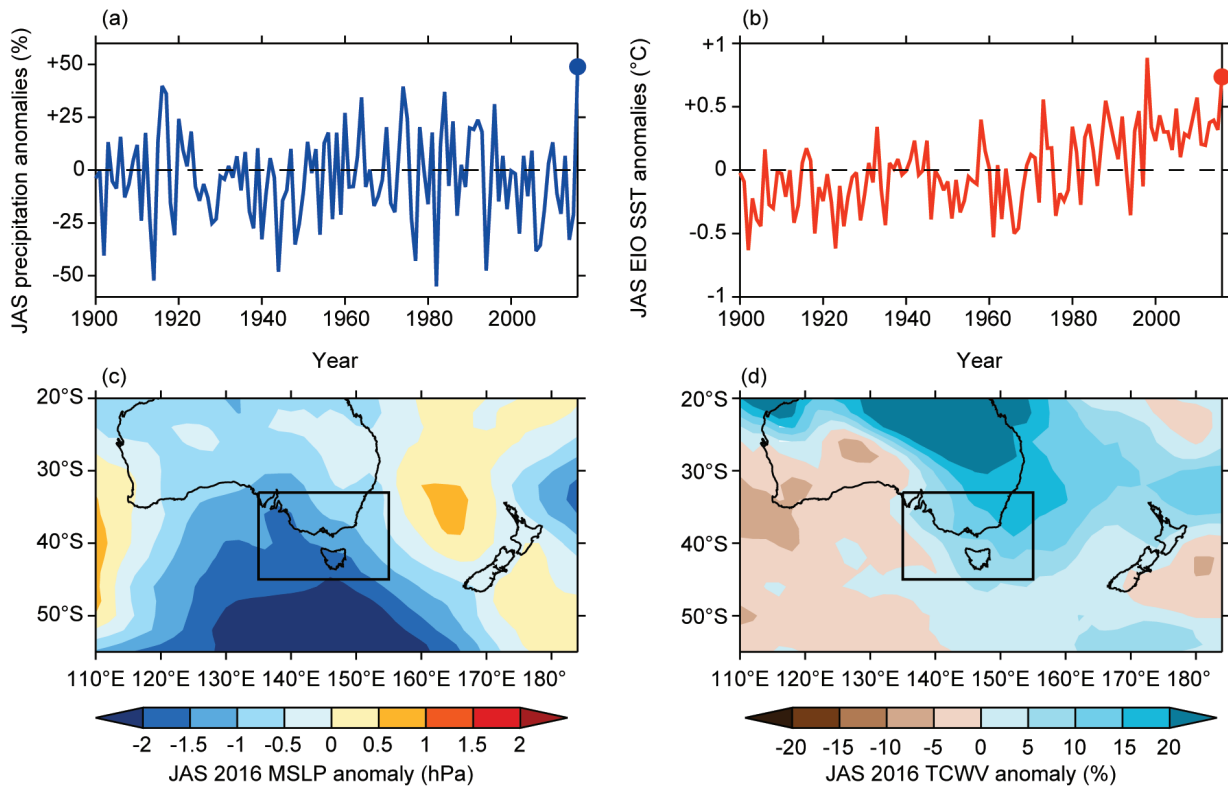
FIG. 27.1. Time series of Jul–Sep (a) SEA rainfall anomalies (%), and (b) EIO SST anomalies (°C), from a 1961–90 baseline with 2016 marked by a dot. Maps of Jul–Sep 2016 (c) mean sea level pressure anomalies (hPa), and (d) TCWV anomalies (%), from a 1981–2000 baseline (due to the length of ERA-Interim). Boxes indicate SEA region.

threshold chosen to increase statistical power. Uncertainties on the estimated change in likelihood were calculated by bootstrap resampling half of the simulations in each ensemble 10 000 times. Future changes in rainfall anomalies under a high greenhouse gas emissions scenario were also investigated (2040–60 in RCP8.5). This period was chosen to represent a near-future scenario with a little more than 2°C of global warming.

The influence of the warmth in the EIO SSTs was estimated by comparing the likelihood of wet JAS periods like 2016 (same threshold as previously) in seasons of above- and below-average detrended EIO SST anomalies in the current world ensemble (2006–26 in RCP8.5). Again, uncertainties on this change in likelihood were estimated through bootstrapping.

Due to a lack of TCWV model data, the climate change and EIO SST relationships with MSLP and TCWV over SEA and the surrounding region were investigated using ERA-20C instead. Correlations (Spearman rank) between EIO SSTs and SEA-average MSLP and TCWV were calculated and subsequent relationships with precipitation anomalies were assessed. The influence of climate change on these vari-

ables was examined through trends over 1900–2010 while the effect of warm EIO SST anomalies was investigated by compositing MSLP and TCWV detrended anomalies under warm EIO SST conditions (above +0.2°C detrended) and all other EIO SST values. Note that this does not constitute an attribution of changes in circulation and moisture to climate change and Indian Ocean SSTs, but it provides an indication of these relationships.

There is a warming trend in the EIO (Fig. 27.1b), but I focus on detrended EIO anomalies since these have a stronger relationship with SEA rainfall. The likely reason is due to the EIO being a source of Rossby waves influencing circulation over SEA (van Rensch and Cai 2014), so the EIO SST relative to other equatorial regions is of greater importance than the absolute EIO SST.

Results. THE ROLE OF ANTHROPOGENIC CLIMATE CHANGE. Human-induced climate change does not appear to be having a significant influence on the likelihood of wet JAS periods in SEA (Fig. 27.2a). High uncertainty exists even in the sign of the change in likelihood of wet JAS periods between the natural world and the
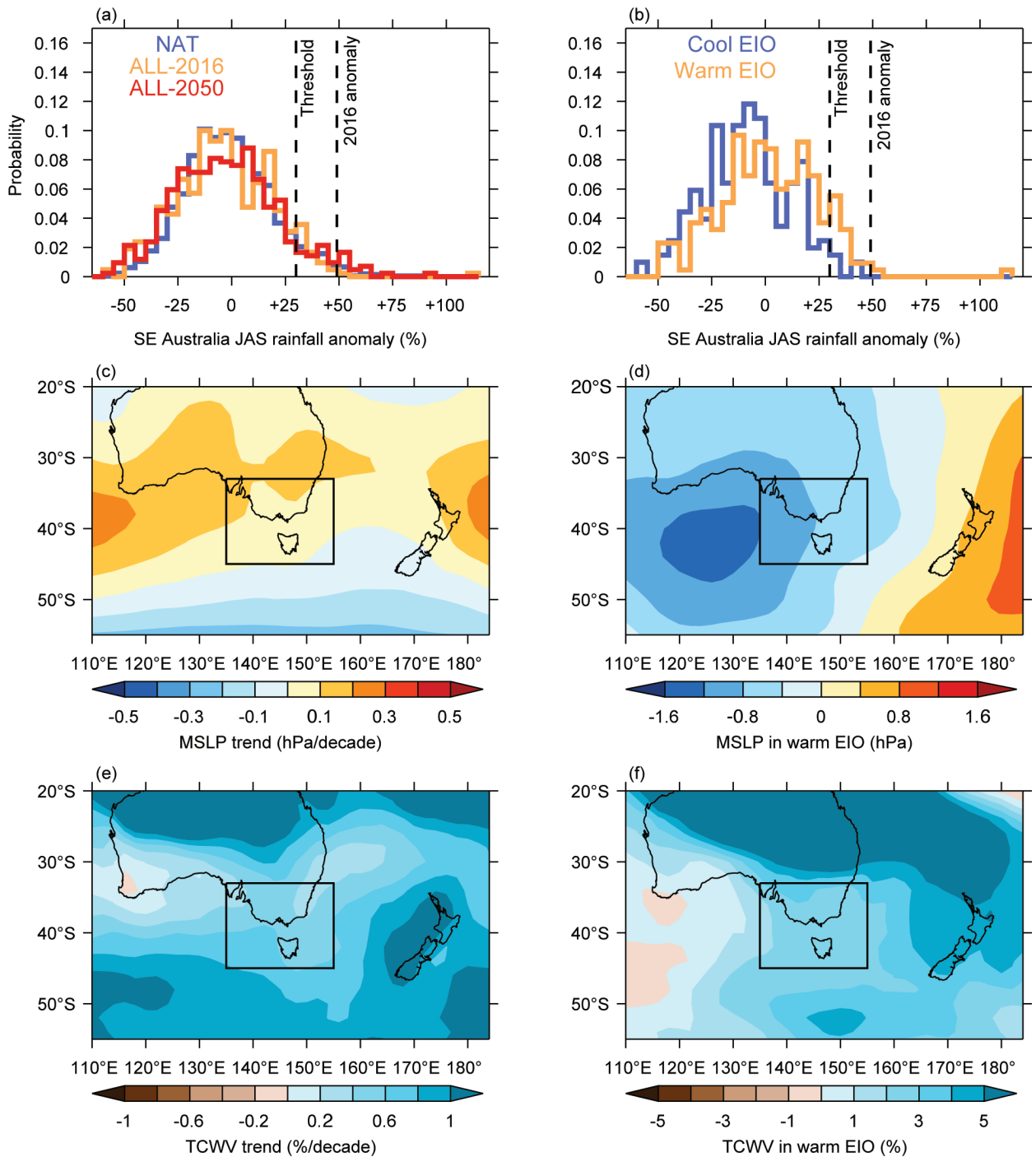
FIG. 27.2. (a) Probability distributions of Jul–Sep SEA rainfall anomalies (%) under natural climate influences only (blue), all climate influences in the current world (orange), and all climate influences in the world of 2050 under continued high greenhouse gas emissions (red). (b) Probability distributions of Jul–Sep SEA rainfall anomalies (%) under cool EIO conditions (blue) and warm EIO conditions (orange) in the current world. Dashed lines in (a) and (b) indicate the 2016 anomaly and the +30% threshold used in FAR calculations. (c) MSLP trend (hPa decade^{-1}) and (d) MSLP average anomalies (hPa) in warm EIO conditions. (e) TCWV trend (% decade^{-1}) and (f) TCWV average anomalies (%) in warm EIO conditions. Boxes indicate the SEA region.

current world based on the 10 000 bootstrapped sub-ensembles. The probability distributions of rainfall anomalies in the natural world and current world are not significantly different. The future world distribution is slightly wider (Fig. 27.2a) due to weak opposing trends in different models (not shown).

The influence of climate change appears to be toward an increase in MSLP (Fig. 27.2c; conducive to a decrease in JAS rainfall in SEA) and an increase in TCWV (Fig. 27.2e; conducive to an increase in JAS rainfall). These effects appear to be largely canceling each other out as demonstrated by the lack of a trend in observed (Fig. 27.1a) and simulated (Fig. 27.2a) rainfall over SEA. The tendency towards higher pressure over southern Australia is well-documented and is related to a poleward movement in the extratropical storm track during austral winter that is predominantly due to greenhouse gas emissions (e.g., Arblaster and Meehl 2006; Delworth and Zeng 2014), although it may, in part, also be related to stratospheric ozone depletion. Over the coming decades the storm track is expected to continue to move polewards due to increased greenhouse gas emissions, even as ozone levels recover (e.g., Bengtsson et al. 2006).

Human-induced climate change is also increasing the ability of the atmosphere to hold water vapor through the Clausius–Clapeyron effect. I do not consider shorter-term extreme rainfall for which the moisture availability and circulation changes may be less balanced.

THE ROLE OF THE EAST INDIAN OCEAN. There is a shift in the probability distributions between SEA rainfall associated with cool and warm EIO SST anomalies whereby warmer conditions favor wetter JAS periods. The warmth in the EIO increased the likelihood of the record wet JAS period in SEA by at least a factor two using the +30% rainfall anomaly threshold (Fig. 27.2b). No events under cool EIO conditions reach the observed JAS 2016 anomaly, and there were just five events above the +30% threshold in that ensemble.

Unlike the climate change influence, the effect of warm conditions in the EIO is to enhance conditions associated with wetter periods. Warmer conditions in the EIO tend to be associated with lower MSLP over the Great Australian Bight (Fig. 27.2d; conducive to higher JAS rainfall in SEA), and higher TCWV (Fig. 27.2f; also conducive to higher JAS rainfall). The water vapor relationship with SST anomalies in the EIO is stronger than the MSLP response to the SSTs (Fig. ES27.1). The EIO is a source region for an equivalent-barotropic Rossby wave train which influences MSLP to the south of Australia (van Rensch and Cai 2014), thus affecting atmospheric circulation in the region. In addition, moisture is advected over the continent during warm episodes in the EIO through northwest cloud bands and these often reach southern Australia and interact with frontal systems.

Conclusions. While the effect of human-induced climate change on this event appears to be minimal, it is estimated that the anomalous warmth in the EIO increased the likelihood of the wet July–September in southeast Australia by at least a factor two. Warmth in the EIO tends to both increase moisture availability and decrease surface pressure, resulting in rainfall increases. In contrast the effects of climate change on circulation and moisture largely cancel each other out.

It is interesting to note that a "mis-attribution" statement was possible in this study if the analysis had been designed more simplistically. I found a positive correlation between EIO SSTs and SEA rainfall, and I also show that EIO SSTs are increasing. Given that this trend is in part related to anthropogenic climate change (e.g., Roxy et al. 2014), an incorrect attribution of the record high rainfall in SEA to human influences could have been made. Also, a simplistic argument that human-caused climate change increases atmospheric water vapor, thus increasing the likelihood of wetter events, would have also been incorrect in this case. The circulation response to anthropogenic climate change is reducing the likelihood of high rainfall over SEA and counteracting the effect of increasing water vapor content. This study highlights the need for carefully designed attribution analyses.

REFERENCES

Arblaster, J. M., and G. A. Meehl, 2006: Contributions of external forcings to southern annular mode trends. *J. Climate*, **19**, 2896–2905, doi:10.1175/JCLI3774.1.

Bengttson, L., K. I. Hodges, and E. Roeckner, 2006: Storm tracks and climate change. *J. Climate*, **19**, 3518–543, doi:10.1175/JCLI3815.1.

Bureau of Meteorology, 2017: Special climate statement 58: Record September rains continue wet period in much of Australia. Bureau of Meteorology, 36 pp. [Available online at www.bom.gov.au/climate/current/statements/scs58.pdf.]

Dee, D. P., and Coauthors, 2011: The ERA-Interim reanalysis: Configuration and performance of the data assimilation system. *Quart. J. Roy. Meteor. Soc.*, **137**, 553–597, doi:10.1002/qj.828.

Delworth, T. L., and F. Zeng, 2014: Regional rainfall decline in Australia attributed to anthropogenic greenhouse gases and ozone levels. *Nat. Geosci.*, **7**, 583–587, doi:10.1038/ngeo2201.

Jones, D. A., W. Wang, and R. Fawcett, 2009: High-quality spatial climate data-sets for Australia. *Aust. Meteor. Oceanogr. J.*, **58**, 233–248.

King, A. D., L. V. Alexander, and M. G. Donat, 2013: The efficacy of using gridded data to examine extreme rainfall characteristics: a case study for Australia. *Int. J. Climatol.*, **33**, 2376–2387, doi:10.1002/joc.3588.

Poli, P., and Coauthors, 2016: ERA-20C: An atmospheric reanalysis of the 20th century. *J. Climate*, **29**, 4083–4097, doi:10.1175/JCLI-D-15-0556.1.

Rayner, N. A., D. E. Parker, E. B. Horton, C. K. Folland, L. V. Alexander, D. P. Rowell, E. C. Kent, and A. Kaplan, 2003: Global analyses of sea surface temperature, sea ice, and night marine air temperature since the late nineteenth century. *J. Geophys. Res.*, **108**, 4407, doi:10.1029/2002JD002670.

Roxy, M. K., K. Ritika, P. Terray, and S. Masson, 2014: The curious case of Indian Ocean warming. *J. Climate*, **27**, 8501–8509, doi:10.1175/JCLI-D-14-00471.1.

Taylor, K. E., R. J. Stouffer, and G. A. Meehl, 2012: An overview of CMIP5 and the experiment design. *Bull. Amer. Meteor. Soc.*, **93**, 485–498, doi:10.1175/BAMS-D-00094.1.

van Rensch, P., and W. Cai, 2014: Indo-Pacific–induced wave trains during austral autumn and their effect on Australian rainfall. *J. Climate*, **27**, 3208–3221, doi:10.1175/JCLI-D-13-00611.1.

28. A MULTIFACTOR RISK ANALYSIS OF THE RECORD 2016 GREAT BARRIER REEF BLEACHING

Sophie C. Lewis and Jennie Mallela

Anthropogenic greenhouse gases likely increased the risk of the extreme Great Barrier Reef bleaching event through anomalously high sea surface temperature and the accumulation of thermal stress.

Introduction. The 2016 global coral bleaching event was severe: 93% of the northern, 700km stretch, of the Australian Great Barrier Reef (GBR) coral was bleached and by June, >60% of this coral was killed in association with heat stress (Hughes et al. 2017; Fig. ES28.1). Bleaching occurred during an extended period of unprecedented global-average heat (Mann et al. 2016). Coral heat stress is accumulated through the magnitude and duration of temperatures above a threshold. A short-duration, high-magnitude event, or a long-duration low-magnitude event can cause bleaching, which is also moderated by thermal stress in preceding seasons (Ainsworth et al. 2016).

While heat stress impacts bleaching risk, coral reef health and resilience also integrates multiple environmental and biotic factors. Resilience is predetermined in part by ecosystem health that depends on historical disturbance events, the present day water quality (e.g., exposure to runoff) and the functional redundancy of the resident reef biota (Bellwood et al. 2003). These factors are also affected by anthropogenic activities (e.g., greenhouse gas emissions, overfishing, pollution), local weather, and large-scale modes of variability (ENSO). The 2016 ENSO episode was among the most severe recorded and may have impacted GBR bleaching.

The integration of multiple interrelated factors by reef ecosystems represents important considerations for attribution of bleaching. This study explores these complexities through a multifactor analysis of climatic and environmental influences contributing to the 2016 GBR bleaching.

Approach. Model and observational datasets were analyzed for ecosystem-relevant climatic and environmental variables (see online supplement). We investigate the influence of anthropogenic greenhouse gases (GHGs) and ENSO conditions on anomalously warm SSTs in the wider Coral Sea region that encompasses the GBR. Although the GBR occupies just a fraction of the Coral Sea region, its seasonal temperatures are highly correlated (Weller et al. 2008). We use CMIP5 climate model data (Taylor et al. 2012; Table ES28.1) to examine bleaching from a climate perspective. We use observational data from HadCRUT4 gridded (Morice et al. 2012) and NOAA OISSTV2 observed sea surface temperatures (SSTs; Reynolds et al. 2002) datasets. We explore a suite of climatic metrics (Fig. 28.1), motivated by the bleaching observed through early 2016 aerial surveys (Cressey 2016; Normile 2016), and

TABLE 28.1. Qualitative assessment of climatic and environmental factors contributing to the GBR bleaching events, with letters denoting primary (P) and secondary (S) influences that potentially made bleaching more likely to occur, and factors that potentially made bleaching less likely (L). Although influences are interrelated (for example, water quality is impacted by local rainfall, human activities, and the resulting runoff), they are broadly categorised as 'anthropogenic,' 'multiple,' or 'natural.'

Category	Factor	Risk of Bleaching		
		2016	2011	1998
Anthropogenic	Climate forcings (greenhouse gases)	P	S	S
Multiple	Local water quality	L	P	—
	Local climate variability	S	P	—
Natural	ENSO conditions	S	S	P
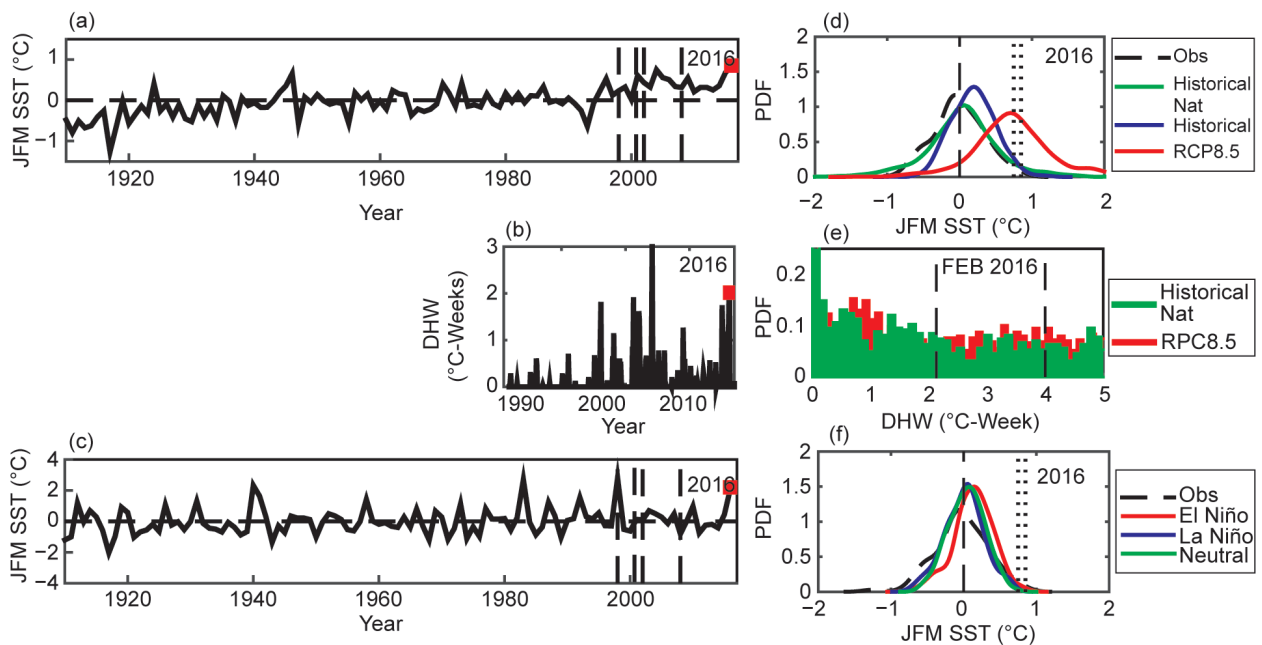
Fig. 28.1. (a) Observed Coral Sea JFM SST anomalies (°C; relative to 1961–90), **(b)** DHW (°C-week) with hottest month calculated over 1981–2016, and **(c)** NIÑO3.4 JFM SST anomalies (°C; relative to 1961–90). Probability density functions for **(d)** Coral Sea region JFM SST anomalies (°C; relative to 1961–90) for observations (dashed black, 1910–2016), historical (blue, 1976–2005 only), historicalNat (green, all years), and RCP8.5 (red, 2006–20) simulations. Vertical lines show bleaching events. **(e)** DHW (°C-week) is compared for historicalNat (green) and RCP8.5 (red), with 4°C-weeks threshold. **(f)** PDFs show comparison of Coral Sea JFM SST anomalies (°C; relative to 1961–90) in El Niño (red), La Niña (green), and neutral (blue) years in the historicalNat experiment.

the record high Coral Sea SSTs (region shown in Fig. 28.2a; Bureau of Meteorology 2016) and significant El Niño conditions observed in 2016.

Analysis of a broad suite of reef-relevant climate metrics allows deeper investigation of the climatic drivers of coral thermal stress. Ainsworth et al. (2016) recently demonstrated that background warming promotes thermal tolerance in reef-building corals and potentially mitigates bleaching events.. As such, a suite of climatic metrics is required. Metrics are:

Metric 1. *(Immediate heat stress)*: Assessed by JFM SSTs in the Coral Sea (Fig. 28.1a). Although both maximum and minimum SSTs are relevant to reef ecosystems, only mean SSTs are provided in CMIP5 (ts variable).

Metric 2. *(Antecedent and coincident heat stress)*: Assessed by the combination of MAM and antecedent (December–February, DJF) SSTs in the Coral Sea (Fig. ES28.2a; Glynn and D'croz 1990).

Metric 3. *(Cumulative stress):* Assessed by anomalously high extended Coral Sea SSTs diagnosed by degree heating week (DHW; Liu et al. 2003) in each month (Fig. 28.1b).

Metric 4. *(Regional conditions):* Assessed by SSTs in the Niño-3.4 region in JFM (Fig. 28.1c).

We further explore bleaching by examining local environmental data. Local stressors, such as degraded water quality, potentially reduce coral resilience to episodic thermal stress and drive bleaching occurrence (Mallela et al. 2016; Carilli et al. 2009; Wooldridge 2016a). By necessity, this study does not explicitly consider all climate and environmental factors that influence coral reef health, including the impact of tropical cyclone frequency and intensity, and natural shelf-edge upwelling. Data used are:

Metric 5. Precipitation anomalies (Fig. 28.2a), which are linked to cloud cover, temperatures and run off.

Metric 6. Cloudiness anomalies (Fig. 28.2b), as increased cloud cover potentially reduces UV exposure and ameliorates thermal stress.

Metric 7. Chlorophyll-a concentrations (Fig. 28.2c), which provide an estimate of the live phytoplankton biomass in the surface layer as a nutrient indictor.

Metric 8. Concentration of particulate organic carbon (Fig. 28.2d), as an indicator of water quality.

Climatic data are examined from an attribution perspective, using fraction of attributable risk (FAR) to quantify anthropogenic GHG influences on record

SST conditions in the Coral Sea (T1; and second hottest occurrence, T2 in 2004), with multimodel ensemble median and 10th percentile values given (see Lewis and Karoly 2013; 2014). Environmental data are examined from a qualitative perspective, providing information of environmental risk factors that impact reef resilience, and either promoted or inhibited bleaching during 2016. We also compare 2016 conditions with previous severe GBR bleaching events of 1997/98, 2001/02, 2005/06 and 2010/11, although the remotely sensed climatic and environmental datasets used here are of limited length, typically commencing in 2002.

Assessment of climatic factors. We compare the occurrence of threshold-exceeding events for Metrics 1–3 in the variously-forced CMIP5 experiments.

Metric 1. The frequency of JFM SST anomalies in the Coral Sea region exceeding T1 and T2 were compared for greenhouse gas (RCP8.5) and natural-only forced simulations (historicalNat; Fig. 28.1d). There is a significant increase in the likelihood of Metric 1 when anthropogenic forcings are included (Median FAR T1 = 0.85; 10th percentile FAR T1 = 0.80).

Metric 2. The 2016 observed conditions for combined antecedent and coincident SST anomalies (DJF, together with MAM conditions) do not occur in CMIP5 without anthropogenic forcings (Fig. ES28.2a).

Metric 3. An increase in accumulated heat in the Coral Sea region (as diagnosed by DHW; Fig. 28.1e) is evident in the RCP8.5 experiment, relative to the historicalNat experiment for °C-weeks above the 2016 values, including above the bleaching risk threshold of 4°C-weeks (Liu et al. 2013), although the FAR value is low (T4°C-weeks = 0.24).

Metric 4. Although Pacific Ocean conditions (Power et al. 1999) influence Australian climatic variability, the relationship between El Niño episodes and positive Coral Sea SST anomalies is weak in observations and CMIP5 simulations both including and excluding anthropogenic influences (Fig. ES28.2). In historicalNat experiments, the likelihood of extreme Coral Sea JFM SST anomalies is increased during El
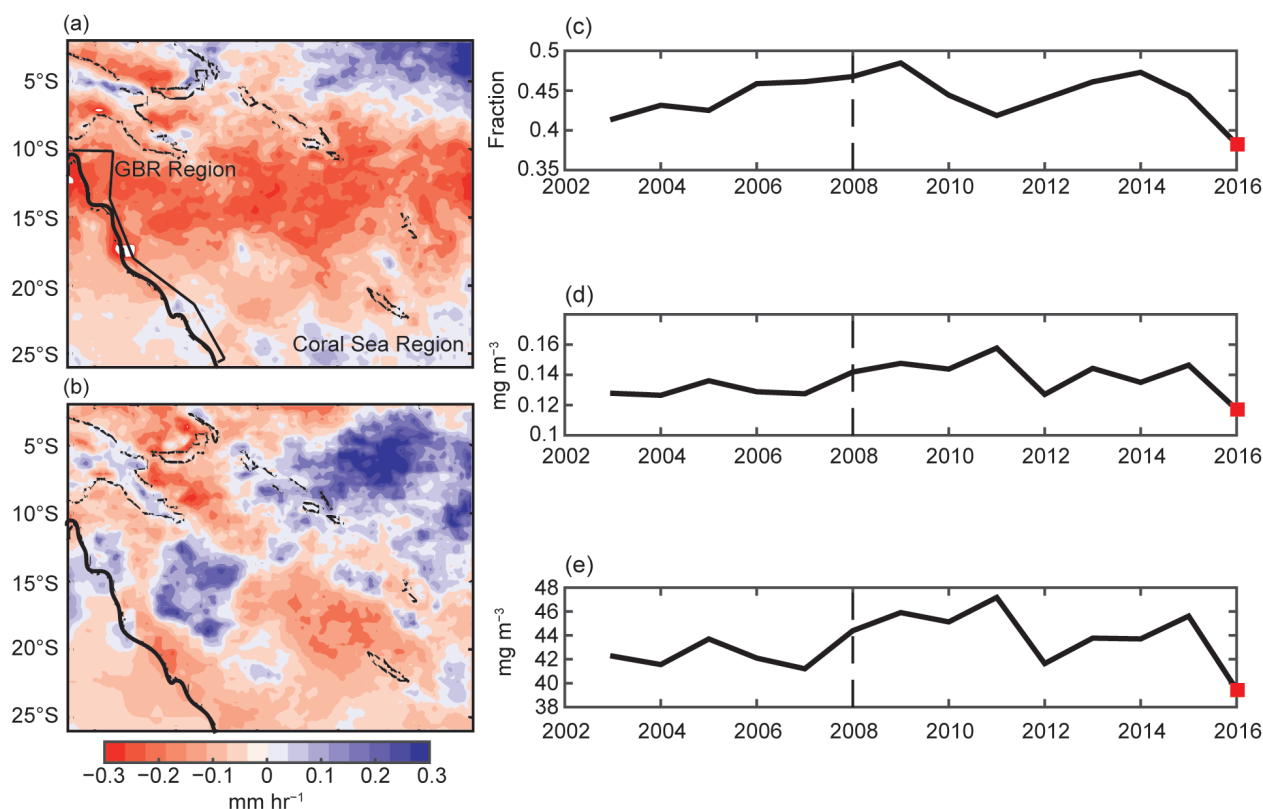
FIG. 28.2. Satellite-derived observational products for JFM precipitation anomalies in the Coral Sea region for (a) 2016 and (b)1998 (mm hr⁻¹; relative to 1998–2016 climatology from TRMM rainfall retrievals for 1998–2016), (c) cloud area fraction (%; daytime) from AIRS/*Aqua* retrieval, 1° × 1° for 2002–16), (d) chlorophyll-*a* concentration (mg m⁻³; from MODIS–*Aqua* 4-km monthly data), and (e) particulate organic carbon (mg m⁻³; from MODIS–*Aqua* 4-km monthly data). The general location of the GBR is shown in (a).

Niño phases (Median FAR T1 = 0.94; 10th percentile FAR T1 = 0.88, relative to La Niña). The distribution of Coral Sea temperatures during El Niño episodes without greenhouse gases is similar to La Niña events in the RCP8.5 experiment.

Assessment of environmental factors. Potential environmental and local coral stressors were examined qualitatively.

Metric 5 and 6. Lower than average JFM rainfall was observed in the Coral Sea region in 2016 (Fig. 28.2a). Regional rainfall can impact coral through several mechanism; increased land-based rainfall impacts runoff levels and water quality (Graham et al. 2015), while decreased rainfall may be associated with reduced cloud cover and increased temperatures (Nicholls 2003). In 2016, reduced Coral Sea rainfall may have increased the risk of bleaching, in combination with increased temperatures. Reduced cloud cover fraction was also observed in 2016, which can impact bleaching through increasing UV exposure (Fig. 28.2b; Leahy et al. 2013).

Metric 7 and 8. Concentrations of chlorophyll-a and particulate organic carbon (Figs. 28.2b,c) were considered as metrics of local water quality and drivers of bleaching risk during JFM. Corals located at sites with better water quality (reduced particulates and nutrient levels) were less prone to bleaching during previous events (Mallela et al. 2016). In 2016, nutrient loads occurred relative to previous years, which may indicate improved water quality and a lower bleaching risk, compared to the long-term average.

Assessment of bleaching drivers. We examined interrelated climatic and environmental conditions in the Coral Sea that altered the risk of GBR bleaching in 2016 (Table 28.1). Analysis demonstrates that anthropogenic GHG-forced trend in regional SSTs had a dominant impact on bleaching resulting in the record high antecedent and coincident SSTs in 2016 (Metrics 1 and 2), and accumulated heat over this period (Metric 3). A combination of natural climate variability and the 2016 El Niño episode also contributed to ocean conditions resulting in the bleaching (Metrics 4, 5, and 6). Hence, the 2016 extreme thermal stress was due to the added effects of natural variability and ENSO imposed on a regional anthropogenic increase in SSTs.

The Coral Sea ocean conditions resulting in the 2016 GBR bleaching were the result of a confluence of increased risk from anthropogenic GHG-forced trend in regional SSTs, weak El Niño forcing and natural variability (Table 28.1). Differences relative to the 1997/98 massive but less severe bleaching event (~43%; Hughes et al. 2017), were extremely strong eastern equatorial Pacific El Niño conditions (Figs. ES28.1a,b). The differences in the flavor of El Niño contributed to local SSTs lower in 1998 than 2016 and higher precipitation (Figs. 28.2a,b). Higher local temperatures than 1997/98 were observed in 2001/02 (~56%) and 2005/06 when bleaching again occurred (Fig. 28.1a). In contrast, during the 2010/11 bleaching, record high rainfall (Bureau of Meteorology 2012) and runoff contributed to freshwater, rather than thermal stress. While differences in anthropogenic GHG forced trend in regional SSTs were negligible between 2016 and 2015, the additional impacts from the El Niño–Coral Sea SST relationship, combined with other natural climate variability influences, were sufficient to trigger the record 2016 bleaching.

Our study demonstrates that GHG warming of regional sea surface temperatures was the primary increase in risk for the 2016 GBR bleaching. This assessment indicates the risk of future bleaching may become more likely with further greenhouse warming, and that local environmental factors, such as water quality and upwelling will have increasingly limited capacity to remediate anthropogenic drivers of temperature-induced bleaching (Wooldridge 2016b). Furthermore, explorations of drivers of reef bleaching require explicit consideration of biological processes, environmental stressors, ENSO dynamics, anthropogenic warming and their interactions, as bleaching events likely have different drivers.

REFERENCES

Ainsworth, T. D., S. F. Heron, J. C. Ortiz, P. J. Mumby, A. Grech, D. Ogawa, E. C Mark, and W. Leggat, 2016: Climate change disables coral bleaching protection on the Great Barrier Reef. *Proc. Natl. Acad. Sci.*, **352**, 338–342, doi:10.1126/science.aac7125.

Bellwood, D. R., A. S. Hoey, and J. H. Choat, 2003: Limited functional redundancy in high diversity systems: resilience and ecosystem function on coral reefs. *Ecol. Lett.*, **6**, 281–285, doi:10.1046/j.1461-0248.2003.00432.x/full.

Bureau of Meteorology, 2012: Special Climate Statement 38—Australia's wettest two-year period on record; 2010–2011. [Australia] Bureau of Meteorology, 10 pp. [Available online at www.bom.gov.au/climate/current/statements/scs38.pdf.]

——, 2016: Special Climate Statement 56—Australia's warmest autumn on record. [Australia] Bureau of Meteorology, 21 pp. [Available online at www.bom.gov.au/climate/current/statements/scs56.pdf.]

Carilli, J. E., R. D. Norris, B. A. Black, S. M. Walsh, and M. McField, 2009: Local stressors reduce coral resilience to bleaching. *PLoS One*, **4**, e6324, doi:10.1371/journal.pone.0006324.

Cressey, D., 2016: Coral crisis: Great Barrier Reef bleaching is "the worst we've ever seen." *Nature*, doi:10.1038/nature.2016.19747.

Glynn, P. W., and L. D'croz, 1990: Experimental evidence for high temperature stress as the cause of El Niño-coincident coral mortality. *Coral Reefs*, **8**, 181–191, doi:10.1007/BF00265009.

Graham, N. A. J., S. Jennings, M. A. MacNeil, D. Mouillot, and S. K. Wilson, 2015: Predicting climate-driven regime shifts versus rebound potential in coral reefs. *Nature*, **518**, 94–97, doi:10.1038/nature14140.

Hughes, T. P., and Coauthors, 2017: Global warming and recurrent mass bleaching of corals. *Nature*, **543**, 373–377, doi:10.1038/nature21707.

Leahy, S. M., M. J. Kingsford, and C. R. Steinberg, 2013: Do clouds save the Great Barrier Reef? Satellite imagery elucidates the cloud-SST relationship at the local scale. *PLoS One*, **8**, e70400–e70412, doi:10.1371/journal.pone.0070400.

Lewis, S. C., and D. J. Karoly, 2013: Anthropogenic contributions to Australia's record summer temperatures of 2013. *Geophys. Res. Lett.*, **40**, 3705–3709, doi:10.1002/grl.50673.

——, and ——, 2014: The role of anthropogenic forcing in the record 2013 Australia-wide annual and spring temperatures [in "Explaining Extremes of 2013 from a Climate Perspective"]. *Bull. Amer. Meteor. Soc.*, **95** (9), S31–S34.

Liu, G., A. E. Strong, and W. Skirving, 2003: Remote sensing of sea surface temperatures during 2002 Barrier Reef coral bleaching. *Eos, Trans. Amer. Geophys. Union*, **84**, 137–141, doi:10.1029/2003EO150001.

——, J. L. Rauenzahn, S. F. Heron, C. M. Eakin, W. Skirving, T. R. L. Christensen, A. E. Strong, and J. Li, 2013: NOAA Coral Reef Watch 50 km satellite sea surface temperature-based decision support system for coral bleaching management. NOAA Tech. Rep. NESDIS 143, 41 pp. [Available online at https://coralreefwatch.noaa.gov/satellite/publications/NOAA.Tech.Report.143.pdf.]

Mallela, J., S. Hetzinger, and J. Halfar, 2016: Thermal stress markers in *Colpophyllia natans* provide an archive of site-specific bleaching events. Coral Reefs, **35**, 181–186, doi:10.1007/s00338-015-1350-7.

Mann, M. E., S. Rahmstorf, B. A. Steinman, M. Tingley, and S. K. Miller, 2016: The likelihood of recent record warmth. *Sci. Rep.*, **6**, 19831, doi:10.1038/srep19831.

Morice, C. P., J. J. Kennedy, N. A. Rayner, and P. D. Jones, 2012: Quantifying uncertainties in global and regional temperature change using an ensemble of observational estimates: The HadCRUT4 data set. *J. Geophys. Res.*, **117**, D08101, doi:10.1029/2011JD017187.

Nicholls, N., 2003: Continued anomalous warming in Australia. *Geophys. Res. Lett.*, **30**, 1370, doi:10.1029/2003GL017037.

Normile, D., 2016: Survey confirms worst-ever coral bleaching at Great Barrier Reef. *ScienceInsider*, doi:10.1126/science.aaf9933.

Power, S., T. Casey, C. Folland, A. Colman, and V. Mehta, 1999: Inter-decadal modulation of the impact of ENSO on Australia. *Climate Dyn.*, **15**, 319–324, doi:10.1007/s003820050284.

Reynolds, R. W., N. A. Rayner, T. M. Smith, D. C. Stokes, and W. Wang, 2002: An improved in situ and satellite SST analysis for climate. *J. Climate*, **15**, 1609–1625, doi:10.1175/1520-0442(2002)015<1609:AIISAS>2.0.CO;2.

Taylor, K. E., R. J. Stouffer, and G. A. Meehl, 2012: An overview of CMIP5 and the experiment design. *Bull. Amer. Meteor. Soc.*, **93**, 485–498, doi:10.1175/BAMS-D-11-00094.1.

Weller, E., M. Nunez, G. Meyers, and I. Masiri, 2008: A climatology of ocean–atmosphere heat flux estimates over the Great Barrier Reef and Coral Sea: Implications for recent mass coral bleaching events. *J. Climate*, **21**, 3853–3871, doi:10.1175/2007JCLI2085.1.

Wooldridge, S. A., 2016a: Excess seawater nutrients, enlarged algal symbiont densities and bleaching sensitive reef locations: 1. Identifying thresholds of concern for the Great Barrier Reef, Australia. *Mar. Pollut. Bull.*, in press, doi:10.1016/j.marpolbul.2016.04.054.

——, 2016b: Understanding coral bleaching risk factors in the remote far-northern Great Barrier Reef (GBR) that make obvious the best "local" management option for maximising the capacity of the GBR to resist thermal stress and bleaching. CTRMS Research Pub. 01. Catchment to Reef Management Solutions, Newcastle, NSW, Australia, 35 pp.

29. SEVERE FROSTS IN WESTERN AUSTRALIA IN SEPTEMBER 2016

Michael R. Grose, Mitchell Black, James S. Risbey, Peter Uhe, Pandora K. Hope, Karsten Haustein, and Dann Mitchell

Human influence may have enhanced the circulation pattern that drives cold outbreaks and frost risk over southwest Western Australia in September 2016, but larger thermodynamic changes may have still made these events less likely.

Introduction. The wheat belt of southwest Western Australia (SWWA) experienced several severe frosts just before harvest in September 2016, leading to a loss of one million tonnes of grain crops (GIWA 2016). Using the Jones et al. (2009) gridded observation dataset, there were 18 frost-risk nights (Tmin <2°C) somewhere in the grain belt through the month and the September frost area and frequency was extensive (Fig. 29.1a), the highest since 1956. The highest count at any grid cell was 13 frost-risk nights, with 9 severe frost-risk nights (Tmin <0°C). Many places saw the highest number of September frost nights since reliable records began in 1910, with most of the region in the top five years (Fig. 29.1b). SWWA also saw below-average rainfall and humidity, southerly monthly wind anomalies, and cool sea surface temperatures (SSTs) immediately adjacent to SWWA in September. There were weak La Niña and negative Indian Ocean Dipole conditions during September.

The effect of human influence on cold extremes is the net result of two influences: rising temperatures of the climate mean state and forced changes to circulation. The SWWA region has warmed by around 1°C since 1910, suggesting a reduction in frost risk (BOM and CSIRO 2016). However, greenhouse gas forcing may drive an increase in the frequency or intensity of some cold extremes through an effect on circulation features, offsetting or countering the effect of the rising mean temperature. There is a hypothesized link between climate change and a shift in circulation linked to increased cold extremes in the northern hemisphere (e.g., Cohen et al. 2014; Zhang et al. 2016; Mann et al. 2017). In some regions of southern Australia, frost frequency and the length of the frost season has been increasing despite an increase in mean temperature in all seasons (Crimp et al. 2016). The driver of the increase is not completely clear but may be linked to circulation changes forced by greenhouse gases. An increase in pressure around the midlatitudes has been attributed to greenhouse gases (e.g., Gillett et al. 2013). This trend has included an intensification of the subtropical ridge, but the ridge has only a weak connection to frost risk through promoting clear skies. The link to frosts may be more a function of the particular mean sea level pressure (MSLP) anomalies.

Cold outbreaks and frost risk in SWWA are often associated with a positive MSLP anomaly over the Indian Ocean west of Australia and a negative MSLP anomaly across southern and southeastern Australia, advecting cold air from the south of Australia over SWWA (Ashcroft et al. 2009; Pook et al. 2011). Numerous days in September 2016 showed this MSLP signature, expressed as slow moving blocking highs in the Indian Ocean sector at ~40°S. An important question, therefore, is whether this circulation anomaly was made more likely due to greenhouse forcing. The peak of blocking in the southeast Australian sector in winter is projected to weaken and move eastward (Grose et al. 2017). However, blocking in the Indian Ocean sector in spring may have a different response. Indeed, exceptionally high MSLP south of Australia in August 2014 was more likely due to human influence (Grose et al. 2015), and this was linked to blocking highs.
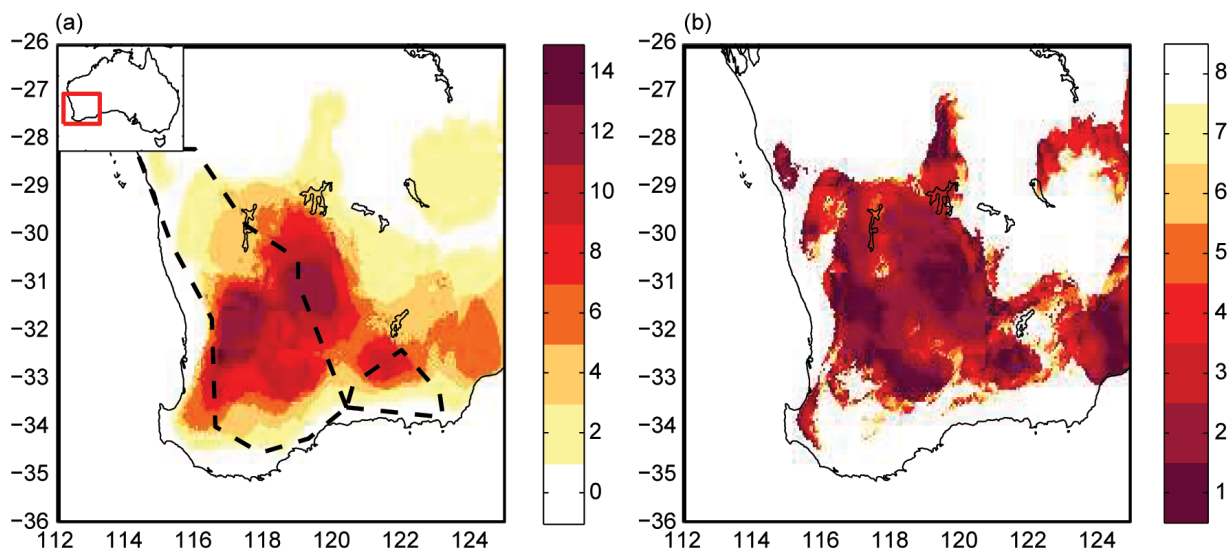
FIG. 29.1. (a) Frost risk nights (Tmin <2°C) in Sep 2016 in the AWAP gridded dataset [number of nights (out of 30)], dashed line shows rough outline of SWWA wheat belt, inset shows the location of SWWA within Australia; (b) rank of Sep 2016 frost frequency within the 1910–2016 record.

While there have been studies on trends in frosts (e.g., Crimp et al. 2016), there have been no previous studies showing a link between a particular cold extreme event or frosts and human influence. Here we examine the SWWA September frosts and whether the MSLP and blocking may have offset or countered the mean warming effects.

Methods. We examined daily minimum temperature, MSLP, the blocking index and blocking events using the Tibaldi and Molteni (1990) index in ERA-Interim reanalysis (Dee et al. 2011), the global *weather@home* modeling system version 2 (Guillod et al. 2017) and the seasonal climate forecasting system Predictive Ocean Atmosphere Model for Australia (POAMA; Hope et al. 2016; Wang et al. 2016).

We examined the difference in circulation between 165 *weather@home* simulations of September 2016 with observed forcings (Factual simulations) and 287 *weather@home* simulations of a counterfactual September 2016 without human influence (Counterfactual simulations). Ensembles were generated by running the model with perturbed atmospheric initial conditions. The Factual simulations used observed SSTs and sea ice, as well as present-day atmospheric composition (long-lived greenhouse gases, ozone, and aerosols). The Counterfactual simulations used SSTs modified to remove different estimates of the warming attributable to anthropogenic forcing and preindustrial atmospheric composition. Estimates of the SST changes due to anthropogenic forcing were separately calculated using twelve CMIP5 models

(Taylor et al. 2012) and the mean of those models (Table ES29.1). These patterns are the difference between the SSTs in the CMIP5 models' historical and historicalNAT simulations and are not the same as warming in observed datasets. The number of simulations from each model did not yield a sufficient sample size, so we examine 287 Counterfactual simulations as a group. Climatologies of 1986–2015 for Factual and Counterfactual were also examined.

POAMA forecasts were initialized after the first week of September 2016 and run for the last 3-week period of the month, see Hope et al. (2018) for more detail. Two 44-member ensemble forecasts were made—one under current levels of carbon dioxide (Factual) and another that removes the influence of the last 55 years of carbon dioxide increase on the ocean warming, atmospheric radiation balance, and land (Counterfactual; see Wang et al. 2016). Note that the POAMA system accounts for changes in greenhouse gases; it does not account for changes in ozone or aerosol. Climatologies for the years 2000–14 under both high and low levels of carbon dioxide were also examined.

The seasonal means of *weather@home* geopotential height in the region are similar to reanalysis (Guillod et al. 2017), and some midlatitude circulation features relevant to extreme temperatures in the northern hemisphere are well reproduced but with too many short-lived blocking events (Mitchell et al. 2017). The Tebaldi and Molteni blocking index and frequency of detections near SWWA is fairly similar between *weather@home* and ERA-Interim

(Fig. ES29.1). POAMA is similar to reanalysis in terms of broad circulation (Wang et al. 2016), but underestimates the strength and frequency of blocking (Marshall et al. 2014).

Results. Examining the observed circulation component of the frost risk, we see enhanced September MSLP west of SWWA and a low anomaly in southeast Australia and a southerly 850-hPa wind anomaly of 2.3 m s^{-1} at the south coast of SWWA (Fig. 29.2a), which is consistent with the typical cold outbreak events (Ashcroft et al. 2009). The monthly MSLP anomaly reflects the presence of persistent highs adjacent to SWWA on many days (not shown), particularly through the middle of the month. In

daily data, MSLP was enhanced at 70°–110°E by up to 18 hPa and/or diminished in the region 110°–140°E with southerly wind anomalies over SWWA on many of the days.

Monthly *weather@home* MSLP was higher in Factual compared to Counterfactual west of SWWA (Fig. 29.2b), creating a higher monthly southerly 850 hPa wind anomaly at the south coast of SWWA (Counterfactual mean was 2.1 m s^{-1}; Factual mean was 2.4 m s^{-1}, giving an enhancement of +0.3 m s^{-1}). Even though these wind anomalies do not penetrate inland, they suggest greater transport of cold air into the broader region and an enhancement of the circulation anomaly favoring frost nights in SWWA. The negative MSLP anomaly in southeast Australia was
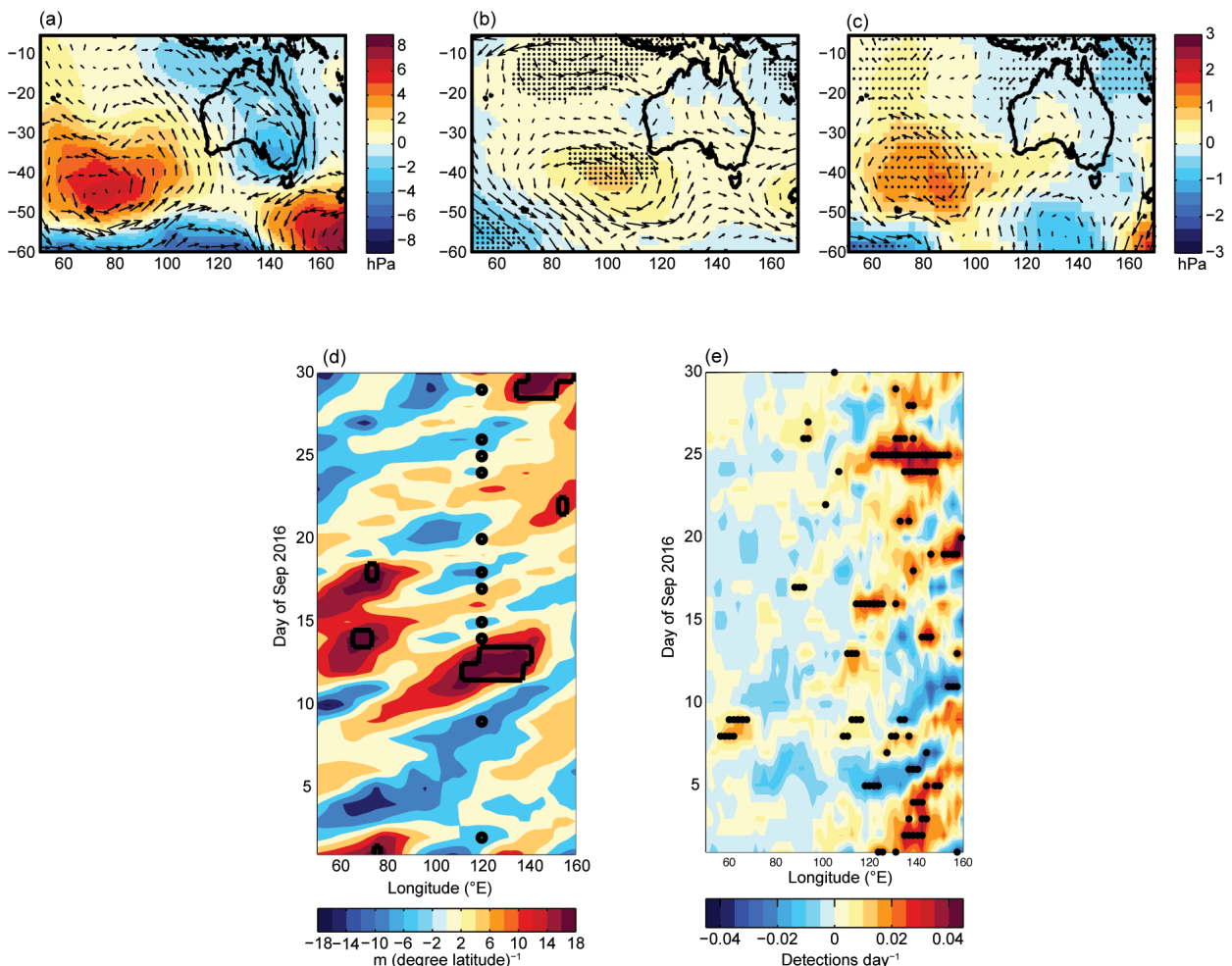
FIG. 29.2. MSLP, wind, and blocking in ERAint and models in Sep 2016; (a) ERAint monthly MSLP anomaly from 1979–2016 mean, arrows indicate the 850-hPa wind anomaly; (b) Factual–Counterfactual MSLP difference in *weather@home* mean, stippling shows where the difference is significant at the 10% level (t test), arrows show the Factual–Counterfactual 850-hPa wind difference; (c) as in (b) in POAMA; (d) ERA-Interim daily blocking index anomaly from 1979–2016 mean, black outlines indicate detected blocking events (no minimum event length threshold applied) and black circles indicate frost events at the approximate longitude of SWWA; (e) Factual–Counterfactual Blocking mean blocking event detections (detections day^{-1}) in *weather@home*, stippling shows where the difference is significant at the 10% level (t test).

not enhanced in Factual compared to Counterfactual (Fig. 29.2b). In daily data, there was higher MSLP west of SWWA and a southerly 850-hPa wind anomaly over SWWA in the ensemble mean of Factual compared to Counterfactual in 14 of the 30 days, with some anomalies over 2 hPa (Fig. ES29.2). POAMA shows a similar MSLP difference in Factual–Counterfactual for the month as *weather@home*, and an enhancement of the southerly wind anomaly at the south coast of SWWA (1.7 m s^{-1} in Counterfactual; 2.1 m s^{-1} in Factual, giving an +0.4 m s^{-1} anomaly; Fig. 29.2c). The wind signal over the wheat belt itself is weaker in POAMA than in *weather@home*; however, the MSLP signal west of SWWA is stronger.

Enhancement of MSLP west of SWWA was also found in the difference between the *weather@home* 1986–2015 Factual September climatology and the equivalent for Counterfactual, and between the POAMA 15-year September climatology of 2000–14 under current levels of carbon dioxide relative to the climatology with low levels (not shown). The consistency between the 2016 results and the climatologies suggests that the pattern is related to the change in the mean state of the atmosphere. The fact that POAMA shows a change similar to *weather@home* suggests that the changes in global carbon dioxide levels are of most importance in driving this signature, rather than ozone or aerosol changes (POAMA accounts only for changes in greenhouse gases; *weather@home* accounts for all forcings).

The blocking index was higher than average near SWWA on many days in September 2016, with seven blocked days detected within 60°–140°E (Fig. 29.2d). Blocking was typically positive to the west of SWWA on the day of or prior to frosts (Fig. 29.2d). On 24 days during the month, there were significantly more blocking days detected in Factual simulations than in Counterfactual somewhere in the sector (stippled red regions in Fig. 29.2e), with only five days where there were significantly fewer (stippled blue). For example, on 25 September 2016 the mean detections at 140°E in Counterfactual is 0.03 detections day^{-1}, and this was enhanced by up to 0.04 detections day^{-1} in Factual. We don't expect the modeled timing of blocks to be precisely in phase with observations, so the exact timing of these differences is not the focus, but the *weather@home* results indicate a greater detection of blocked days on average across the region throughout.

weather@home showed warmer daily minimum temperatures and fewer frost risk days in the Factual simulations compared to the Counterfactual simulations (significant at the 5% level), suggesting

that the frost risk was lower due to human influence (Fig. ES29.3). Using a FAR analysis, experiencing 13 frost nights at a site in the wheat belt was in fact 45% less likely in Factual compared to Counterfactual. POAMA simulations also showed lower numbers of frost-risk days in Factual compared to Counterfactual (not shown). If the models simulated all the relevant processes regarding daily Tmin with sufficient fidelity, then these results suggest that the circulation influence due to human influence did not fully offset the effect from a warmer mean temperature, so the net human influence was for fewer frosts. However, it is also likely that the models did not simulate all the dynamics required to produce frost nights, so the forced circulation difference may not have been expressed correctly in daily Tmin. For example, the coarse resolution of the model may prevent the simulation of relevant mesoscale meteorological processes, and indeed the frequency in the Factual is lower than in the observed (Figs. 29.1a and ES29.3b).

Conclusion. Differences in MSLP, winds, and blocking between Factual and Counterfactual simulations from two modeling systems suggest that the circulation pattern associated with cold outbreaks was enhanced by human influence over southwest Western Australia in September 2016. However, the results also suggest warmer temperatures may have offset or countered this effect of the circulation driver on the overall frost risk for the month. Further work is needed to support this preliminary finding, including an assessment of the simulation of the circulation features and of minimum temperatures.

REFERENCES

Ashcroft, L., A. Pezza, and I. Simmonds, 2009: Cold events over Southern Australia: Synoptic climatology and hemispheric structure. *J. Climate*, **22**, 6679–6698, doi:10.1175/2009JCLI2997.1.

BOM and CSIRO, 2016: State of the Climate 2016. Bureau of Meteorology and CSIRO, 22 pp. [Available online at www.bom.gov.au/state-of-the-climate/State-of-the-Climate-2016.pdf.]

Cohen, J., and Coauthors, 2014: Recent Arctic amplification and extreme mid-latitude weather. *Nat. Geoscience*, **7**, 627–637, doi:10.1038/ngeo2234.

Crimp, S. J., D. Gobbett, P. Kokic, U. Nidumolu, M. Howden, and N. Nicholls, 2016: Recent seasonal and long-term changes in southern Australian frost occurrence. *Climatic Change*, **139**, 115–128, doi.org/10.1007/s10584-016-1763-5.

Dee, D. P., and Coauthors, 2011: The ERA-Interim reanalysis: configuration and performance of the data assimilation system. *Quart. J. Roy. Meteor. Soc.*, **137**, 553–597, doi:10.1002/qj.828.

Gillett, N. P., J. C. Fyfe, and D. E. Parker, 2013: Attribution of observed sea level pressure trends to greenhouse gas, aerosol, and ozone changes. *Geophys. Res. Lett.*, **40**, 2302–2306, doi:10.1002/grl.50500.

GIWA, 2016: October crop report [2016]. Grain Industry Association of Western Australia, 5 pp. [Available online at www.giwa.org.au/_literature_220446/GIWA_Crop_Report_-_October_2016.]

Grose, M. R., J. S. Risbey, M. T. Black, and D. J. Karoly, 2015: Attribution of exceptional mean sea level pressure anomalies south of Australia in August 2014 [in "Explaining Extreme Events of 2014 from a Climate Perspective"]. *Bull. Amer. Meteor. Soc.*, **96** (12), S158–S162, doi:10.1175/BAMS-D-15-00116.1.

——, ——, A. F. Moise, S. Osbrough, C. Heady, L. Wilson, and T. Erwin, 2017: Constraints on Southern Australian rainfall change based on atmospheric circulation in CMIP5 simulations. *J. Climate*, **30**, 225–242, doi:10.1175/JCLI-D-16-0142.1.

Guillod, B. P., and Coauthors, 2017: weather@home 2: Validation of an improved global–regional climate modelling system. *Geosci. Model Dev.*, **10**, 1849-1872, doi:10.5194/gmd-10-1849-2017.

Hope, P., E.-P. Lim, G. Wang, H. H. Hendon, and J. M. Arblaster, 2016: What caused the record-breaking heat across Australia in October 2015? [in "Explaining Extreme Events of 2015 from a Climate Perspective"]. *Bull. Amer. Meteor. Soc.*, **97** (12), S122–S126, doi:10.1175/BAMS-D-16-0142.1.

——, ——, H. H. Hendon, and G. Wang, 2018: The effect of increasing CO_2 on the extreme September 2016 rainfall across south eastern Australia [in "Explaining Extreme Events of 2016 from a Climate Perspective"]. *Bull. Amer. Meteor. Soc.*, **99** (1), S133–S138, doi: 10.1175/BAMS-D-17-0094.1.

Jones, D. A., W. Wang, and R. Fawcett, 2009: High-quality spatial climate data-sets for Australia. *Aust. Meteor. Oceanogr. J.*, **58**, 233–248.

Mann, M. E., S. Rahmstorf, K. Kornhuber, B. A. Steinman, S. K. Miller, and D. Coumou, 2017: Influence of anthropogenic climate change on planetary wave resonance and extreme weather events. *Sci. Rep.*, **7**, 45242, doi:10.1038/srep45242.

Marshall, A. G., D. A. Hudson, H. H. Hendon, M. J. Pook, O. Alves, and M. C. Wheeler, 2014: Simulation and prediction of blocking in the Australian region and its influence on intra-seasonal rainfall in POAMA-2. *Climate Dyn.*, **42**, 3271–3288, doi:10.1007/s00382-013-1974-7.

Mitchell, D., and Coauthors, 2017: Assessing mid-latitude dynamics in extreme event attribution systems. *Climate Dyn.*, **48**, 3889–3901, doi:10.1007/s00382-016-3308-z.

Pook, M. J., J. S. Risbey, and P. C. McIntosh, 2011: The synoptic climatology of cool-season rainfall in the central wheatbelt of Western Australia. *Mon. Wea. Rev.*, **140**, 28-43, doi:10.1175/MWR-D-11-00048.1.

Taylor, K. E., R. J. Stouffer, and G. A. Meehl, 2012: An overview of CMIP5 and the experiment design. *Bull. Amer. Meteor. Soc.*, **93**, 485–498, doi:10.1175/BAMS-D-00094.1.

Tibaldi, S. and F. Molteni, 1990: On the operational predictability of blocking. *Tellus A*, 42, 343–365, doi:10.1034/j.1600-0870.1990.t01-2-00003.x

Wang, G., P. K. Hope, E.-P. Lim, H. H. Hendon, and J. M. Arblaster, 2016: Three methods for the attribution of extreme weather and climate events. [Australia] Bureau of Meteorology Research Rep. 018, 32 pp. [Available online at www.bom.gov.au/research/publications/researchreports/BRR-018.pdf.]

Zhang, J., W. Tian, M. P. Chipperfield, F. Xie, and J. Huang, 2016: Persistent shift of the Arctic polar vortex towards the Eurasian continent in recent decades. *Nat. Climate Change*, **6**, 1094–1099, doi:10.1038/nclimate3136.

30. FUTURE CHALLENGES IN EVENT ATTRIBUTION METHODOLOGIES

Peter A. Stott, Nikos Christidis, Stephanie C. Herring, Andrew Hoell,
James P. Kossin, and Carl J. Schreck III

Since these reports began five years ago, they have played an important part in the development and remarkable advancement of the science of event attribution. At the start of this endeavor, only a few events had been studied, geographical coverage was limited, and the focus had been mainly on extreme temperature events. Now, the range of events covered includes rain storms, droughts, tropical storms, and wildfires, as well as heat waves.

The website Carbon Brief[1] has produced a graphical inventory of studies from this report along with other peer-reviewed literature. It shows a growing geographical coverage over the last five years and a developing wealth of evidence pointing to the significant effects of human-induced climate change on many extreme events. The majority of attribution studies have been published in these annual reports. This demonstrates the important role these reports have taken, thanks to the continuing engagement by the scientific community in this endeavor.

The breadth and depth of these articles demonstrate a notable developing maturity of this science. At the same time, a few important challenges still remain, and this latest report highlights three of these. They are: 1) the role of methodological choices in determining the outcome of event attribution studies; 2) the need to better assess the influence of human-induced climate change on the impacts of extreme events; and 3) the growing needs of a wider range of stakeholders to inform decision making.

First, it is becoming increasingly apparent that different methodological choices can lead to important differences in the results of event attribution studies. To take one example from this report, the study of the air pollution episode in Europe in December 2016 (Vautard et al. 2018) found different results depending on the type of climate model used. With a multimodel

---

[1] www.carbonbrief.org/mapped-how-climate-change-affects-extreme-weather-around-the-world

AFFILIATIONS: Herring—NOAA/National Centers for Environmental Information, Boulder, Colorado; Hoell and Kossin—NOAA/National Centers for Environmental Information, Madison, Wisconsin; Schreck—Cooperative Institute for Climate and Satellites–North Carolina, North Carolina State University, Asheville, North Carolina; Stott—Met Office Hadley Centre and University of Exeter, Exeter, United Kingdom

ensemble, a significant human-induced effect was found on the stagnant winter time conditions that prevailed over northwestern Europe during that month, but this was not found with two single-model ensembles. The record 2016 heat in Asia was found not to be possible without human-caused climate change, and the authors concluded the fraction of attributable risk (FAR) to climate change was effectively 1. This result is based on the atmospheric general circulation model (AGCM) simulations using the observed sea surface temperatures (SST). Thus, it is suggested that "the observed heat anomaly have zero probability of occurrence with the certain, observed, SST variability pattern." However, it is not clear how the FAR would be impacted if the uncertainty of the natural variability of SST were considered.

Attribution results are potentially sensitive to methodological choices. Thus, it is important to clearly communicate the methodological choices within each study and, when possible, also to explore such methodological sensitivities in the study itself. In last year's issue, we included additional information on the methods used in the summary Table 1.1 (pages S4–S5), and this year we continue with this additional contextual information. Even so, there is an ongoing debate in the scientific community about the effects of methodological choices and optimal strategies for attribution of extreme events. For example, two recent companion pieces in *Climatic Change* took alternative viewpoints about the role of statistical paradigms in event attribution studies (Mann et al. 2017; Stott et al. 2017). Further work is needed to fully understand the effects such choices are having, as summarized by the statistics in Table 1.1 of the results in this report (p. S4).

Second, clearly much more should be done to better assess any links between the impacts of extreme

events to human-induced climate change. Traditionally, those who are part of the impacts community have focused on assessing the extent to which impacts such as changes in ecosystems can be attributed to variations in climate, howsoever caused. Ultimately, however, if we wish to make statements about links between impacts and human-induced climate change we need to differentiate possible natural climatic effects from human-induced ones. This is a challenge. We have been keen to encourage contributions to this latest report that address impacts. The submissions provide important new information but also illustrate the challenges in making such links.

Brainard et al. find that coral reef and seabird communities were disrupted by the record-setting sea surface temperatures of the central equatorial Pacific during the 2015/16 El Niño. This, by linking a particular meteorological event to impacts on marine ecosystem, is in itself an important conclusion. But this conclusion by itself would not be sufficient to be included in this issue because it does not assess the link to anthropogenic climate change. However, by making a link to a companion paper in this issue by Newman et al., which shows evidence that record warm central equatorial Pacific temperatures during the 15/16 El Niño reflect an anthropogenically forced trend, Brainard et al. are able to make an indirect two-step link to human-induced climate change. Such a two-step approach as illustrated here in Brainard et al. has been recognized by IPCC as a suitable method for attributing impacts (Hegerl et al. 2009). The value of this type of information to the marine resource management community is included as a Perspectives piece co-authored by the NOAA National Marine Fisheries chief scientist (Webb and Werner 2018). The authors describe the value of attribution results that assess the different drivers impacting living marine resources when making management decisions, in particular for considering potential future impacts to resources such as fisheries stocks.

Third, as the science matures and a mounting focus builds on possible links between extreme events and climate change, with a view to better adapting and to better partitioning the costs of climate change, there is increasing interest in applying this science. In the legal field, for example, there is an argument that attribution studies can be used to help courts determine liability for climate-related harm (Marjanan et al. 2017). In the past, beyond the scientific community, these results have primarily been used with stakeholders for whom very rapid analyses may be particularly relevant, for example those engaged in building resilience in the aftermath of an extreme event, or the media and other climate change science communicators. Today, stakeholders have expanded to include those involved in the regulatory, legal, and management frameworks who increasingly may find such approaches potentially useful.

While it represents a considerable challenge to provide robust results that are clearly communicated for stakeholders to use as part of their decision-making processes, these annual reports are increasingly showing their potential to help meet such growing needs. By taking a middle road in terms of timescale of delivery—longer than the very rapid results needed by the media but shorter than many academic contributions—and by using relatively standard approaches that have been previously peer reviewed, advances being made in these reports point the way forward toward a greater use of event attribution studies in decision-making contexts.

REFERENCES

Brainard, R., and Coauthors, 2018: Ecological impacts of the 2015/16 El Niño in the central equatorial Pacific. *Bull. Amer. Meteor. Soc.*, **99** (1), S21–S26, doi:10.1175/10.1175/BAMS-D-17-0128.1.

Hegerl, G. C., O. Hoegh-Guldberg, G. Casassa, M. P. Hoerling, R. S. Kovats, C. Parmesan, D. W. Pierce, and P. A. Stott, 2010: Good practice guidance paper on detection and attribution related to anthropogenic climate change. *Intergovernmental Panel on Climate Change Expert Meeting on Detection and Attribution of Anthropogenic Climate Change,* T. F. Stocker et al., Eds. IPCC Working Group I Technical Support Unit, Bern, Switzerland, 8 pp. [Available online at https://wg1.ipcc.ch/guidancepaper/IPCC_D&A_GoodPractice GuidancePaper.pdf.]

Mann, M. E., E. A. Lloyd, and N. Oreskes, 2017: Assessing climate change impacts on extreme weather events: the case for an alternative (Bayesian) approach. *Climatic Change*, **144**, 131–142, doi:10.1007/s10584-017-2048-3.

Marjanan, S., L. Patten, and J. Thornton, 2017: Acts of God, human influence and litigation. *Nat. Geosci.*, **10**, 616–619, doi:10.1038/ngeo3019.

Newman, M., A. Wittenberg, L. Cheng, G. P. Compo, and C. A. Smith, 2018: The extreme 2015/16 El Niño, in the context of historical climate variability and change, [in "Explaining Extreme Events of 2016 from a Cliamte Perspective"]. *Bull. Amer. Meteor. Soc.*, **99** (1), S16–S20,10.1175/10.1175/BAMS-D-17-0116.1.

Stott, P. A., D. J., Karoly, and F. W. Zwiers, 2017: Is the choice of statistical paradigm critical in extreme event attribution studies? *Climatic Change*, **144**, 143–150, doi:10.1007/s10584-017-2049-2.

Vautard, R., A. Colette, E. van Meijgaard, F. Meleux, G. J. van Oldenborgh, F. Otto, I. Tobin, and P. Yiou, 2018: Attribution of wintertime anticyclonic stagnation contributing to air pollution in western Europe [in "Explaining Extreme Events of 2016 from a Climate Perspective"]. *Bull. Amer. Meteor. Soc.*, **99** (1), S70–S75, doi:10.1175/D-17-0113.1.

Webb, R. S., and F. E. Werner, 2018: Explaining extreme ocean conditions impacting living marine resources [in "Explaining Extreme Events of 2016 from a Climate Perspective"]. *Bull. Amer. Meteor. Soc.,* **99** (1), S7–S10, doi:10.1175/D-17-0265.1.

Coral bleaching at Lizard Island

A panoramic image of the coral bleaching at Lizard Island in Australia
captured by the XL Catlin Seaview Survey in March 2016.